

Molecular imaging as a tool in drug delivery, oncology, and regenerative medicine

Citation for published version (APA):

Silva Leitao Gomes Sanches, da, P. (2014). *Molecular imaging as a tool in drug delivery, oncology, and regenerative medicine*. [Phd Thesis 1 (Research TU/e / Graduation TU/e), Biomedical Engineering]. Technische Universiteit Eindhoven. <https://doi.org/10.6100/IR781432>

DOI:

[10.6100/IR781432](https://doi.org/10.6100/IR781432)

Document status and date:

Published: 26/11/2014

Document Version:

Publisher's PDF, also known as Version of Record (includes final page, issue and volume numbers)

Please check the document version of this publication:

- A submitted manuscript is the version of the article upon submission and before peer-review. There can be important differences between the submitted version and the official published version of record. People interested in the research are advised to contact the author for the final version of the publication, or visit the DOI to the publisher's website.
- The final author version and the galley proof are versions of the publication after peer review.
- The final published version features the final layout of the paper including the volume, issue and page numbers.

[Link to publication](#)

General rights

Copyright and moral rights for the publications made accessible in the public portal are retained by the authors and/or other copyright owners and it is a condition of accessing publications that users recognise and abide by the legal requirements associated with these rights.

- Users may download and print one copy of any publication from the public portal for the purpose of private study or research.
- You may not further distribute the material or use it for any profit-making activity or commercial gain
- You may freely distribute the URL identifying the publication in the public portal.

If the publication is distributed under the terms of Article 25fa of the Dutch Copyright Act, indicated by the "Taverne" license above, please follow below link for the End User Agreement:

www.tue.nl/taverne

Take down policy

If you believe that this document breaches copyright please contact us at:

openaccess@tue.nl

providing details and we will investigate your claim.

Molecular imaging as a tool in drug
delivery, oncology, and
regenerative medicine

PROEFSCHRIFT

ter verkrijging van de graad van doctor aan de
Technische Universiteit Eindhoven, op gezag van de
rector magnificus prof.dr.ir. C.J. van Duijn,
voor een commissie aangewezen door het College
voor Promoties, in het openbaar te verdedigen op
woensdag 26 november 2014 om 14:00 uur

door

Pedro da Silva Leitão Gomes Sanches

geboren te Lissabon, Portugal

Dit proefschrift is goedgekeurd door de promotoren en de samenstelling van de promotiecommissie is als volgt:

voorzitter: prof.dr. P.A.J. Hilbers
1^e promotor: prof.dr. H. Gröll
copromotor(en): prof.dr. K. Nicolay
leden: prof.dr. K. Kostarelos (University of Manchester)
prof.dr.med. F. Kiessling (RWTH Aachen University)
prof.dr. C.T.W. Moonen (UU-UMCU)
prof.dr. Silvio Aime (Università degli Studi di Torino)
prof.dr. C.V.C. Bouten

Financial support by Philips for the publication of this thesis is gratefully acknowledged.

This project was funded in part by the EU Project Sonodrugs (NMP4-LA-2008-213706).

Cover design: T rence Coton
Printed by: Ipskamp Drukkers

A catalogue record is available from the Eindhoven University of Technology Library
ISBN: 978-90-386-3722-8

Copyright   P.G. Sanches, 2014

CONTENTS

CHAPTER 1: Introduction: Molecular imaging as a tool in (pre)clinical research	5
CHAPTER 2: See, reach, treat: ultrasound-triggered image-guided drug delivery	15
CHAPTER 3: Real-time imaging and kinetics measurements of focused ultrasound-induced extravasation in skeletal muscle using SPECT/CT	27
CHAPTER 4: Ultrasound-mediated gene delivery of naked plasmid DNA in skeletal muscles: a case for bolus injections	55
CHAPTER 5: Bone metastasis imaging with SPECT/CT/MRI: a preclinical toolbox for therapy studies	81
CHAPTER 6: Imaging regeneration: the axolotl way	113
CHAPTER 7: General discussion	147

Ethical paragraph

Summary

Acknowledgements

Curriculum Vitae

List of Publications



Introduction:

**Molecular imaging as a
tool in (pre)clinical
research**

Diagnostic imaging and molecular imaging

Diagnostic imaging plays a pivotal role in healthcare for diagnosis of diseases, staging, and during the follow-up period of a therapy. The radiological techniques Ultrasound (US), Magnetic Resonance Imaging (MRI), and Computed Tomography (CT) are mainly used to gain morphological information, where each imaging modality has its particular strengths in terms of sensitivity, contrast generation, spatial or temporal resolution [1, 2]. All of above techniques provide images based on natural contrast present in the body but can also be used in combination with contrast agents that have been developed for each modality. The nuclear imaging techniques Single Photon Emission Computed Tomography (SPECT) and Positron Emission Tomography (PET) generate images based on radiation emitted from administered radiotracers with a sensitivity that allows detection of nano- to picomolar tracer concentrations. The complementary character of radiological and nuclear imaging techniques led to multimodal imaging approaches, such as PET/CT, SPECT/CT or PET/MRI that allow quantification and localization of radiotracers within the morphological context. The possibility of above imaging technologies to provide non-invasive information about diseases and, in the widest sense, biological research questions, triggered the use of imaging as a research tool in preclinical and translational research. This trend spurred the development of dedicated imaging systems for small laboratory animals that provide higher resolution and sensitivity compared to the clinical systems. Also on the agent side, more contrast and imaging agents have been developed and are used in preclinical and biological research. The application of imaging systems together with specific agents to non-invasively visualize biological processes on tissue, cellular or even molecular level *in vivo* was coined "molecular imaging" [3, 4]. At the same time, optical techniques such as fluorescence or bioluminescence that were previously used in cellular studies have been developed further into preclinical *in vivo* imaging techniques. The strength of these optical techniques is the detection of optical active probes with high sensitivity. As penetration depth of light is limited, these techniques are applied mainly in small animals or in dedicated medical applications, where light absorption in tissue is not limiting. Yet, light absorption and scattering impairs gathering of quantitative data. Table 1.1 gives an overview over the different imaging techniques in the clinical and preclinical setting.

For application in molecular imaging, the applied techniques and obtained images have to fulfill certain criteria, mainly quantification, sensitivity, and reproducibility [1]. Above criteria also ask for standardization to allow comparison of images obtained with systems from different vendors, or comparative imaging studies across different laboratories. The possibility to gather quantitative images over time is also essential to gain temporal information about biological processes, such as tumor growth, metastasis

formation or tumor response to therapy. The development of existing and new molecular imaging technologies is progressing at an enormous pace and many breakthroughs are expected in the coming years. Many more imaging options exist that were not discussed here in view of space restrictions and the scope of this work, but have been extensively reviewed by others [2].

Table 1.1 Overview of common molecular imaging modalities.

Technique	Resolution*	Depth	Time**	Quantitative***	Target	Main small animal use	Clinical use
MRI	10-100 μm	no limit	minutes to hours	yes	anatomical, physiological, molecular	versatile imaging modality	yes
CT	50 μm	no limit	minutes	yes	anatomical, physiological	imaging lungs and bone	yes
Ultrasound	50 μm	cm	seconds to minutes	yes	anatomical, physiological	vascular and interventional imaging	yes
PET	1-2 mm	no limit	minutes to hours	yes	physiological, molecular	versatile imaging modality with many tracers	yes
SPECT	1-2 mm	no limit	minutes to hours	yes	physiological, molecular	imaging labeled antibodies, proteins and peptides	yes
Bioluminescence imaging	several mm	cm	minutes	no	molecular	gene expression, cell and bacterium tracking	no

Legend: *for high resolution small animal imaging systems (clinical imaging systems differ); **time for image acquisition; ***quantitative here means inherently quantitative. All approaches allow relative quantification. Table adapted from [4].

Imaging agents

For the radiological imaging methods US, MRI, CT, agents exist that either enhance existing contrast or add new contrast and are therefore termed “contrast agents”. For the nuclear modalities PET and SPECT, radiolabeled agents are the essential source of radiation that is visualized and quantified. These agents are termed imaging agents or radiotracers. In below text, “imaging agent” is used within the context of molecular imaging as a more general term and comprises contrast as well as imaging agents or radiotracers (Table 1.2).

Table 1.2 *Imaging agents.*

Technique	Main property of imaging agents	Example type of imaging agent
CT	electro dense material	iodinated molecules
MRI	paramagnetic ions	Gd ³⁺ chelate
US	echogenicity	encapsulated gas microbubbles
PET	pairs of 511 keV gamma photons	positron emitting isotopes
SPECT	isotropic gamma photons	gamma emitting isotopes
Bioluminescence imaging	light photons	photons from enzymatic reactions

Molecular imaging makes use of specific imaging agents that report on a biological process of interest. An imaging agent needs to possess two functionalities as it has to be “observable and quantifiable” for the respective imaging modality while, if targeted, having an entity that provides biological targeting. For the latter, different mechanisms can be exploited. Imaging agents can be designed to target biological pathways leading to e.g. an entrapment and accumulation of agents in cells of interest, or to bind to intracellular or extracellular targets (Fig. 1.1). A plethora of different targeting moieties exist based on e.g. small molecules, peptides or antibodies that were modified with a signal providing entity, e.g. fluorescent groups, paramagnetic chelates, or radionuclides. Irrespectively of the exact mechanism, above agents lead to an observable signal via accumulation at the place of interest. Optical and MR agents can be designed that change their contrast upon interaction with targets. For paramagnetic MR agents, interaction with a target leads typically to a modulation of physico-chemical properties that translate into a change of the spin-spin or spin-lattice relaxation rate and thus to a change of the observed MR contrast [5]. For optical probes, interaction with a substrate can modulate the optical properties that lead to an observable change of the optical properties [4, 6]. On the other hand, reactive probes will only send a signal upon interaction with their target. The enzyme luciferase, used in BLI, is an example of a reactive probe as it only emits light upon interaction with its substrate.

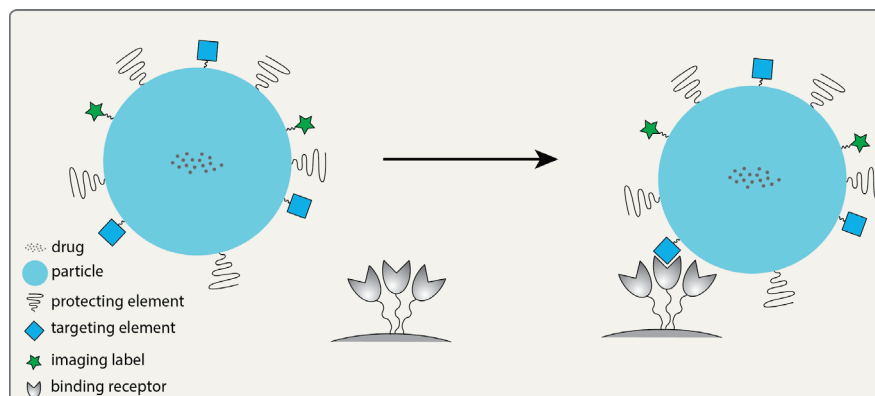


Figure 1.1 Schematic representation of a molecular imaging agent. Here, the particle represents both artificial and biological engineered agents. The protecting elements are typically used to influence the particle's circulation pharmacodynamics. The particle can also be used without any of the bound elements. The imaging agent can also be used as a drug delivery vehicle.

In drug delivery applications, the drug delivery vehicle has been rendered visible through the conjugation with contrast or imaging agents. As this approach combines therapy and diagnostics aspects, it is termed "theranostics". Figure 1.1 shows a general cartoon of a theranostic particle, which combines targeting, imaging functionalities with drug delivery. The advantage is that pharmacodynamic and -kinetic properties as well as biodistribution of drugs can be quantified with imaging for each patient leading to a personalized approach in treatment strategies. [7, 8].

Molecular imaging has developed into a vast and varied field throughout the past decades. While imaging technologies were brought more than a decade ago from a clinical into preclinical setting for molecular imaging research, more and more molecular imaging applications are now brought into clinical practice. Overall, molecular imaging has enormous potential applications in the discovery, development, and delivery of drugs in a preclinical and clinical phase [9-11], in diagnostics [1, 12, 13], in personalized medicine [14, 15], and in theranostics [1, 8].

Aim and outline of this thesis

The aim of this thesis is to explore the use of molecular imaging as a tool in research question of drug delivery, oncology, and regenerative medicine.

Chapter two gives a more detailed introduction to US-mediated drug delivery to put **chapter three and four** into perspective of ongoing research and the research question that is addressed in this thesis.

Chapter three and four describe experiments, where molecular imaging is used to study US-induced drug delivery and gene transfection. Site directed delivery of drugs or genetic constructs remains one of the biggest challenges in

pharmaceutical research to improve efficacy while reducing side effects. While small molecular drugs can still be engineered to reach their target to some degree via free diffusion, promising new therapeutics based on biologicals or genetic material are usually too charged, hydrophilic and too large to passively cross biological barriers such as the endothelium and cellular membranes to reach their targets. Ultrasound may offer a solution to this problem as the pressure waves of US can induce a local and transient permeabilization of the blood vessel endothelium (extravasation) as well as cellular membranes (sonoporation). Consequently, US-based delivery approaches have been investigated in the past in cells as well as *in vivo*. These delivery strategies suffer from the fact that the possible experimental parameter space is huge, with different US transducers, US protocols, presence of microbubbles, treated tissues or different drugs. Consequently, US-mediated drug delivery studies presented in literature are difficult to compare and show large variations. In **chapter three**, molecular imaging with SPECT is used to follow the extravasation of a radiolabeled model drug from the vascular system subsequent to a sonication with focused US in the presence of microbubbles. With SPECT, the kinetics of extravasation as well as the overall amount of extravasated drug was determined. This study provides essential information for the development of US based strategies for localized drug delivery.

Next, US-induced delivery and transfection of gene vectors is explored, which is described in detail in **chapter four**. In gene therapy, nucleic acids (DNA or RNA) are used to cure, prevent, or treat human disorders. Most current applications focus on the insertion of exogenous nucleic acids to either promote or inhibit the expression of a missing/damaged protein, or on *ex vivo* gene manipulation of the patient's own cells followed by autologous transplantation [16]. Typically, the delivery of genetic vectors is based on either viral or non-viral approaches. Viral vectors have the distinct advantage of easily entering the cells and nuclei leading to high levels of transduction and expression over a long period of time. However, their safety profile is yet a point of concern because of immune reactions and more importantly insertional mutagenesis [16]. Non-viral vectors have a better safety profile but do not passively cross cellular membranes and as such have low levels of transfection and expression, which normally last only for a few months [17]. In **chapter four**, US-mediated delivery of a genetic vector in the muscle tissue of mice is described, where optical imaging is used to localize and quantify gene expression. To this aim, a genetic plasmid construct is used that carries an optical reporter gene encoding for the enzyme luciferase, allowing bioluminescence imaging as readout for gene expression. This study explores how different experimental parameters influence the US-based transfection efficiency.

Chapter five explores the use of molecular imaging in oncology to investigate the formation of bone metastases of breast cancer. Metastases are formed from

circulating tumor cells that originate from primary cancers. Currently, once bone metastases appear the disease is termed incurable and patients will have limited life expectancy going along with a decreasing quality of life. Consequently, current research effort is directed to better understand the processes behind bone metastasis formation and growth and its response to different treatments.

To this aim, the concept of reporter gene imaging was extended to follow and quantify the formation of bone metastases using a multimodal SPECT/MRI approach. A breast cancer cell line was genetically modified to stably express the reporter gene *herpes simplex virus-1 thymidine kinase*, which allows sensitive quantification of cancer cells with the radiotracer [¹²³I]FIAU and SPECT imaging. The process of bone metastasis formation from these cells and the kinetics of growth were studied using SPECT/MRI. This tool could be used for studying therapies targeting the formation for bone metastasis.

Chapter six finally applies imaging and molecular imaging tools to investigate processes in regenerative medicine. Today, regenerative medicine based approaches are studied to restore tissue functionalities in humans that were for example compromised due to a disease or injuries. Regeneration of lost or injured structures is limited and often restricted to specific tissues, e.g. the liver may regenerate a large portion up to its original size when enough hepatocytes remain to proliferate (1). In most other cases, the wound healing mechanisms lead to scar formation (2). Thus, regenerative medicine approaches in humans rely typically on the use of stem cell therapies to restore tissue functionality. For example, stem cells based therapies have been investigated and clinically tested after a cardiac infarct to restore cardiac functions [18] and also after spinal cord injuries to regenerate nerves [19].

An example in nature known for its extraordinary capability of regeneration is the aquatic salamander (axolotl). Axolotls have the unique capability to regrow limbs and other organs, e.g. the heart, after amputation or other damages. Regenerative processes in axolotls are the subject of intense biological research on genetic and cellular level with microscopy as the main imaging tool. Other imaging techniques to follow regeneration at a tissue or whole body level were barely used in the past. Inspired by that insight, a completely new area of research was set up to follow and study with MRI and CT regenerative processes in axolotls. In particular, the first imaging studies focused on non-invasive quantification of cardiac function of axolotls as well as regeneration of the tail after amputation.

The anatomy of the cardiac structure and the dynamics of the heart beat were imaged and quantified by MRI. The ejection fraction and cardiac output were then calculated.

The cardiac study established the MR imaging protocols to follow, in a future experiment, heart regeneration and its functional recovery after an infarct.

Tail regeneration was imaged using MRI and CT to provide insights on how

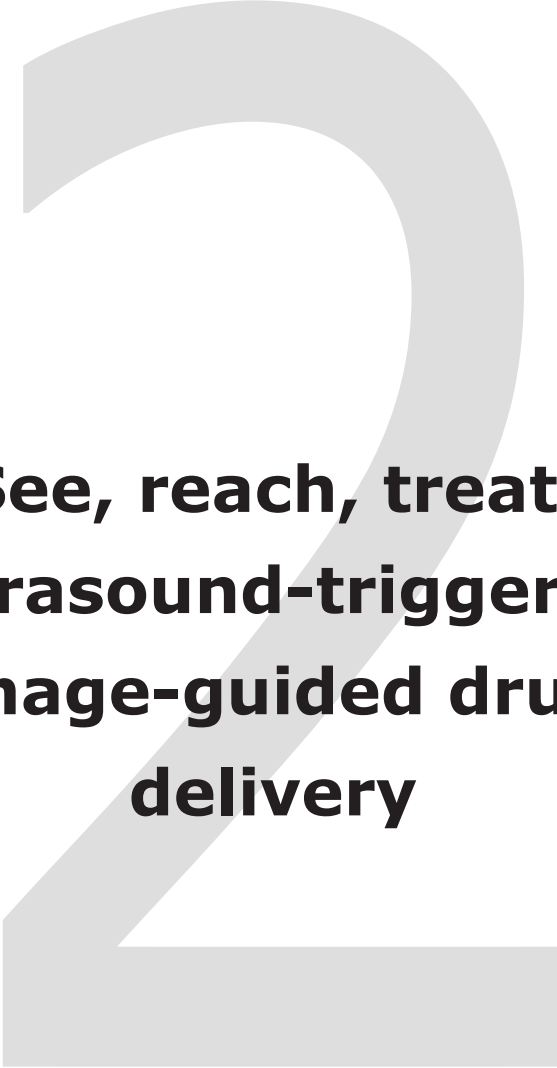
different tissues such as vertebrae, muscles, nerves, etc. but also functionality are restored.

The thesis ends with **chapter seven**, giving a summarizing discussion, sketching the future perspectives of molecular imaging in biomedical research.

References

- [1] M.L. James, S.S. Gambhir, A molecular imaging primer: modalities, imaging agents, and applications, *Physiological reviews*, 92 (2012) 897-965.
- [2] R. Weissleder, A. Rehemtulla, S.S. Gambhir, *Molecular Imaging: principles and practice*, PMPH - USA, Connecticut, 2010.
- [3] R. Weissleder, *Molecular imaging: exploring the next frontier*, *Radiology*, 212 (1999) 609-614.
- [4] R. Weissleder, M.J. Pittet, *Imaging in the era of molecular oncology*, *Nature*, 452 (2008) 580-589.
- [5] W.D. Foltz, D.A. Jaffray, *Principles of magnetic resonance imaging*, *Radiation research*, 177 (2012) 331-348.
- [6] J. Muller, A. Wunder, K. Licha, *Optical imaging*, *Recent results in cancer research. Fortschritte der Krebsforschung. Progres dans les recherches sur le cancer*, 187 (2013) 221-246.
- [7] A. Chopra, L. Shan, W.C. Eckelman, K. Leung, M. Lattner, S.H. Bryant, A. Menkens, *Molecular Imaging and Contrast Agent Database (MICAD): evolution and progress*, *Molecular imaging and biology : MIB : the official publication of the Academy of Molecular Imaging*, 14 (2012) 4-13.
- [8] B. Theek, L.Y. Rizzo, J. Ehling, F. Kiessling, T. Lammers, *The Theranostic Path to Personalized Nanomedicine*, *Clinical and translational imaging : reviews in nuclear medicine and molecular imaging*, 2 (2014) 66-76.
- [9] J.K. Willmann, N. van Bruggen, L.M. Dinkelborg, S.S. Gambhir, *Molecular imaging in drug development*, *Nature reviews. Drug discovery*, 7 (2008) 591-607.
- [10] D.S. Tan, G.V. Thomas, M.D. Garrett, U. Banerji, J.S. de Bono, S.B. Kaye, P. Workman, *Biomarker-driven early clinical trials in oncology: a paradigm shift in drug development*, *Cancer J*, 15 (2009) 406-420.
- [11] M. Rudin, R. Weissleder, *Molecular imaging in drug discovery and development*, *Nature reviews. Drug discovery*, 2 (2003) 123-131.
- [12] P. Brader, I. Serganova, R.G. Blasberg, *Noninvasive molecular imaging using reporter genes*, *Journal of nuclear medicine : official publication, Society of Nuclear Medicine*, 54 (2013) 167-172.
- [13] F.C. Wong, E.E. Kim, *A review of molecular imaging studies reaching the clinical stage*, *European journal of radiology*, 70 (2009) 205-211.
- [14] I. Wistuba, J.G. Gelovani, J.J. Jacoby, S.E. Davis, R.S. Herbst, *Methodological and practical challenges for personalized cancer therapies*, *Nature reviews. Clinical oncology*, 8 (2011) 135-141.
- [15] R. Frank, R. Hargreaves, *Clinical biomarkers in drug discovery and development*, *Nature reviews. Drug discovery*, 2 (2003) 566-580.
- [16] K.B. Kaufmann, H. Buning, A. Galy, A. Schambach, M. Grez, *Gene therapy on the move*, *EMBO molecular medicine*, 5 (2013) 1642-1661.
- [17] C. Scholz, E. Wagner, *Therapeutic plasmid DNA versus siRNA delivery: common and different tasks for synthetic carriers*, *Journal of controlled release : official journal of the Controlled Release Society*, 161 (2012) 554-565.
- [18] B.A. Nasser, W. Ebell, M. Dandel, M. Kukucka, R. Gebker, A. Doltra, C. Knosalla, Y.H. Choi, R. Hetzer, C. Stamm, *Autologous CD133+ bone marrow cells and bypass grafting for regeneration of ischaemic myocardium: the Cardio133 trial*, *European heart journal*, 35 (2014) 1263-1274.
- [19] G. Dai, X. Liu, Z. Zhang, Z. Yang, Y. Dai, R. Xu, *Transplantation of autologous bone marrow mesenchymal stem cells in the treatment of complete and chronic cervical spinal cord injury*, *Brain research*, 1533 (2013) 73-79.





**See, reach, treat:
ultrasound-triggered
image-guided drug
delivery**

Based on:

P.G. Sanches, H. Gröll, O.C. Steinbach, See, reach, treat: ultrasound-triggered image-guided drug delivery, *Ther Deliv*, 2 (2011) 919-934.

Principles of ultrasound

Ultrasound is a traveling pressure wave with frequencies above 20 kHz. The pressure fluctuations cause the particles in a medium to vibrate back and forth, which in turn induces variations in the medium's density. The devices used to produce US waves are called transducers. Medical US exploits these properties and behavior of sound waves for both diagnostic imaging and therapy [1].

Several parameters are needed in order to describe US (Fig. 2.1a) [2]. Frequency can be defined as the number of complete cycles of pressure per second and wavelength is the length of space over which one cycle occurs. The time that it takes for one cycle to occur is called the period which is also defined as the inverse of the frequency. Higher frequency waves have shorter wavelengths and therefore have more interaction with the tissue. Consequently, the penetration depth of an US wave is inversely proportional to its frequency. In medical US imaging, the frequencies are typically within 1-15 MHz. Finally, the propagation speed of a sound wave is the speed at which it moves through a medium. It is mostly determined by the medium's density and stiffness. Thus, propagation speeds are lower in gases, higher in liquids and highest in solids. These parameters are sufficient to describe continuous wave US where the cycles repeat indefinitely. However, most medical and therapeutic applications use pulsed US, where a few cycles of US are separated in time with intervals of no US. Additional parameters are thus necessary for a complete description (Fig. 2.1b). Pulse repetition frequency (PRF) is the number of pulses occurring in one second and pulse repetition period (PRP) is the time from the beginning of one pulse to the beginning of the next. Diagnostic US transducers typically emit a few thousand pulses per second. The time it takes for one pulse to occur is the pulse duration. Another important parameter is the duty cycle (DC), which is defined as the fraction of time that pulsed US is ON. The duty cycle is calculated by dividing the pulse duration with the PRP. The length of space that a pulse takes up is the spatial pulse length. Finally, the strength of the sound wave must also be known, namely the amplitude and intensity. Amplitude is the maximum variation in pressure and intensity is the rate of energy per surface area.

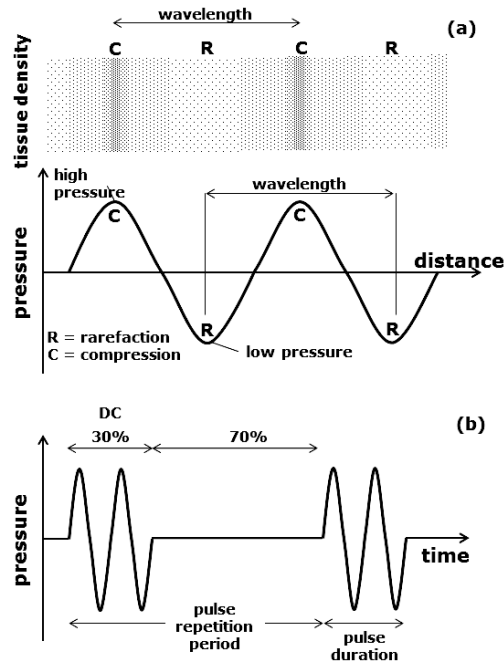


Figure 2.1 A schematic representation of a continuous US wave (a) and a pulsed US wave (b). DC: duty cycle.

Propagating acoustic waves in biological tissues are mostly attenuated by absorption but also by scattering and reflection. This energy dissipation provides either a mechanical stimulus, or – depending on the length of time the US is applied – leads to local heating.

At US frequencies the tissue does not respond fast enough to the varying pressures resulting in momentum transfer in the direction of propagation. Displacement forces, known as radiation forces, are thus generated. They can lead to localized particle movements and acoustic streaming. For the latter, two main effects are possible: (1) fluids are moved in the direction of the sound waves as a bulk which can effectively move particles in suspension; (2) microstreaming in which localized currents are generated next to cavitating bodies (see below) that can induce shear stresses on nearby surfaces [3]. Another important US driven effect is acoustic cavitation. It can be broadly defined as the growth, oscillation, and collapse of gas bubbles under an US field. In most tissues gas bubbles are scarce. However, under certain pressure amplitude and frequency conditions, dissolved gas in tissues can concentrate to form gas bubbles effectively creating cavitation nuclei/elements. There are two main cavitation regimes: stable (non-inertial) and transient (inertial). Stable cavitation involves the sustained oscillation of a gas bubble around a mean diameter value. In inertial cavitation, the bubbles oscillate unstably, expanding

up to three times their size, and eventually collapse originating a high energy release. Consequently, a new quantity termed mechanical index (M.I.) has been formulated to help evaluate the likelihood of cavitation-related adverse biological effects under normal imaging exposures [4]. The M.I. is defined as the ratio of the peak negative pressure with the square root of the US frequency [1]. The maximum M.I. allowed in commercial imaging devices is 1.9.

Microbubbles

Ultrasound contrast agents are gas-filled microbubbles (MBs) with a mean diameter around 2 μm , which are able to circulate through the lung capillary bed. These MBs efficiently interact with the US waves since the encapsulated gas is orders of magnitude more compressible than the surrounding biological tissues [5]. As for gas bubbles, the MBs can oscillate by stable cavitation and/or by inertial cavitation. In fact, when MBs are used the threshold for cavitation is greatly reduced from an M.I. of 1.9 to < 0.8 , under the same US exposure conditions respectively [3, 6-14]. Also, the MB diameter directly affects its resonant frequency and it has been shown that at the same frequency the threshold for generating bioeffects is decreasing for larger MBs[15].

The MBs are stabilized by a shell, which can be made up from lipids, proteins or biodegradable polymers. The only clinically approved microbubbles for contrast enhanced ultrasound imaging are Optison[®], which is stabilized with a protein layer, and the lipid-based SonoVue[®], Sonazoid[®], and Definity[®] MBs. Typically, these MBs are filled with a hydrophobic gas such as SF₆ or perfluorocarbons to slow down gas dissolution in blood. Also polymer-based microbubbles were clinically tested, which have a thicker and harder shell of ca. 20-100 nm thickness. These polymeric MBs do not necessarily need to use hydrophobic gases to remain stable in circulation. However, the mechanical stiffness of the polymer-shelled bubbles requires sufficiently high ultrasound pressures to generate sufficient US contrast compared to lipid- and protein-shelled agents [15].

Once injected, MBs are rapidly cleared from circulation with typical half-life of few minutes for mice and rats and 20 minutes for humans. Primary clearing occurs via the reticulo-endothelial system with liver and spleen as the primary uptake organs [16]. In the clinic, MBs are approved for imaging in contrast echocardiography. Additionally, in Europe, there is approval for imaging in the liver, brain, carotids, and peripheral arteries [17, 18].

Permeabilization mediated by ultrasound

It has been recognized that the bio-effects from US-mediated cavitation (also radiation forces albeit to a lesser extent) can lead to a transient permeabilization of surrounding biological tissues (endothelium and cellular membranes) which has important implications in drug delivery [5, 12, 19-22]. The increase in

permeability can facilitate extravasation of drug compounds out of the vasculature into the interstitial space as well as uptake of these compounds into the cell.

The use of MBs greatly amplifies the US cavitation biophysical effects by lowering the threshold for cavitation. Oscillating MBs present in the vascular system affect the endothelium barrier creating temporary fenestrations and/or pores (Fig. 2.1a). Proximity to the surface is essential for these effects. Direct contact is needed in the case of stable cavitation while distances of up to one MB diameter should not be exceeded in inertial cavitation. Above effects can be exploited in US mediated drug delivery, as these pores subsequently allow extravasation of macromolecules or particles into the interstitial space that would otherwise stay in the blood pool. Marty et al. have proposed a mathematical model that formulates the relationship between the size of the pores formed in the endothelial layer and the duration of the extravasation in terms of the size of a particle [23]. The cavitation induces pores of certain size and size distribution. Subsequently, the pores close exponentially with a rate that depends on the mechanical and elastic properties of the tissue. The duration of extravasation is inversely proportional to the particle's size.

Cavitation can also induce transcytosis where macromolecules are transported across the interior of a cell in vesicles [5]. Above effects are known as US-enhanced extravasation and they can last up to a few hours.

On a cellular membrane level, the permeabilization process is termed sonoporation (Fig. 2.1b). Transient pores are also formed on cellular membranes, which will close within milliseconds to seconds. It has been shown that endocytosis which can be promoted by US and both cavitation regimes plays an important role in cellular uptake of macromolecules [12]. The size of the sonoporation pores created with stable cavitation was measured to range from a few nanometers to hundreds of nanometers. In inertial cavitation, pore sizes up to micrometers have been reported [12].

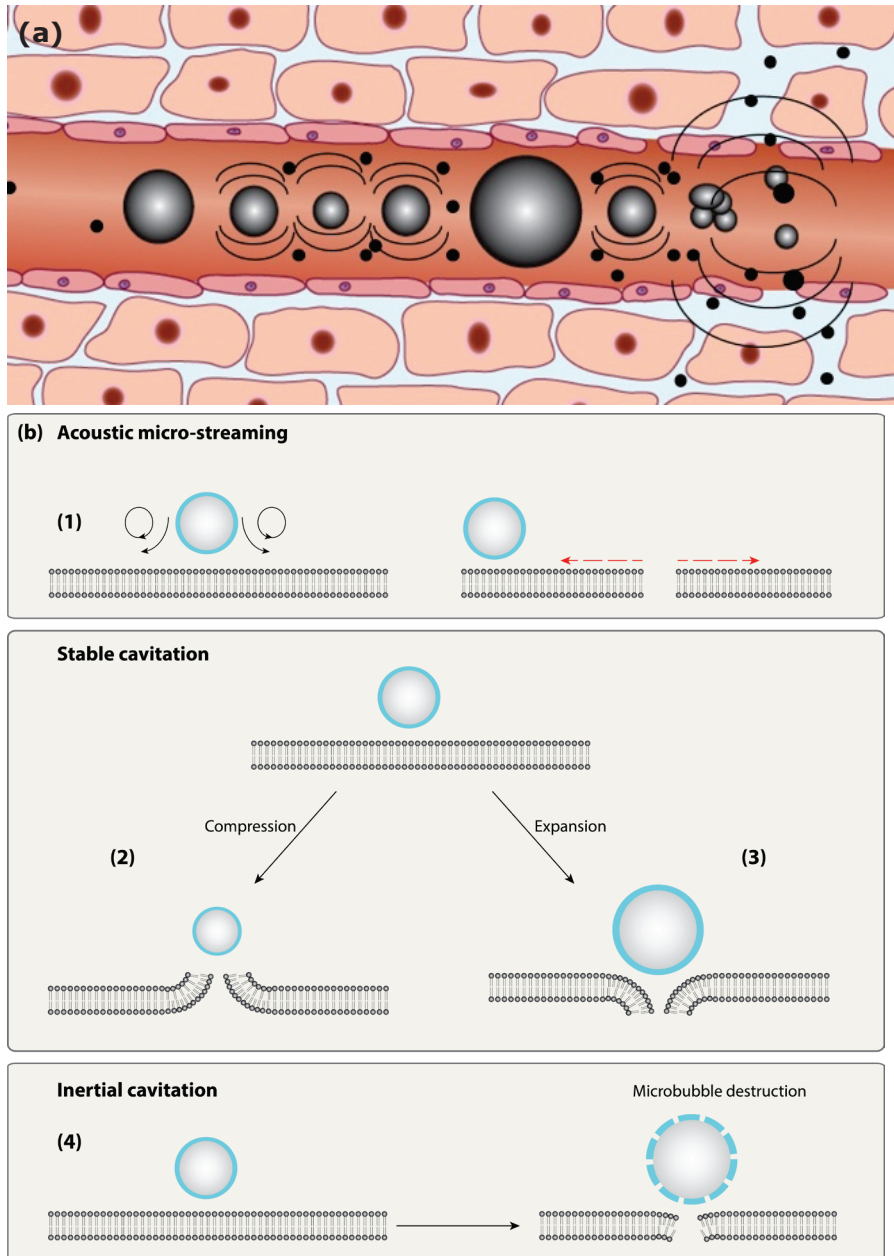


Figure 2.1 Biophysical effects of stably and inertial cavitating MBs. (a) Ultrasound-induced permeabilization of the endothelial layer of blood vessels leading to enhanced extravasation, mainly by destabilizing tight junctions due to MBs oscillations (and eventual collapse), acoustic streaming, and radiation forces. (b) Mechanisms of sonoporation. (1) Stable oscillation of a microbubble creates microstreamings in the surrounding fluid, which exert mechanical stress on the cell membrane, causing pore formation; (2) MB compression leading to invagination and membrane opening; (3) MB expansion leading to membrane

See, reach, treat: ultrasound-triggered
image-guided drug delivery

extension (push-force) and opening; (4) MB destruction releasing acoustic shock-waves and jet streams that permeabilize the membrane. Image (b) adapted from [17].

Drug delivery and the ultrasound method

The biggest challenge in systemic drug treatments is to achieve sufficient drug concentration within the targeted tissues or cells, while sparing healthy tissue in order to minimize side effects [25-28]. Administered drugs have to overcome several barriers such as the endothelial lining of blood vessels, crossing of the interstitial space, and finally cellular or even nuclear membranes depending on the exact nature and localization of the drug target [28]. While small molecular drugs with a balanced hydrophilicity can reach to some extent their targets via diffusion, charged or larger hydrophilic pharmaceutically-active compounds such as proteins or nucleic acids are not able to passively cross the aforementioned barriers. Ultrasound has been investigated as a possible solution to address the local delivery problem of this class of drugs [5, 13, 29]. Ultrasound can penetrate through tissue, which allows targeting deep seated structures. Additionally, ultrasound can be focused leading to a high intensity in the focal volume, therefore also termed (high intensity) focused ultrasound (HIFU, sometimes also fUS or HIFUS). In the focus spot, pressure intensities can be 3-4 orders of magnitude higher than in the far and near field of the transducer. Energy dissipation in the focus spot also leads to local heating, where obtained tissue temperatures depend on the exact US protocol used, but also tissue perfusion. Both pressure and temperature stimuli can be exploited for local drug delivery applications (Fig. 2.2) [8, 20, 21, 29-31]. The use of HIFU for thermal therapies is already at a clinical stage and holds great promise for localized drug delivery of small permeable drugs using temperature sensitive drug delivery vehicles. This approach provides high local concentrations of a small molecular drug once it is released from its carrier inside tumor tissue. Subsequent drug uptake of the tumor is driven by diffusion and solely depends on the molecular drug properties. Thus, temperature induced delivery schemes using HIFU, unlike pressure-based stimuli, do not address the delivery issue of biologicals or nucleic acid based drugs across barriers.

In this thesis we have focused on the development of pressure-mediated delivery strategies using ultrasound to overcome these biological barriers. Therefore, thermal delivery strategies will not be further discussed.

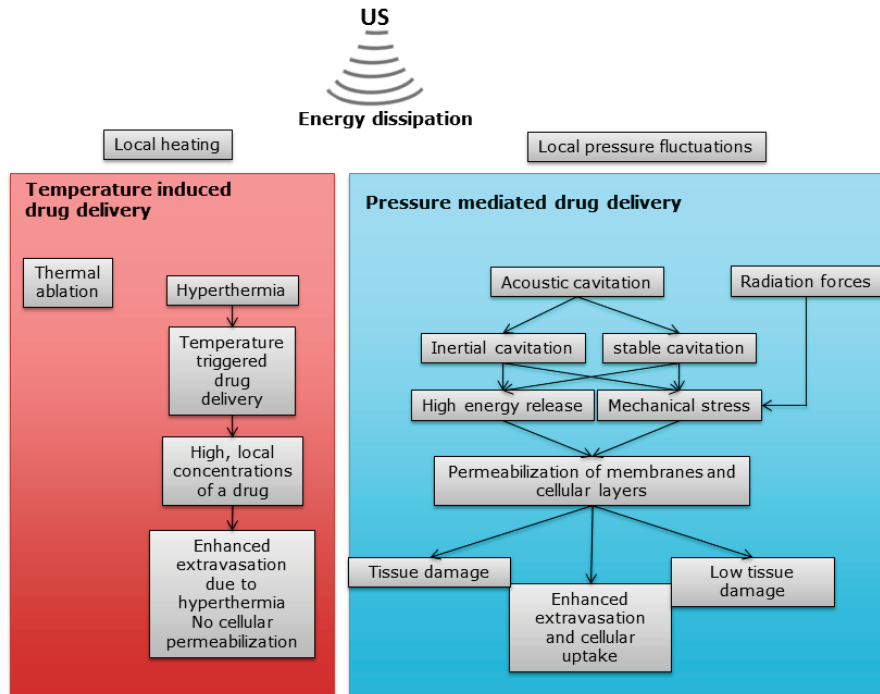


Figure 2.2 Schematic representation of physical interactions between US waves and biological tissues that create bio-effects.

Microbubbles as drug carriers

Microbubbles can also serve as drug carriers, where local release is triggered with (focused) ultrasound [3, 13]. Upon cavitation, these drug loaded microbubbles release their payload, while simultaneously inducing tissue permeabilization to mediate drug uptake. As the latter effects are transient in nature and remain only for a limited time, a high local drug concentration is needed. Several concepts have been developed to realize drug loaded MBs such as drug conjugation or drug absorption to the shell, integration of drugs in the shell, or dissolving the drugs in a liquid reservoir that is inside the shell. Also more complex MB-based drug delivery vehicles were explored by attaching drug loaded liposomes to the outer shell of a MB (Fig. 2.3) [32, 33]. However, the short circulation half-life of microbubbles, which implies that after systemic injection only a fraction of them will pass through the targeted tissue during sonication with US, and the limited drug load per MB present a limitation of the overall amount of drug that can be delivered using this approach [21, 34].

A new class of US activatable agents are based on emulsions having a fluorocarbon-based interior phase. The fluorocarbon oil is liquid at body temperature but quickly vaporize upon insonation forming acoustically active MBs. The nanometer size while in liquid form provides a long circulation time and

allows the emulsion particles to naturally extravasate into a tumorous tissue exploiting for example the EPR effect. Subsequently, these agents can be activated with ultrasound. Formulations based on phase converting agents loaded with drugs such as doxorubicin are being investigated [3].

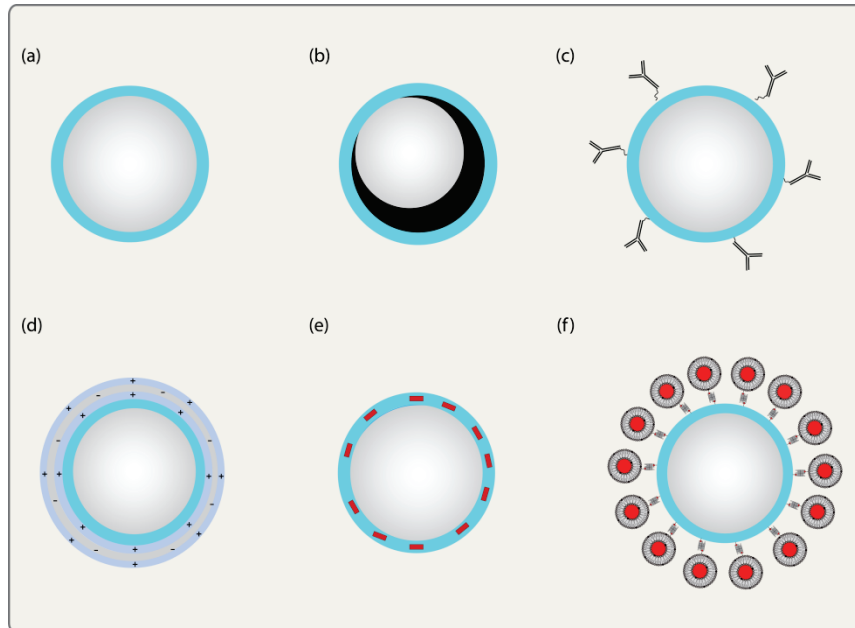


Figure 2.3 Microbubbles as drug carriers and targeted agents. (a) standard MB; (b) drugs incorporated inside Polymer-shelled microbubbles (A) have a thicker shell into which drugs can be incorporated directly, hydrophilic drugs can be incorporated with a double emulsion method [60] (B). Half-oil filled polymer-shelled microbubbles (C) give an additional liquid reservoir into which hydrophobic drugs can be incorporated.

Targeting of microbubbles

The concept of using MBs for imaging and drug delivery has been extended to targeted applications [17]. Due to their micrometer size MBs remain inside the vasculature and do not extravasate to the interstitial space. This has the advantage of reducing unspecific signals of unspecifically trapped MB, but it also restricts targeting to intravascular markers, such as endothelial cell surface markers related to tumors, or cardiovascular diseases [19, 35]. To this end, the MB shell is conjugated with ligands, commonly ones that specifically bind to markers of angiogenesis and/or inflammation [36-38]. Preclinical studies with markers other than the ones involved in inflammation and angiogenesis are mainly targeting cancer [39, 40]. Recently, a lipopeptide-based MB targeted to the vascular endothelial growth factor receptor-2, BR55[®] (Bracco), has entered clinical trials [41]. Most work with the BR55[®] so far has involved imaging angiogenesis related to cancer.

Challenges in ultrasound-mediated drug delivery

The most important parameters involved in US-mediated drug delivery have been described above. The outcome of experiments using this process depends on the fine tuning of all these parameters. However, the variability in the parameters used in published studies is enormous. Often, non-commercially available MBs and US devices are used. Unfortunately, most US drug delivery studies do not report their parameters or only give an incomplete description [2]. Also small experimental details concerning the exact experimental setup are often not reported, e.g. use of US absorbers, degassing of US gel, distance between transducer and target, etc.) This is one of the great challenges in US-mediated drug delivery research as direct inter-study comparisons are often not possible. Figure 2.4 summarizes the main components and parameters involved in an *in vivo* US drug delivery protocol and emphasizes the complexities of a US drug delivery study.

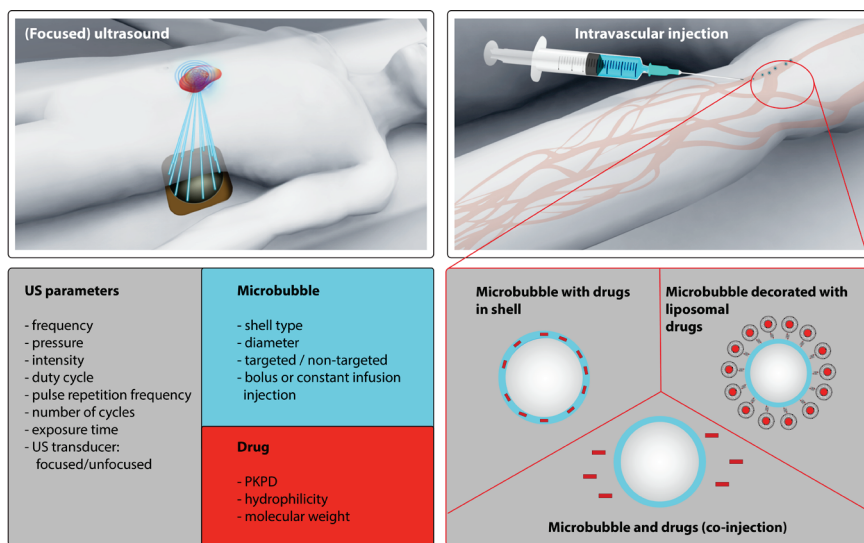


Figure 2.4 Ultrasound-mediated drug delivery.

Biological detrimental effects

Diagnostic US imaging is expected to not induce any cavitation in tissues below a mechanical index of 1.9 (clinical maximum) and is therefore considered "safe" in this operational limit. However, when US is used in combination with cavitation nuclei such as MBs this threshold is more than halved [42].

Possible risks and side effects of using US in the presence of gas bubbles are associated with detrimental bioeffects in healthy tissue. The occurrence of

See, reach, treat: ultrasound-triggered
image-guided drug delivery


tissue hemorrhage and endothelial cell damage after US exposure of cultured cells and organs containing air, such as the lungs or the intestine has been reported [4, 42-46]. In humans, premature ventricular contractions have been detected during contrast-enhanced echocardiographic imaging [47, 48]. In laboratory animals, simultaneous exposure of high-energy US to MBs resulted in: a reversible and transient decrease in left ventricular contractile performance; increase in the coronary perfusion pressure; increase in the myocardial lactate release; and presence of intramural hemorrhage in the plane of US transmission [14]. On tissue level, capillary rupture with erythrocyte extravasation and endothelial cell damage have been observed [46]. These studies indicate that US induced cavitation, with or without MBs being present, seems to be necessary to induce tissue permeability facilitating local drug delivery. However, these cavitations will cause to a certain extend local damage on tissue level [42]. Thus, careful optimization of the US parameters and the overall protocol as shown in Figure 2.4 is important to derive new drug delivery applications for existing and new drugs [42, 49].

In this thesis, the kinetics of ultrasound mediated extravasation is investigated in **chapter 3**. In **chapter 4** the influence of different US parameters on the delivery of genetic vectors *in vivo* is studied.

References

- [1] F.W. Kremkau, Diagnostic ultrasound: principles and instruments, W.B. Saunders, 2002.
- [2] G. ter Haar, A. Shaw, S. Pye, B. Ward, F. Bottomley, R. Nolan, A.M. Coady, Guidance on reporting ultrasound exposure conditions for bio-effects studies, *Ultrasound Med Biol*, 37 (2011) 177-183.
- [3] S.R. Sirsi, M.A. Borden, State-of-the-art materials for ultrasound-triggered drug delivery, *Advanced drug delivery reviews*, 72C (2014) 3-14.
- [4] G.R. ter Haar, Ultrasonic contrast agents: safety considerations reviewed, *Eur J Radiol*, 41 (2002) 217-221.
- [5] J.J. Rychak, A.L. Klibanov, Nucleic acid delivery with microbubbles and ultrasound, *Advanced drug delivery reviews*, 72C (2014) 82-93.
- [6] P. Marmottant, S. Hilgenfeldt, Controlled vesicle deformation and lysis by single oscillating bubbles, *Nature*, 423 (2003) 153-156.
- [7] H. Pan, Y. Zhou, O. Izadnegahdar, J. Cui, C.X. Deng, Study of sonoporation dynamics affected by ultrasound duty cycle, *Ultrasound Med Biol*, 31 (2005) 849-856.
- [8] G. ter Haar, Therapeutic applications of ultrasound, *Progress in biophysics and molecular biology*, 93 (2007) 111-129.
- [9] A. van Wamel, K. Kooiman, M. Hartevelde, M. Emmer, F.J. ten Cate, M. Versluis, N. de Jong, Vibrating microbubbles poking individual cells: drug transfer into cells via sonoporation, *J Control Release*, 112 (2006) 149-155.
- [10] Y. Zhou, J. Cui, C.X. Deng, Dynamics of sonoporation correlated with acoustic cavitation activities, *Biophys J*, 94 (2008) L51-53.
- [11] Y. Zhou, R.E. Kumon, J. Cui, C.X. Deng, The size of sonoporation pores on the cell membrane, *Ultrasound Med Biol*, 35 (2009) 1756-1760.
- [12] I. Lentacker, I. De Cock, R. Deckers, S.C. De Smedt, C.T. Moonen, Understanding ultrasound induced sonoporation: Definitions and underlying mechanisms, *Advanced drug delivery reviews*, 72C (2014) 49-64.
- [13] B. Geers, H. Dewitte, S.C. De Smedt, I. Lentacker, Crucial factors and emerging concepts in ultrasound-triggered drug delivery, *J Control Release*, 164 (2012) 248-255.
- [14] D.L. Miller, Overview of experimental studies of biological effects of medical ultrasound caused by gas body activation and inertial cavitation, *Progress in biophysics and molecular biology*, 93 (2007) 314-330.
- [15] S.P. Qin, C.F. Caskey, K.W. Ferrara, Ultrasound contrast microbubbles in imaging and therapy: physical principles and engineering, *Physics in Medicine and Biology*, 54 (2009) R27-R57.
- [16] M.R. Bohmer, A.L. Klibanov, K. Tiemann, C.S. Hall, H. Gruell, O.C. Steinbach, Ultrasound triggered image-guided drug delivery, *Eur J Radiol*, 70 (2009) 242-253.
- [17] F. Kiessling, S. Fokong, J. Bzyl, W. Lederle, M. Palmowski, T. Lammers, Recent advances in molecular, multimodal and theranostic ultrasound imaging, *Advanced drug delivery reviews*, 72C (2014) 15-27.
- [18] D.A. Merton, Ultrasound contrast agents, in, *International Contrast Ultrasound Society*, 2012.
- [19] C.R. Mayer, R. Bekeredjian, Ultrasonic gene and drug delivery to the cardiovascular system, *Advanced*

- drug delivery reviews, 60 (2008) 1177-1192.
- [20] V. Frenkel, Ultrasound mediated delivery of drugs and genes to solid tumors, *Advanced drug delivery reviews*, 60 (2008) 1193-1208.
- [21] Y.Z. Zhao, L.N. Du, C.T. Lu, Y.G. Jin, S.P. Ge, Potential and problems in ultrasound-responsive drug delivery systems, *International journal of nanomedicine*, 8 (2013) 1621-1633.
- [22] E. Unger, T. Porter, J. Lindner, P. Grayburn, Cardiovascular drug delivery with ultrasound and microbubbles, *Advanced drug delivery reviews*, 72C (2014) 110-126.
- [23] B. Marty, B. Larrat, M. Van Landeghem, C. Robic, P. Robert, M. Port, D. Le Bihan, M. Pernot, M. Tanter, F. Lethimonnier, S. Meriaux, Dynamic study of blood-brain barrier closure after its disruption using ultrasound: a quantitative analysis, *Journal of cerebral blood flow and metabolism : official journal of the International Society of Cerebral Blood Flow and Metabolism*, 32 (2012) 1948-1958.
- [24] A.M. Takalkar, A.L. Klibanov, J.J. Rychak, J.R. Lindner, K. Ley, Binding and detachment dynamics of microbubbles targeted to P-selectin under controlled shear flow, *J Control Release*, 96 (2004) 473-482.
- [25] T. Lammers, F. Kiessling, W.E. Hennink, G. Storm, Drug targeting to tumors: principles, pitfalls and (pre-) clinical progress, *J Control Release*, 161 (2012) 175-187.
- [26] T.M. Allen, P.R. Cullis, Drug delivery systems: entering the mainstream, *Science*, 303 (2004) 1818-1822.
- [27] A.I. Minchinton, I.F. Tannock, Drug penetration in solid tumours, *Nature reviews*, 6 (2006) 583-592.
- [28] S. Mitragotri, Devices for overcoming biological barriers: the use of physical forces to disrupt the barriers, *Advanced drug delivery reviews*, 65 (2013) 100-103.
- [29] N. Hijnen, S. Langereis, H. Grull, Magnetic resonance guided high-intensity focused ultrasound for image-guided temperature-induced drug delivery, *Advanced drug delivery reviews*, 72C (2014) 65-81.
- [30] R. Deckers, C.T. Moonen, Ultrasound triggered, image guided, local drug delivery, *J Control Release*, (2010).
- [31] R. Deckers, C. Rome, C.T. Moonen, The role of ultrasound and magnetic resonance in local drug delivery, *J Magn Reson Imaging*, 27 (2008) 400-409.
- [32] P.G. Sanches, H. Grull, O.C. Steinbach, See, reach, treat: ultrasound-triggered image-guided drug delivery, *Ther Deliv*, 2 (2011) 919-934.
- [33] B. Geers, I. Lentacker, N.N. Sanders, J. Demeester, S. Meairs, S.C. De Smedt, Self-assembled liposome-loaded microbubbles: The missing link for safe and efficient ultrasound triggered drug-delivery, *J Control Release*, 152 (2011) 249-256.
- [34] K. Ferrara, R. Pollard, M. Borden, Ultrasound microbubble contrast agents: fundamentals and application to gene and drug delivery, *Annual review of biomedical engineering*, 9 (2007) 415-447.
- [35] S.T. Laing, D.D. McPherson, Cardiovascular therapeutic uses of targeted ultrasound contrast agents, *Cardiovascular research*, 83 (2009) 626-635.
- [36] Y. Wallez, P. Huber, Endothelial adherens and tight junctions in vascular homeostasis, inflammation and angiogenesis, *Biochim Biophys Acta*, 1778 (2008) 794-809.
- [37] D.A. Walsh, Pathophysiological mechanisms of angiogenesis, *Adv Clin Chem*, 44 (2007) 187-221.
- [38] F.S. Villanueva, R.J. Jankowski, S. Klibanov, M.L. Pina, S.M. Alber, S.C. Watkins, G.H. Brandenburger, W.R. Wagner, Microbubbles targeted to intercellular adhesion molecule-1 bind to activated coronary artery endothelial cells, *Circulation*, 98 (1998) 1-5.
- [39] L. Wang, L. Li, Y. Guo, H. Tong, X. Fan, J. Ding, H. Huang, Construction and in vitro/in vivo targeting of PSMA-targeted nanoscale microbubbles in prostate cancer, *The Prostate*, 73 (2013) 1147-1158.
- [40] K. Foygel, H. Wang, S. Machtaler, A.M. Lutz, R. Chen, M. Pysz, A.W. Lowe, L. Tian, T. Carrigan, T.A. Brentnall, J.K. Willmann, Detection of pancreatic ductal adenocarcinoma in mice by ultrasound imaging of thymocyte differentiation antigen 1, *Gastroenterology*, 145 (2013) 885-894 e883.
- [41] S. Pochon, I. Tardy, P. Bussat, T. Bettinger, J. Brochet, M. von Wronski, L. Passantino, M. Schneider, BR55: a lipopeptide-based VEGFR2-targeted ultrasound contrast agent for molecular imaging of angiogenesis, *Invest Radiol*, 45 (2010) 89-95.
- [42] D.L. Miller, M.A. Averkiou, A.A. Brayman, E.C. Everbach, C.K. Holland, J.H. Wible, Jr., J. Wu, Bioeffects considerations for diagnostic ultrasound contrast agents, *J Ultrasound Med*, 27 (2008) 611-632; quiz 633-616.
- [43] T. Ay, X. Havaux, G. Van Camp, B. Campanelli, G. Gisellu, A. Pasquet, J.F. Deneff, J.A. Melin, J.L. Vanoverschelde, Destruction of contrast microbubbles by ultrasound: effects on myocardial function, coronary perfusion pressure, and microvascular integrity, *Circulation*, 104 (2001) 461-466.
- [44] G. Van Camp, T. Ay, A. Pasquet, V. London, A. Bol, G. Gisellu, G. Hendrickx, P. Rafters, J.A. Melin, J.L. Vanoverschelde, Quantification of myocardial blood flow and assessment of its transmural distribution with real-time power modulation myocardial contrast echocardiography, *J Am Soc Echocardiogr*, 16 (2003) 263-270.
- [45] J.L. Vanoverschelde, D. Vancrayenest, T. Ay, M. Peltier, A. Pasquet, Assessment of myocardial blood flow using myocardial contrast echocardiography, *Am J Cardiol*, 90 (2002) 591-641.
- [46] D.L. Miller, WFUMB Safety Symposium on Echo-Contrast Agents: in vitro bioeffects, *Ultrasound Med Biol*, 33 (2007) 197-204.
- [47] S. Chapman, J. Windle, F. Xie, A. McGrain, T.R. Porter, Incidence of cardiac arrhythmias with therapeutic versus diagnostic ultrasound and intravenous microbubbles, *J Ultrasound Med*, 24 (2005) 1099-1107.
- [48] P.A. van Der Wouw, A.C. Brauns, S.E. Bailey, J.E. Powers, A.A. Wilde, Premature ventricular contractions during triggered imaging with ultrasound contrast, *J Am Soc Echocardiogr*, 13 (2000) 288-294.
- [49] J.M. Tsutsui, F. Xie, R.T. Porter, The use of microbubbles to target drug delivery, *Cardiovasc Ultrasound*, 2 (2004) 23.



**Real-time imaging
and kinetics
measurements of
focused ultrasound-
induced extravasation
in skeletal muscle using
SPECT/CT**

Based on:

P.G. Sanches, R. Rossin, M. Bohmer, K. Tiemann, H. Grull, *Real-time imaging and kinetics measurements of focused ultrasound-induced extravasation in skeletal muscle using SPECT/CT*, J Control Release, 168 (2013) 262-270

K. Park, *A new look at ultrasound-mediated extravasation*, J Control Release, 168 (2013) 341

Abstract

Drugs need to overcome several biological barriers such as the endothelium and cellular membranes in order to reach their target. Promising new therapeutics, many of which are charged and macromolecular, are not able to passively extravasate, let alone cross cell membranes, and stay mainly in the blood pool upon intravenous injection until clearance. Using focused ultrasound (fUS) in combination with circulating microbubbles (MBs) leads to temporary localized tissue permeabilization allowing extravasation of (macro) molecules from the vascular system. Thus, fUS is a promising approach for localized drug delivery. However, little is known about the permeabilization kinetics in skeletal muscle. In this study, we used single photon emission computed tomography (SPECT) to characterize the kinetics of extravasation of ^{111}In -labeled bovine serum albumin (BSA), a model macromolecular drug, in muscle treated with fUS and MBs. The same fUS protocol was applied to 6 groups of mice with different times, Δt , between fUS application and BSA injection ($\Delta t = -10, 2.5, 10, 30, 60, 90$ min) followed by SPECT imaging. For $\Delta t \leq 30$ min we observed an exponential accumulation of activity in an area of the treated muscle which extended to a volume larger than the fUS pattern with highest accumulation for short waiting times Δt . The extent of extravasation decreased exponentially with increasing Δt , with a calculated half-life of ca. 21 min, defining the time window of extravasation. The same treatment without MBs did not induce extravasation of BSA thus supporting MBs and drug co-injection strategies. These results provide essential information for the development of fUS based strategies for localized drug delivery.

Keywords: focused ultrasound, drug delivery, SPECT, extravasation, microbubbles, Evans blue

Introduction

Site directed delivery of drugs remains one of the biggest challenges in pharmaceutical research to improve efficacy while reducing side effects. Typical drugs have molecular weights around 500 Da or lower, a balanced hydrophilicity/hydrophobicity, and low or no charge. Upon intravenous injection, these drugs have to overcome multiple barriers, such as the endothelium to extravasate into the extravascular/extracellular space to reach e.g. cell surface receptors or they even have to cross cellular membranes to reach intracellular targets. Unfortunately, the passive distribution of drugs across tissues leads typically to relatively low concentrations in the target and an unwanted burden for healthy tissues, limiting the therapeutic window [1]. Many new potent macromolecular drugs face an even greater delivery challenge due to even more unfavorable pharmacokinetic properties (PK). Namely, charged and hydrophilic drug candidates such as plasmid DNA and small interfering RNA have tremendous therapeutic potential for the treatment of cancer as well as metabolic and cardiovascular diseases, but do not extravasate or cross cellular membranes [2, 3].

Focused ultrasound (fUS) may offer a solution to this delivery dilemma. The pressure waves of ultrasound can drive circulating microbubbles (MBs), clinically used as ultrasound contrast agents, into a forced oscillation state inducing transient permeability of the blood vessel endothelium (mediating extravasation) as well as cell membranes (sonoporation) [4-8] (Fig. 3.1). With the possibility to non-invasively focus sound waves at structures deep inside the body, fUS can be used to mediate extravasation and increase cellular permeability in a highly localized manner [9]. Various publications have shown the potential of fUS to induce drug extravasation in different organs such as skeletal muscle [6], heart [10], brain [11-17] and tumors [18-20].

The sonoporation effect induced by ultrasound was first recognized by Williams in 1971 [21] (although the term sonoporation appeared in the literature only in 1997 [22]) and then was extensively studied *in vitro* [5, 23-25]. Recently, Yudina *et al.* [26] showed that ultrasound induced permeability of cell membranes to a small non-cell permeable optical chromophore *in vitro* is a transient effect lasting up to 24 h. The exact mechanism causing the sonoporation is still under investigation with temporary membrane pore formation and induced endocytosis being two main hypotheses [23, 27]. *In vivo*, the increase in vascular permeability following fUS points, among others, at the opening of endothelial junctions, fluid jet formation, and shear stresses induced by oscillating MBs (non-inertial cavitation), eventual bubble collapse at high enough pressures (inertial cavitation), and acoustic forces [8]. This allows extravasation into the interstitial space of compounds with unfavourable PK or with sizes too large to pass the intact endothelial layer [28]. Therefore, fUS

induced extravasation can be exploited *in vivo* for triggered local delivery of drugs and nanoparticles [6, 19].

Extravasation of macromolecular drugs and nanoparticles depends on their plasma concentration as the concentration gradient is the ultimate driving force of passive diffusion, but also on their size compared to the induced openings in the endothelial layer. Since the endothelium recovers with time and the openings between neighbouring cells close, extravasation is expected to reduce over time. So far, most information over the kinetics of fUS-induced extravasation was gathered for the blood-brain-barrier (BBB) [14-17], but little quantitative information is available for muscle [6, 29, 30]. Nuclear imaging techniques such as single photon emission computed tomography/computed tomography (SPECT/CT) can be used to non-invasively image and analyze the distribution of radiolabeled compounds *in vivo* with high spatial resolution and sensitivity. This imaging approach was used earlier to follow ultrasound induced extravasation in the BBB by imaging the accumulation of ^{99m}Tc -DTPA in the rat brain with SPECT/CT over time after MBs injection and fUS treatment [12, 13]. In this study we have imaged and quantified the fUS mediated extravasation of a model drug, ^{111}In -DTPA-labeled bovine serum albumin (BSA) in combination with Evans blue (EB), an albumin binding dye, in the hindlimb skeletal muscles of mice using dynamic small animal SPECT/CT *in vivo*. The time between fUS treatment and injection of BSA was increased for different groups of animals making it possible to probe the transient effects of fUS-induced extravasation *in vivo* and thus obtaining a time window for the applied treatment.

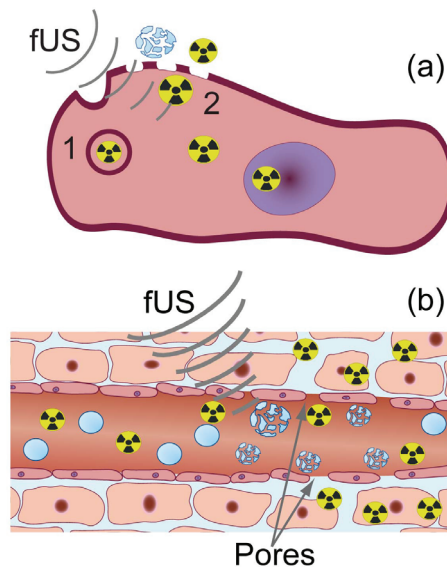


Figure 3.1 (a) Ultrasound induced sonoporation of a cell membrane and subsequent uptake of a drug into the cell. Two potential mechanisms involved are depicted: (1) endocytosis and (2) temporary pore formation. (b) Ultrasound-induced permeabilization of the endothelial

layer of blood vessels leading to enhanced extravasation, mainly by destabilizing tight junctions due to MBs oscillations (and eventual collapse), acoustic streaming, and radiation forces. The radioactivity symbol represents a radiolabeled drug with little to none natural extravasation or passage across the cell membrane.

Materials and Methods

Materials

All reagents and solvents were obtained from Sigma-Aldrich (St. Louis, MO) and used without further purification, unless otherwise stated. The DTPA-BSA (carrying ca. 20 DTPA groups per molecule) was obtained from SyMO-Chem (Eindhoven, the Netherlands). $^{111}\text{InCl}_3$ solutions were obtained from Perkin Elmer (Waltham, MA). CD-1 mouse serum was purchased from Innovative Research (Novi, MI). The labeling buffers were treated with Chelex-100 resin (BioRad Laboratories, Hercules, CA) overnight and filtered through 0.22 μm before use. Zeba spin desalt columns were purchased from Pierce (Thermo Scientific, Waltham, MA).

Hydrodynamic radius of DTPA-BSA

A 4 mg/mL solution of DTPA-BSA in saline was passed through a 0.1 μm sterile filter and the hydrodynamic radius was determined using dynamic light scattering (DLS) on an ALV/CGS-3 Compact Goniometer System (ALV-GmbH, Langen, Germany) at 22 °C. Intensity correlation functions were measured at a 90° scattering angle using a wavelength of 632.8 nm. The diffusion coefficient (D) was obtained from cumulant fits of the intensity correlation function using the ALV software.

Carrier-added ^{111}In -DTPA-BSA labeling

$^{111}\text{InCl}_3$ in 0.05 M HCl (10 μL , ca. 80 MBq) was added to a mixture of 35 μg DTPA-BSA, InCl_3 (ca. 0.8 equivalents to DTPA), in a total volume of 65 μL 1 M ammonium acetate buffer pH 6.0. The mixture was incubated at 37 °C and mixed at 400 rpm. After 1 h incubation, EDTA challenge (10 μL of 10 mM EDTA in 0.9 % NaCl) was performed for 20 min in the same conditions. Removal of low molecular weight impurities and buffer exchange to 0.9 % NaCl was performed twice using a Zeba spin desalt column (0.5 mL, 7 kDa MW cut-off) according to the manufacturer's protocol. The labeling yields (before purification) and radiochemical purity (after purification) were determined by radio-thin layer chromatography (radio-TLC), using instant TLC strips (iTLC-SG, Varian Inc., Palo Alto, CA) eluted with 10 mM EDTA in 0.9 % NaCl. The iTLC strips were scanned on a phosphor imager (FLA-7000, Fujifilm Life Science, Tokyo, Japan) and quantified with the AIDA software (Raytest, Straubenhardt, Germany). In these conditions ^{111}In -DTPA-BSA remained at the baseline and ^{111}In -EDTA migrated with an $R_f = 0.9$. Radio-TLC analysis showed 73.0 ± 3.2 % labeling yield ($n =$

13) and greater than 95 % radiochemical purity at the time of injection. The albumin binding dye EB was diluted to 100 mg/mL in 0.9 % NaCl, passed through a 0.22 µm filter and added to the final solution. Each mouse was injected with a solution containing ca. 30 µg ¹¹¹In-DTPA-BSA, 170 µg unlabeled DTPA-BSA and 0.5 mg EB in 50 µL 0.9 % NaCl. When multiple mice were injected during the same day, the purity of the injectate was confirmed by radio-TLC before each injection.

Stability of ¹¹¹In-DTPA-BSA

¹¹¹In-DTPA-BSA was incubated in 100 µL mouse serum / 0.9 % NaCl (1:1) at 37 °C for 2.5 h. At 30 min intervals, 5 µL samples were challenged with 1 µL 10 mM EDTA (10 min), 10-fold diluted with 0.9 % NaCl and analyzed by radio-TLC as described above.

Animal Studies

All animal procedures were approved by the ethical review committee of the Maastricht University Hospital (The Netherlands) and were performed according to the principles of laboratory animal care [31] and the Dutch national law "Wet op Dierproeven" (Stb 1985, 336). Female Swiss mice (25-36 g body weight; Charles River Laboratories, L'Arbresle Cedex, France) were housed in an enriched environment under standard conditions (23-25 °C, 50-60 % humidity, and 12 h light-dark cycles) for at least 1 week before the experiment, with food and water given *ad libitum*.

Animal preparation

The mice were anesthetized with isoflurane and their hindlimbs were first shaved and then depilated with commercial hair removal cream (Veet®, Slough, UK). A 20 cm catheter (PE tubing with 0.4 and 0.8 mm internal and external diameter, respectively, connected to a 27G needle) was inserted in the tail vein. Then the mice were placed on a heating plate to maintain a 37 °C body temperature, with an acoustic absorber (Sorbothane, McMaster-Carr, Chicago, IL) underneath the hindlimbs. Degassed ultrasound transmission gel, pre-heated to 37 °C (Aquasonics 100, Parker Laboratories, Fairfield, NJ), was applied between the absorber and the limbs and between the limbs and the ultrasound transducer to create an acoustic window.

Experimental protocol

Figure 3.2 shows the timeline and methods used in the experimental procedures.

Real-time imaging and kinetics measurements of focused ultrasound-induced extravasation in skeletal muscle using SPECT/CT

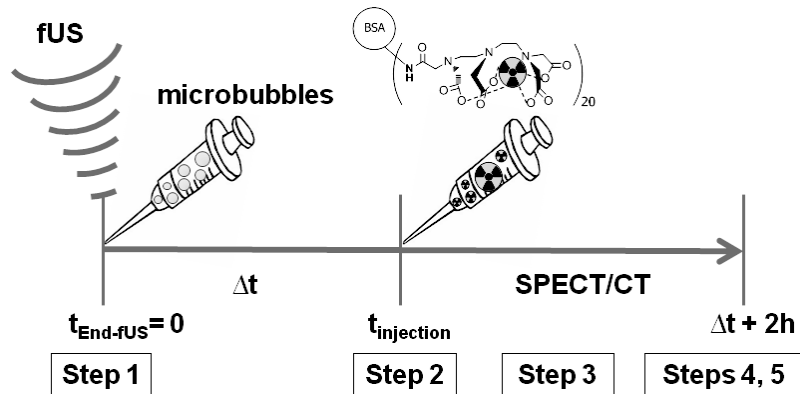


Figure 3.2 Experimental timeline. Step 1: Skeletal muscle is exposed to fUS (10 minutes total treatment time) while MBs are being infused intravenously during fUS exposure. Step 2: At specific times (Δt) after fUS exposure the radiolabeled model drug (^{111}In -DTPA-BSA) is injected intravenously. Step 3: The animal is imaged with consecutive SPECT scans followed by a CT scan. Step 4: The animal is euthanized 2 h after BSA injection and organs and tissues are harvested for γ -counting and histology (step 5).

Step 1. Microbubble infusion and ultrasound treatment

Polymer-shelled MBs (poly-L-lactide shell with N_2 core and mean diameter of 2 μm) prepared by a single emulsion method [6, 32] were used at a concentration of 1.1×10^9 MBs/mL in 0.9 % NaCl. A therapy and imaging probe system (TIPS, Philips, Amsterdam, the Netherlands) [9], co-aligned with a clinical ultrasound transducer (P7-4, HDI5000, Philips) for image guidance, was used for the fUS treatment. The technical details of the fUS system and its calibration are reported elsewhere [9]. The ultrasound treatment (ellipsoidal focus ca. $1 \times 1 \times 9$ mm^3 ; 1.2 MHz, 2 MPa (ca. 68 W/cm^2 spatial-average temporal-peak), 10000 cycles, and 4 s waiting time between points), triggered at each point, was applied in a 7-point pattern (Fig. 3.3) with 2.25 mm between points, focused 1.5 mm below the skin. The pattern was repeated 22 times. The overall fUS treatment protocol took 10 minutes. The MBs were infused via the tail vein catheter for 10 min at 0.6 mL/min using a syringe pump (PicoPlus, Harvard Apparatus, Holliston, MA) and the fUS treatment started 20 s after the MBs entered circulation. The target tissue was the skeletal muscle of the left hindlimb and the contra-lateral hindlimb was used as negative control.

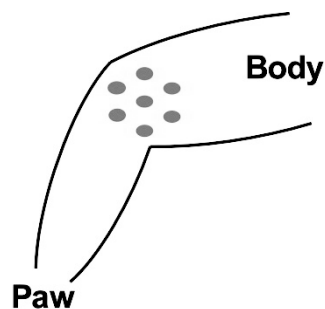


Figure 3.3 Schematic of the focused ultrasound treatment pattern. The center of the 7-point pattern is aimed at the left hindlimb muscle of the mouse.

Step 2. Injection of radiolabeled BSA and

experimental groups

The end of the fUS treatment is used as time reference ($t = 0$). After a defined time Δt (2.5, 10, 30, 60 and 90 min) post-ultrasound treatment the mice were injected with the solution containing ^{111}In -DTPA-BSA and EB. One group received an injection of ^{111}In -DTPA-BSA and EB at the start of the fUS treatment, thus the waiting time is $\Delta t = -10$ min. Another group (No MBs group) was injected with saline at $\Delta t = -10$ min to investigate the influence of MBs in the fUS protocol. Groups of 5 and 4 mice were used for $\Delta t = 10$ min and 30 min, respectively. All other groups consisted of 3 mice each.

Step 3. In vivo SPECT/CT imaging

Non-invasive imaging was performed using a dedicated small-animal SPECT/CT system equipped with four detector heads and converging multi-pinhole collimators (nine pinholes per collimator, 1.4 mm aperture, nanoSPECT/CT, Bioscan, Washington, DC).

Consecutive SPECT scans (4.5 min/scan - 12 projections, 45 s/projection, energy window: 15 % for 245 keV and 20 % for 171 keV) were performed over a 1.5 h period followed by a CT scan (45 kVp, 240 projections, 2000 ms/projection). The SPECT scanner was calibrated with cylindrical phantoms filled with ^{111}In solutions of known activity. For the groups $\Delta t \leq 10$ min a ca. 10 min delay existed between tracer injection and beginning of the imaging session as these animals had to be injected on the fUS table and then positioned in the SPECT/CT animal bed.

Step 4. Ex vivo biodistribution

After the CT scan the mice were euthanized 2 h post-injection of tracer by cervical dislocation. Organs and tissues of interest were harvested and weighed. In order to minimize variability, skeletal muscle samples from the treated hindlimbs were taken over an area wider than the treatment zone, covering most of the posterior muscles. With the visual aid of the extravasated EB, the treated skeletal muscles were dissected into three pieces: two pieces within the area treated with fUS and a third piece from an area in close proximity. Control muscle samples were taken from the contra-lateral hindlimb. The muscle samples were immediately placed in 4 % paraformaldehyde buffered to pH 7. Sample radioactivity was measured in a γ -counter (Wizard 1480, Perkin-Elmer, Waltham, MA) along with standards to determine the injected dose per gram (%ID/g). The energy window of the counter was set to 100-510 keV for ^{111}In . Evans Blue quantification was not performed as the dye served only as a visual marker.

Step 5. Histology

The formaldehyde fixed skeletal muscle samples were embedded in paraffin,

sliced into 5 μm -thick sections (Microtome Shandon Finesse ME+, Thermo Scientific) and stained with heamatoxylin-eosin (H&E).

Image analysis

The activity uptake in the treated and control muscles was quantified from the SPECT/CT images in terms of injected dose per cubic centimeter ($\%ID/\text{cm}^3$) using the vendor's imaging software (InVivo Scope). Specifically, regions of interest surrounding the posterior muscles were drawn on the CT images for both treated and control hindlimb (corresponding to the excised areas used for γ -counting). The respective $\%ID/\text{cm}^3$ values were calculated from each consecutive SPECT scan and plotted as a function of time. The dynamic data for each animal were fitted to single exponential curves using commercial software (Origin, OriginLab, Northampton, MA). The $\%ID/\text{cm}^3$, per animal, was extrapolated to 2 h post-tracer injection (time of euthanasia) from the fitted curves, averaged within each Δt group and used for the comparison with the averaged $\%ID/\text{g}$ from γ -counting.

Statistical analysis

Commercial software (Statgraphics Centurion, Stat Point Technologies Inc., Warrenton, VA) was used for statistical analysis (Student-t and Fisher's tests). The fitted curves for the temporal window were compared using the using the option "compare two datasets (F-test)" in the Origin software. Statistical significance was considered at the 95 % confidence level.

Results

Hydrodynamic diameter by DLS

The hydrodynamic diameter, d_h , of DTPA-BSA obtained from a volume-weighted analysis was 8 nm.

Stability

No release of ^{111}In from radiolabeled DTPA-BSA was observed for more than 5 h in saline at room temperature, as confirmed by radio-TLC (> 95 % radiochemical purity). In 50 % mouse serum at 37 °C the tracer was stable for at least 2.5 h (> 95 % radiochemical purity).

Extravasation imaging

The radiolabeled BSA was injected at various times (Δt) after fUS treatment and the extravasation process was imaged using dynamic SPECT. Figure 3.4 shows three SPECT/CT images ($t_{\text{pi}} = 10, 30$ and 60 min; t_{pi} = time elapsed between tracer injection and SPECT scan) from a mouse of the $\Delta t = 10$ min group. Ten minutes after tracer injection the treated hindlimb showed distinct radioactive

spots (white arrows). At later time points ($t_{pi} = 30$ and 60 min) the radioactivity uptake in the treated muscle and surrounding areas increased and the distribution became more homogeneous (see animated sequences in supplementary information Fig. S3.1). In comparison, little radioactivity uptake was observed in the contra-lateral hindlimb (see also supplementary information, Fig. S3.2). In some animals (especially in groups $\Delta t \geq 30$ min), the 7-point pattern was visible in the SPECT images (Fig. 3.5a) with measured inter-point distances around 2-3 mm. Ultrasound induced extravasation was also visible *ex vivo*. Figure 3.5b and 3.5c, respectively, show the hindlimb muscles of a mouse injected with BSA and EB immediately before fUS (group $\Delta t = -10$ min) and that of a mouse with a delayed drug injection (group $\Delta t = 60$ min). In the first animal a large portion of the muscle exhibited a diffuse blue color due to extravasation of albumin-bound EB (Fig. 3.5b). On the contrary, the color was much less noticeable in the second mouse (Fig. 3.5c) due to decreased dye extravasation with increasing Δt , which is consistent with SPECT quantification and γ -counting of activity (*vide infra*). Notably, the second mouse distinctively showed the red spots corresponding to the 7-point fUS pattern, which were greatly masked by the blue color in the previous one, but no gross sign of hemorrhage could be detected.

Real-time imaging and kinetics measurements of focused ultrasound-induced extravasation in skeletal muscle using SPECT/CT

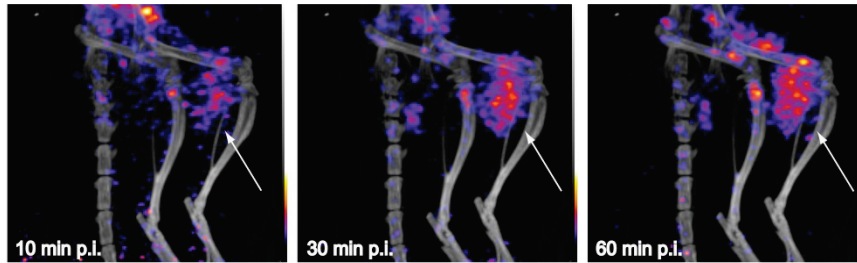


Figure 3.4 *In vivo* dynamic SPECT/CT imaging. Maximum intensity projections of a mouse from group $\Delta t = 10$ min acquired 10, 30 and 60 min post-injection of radiolabeled BSA. White arrows point to the treated area. All images are on the same scale (color scale from SPECT and grey scale from CT).

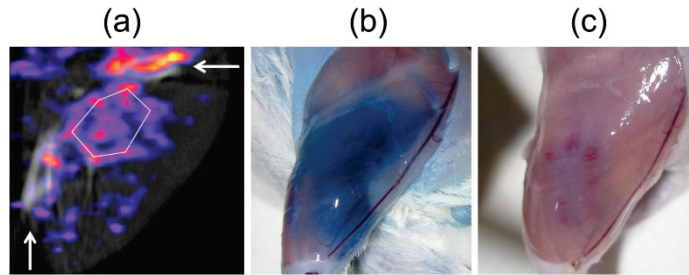


Figure 3.5 *Visible Extravasation*. (a) SPECT/CT image of a mouse from group $\Delta t = 60$ min where the 7-point pattern is visible (white lines). The tibia (vertical arrow) and femur (horizontal arrow) are marked for orientation. The bright spot next to the horizontal arrow is activity accumulated in the femur's bone marrow and is also observed in controls. (b) Evans blue extravasation in treated hindlimb muscle of a mouse from the group $\Delta t = -10$ min and (c) $\Delta t = 60$ min. In (c) the red spots on the muscle correspond to the 7-point pattern from the fUS treatment.

Quantification of extravasation using SPECT/CT and γ -counting

The ^{111}In activity in treated and control muscles was quantified over a time span of 1.5 h (t_{pi}) from the dynamic SPECT scans (5 min frames). Figure 3.6 shows the activity profiles, as $\%ID/cm^3$, of a representative mouse from each Δt group.

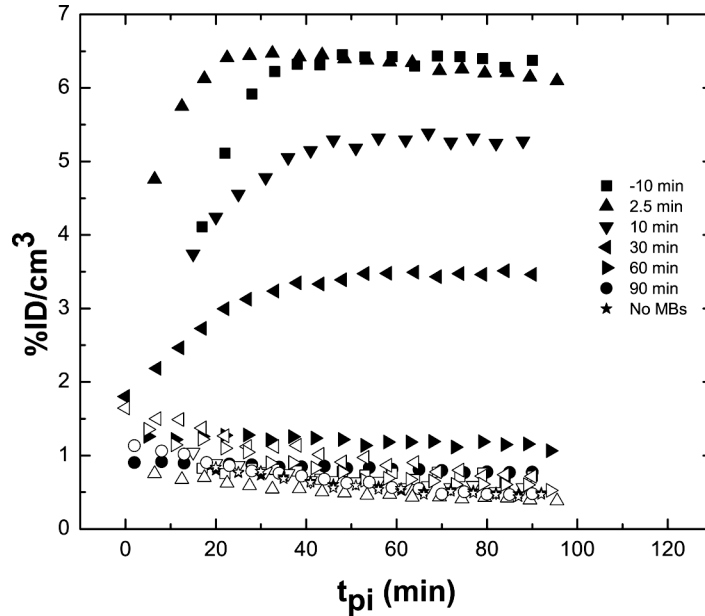


Figure 3.6 Kinetics of Extravasation. Activity per tissue volume from SPECT/CT data in treated and control muscles plotted as a function of time post-BSA injection (t_{pi}) for a representative mouse from each Δt group. Solid and empty symbols represent treated and control areas, respectively.

In general, the kinetics of activity accumulation per unit volume of tissue can be described using a single exponential fit:

$$\text{Equation 3.1} \quad \%ID/cm^3 = y_0 + A * e^{kt_{pi}}$$

with t_{pi} being the time post-injection in minutes, y_0 the offset activity, A the activity at $t_{pi} = 0$, and k being the rate of activity accumulation.

Short Δt between fUS treatment and BSA injection resulted in fast accumulation of activity in the treated area and also in a high final $\%ID/cm^3$ shown in Figure 3.6. The kinetics of each individual animal was fitted with Eq. 3.1 (for parameters see supplementary information, Table S3.1). For $\Delta t = 2.5$ min the k 's are lower than for animals in group $\Delta t = -10$ min, indicating the latter group shows a higher accumulation rate in the treated areas. For each animal, the time to reach 95 % of the $\%ID/cm^3$ (at 2 h p.i.) was calculated and averaged for each group (Table 3.1). For instance, in the $\Delta t = 2.5$ min group the activity in the treated muscle reached 95 % after 17 min while it took 39 min for the $\Delta t = 30$ min group. Since for $\Delta t = 60, 90$, and No MBs the activity was decreasing the values were not calculated. No significant difference was observed between the treated areas of the No MBs and the control areas of all other groups. In the $\Delta t = 60$ min group the activity in the treated muscle was significantly higher than in

the control muscle (ratio ca. 2). On the contrary, no significant increase in activity with respect to the control hindlimb was observed for the $\Delta t = 90$ min and No MBs groups. The *ex vivo* analysis of ^{111}In -DTPA-BSA distribution in different organs showed no significant differences between the animal groups (see supplementary information Fig. S3.3) except for the treated vs. control muscle.

Table 3.1 Kinetics of activity accumulation in treated areas. Data presented as the mean \pm standard deviation ($n = 5$ for $\Delta t = 10$ min; $n = 4$ for $\Delta t = 30$ min; and $n = 3$ for all other groups).

Δt	t_{95} (min)
-10	32 \pm 1
2.5	17 \pm 4
10	29 \pm 7
30	39 \pm 20

$$t_{95} = t[0.95 * \%ID/cm^3 \text{ at } 2 \text{ h p.i.}]$$

Time Window of Extravasation

Figure 3.7 shows the averaged accumulated activity within the fUS treatment and control volumes at 2 h post-BSA injection derived from the extrapolated *in vivo* SPECT data ($\%ID/cm^3$ at $t_{pi} = 2\text{h}$) and from *ex vivo* γ -counting ($\%ID/g$) for each group as a function of Δt . The SPECT data agree with the corresponding γ -counting data for the dissected muscle sections (Table 3.2 and supplementary information, Fig. S3.4). As previously observed, the amount of extravasated activity after 2 h in the treated muscle is highest for short Δt and exponentially reduces with increasing Δt (Fig. 3.7). The averaged data can be fitted using a single exponential curve (Eq. 3.2)

$$\text{Equation 3.2: } \%ID/[cm^3, g](\Delta t) = A_0(\%ID/[cm^3, g]) * e^{-\frac{\Delta t}{\tau}} + y_0(\%ID/[cm^3, g])$$

where Δt is waiting time in minutes and τ the time constant of the curves representing the rate of gap closing from the permeabilized areas. The half-life, $t_{1/2}$, calculated from the curve characterizes the time window for fUS-induced drug extravasation in terms of $\%ID/cm^3$ or $\%ID/g$ over time. For the experimental conditions used (i.e., type of fUS transducer, fUS treatment parameters, type and concentration of MBs), the calculated $t_{1/2}$ of fUS-induced BSA extravasation is 21.4 ± 11.1 min according to SPECT and 15.2 ± 7.1 min according to *ex vivo* γ -counting (Table 3.2). Again, the data clearly show that without MBs co-injection during the fUS treatment, no significant BSA accumulation is obtained in the treated area (Fig. 3.7, right panel). The group $\Delta t = -10$ min was not included in this analysis as the activity was injected in the mice before the fUS treatment.

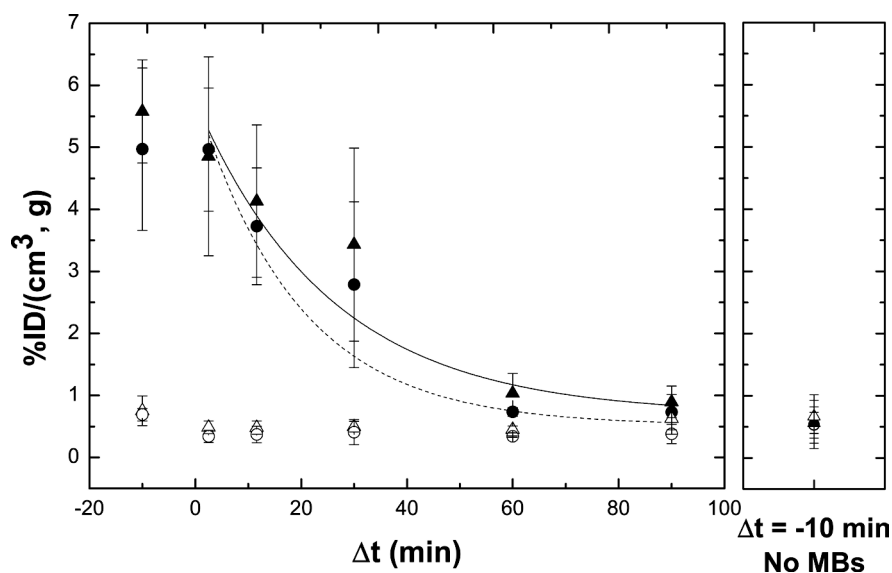


Figure 3.7 Time window for extravasation. Averaged SPECT/CT (\blacktriangle treated and \triangle control) data (%ID/cm³) and γ -counting (\bullet treated and \circ control) data (%ID/g) for each Δt group 2 h post-BSA injection plotted as a function of Δt . Data are fitted with an exponential curve (solid line is SPECT data; Eq. 3.2). Error bars represent standard deviations ($n = 5$ for $\Delta t = 10$ min; $n = 4$ for $\Delta t = 30$ min; and $n = 3$ for all other groups).

Table 3.2 Fit parameters for the exponential fit (Eq. 3.2) and calculated half-lives for enhanced extravasation effect. Data presented as mean \pm standard deviation ($n = 5$ for $\Delta t = 10$ min; $n = 4$ for $\Delta t = 30$ min; and $n = 3$ for all other groups).

Δt	Activity at 2 h p.i.			
	SPECT (%ID/cm ³)		γ -counting (%ID/g)	
	Treated	Control	Treated	Control
-10	5.58 \pm 0.83	0.75 \pm 0.24	4.97 \pm 1.31	0.69 \pm 0.1
2.5	4.85 \pm 1.6	0.49 \pm 0.1	4.96 \pm 0.99	0.34 \pm 0.1
10	4.13 \pm 1.23	0.48 \pm 0.12	3.73 \pm 0.94	0.37 \pm 0.13
30	3.43 \pm 1.56	0.5 \pm 0.09	2.79 \pm 1.34	0.41 \pm 0.2
60	1.04 \pm 0.32	0.45 \pm 0.05	0.73 \pm 0.07	0.34 \pm 0.01
90	0.9 \pm 0.25	0.63 \pm 0.26	0.73 \pm 0.28	0.38 \pm 0.15
No MBs	0.56 \pm 0.17	0.67 \pm 0.35	0.53 \pm 0.29	0.54 \pm 0.39

Fitted Curves	y_0 (%ID/g)	A_0 (%ID/g)	τ (min)	R^2	$t_{1/2}$ (min)
SPECT/CT	0.7 \pm 0.3	5.1 \pm 1.0	25.4 \pm 10.7	0.87	21.4 \pm 11.1
ex vivo γ -counting	0.5 \pm 0.3	5.3 \pm 0.9	19.2 \pm 7.5	0.91	15.2 \pm 7.1

Histology

The excised hindlimb muscles were divided into 2 parts: part 1 included a region from the middle of the 7-point pattern containing at least one of the red points, and part 2 was taken in the region immediately surrounding the red spots. For all Δt groups, H&E staining of slices obtained from part 1 of the treated muscle showed few damaged fibers, enlarged gaps between fibers and some erythrocytes between muscle fibers outside the vasculature (Fig. 3.8a, b and d). On the contrary, the region immediately surrounding the 7-point pattern (Fig. 3.8e) shows no visible difference with the control tissues. No damage was observed also in the treated muscle samples harvested from the mice that did not receive MB infusion before fUS (No MBs group, Fig. 3.8c).

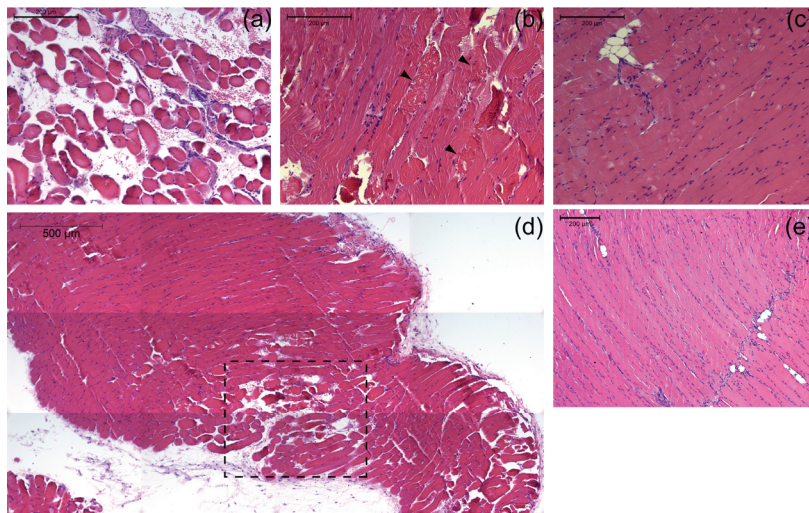


Figure 3.8 Histology. Representative images of H&E stained slices of muscle. a) extravasated red blood cells are visible (treated, $\Delta t = 10$ min group); b) some damaged fibers (arrows; treated, $\Delta t = 10$ min group); c) no damage (treated, No MBs group); d) some red blood cells and damaged fibers are visible in an area about $500 \mu\text{m}$ wide (inside box) in between unaffected tissue ($\Delta t = 10$ min group); e) region immediately surrounding 7-point pattern ($\Delta t = 10$ min group). Scale is $200 \mu\text{m}$ for all panels except (d) which is $500 \mu\text{m}$.

Discussion

The use of fUS in combination with MBs has been shown to temporarily permeabilize the vasculature leading to a localized extravasation of compounds that otherwise remain intravascular. However, little quantitative information was available on the kinetics of fUS-induced extravasation in muscle and its evolution in time [6, 33]. Here, a non-invasive volumetric method was applied to image and quantify this phenomenon in skeletal muscle *in vivo* using radiolabeled BSA as a model drug and SPECT/CT imaging. In order to obtain information on the time-dependent changes in permeabilization, we systematically increased the

waiting time Δt between ultrasound treatment and tracer injection thus giving more time for the endothelium to normalize. Enhancing the extravasation of albumin is of special importance as this protein serves as a carrier vehicle for several albumin-associated drugs [34] and is often used as an extravasation marker, also in combination with the albumin-binding dye EB [35-38], which here was used as a visual marker to guide tissue dissection *ex vivo*.

Following ^{111}In -DTPA-BSA intravenous injection in mice, *in vivo* imaging showed high activity in blood at early time points and accumulation of radioactivity in the liver over time, as expected for a radiolabeled protein. An activity build-up in the bladder was also observed with time. As ^{111}In -DTPA-BSA was found to be stable in serum *in vitro*, we assume that BSA liver uptake followed by fast metabolism and subsequent renal excretion of small radio-metabolites is responsible for the observed activity in the urine [39]. However, this process did not affect or limit the extravasation study in the hindlimb muscle. In fact, SPECT imaging started shortly after ^{111}In -DTPA-BSA injection, which was performed at various Δt after the fUS treatment. Therefore, all mice had approximately the same BSA concentration in blood at the time of SPECT imaging and the observed differences in muscle uptake among the groups result from the different Δt . With the applied acoustic pressure, extravasation was observed only in the groups where MBs were injected, indicating that the mechanical effects induced by oscillating MBs are necessary to induce endothelium permeabilization.

The radioactivity concentration in the fUS treated regions increased exponentially and leveled off between 17 and 40 min in all animals that received the tracer shortly after treatment ($\Delta t \leq 30$ min), while the extravasation kinetics as well as the plateau values decreased for longer Δt . Overall, the maximum radioactivity concentration (2 h post-BSA injection) in the treated muscle decreased exponentially with Δt with a half-life of 21 ± 11.1 min and 15 ± 7.1 min according to SPECT and γ -counting ($p > 0.8$), respectively, characterizing the time window for extravasation after fUS treatment. Group $\Delta t = -10$ min was not included in the fit for the time window calculation. In this group, when the fUS treatment ended the activity concentration was already distributed in the blood stream. The other groups, except the NoMBs, received a bolus injection of tracer when the tissue was already permeabilized (after the fUS treatment). Thus the conditions for $\Delta t = -10$ min are not identical to the other treated animals. Still, the amount of extravasated tracer is comparable to the one from group $\Delta t = 2.5$ min.

Our findings on extravasation kinetics are in agreement with published data (Table 3.3). In fact, Böhmer *et al.* [6] found that EB extravasation in skeletal muscle was more than two-fold decreased when the dye was injected 60 min after fUS treatment instead of immediately after and a closing time of at least 1 h. In a study by Yang *et al.* [11], fUS caused BBB disruption (BBBD) and EB was injected at different time points after treatment. Although the authors of this

study did not report the exact value, from their data an approximate 20-25 min half-life can be estimated for EB. Also, in a recent study, Marty *et al.* [14] published data on BBBD using fUS in combination with MBs. In order to probe closure of the BBB, MRI contrast agents of different sizes were injected in that study at different times after the fUS. The authors proposed a simple model, where (circular) openings in the endothelium were induced by the fUS treatment. These openings with a characteristic diameter were assumed to close exponentially with a closure rate constant of $1.54 \times 10^{-5} \text{ s}^{-1}$. Based on this model, the time window of extravasation for molecules of a certain size after BBBD can be calculated as:

Equation 3.3:
$$t_{1/2} = \frac{A}{1+B \cdot d_h^2}$$

with $A = 2.35 \times 10^4 \text{ s}$, $B = 0.2106 \text{ nm}^{-2}$, and d_h (nm) being the hydrodynamic diameter of the molecule. For radiolabeled BSA, with $d_h = 8 \text{ nm}$, the estimated half-life of extravasation is 27.1 min according to this model. This model (Eq. 3.3) is also very sensitive to the particle's diameter with 1 nm differences changing the half-life value in 6.5 min (ca. 25 %), within the range of 7-9 nm. These values found from the BBBD and skeletal muscle compare well to our measured values in muscle tissue, considering that different ultrasound parameters, setup, organ (muscle vs. brain) and animal model (mouse vs. rat) were used. Focused US was shown to promote local extravasation of 100 nm [40] and 150 nm [33] nanoparticles in skeleton muscle (Table 3.3) or to induce delivery of genetic vectors [7]. However, these studies do not provide information on the time window of extravasation as the particles are injected as close as possible to the fUS treatment. Also, in BBBD differently sized agents have been delivered, e.g. Gd-chelates (< 1 nm), antibodies (ca. 10 nm), liposomal doxorubicin (70-90 nm) and genetic vectors (100-250 nm) [16, 17, 41-43]. In particular, for Gd-chelates, Marty *et al.* [14] found half-life closure times of ca. 5 h, Park *et al.* [15] obtained 2.2 h, while Hynynen *et al.* [44, 45] found 1 or 2 h depending on the pressure used (Table 3.3). In these experiments different fUS settings, MBs concentrations, and animal models were used which could explain these differences, especially for the smaller particles (< 1 nm).

Still, in most studies the BBB recovered within 6-12 h, with some cases up to 24 h [16]. For larger particles, effective extravasation was seen when the particles were injected before or immediately after fUS treatment with shorter BBBD recovery times [14, 17].

Table 3.3 Selected studies on fUS delivery. Enhanced accumulation time is defined as the maximum period of time for which significant extravasation was observed.

Publication	Species + target organ	Drug/Tracer	MBs	Ultrasound settings			Treatment time (s)	Enhanced accumulation time	
				Frequency (MHz)	Pressure (MPa)	PRF (Hz)			
Marty et al. [14]	rat (brain)	MR contrast agents (<1 to 65 nm)	Sonovue® (3•10 ⁷ MBs)	1.5	0.45	0.1	3	60	1 nm: >10 h (t _{1/2} ≈ 5 h) 4 nm: < 2 h (t _{1/2} ≈ 1 h) 7 nm: > 1.5 h (t _{1/2} ≈ 35 min) 25 nm: < 10 min (t _{1/2} ≈ 3 min) 65 nm: < 1 min (t _{1/2} ≈ 0.5 min)
Hynnen et al. [44]	rabbit (brain)	Gd-chelate (< 1 nm)	Optison® (ca. 1•10 ⁸ MBs)	0.69	0.8	1	10	20	< 5 h (t _{1/2} ≈ 1 h)
Hynnen (2) et al. [45]	rabbit (brain)	Gd-chelate (< 1 nm)	Optison® (ca. 1•10 ⁸ MBs)	1.63	1 – 3.3	1	10	20	up to 6 h (t _{1/2} ≈ 1 h for 1 MPa and ≈ 2 h for 3.3 MPa)
Park et al. [15]	rat (brain)	Gd-chelate (< 1 nm)	Definity® (ca. 3.6•10 ⁶ MBs)	0.69	ca. 0.65	1	10	60	up to 4.5 h (t _{1/2} ≈ 2.2 h) (values from k _{trans})
Yang et al. [11]	rat (brain)	(ca. 8 nm bound to BSA)	SonoVue® (ca. 1•10 ⁷ MBs)	1	0.9	1	50	60	at least 40 min (t _{1/2} ≈ 20-25 min)
Song et al. [40]	rat (skeletal muscle)	PM (100 nm)	Optison® (400 µL of 50 % stock concentration)	1	0.75	0.1 – 1	0.1	10 – 40	-
Burke et al. [33]	mouse (skeletal muscle)	PLGA NPs (150 nm)	Albumin (ca 2.5•10 ⁶ MBs)	1	0.75	0.2	ca. 1.5	720	at least 1 h
Böhmer et al. [6]	mouse (skeletal muscle)	EB (ca. 8 nm bound to BSA)	Polymer (5•10 ⁷ MBs)	1.2	2	-	8.3	300	at least 1 h
Lin et al. [19]	mouse (tumor)	LOD (130 nm)	SonoVue® (1•10 ⁶ MBs)	1	1.2	1	10	120	up to 12 h

Legend: BSA - bovine serum albumin; enhanced accumulation time - maximum period of time for which significant extravasation was observed; EB - evans blue; LQD - lipid-coated quantum dots; MB - microbubble; NP - nanoparticle; PLGA - poly(lactic-co-glycolic acid); PM - polymer microsphere; PRF - pulse repetition frequency; $t_{1/2}$ - half-life value for the time window of extravasation

Following the suggestions of earlier publications [14, 41, 46], we believe that oscillating MBs and other acoustic forces induce gaps between endothelial cells. We propose that vessel integrity is subsequently restored with a similar rate in all blood vessels regardless of the specific tissue. Therefore, the time window of extravasation is governed by the size of the extravasating molecules compared to the gap size. As the gaps are created by oscillating MBs and other acoustic forces, their characteristics depend on the treatment protocol, i.e. on the fUS settings and on the injected MBs. In the brain, Marty *et al.* [14] registered a maximum gap size of ca. 65 nm while Treat *et al.* [47] were able to extravasate liposomes greater than 80 nm, and in skeletal muscle particles of 150 nm could be delivered [33]. We further propose that the achievable amount of extravasation in skeletal muscle correlates with the number of gaps created, which depends on the vascular surface area within the treated volume. This effect is expected to increase with the number of MBs. In fact, increased BBBD and tissue damage was correlated to increased MBs dosage in several studies [16, 47, 48]. The same was seen by Lin *et al.* [19] in tumors. To draw a final conclusion if relaxation mechanisms of endothelial layers are independent of tissues and have the same rate constant in muscle or brain, a similar study would be needed with tracers of different sizes, and ideally across species, which is beyond the scope of this paper.

Based on published studies, inertial cavitation of MBs leads to some unavoidable collateral damage [17, 49] such as microvascular leakage accompanied by capillary damage, and erythrocyte extravasation with resulting edema and inflammation [8, 38]. Furthermore, local and fast resolving temperature increases in the vicinity of collapsing MBs are likely, though it is not expected that these lead to macroscopic temperature elevations on tissue level for the used treatment scheme [50]. We speculate that the onset of such a variety of biological reactions following the fUS treatment contributes to the large deviations observed within the treated groups since at the applied pressure the MBs are expected to be driven into both inertial and non-inertial cavitation regimes.

In the treated area the histology results show enlarged gaps between muscle fibers, which are expected as the volume of interstitial fluid increases by inducing extravasation. In muscle areas where the fUS was applied some erythrocyte leakage was observed together with infiltration of some inflammatory cells, which are known to rapidly invade muscle areas subjected to injury or increased loading [51]. The 7-point fUS treatment pattern could be traced back on the treated skeletal muscle, both in the initial dynamic SPECT/CT

images and *ex-vivo* in the form of 7 red points. As the dimension of the ellipsoidal US focus spot is ca. $1 \times 1 \times 9 \text{ mm}^3$, the depth of treatment extends throughout the whole muscle from anterior to posterior. Importantly, the muscle tissue immediately adjacent to the treated area, where EB extravasation was visible, showed very little to no erythrocyte leakage and/or damage on histology. Moreover, in a parallel experiment (data not shown) the animals showed no signs of pain or distress after fUS treatment at least until 16 h post-treatment. This shows the precision of fUS in locally targeting tissues in the body while leaving the surrounding tissue untouched. Interestingly, both radiolabeled BSA and EB extravasated to areas larger than the treatment zone. This is in accordance to previous work in which extravasation in skeletal muscle was seen over wide areas [6]. We believe that once the endothelial layer of a vessel around a muscle fiber is permeabilized, extravasation occurs with subsequent diffusion of the extravasated species along the muscle fibers leading to a distribution in an area slightly larger than the treatment volume.

Overall, our results on fUS-induced extravasation show that the pharmacokinetics of drug accumulation in both treated and control areas can be imaged and quantified *in vivo* non-invasively with SPECT/CT.

Conclusion

In this study, we have developed a method to probe and quantify non-invasively the dynamics of fUS-mediated extravasation in skeletal muscles with SPECT/CT imaging. We determined the temporal window for fUS-mediated drug delivery in skeletal muscle for a tracer with a size of ca. 8 nm for the first time. Our results agree with previous findings on BBBB, therefore suggesting that for the same US treatment conditions the time needed for the blood vessel to repair after a mechanical stress caused by oscillating MBs and other acoustic forces may in fact be an intrinsic mechanical property of the endothelial layer and potentially independent of the specific tissue.

Acknowledgements

The authors would like to thank Caren van Kamen and Carlijn van Helvert for assistance with animal handling, Monique Berben for support in biodistribution, and Ralf Seip and Balasundar Raju for technical discussions about the fUS system.

This project was funded in part by the EU FP7 project Sonodrugs (NMP4-LA-2008-213706).

References

- [1] D.A. Smith, H.v.d. Waterbeemd, D.K. Walker, Pharmacokinetics and metabolism in drug design, 2nd

Real-time imaging and kinetics measurements of focused ultrasound-induced extravasation
in skeletal muscle using SPECT/CT

ed., Wiley-VCH, Weinheim, 2006.

- [2] C.V. Pecot, G.A. Calin, R.L. Coleman, G. Lopez-Berestein, A.K. Sood, RNA interference in the clinic: challenges and future directions, *Nat Rev Cancer*, 11 (2011) 59-67.
- [3] M. Nishikawa, Y. Takakura, M. Hashida, Theoretical considerations involving the pharmacokinetics of plasmid DNA, *Adv Drug Deliv Rev*, 57 (2005) 675-688.
- [4] K. Ferrara, R. Pollard, M. Borden, Ultrasound microbubble contrast agents: fundamentals and application to gene and drug delivery, *Annual review of biomedical engineering*, 9 (2007) 415-447.
- [5] A. van Wamel, K. Kooiman, M. Hartevelde, M. Emmer, F.J. ten Cate, M. Versluis, N. de Jong, Vibrating microbubbles poking individual cells: drug transfer into cells via sonoporation, *J Control Release*, 112 (2006) 149-155.
- [6] M.R. Bohmer, C.H. Chlon, B.I. Raju, C.T. Chin, T. Shevchenko, A.L. Klibanov, Focused ultrasound and microbubbles for enhanced extravasation, *J Control Release*, 148 (2010) 18-24.
- [7] P.G. Sanches, H. Grull, O.C. Steinbach, See, reach, treat: ultrasound-triggered image-guided drug delivery, *Ther Deliv*, 2 (2011) 919-934.
- [8] S. Qin, C.F. Caskey, K.W. Ferrara, Ultrasound contrast microbubbles in imaging and therapy: physical principles and engineering, *Phys Med Biol*, 54 (2009) R27-57.
- [9] R. Seip, C.T. Chin, C.S. Hall, B.I. Raju, A. Ghanem, K. Tiemann, Targeted ultrasound-mediated delivery of nanoparticles: on the development of a new HIFU-based therapy and imaging device, *IEEE Trans Biomed Eng*, 57 (2010) 61-70.
- [10] C.R. Mayer, R. Bekeredjian, Ultrasonic gene and drug delivery to the cardiovascular system, *Advanced drug delivery reviews*, 60 (2008) 1177-1192.
- [11] F.Y. Yang, Y.S. Lin, K.H. Kang, T.K. Chao, Reversible blood-brain barrier disruption by repeated transcranial focused ultrasound allows enhanced extravasation, *J Control Release*, 150 (2011) 111-116.
- [12] K.J. Lin, H.L. Liu, P.H. Hsu, Y.H. Chung, W.C. Huang, J.C. Chen, S.P. Wey, T.C. Yen, I.T. Hsiao, Quantitative micro-SPECT/CT for detecting focused ultrasound-induced blood-brain barrier opening in the rat, *Nucl Med Biol*, 36 (2009) 853-861.
- [13] F.Y. Yang, H.E. Wang, G.L. Lin, M.C. Teng, H.H. Lin, T.T. Wong, R.S. Liu, Micro-SPECT/CT-based pharmacokinetic analysis of ^{99m}Tc-diethylenetriaminepentaacetic acid in rats with blood-brain barrier disruption induced by focused ultrasound, *J Nucl Med*, 52 (2011) 478-484.
- [14] B. Marty, B. Larrat, M. Van Landeghem, C. Robic, P. Robert, M. Port, D. Le Bihan, M. Pernot, M. Tanter, F. Lethimonnier, S. Meriaux, Dynamic study of blood-brain barrier closure after its disruption using ultrasound: a quantitative analysis, *Journal of cerebral blood flow and metabolism : official journal of the International Society of Cerebral Blood Flow and Metabolism*, 32 (2012) 1948-1958.
- [15] J. Park, Y. Zhang, N. Vykhodtseva, F.A. Jolesz, N.J. McDannold, The kinetics of blood brain barrier permeability and targeted doxorubicin delivery into brain induced by focused ultrasound, *J Control Release*, 162 (2012) 134-142.
- [16] M.A. O'Reilly, K. Hynynen, Ultrasound enhanced drug delivery to the brain and central nervous system, *Int J Hyperthermia*, 28 (2012) 386-396.
- [17] K. Hynynen, Ultrasound for drug and gene delivery to the brain, *Adv Drug Deliv Rev*, 60 (2008) 1209-1217.
- [18] C.R. Mayer, N.A. Geis, H.A. Katus, R. Bekeredjian, Ultrasound targeted microbubble destruction for drug and gene delivery, *Expert Opin Drug Deliv*, 5 (2008) 1121-1138.
- [19] C.Y. Lin, Y.L. Huang, J.R. Li, F.H. Chang, W.L. Lin, Effects of focused ultrasound and microbubbles on the vascular permeability of nanoparticles delivered into mouse tumors, *Ultrasound Med Biol*, 36 (2010) 1460-1469.
- [20] V. Frenkel, Ultrasound mediated delivery of drugs and genes to solid tumors, *Advanced drug delivery reviews*, 60 (2008) 1193-1208.
- [21] A.R. Williams, Disorganization and Disruption of Mammalian and Amoeboid Cells by Acoustic Microstreaming, *J Acoust Soc Am*, 52 (1972) 688-693.
- [22] S. Bao, B.D. Thrall, D.L. Miller, Transfection of a reporter plasmid into cultured cells by sonoporation in vitro, *Ultrasound Med Biol*, 23 (1997) 953-959.
- [23] Y. Zhou, R.E. Kumon, J. Cui, C.X. Deng, The size of sonoporation pores on the cell membrane, *Ultrasound Med Biol*, 35 (2009) 1756-1760.
- [24] K. Kooiman, M. Foppen-Hartevelde, N. de Jong, Ultrasound-mediated targeted microbubble sonoporation of endothelial cells, *J Control Release*, 148 (2010) e62-63.
- [25] D.L. Miller, A review of the ultrasonic bioeffects of microsonation, gas-body activation, and related cavitation-like phenomena, *Ultrasound Med Biol*, 13 (1987) 443-470.
- [26] A. Yudina, M. Lepetit-Coiffe, C.T. Moonen, Evaluation of the temporal window for drug delivery following ultrasound-mediated membrane permeability enhancement, *Mol Imaging Biol*, 13 (2011) 239-249.
- [27] B. Krasovitski, V. Frenkel, S. Shoham, E. Kimmel, Intramembrane cavitation as a unifying mechanism for ultrasound-induced bioeffects, *Proc Natl Acad Sci U S A*, 108 (2011) 3258-3263.
- [28] J.M. Escoffre, A. Zeghimi, A. Novell, A. Bouakaz, In vivo gene delivery by sonoporation: progress and prospects, *Curr Gene Ther*, in press (2012).
- [29] P. Sanches, R. Rossin, M. Böhmer, K. Tiemann, H. Grull, In vivo SPECT/CT imaging of focused ultrasound induced extravasation, *Nucl Med Biol*, 37 (2010) 722.
- [30] P. Sanches, R. Rossin, M. Böhmer, K. Tiemann, H. Grull, In vivo SPECT/CT imaging of focused ultrasound induced extravasation, in: U. Mazzi, W.C. Eckelman, W.A. Volkert (Eds.) *Technetium and Other Radiometals in Chemistry and Medicine*, SGEitorali, Padova, Italy, 2010, pp. 547-550. ISBN 9788889884140.
- [31] Institute of Laboratory Animal Resources (U.S.). Committee on Care and Use of Laboratory Animals., *Guide for the care and use of laboratory animals*, in: NIH publication, U.S. Dept. of Health and Human Services, Public Health Service, Bethesda, Md., pp. v.
- [32] C. Chlon, C. Guedon, B. Verhaagen, W.T. Shi, C.S. Hall, J. Lub, M.R. Bohmer, Effect of molecular

Chapter 3

weight, crystallinity, and hydrophobicity on the acoustic activation of polymer-shelled ultrasound contrast agents, *Biomacromolecules*, 10 (2009) 1025-1031.

[33] C.W. Burke, Y.H. Hsiang, E.t. Alexander, A.L. Kilbanov, R.J. Price, Covalently linking poly(lactic-co-glycolic acid) nanoparticles to microbubbles before intravenous injection improves their ultrasound-targeted delivery to skeletal muscle, *Small*, 7 (2011) 1227-1235.

[34] B. Elsadek, F. Kratz, Impact of albumin on drug delivery — New applications on the horizon, *J Control Release*, (2011).

[35] S.Y. Yuan, R.R. Rigor, Regulation of Endothelial Barrier Function, in: Chapter 3: Methods for Measuring Permeability. Available from: <http://www.ncbi.nlm.nih.gov/books/NBK54124/>, Morgan & Claypool Life Sciences, San Rafael (CA), 2010.

[36] P.W. Hamer, J.M. McGeachie, M.J. Davies, M.D. Grounds, Evans Blue Dye as an in vivo marker of myofibre damage: optimising parameters for detecting initial myofibre membrane permeability, *J Anat*, 200 (2002) 69-79.

[37] D.L. Miller, J. Quddus, Diagnostic ultrasound activation of contrast agent gas bodies induces capillary rupture in mice, *Proc Natl Acad Sci U S A*, 97 (2000) 10179-10184.

[38] D.L. Miller, M.A. Averkiou, A.A. Brayman, E.C. Everbach, C.K. Holland, J.H. Wible, Jr., J. Wu, Bioeffects considerations for diagnostic ultrasound contrast agents, *J Ultrasound Med*, 27 (2008) 611-632; quiz 633-616.

[39] K.J. Harrington, G. Rowlinson-Busza, K.N. Syrigos, P.S. Uster, R.M. Abra, J.S. Stewart, Biodistribution and pharmacokinetics of ¹¹¹In-DTPA-labelled pegylated liposomes in a human tumour xenograft model: implications for novel targeting strategies, *Br J Cancer*, 83 (2000) 232-238.

[40] J. Song, J.C. Chappell, M. Qi, E.J. VanGieson, S. Kaul, R.J. Price, Influence of injection site, microvascular pressure and ultrasound variables on microbubble-mediated delivery of microspheres to muscle, *J Am Coll Cardiol*, 39 (2002) 726-731.

[41] N. Vykhotseva, N. McDannold, K. Hynynen, Progress and problems in the application of focused ultrasound for blood-brain barrier disruption, *Ultrasonics*, 48 (2008) 279-296.

[42] A.M. Morao, J.C. Nunes, F. Sousa, M.T.P. de Amorim, I.C. Escobar, J.A. Queiroz, Ultrafiltration of supercoiled plasmid DNA: Modeling and application, *J Memb Sci*, 378 (2011) 280-289.

[43] D.R. Latulippe, A.L. Zydney, Radius of gyration of plasmid DNA isoforms from static light scattering, *Biotechnol Bioeng*, 107 (2010) 134-142.

[44] K. Hynynen, N. McDannold, N.A. Sheikov, F.A. Jolesz, N. Vykhotseva, Local and reversible blood-brain barrier disruption by noninvasive focused ultrasound at frequencies suitable for trans-skull sonications, *Neuroimage*, 24 (2005) 12-20.

[45] K. Hynynen, N. McDannold, N. Vykhotseva, F.A. Jolesz, Noninvasive MR imaging-guided focal opening of the blood-brain barrier in rabbits, *Radiology*, 220 (2001) 640-646.

[46] S. Jalali, Y. Huang, D.J. Dumont, K. Hynynen, Focused ultrasound-mediated bbb disruption is associated with an increase in activation of AKT: experimental study in rats, *BMC Neurol*, 10 (2010) 114.

[47] L.H. Treat, N. McDannold, N. Vykhotseva, Y. Zhang, K. Tam, K. Hynynen, Targeted delivery of doxorubicin to the rat brain at therapeutic levels using MRI-guided focused ultrasound, *Int J Cancer*, 121 (2007) 901-907.

[48] F.Y. Yang, P.Y. Lee, Efficiency of drug delivery enhanced by acoustic pressure during blood-brain barrier disruption induced by focused ultrasound, *Int J Nanomedicine*, 7 (2012) 2573-2582.

[49] D.L. Miller, Overview of experimental studies of biological effects of medical ultrasound caused by gas body activation and inertial cavitation, *Progress in biophysics and molecular biology*, 93 (2007) 314-330.

[50] A.R. Klotz, L. Lindvere, B. Stefanovic, K. Hynynen, Temperature change near microbubbles within a capillary network during focused ultrasound, *Phys Med Biol*, 55 (2010) 1549-1561.

[51] J.G. Tidball, Inflammatory processes in muscle injury and repair, *Am J Physiol Regul Integr Comp Physiol*, 288 (2005) R345-353.

Supplementary information

Real-time imaging and kinetics measurements of focused ultrasound-induced extravasation
in skeletal muscle using SPECT/CT

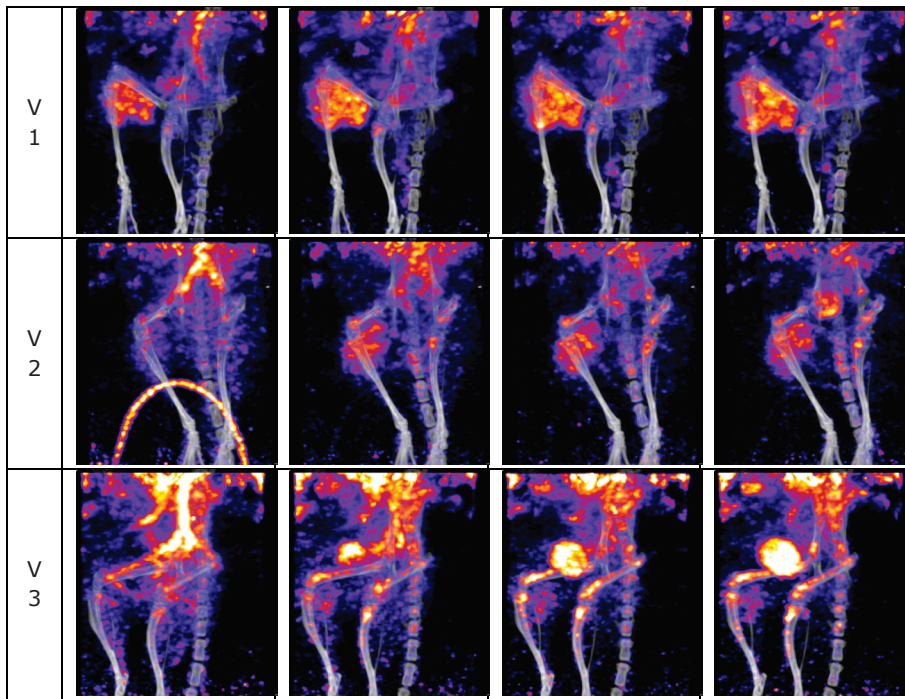


Figure S3.1 The dynamics of extravasation *in vivo*. Stills from animated sequences of 15-18 consecutive SPECT scans of mice from groups $\Delta t = -10$ (V1: frames 1, 4, 9, 15); $\Delta t = 10$ (V2: frames 1, 5, 11, 18), and $\Delta t = 60$ (V3: frames 1, 5, 11, 18) min. Sequences not at the same scale.

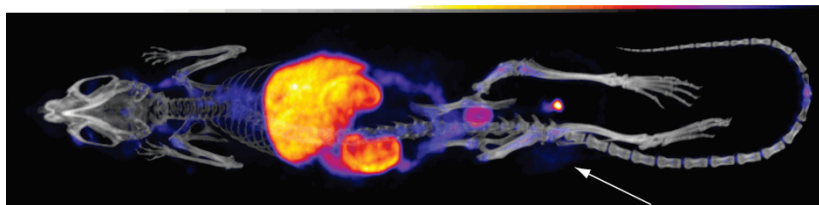


Figure S3.2 Post-mortem SPECT/CT projection of a mouse injected with ^{111}In -DTPA-BSA (group $\Delta t = 30$ min). ^{111}In activity accumulates in the liver (within $t_{pi} = 10$ -15 min, $\%ID/g = 31 \pm 5$, $t_{pi} = 2$ h) and later in the kidneys ($\%ID/g = 22 \pm 6$, $t_{pi} = 2$ h) and urine (within $t_{pi} = 30$ min). The white arrow indicates activity accumulated in the treated hindlimb.

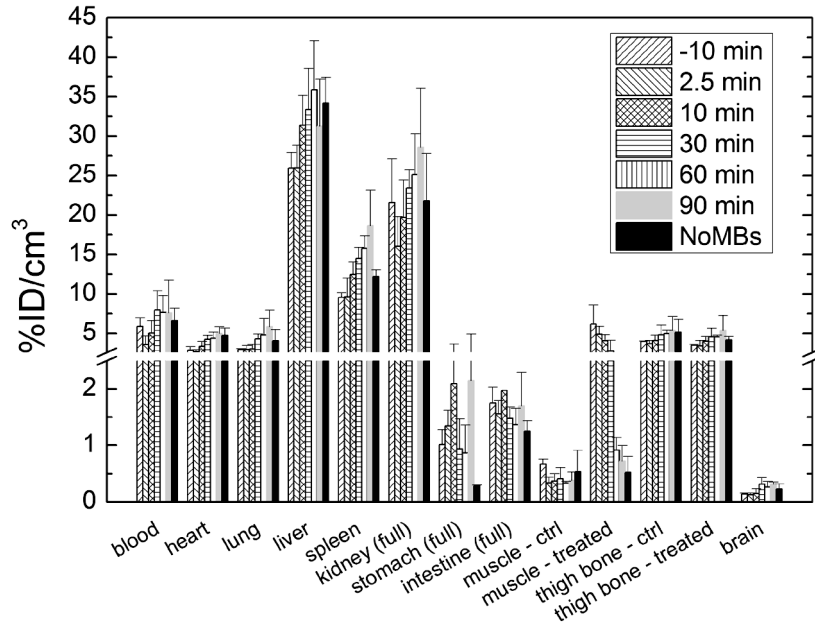


Figure S3.3 Biodistribution of ^{111}In -DTPA-BSA. Activity calculated per organ in terms of %ID/g by γ -counting. No significant difference was found between the Δt groups, except for the treated muscle.

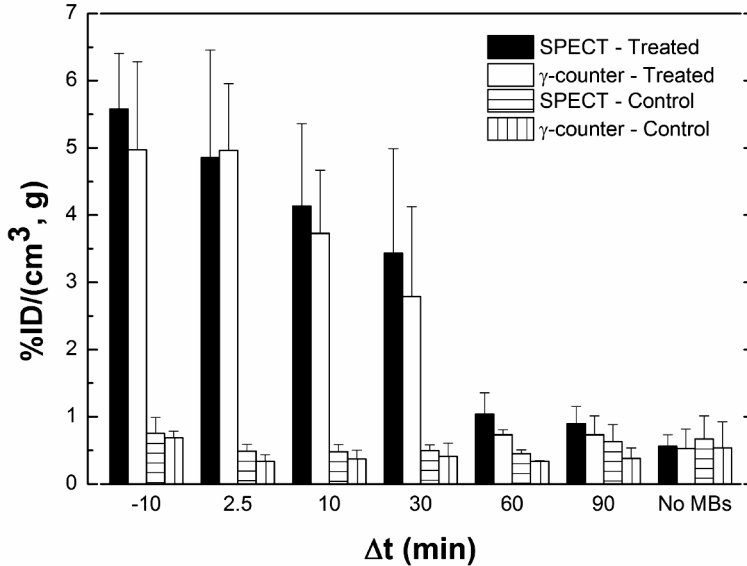


Figure S3.4 Quantification of Activity. Activity calculated for SPECT/CT ($\%ID/\text{cm}^3$) and from γ -counting ($\%ID/g$). The SPECT/CT values correspond to the extrapolated 2 h p.i. data points from each individual exponential fit of the kinetics data (Fig.6), averaged per Δt group. The bars and error bars represent the mean and standard deviation ($n = 5$ for $\Delta t = 10$ min; $n = 4$ for $\Delta t = 30$ min; and $n = 3$ for all other groups).

Real-time imaging and kinetics measurements of focused ultrasound-induced extravasation
in skeletal muscle using SPECT/CT

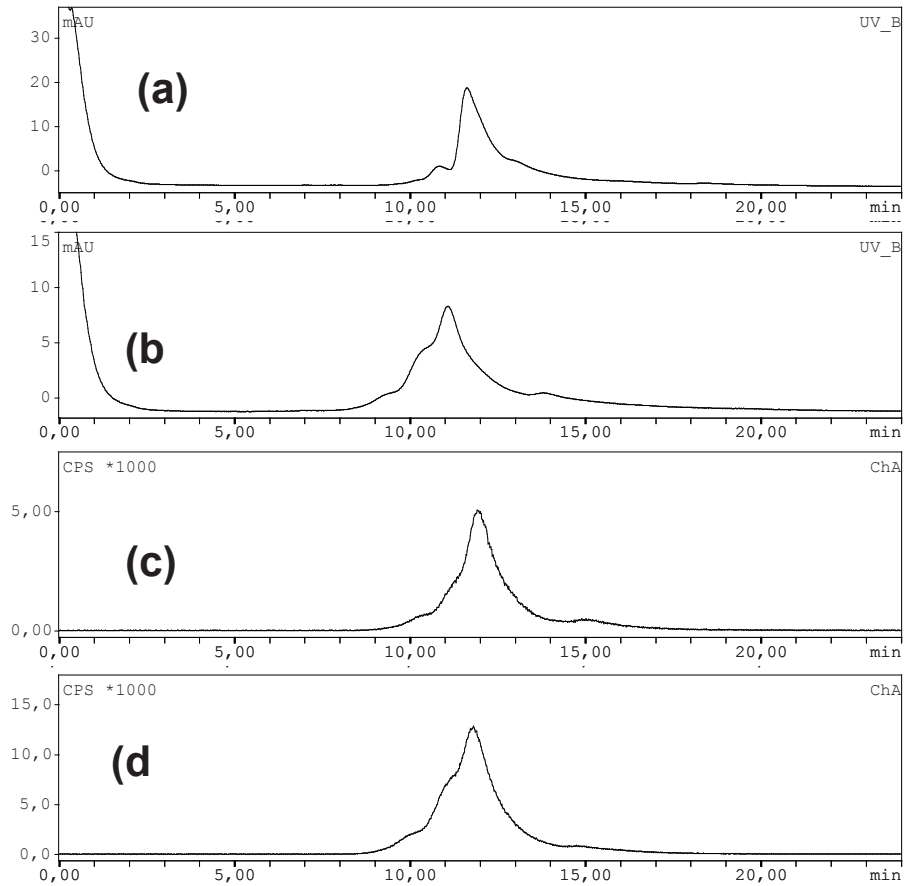


Figure S3.5 Size exclusion HPLC analysis of (a) BSA, (b) DTPA-BSA, (c) carrier-added ^{111}In -DTPA-BSA and (d) non-carrier-added ^{111}In -DTPA-BSA (a and b are the UV profiles at 180 nm, c and d are the radioactive profiles). Size exclusion (SEC) HPLC was carried out on an Agilent 1200 system equipped with a Gabi radioactive detector. The samples were loaded on a BioSep-SEC-S300 column (Phenomenex) and eluted with 10 mM phosphate buffer pH 7.4 at 1 mL/min. The UV wavelength was preset at 260 and 280 nm.

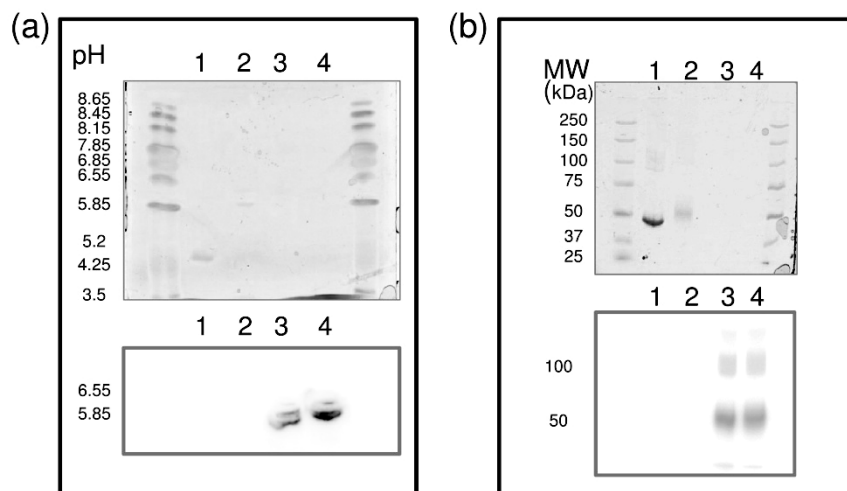


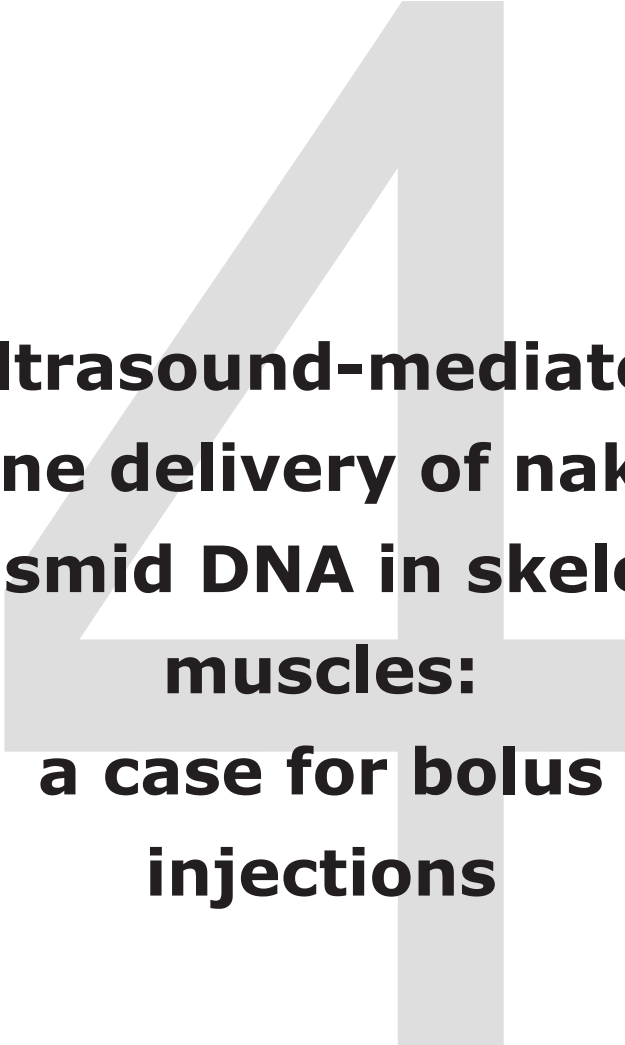
Figure S3.6 Electrophoresis analysis. (a) isoelectric focusing and (b) SDS-PAGE analysis of (lane 1) BSA, (lane 2) DTPA-BSA, (lane 3) carrier added ¹¹¹In-DTPA-BSA, (lane 4) non-carrier added ¹¹¹In-DTPA-BSA. Top panels: protein stains; bottom panels: radiograms. The left and right lanes are the pH and MW calibration standards.

Isoelectric focusing (IEF) analysis and SDS-PAGE were performed on a Phastgel system using IEF-3-9 gels and 7.5% PAGE homogeneous gels (GE Healthcare Life Sciences), respectively. The IEF calibration solution (broad PI, pH 3-10) was purchased from GE Healthcare and the protein MW standard solution (Precision Plus dual color standard) was purchased from BioRad. Upon electrophoresis, the gels were stained for 2 h with gelcode blue, destained overnight in water and then digitized with a conventional flat bed scanner. The radioactivity distribution on TLC plates and IEF/SDS-PAGE gels was evaluated with a phosphor imager (FLA-7000, Fujifilm) with the AIDA software (Raytest). The ¹¹¹In-labeling yields were determined by radio-TLC, using iTLC-SG strips (Varian Inc.) eluted with 10 mM EDTA in 0.9% aq. NaCl. In these conditions, free ¹¹¹In migrates with $R_f = 0.9$, while ¹¹¹In-DTPA-BSA remains at the origin.

Table S3.1. Fit parameters (Eq. 1 - $\%ID/cm^3 = y_0 + A * e^{kt_{pi}}$).of each individual animal. One animal from $\Delta t = 60$ min and No MBs group was fitted linearly.

Δt (min)	y_0 (%ID/cm ³)	A (%ID/cm ³)	k (min ⁻¹)	R ²
-10	4.74	-14.03	-0.12	0.99
-10	6.40	-24.08	-0.14	0.99
-10	5.59	-2.83	-0.06	0.99
2.5	5.10	-5.18	-0.21	0.89
2.5	6.32	-5.74	-0.20	0.90
2.5	3.14	-2.58	-0.13	0.93
10	5.59	-3.17	-0.11	0.99
10	5.33	-5.16	-0.08	0.98
10	3.09	-1.44	-0.10	0.96
10	3.90	-0.08	0.02	0.77
10	3.52	-1.96	-0.08	0.99
30	1.47	-0.36	-0.17	0.82
30	3.54	-1.81	-0.05	0.99
30	3.46	-2.24	-0.06	0.99
30	5.29	-3.94	-0.05	1.00
60	1.32	-0.05	0.01	0.66
60	0.58	0.48	-0.01	0.97
90	0.76	1.04	-0.03	0.99
90	164.40	-162.86	0.00002	0.78
90	26.25	-25.33	0.00007	0.95
No MBs	0.71	0.66	-0.02	0.89
No MBs	0.42	0.66	-0.03	0.97





**Ultrasound-mediated
gene delivery of naked
plasmid DNA in skeletal
muscles:
a case for bolus
injections**

Based on:

P.G. Sanches, M. Muhlmeister, R. Seip, E. Kaijzel, C. Löwik, M. Böhmer, K. Tiemann, H. Grüll, Ultrasound-mediated gene delivery of naked plasmid DNA in skeletal muscles: A case for bolus injections, *J Control Release*, (2014).

Abstract

Localized gene delivery has many potential clinical applications. However, the nucleic acids (e.g. pDNA and siRNA) are incapable of passively crossing the endothelium, cell membranes and other biological barriers which must be crossed to reach their intracellular targets. A possible solution is the use of ultrasound to burst circulating microbubbles inducing transient permeabilization of surrounding tissues which mediates nucleic acid extravasation and cellular uptake. In this study we report on an optimization of the ultrasound gene delivery technique. Naked pDNA (200 µg) encoding luciferase and SonoVue® microbubbles were co-injected intravenously in mice. The hindlimb skeletal muscles were exposed to ultrasound from a non-focused transducer (1 MHz, 1.25 MPa, PRI 30 s) and injection protocols and total amounts as well as ultrasound parameters were systemically varied. Gene expression was quantified relative to a control using a bioluminescence camera system at day 7 after sonication. Bioluminescence ratios in sonicated/control muscles of up to 101x were obtained. In conclusion, we were able to specifically deliver genetic material to the selected skeletal muscles and overall, the use of bolus injections and high microbubble numbers resulted in increased gene expression reflected by stronger bioluminescence signals. Based on our data, bolus injections seem to be required in order to achieve transient highly concentrated levels of nucleic acids and microbubbles at the tissue of interest which upon ultrasound exposure should lead to increased levels of gene delivery. Thus, ultrasound mediated gene delivery is a promising technique for the clinical translation of localized drug delivery.

Keywords: gene delivery; luciferase; ultrasound; microbubbles; skeletal muscle

Introduction

Gene therapy has an immense therapeutic potential for treating diseases caused by a genetic disorder as it can effectively compensate for a gene mutation rather than treating the disease on a symptomatic level. The large effort devoted to gene therapy has resulted in more than 1800 clinical trials to date on gene therapy, which have been completed, are ongoing or have been approved [1]. The treatments are mostly utilizing an engineered gene vector that must be delivered into specific cells/tissues either via viral or non-viral routes. Viral vectors that naturally reach a passive high transduction and transgene expression levels are therefore most commonly used in clinical trials (66.8%) [1]. However, safety concerns (e.g. insertional mutagenesis) and their limited capacity to accommodate a larger DNA load have inspired the development and use of nonviral vectors (25.6%) mostly using naked plasmid DNA (pDNA; 18.3%). Although these vectors are safer, naked plasmid-based gene therapy faces an enormous delivery challenge. Plasmid DNA is a large hydrophilic and charged molecule that is not able to extravasate after intravenous injection into the interstitial space, nor does it passively cross cell membranes for eventual nuclear uptake. Furthermore, pDNA can be rapidly degraded in vivo by systemic and cellular nucleases. One approach to address these shortcomings is the use of delivery vehicles, such as cationic lipids and/or polymers to help protect pDNA in circulation and facilitate the crossing of biological membranes. Although considerable protection is obtained, toxicity and unspecific delivery concerns are not yet addressed [2].

A physical approach such as ultrasound-mediated gene delivery (UMGD), is a potential solution to this problem [3]. This technique employs non-invasive ultrasound (US) waves and intravenously administered microbubbles (MBs) that are currently also used as US contrast agents. These MBs are gas spheres with diameters typically in the range of 1-10 μm that are stabilized with a lipid layer to prevent rapid dissolution in the blood. Upon insonation these circulating MBs are driven to a forced oscillation state led by compression and decompression cycles of their gas core. Depending on the US intensity, the MBs can either simply vibrate and/or collapse. The ensuing mechanical forces, together with the US pressure waves themselves, induce pores in the surrounding endothelium which promotes extravasation of macromolecules that would otherwise remain intravascular. The number of pores and thus the induced overall permeability is expected to increase with the number of MBs [4-6]. Permeability is temporary as the pores close over time leaving a time window for molecules to extravasate that scales inversely with molecule size [7]. Furthermore, oscillating MBs and mechanical forces can induce a transient permeability of cellular membranes, termed sonoporation, which allows cellular uptake of charged molecules like pDNA (Fig. 4.1). Some authors have used MBs as delivery agents themselves by

chemical modifications namely: (multilayer) (antibody targeted) cationic MBs that bind pDNA on the surface; incorporation of pDNA in the MBs; and pDNA carrying nanoparticles linked to MBs [2]. Independently from the route of administration (direct or intravenous injections), several preclinical studies have shown the feasibility of the US-MB technique in a multitude of organs including skeletal muscle [8-15], liver [16, 17], heart [18, 19], pancreas [20], kidney [21, 22], brain [23], tendon [24, 25], and tumor [26-29]. In particular, the works of Fujii et al. [19] in improving myocardial perfusion, Sheyn et al. [30] in inducing ectopic bone growth, and Vu et al. [12] in showing improved glucose homeostasis by targeting the skeletal muscle clearly demonstrated the therapeutic potential of UMGD. Thus, it is possible to systemically co-inject MBs and pDNA and reach local transfection only in the areas subjected to US without any further need for transfection and/or binding agents.

A key factor in this approach is that higher concentrations of pDNA at the site of sonication translates into higher transfection efficiency [31]. Many publications have used direct injections (e.g. intramuscular) to tackle this challenge but its localized nature relative to injection site and invasiveness is problematic [8]. In this study, we explore a simpler approach to locally achieve higher amounts of pDNA encoding a luciferase reporter gene by co-injecting MBs and naked pDNA intravenously in concentrated bolus volumes. A set of UMGD optimization experiments using bioluminescence imaging to quantify the relative expression of luciferase in sonicated areas was performed to explore the most relevant experimental parameters, such as injection type (infusion vs. bolus vs. multiple-boli), MB concentration, and US parameters (e.g. number of cycles).

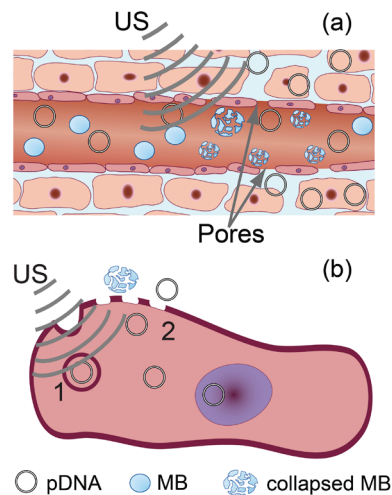


Figure 4.1 (a) Ultrasound induced permeabilization of the endothelium and (b) sonoporation of a cell membrane mediating extravasation of pDNA with subsequent intracellular uptake. Two potential mechanisms involved are depicted: (1) endocytosis and (2) temporary pore formation by sonoporation. The symbols are not to scale.

Materials and Methods

Materials

All reagents and solvents were obtained from Sigma-Aldrich and used without further purification, unless otherwise stated. The plasmid DNA purification kits were obtained from Qiagen (Hilden, Germany).

Animal Studies

All experiments performed in the study were in accordance with the German Law on the Care and Use of Laboratory Animals and approved by the Landesamt für Natur, Umwelt und Verbraucherschutz Nordrhein-Westfalen (LANUV). Female CD-1 mice (25-36 g body weight; Charles River Laboratories, Sulzfeld, Germany) were housed in an enriched environment under standard conditions (23-25 °C, 50-60% humidity, and 12 h light-dark cycles) for at least 1 week before the experiment, with food and water given *ad libitum*.

Experimental protocol

Throughout the text the terms 'bolus' and 'infusion' are defined as follows: 'bolus' refers to a rapid manual injection of a solution volume directly into the bloodstream (injection rate approx. 10 $\mu\text{L/s}$); and 'infusion' is a slow injection (injection rate $\leq 10 \mu\text{L/min}$) of a solution volume, controlled by a syringe pump, directly into the bloodstream.

The experimental protocol consisted of five main steps described in Figure 4.2.

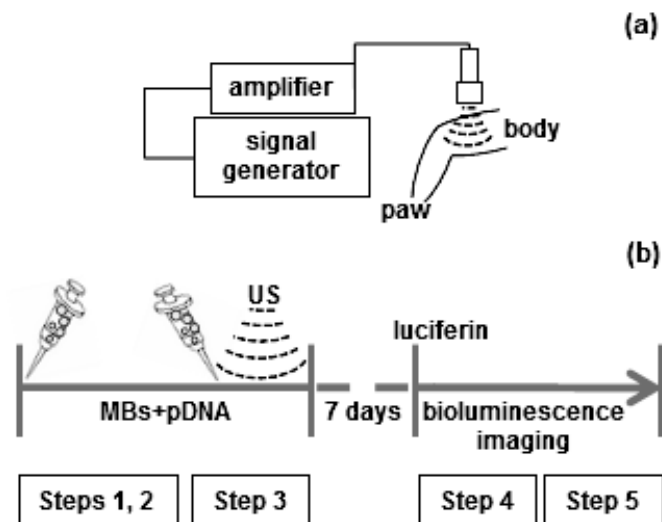


Figure 4.2 Schematic representation of experimental protocol. (a) US setup with signal

generator providing the signal to the amplifier that drives the transducer. Transmission gel (1.5 cm) was placed between transducer and hindlimbs; (b) experimental protocol: step (1) animal preparation; (2) MBs + pDNA solution infused for one minute; (3) US sonication applied to right hindlimb together with bolus and/or infusion of MBs; steps 2 and 3 repeated for left hindlimb; (4) luciferin *i.p.* injection with *in vivo* bioluminescence imaging followed seven days after; (5) animals were euthanized immediately after the imaging scans and skeletal muscle samples prepared for histology.

(1) Animal preparation

The mice were anesthetized with isoflurane and their hindlimbs were shaved and then depilated with commercial hair removal cream (Veet[®], Reckitt Benckiser, Slough, UK). A 26G permanent venous catheter (BD Vasculon[®] Plus, Becton Dickinson GmbH, Heidelberg) was inserted in the tail vein. The mice were then placed in prone position on a heating plate to maintain a 37 °C body temperature, with an acoustic absorber (Aptflex F28, Precision Acoustics, Dorset, UK) underneath to minimize US reflections back into the animal. Degassed US transmission gel (Aquasonics 100, Parker Laboratories) was applied between the absorber and the limbs and between the limbs and the US transducer to create an acoustic path from the transducer to the target region.

(2) MBs + pDNA preparation and injections

SonoVue[®] MBs (2.5 µm mean diameter [32], Bracco, Konstanz, Germany) were re-constituted in saline following a slightly modified protocol from the vendor's instructions, due to the high concentrations used. Briefly, a 24G needle connected to a 1 mL syringe filled with saline was inserted through the rubber cap containing a second 24G needle for venting. After unloading the syringe both needles were removed and the vial was manually shaken according to the vendor's instructions. Then a 20G needle was used to load a 1 mL syringe with the MB suspension and a cap used to close the syringe. The syringe was manually rotated, periodically, until used, to prevent MB aggregation.

The pDNA-luc (pcDNA3.1 backbone with a CMV promoter, Life Technologies, Carlsbad, CA) were amplified in *E. coli* bacteria (One Shot TOP10 chemically competent, Life Technologies) which were transformed by heat shock and plated in LB-agar with 100 µg/mL ampicillin. Subsequently, a single colony was selected and grown overnight in LB media with 100 µg/mL ampicillin. The pDNA was then purified from the lysed bacteria cells using a commercial kit (Endotoxin free Gigaprep, Qiagen) according to the manufacturer's instructions, re-suspended in endotoxin free T.E. buffer, and kept at < -20 °C until use. Plasmid DNA concentration and quality were measured by spectrophotometry (Nanodrop 1000, Wilmington, DE) and used only when the absorbance ratio 260/280 and 260/230, in nm, were higher than 1.8. The maximum pDNA concentration achievable was 5 µg/µL as it represents the upper limit before reaching solubility limits and the solution becomes too viscous.

A solution containing MBs and pDNA (100 µL per sonication/200 µL in total) was mixed immediately before injection in a 1 mL syringe. The osmolarity of the

injected solution containing MBs and pDNA is estimated to be between 150 and 300 mosmol/L (see supplementary information). The syringe was connected to the catheter tubing inserted in the tail vein via a dead volume reducing adapter. Due to the negatively charged surface of the MBs and the negative charge of pDNA, it can be expected that the pDNA does not adhere to the MBs surface [33, 34]. Both bolus injections and constant infusion were performed (Table 4.1) using a syringe pump (Harvard Apparatus, Holliston, MA) for the latter. Before each sonication a pre-infusion of MB + pDNA solution was injected at 10 μ L/min for 1 min in order to reduce pDNA degradation and MB clearance during the later performed sonication step, when MB + pDNA are injected again. For the groups with bolus injections the syringe was then removed from the syringe pump and the boli were given manually at a rate of ca. 10 μ L/s. A total volume of 100 μ L was used per sonication. In order to avoid MBs' aggregating and adhering to the syringe's walls, the syringe was manually rotated periodically during use.

(3) Ultrasound application

An unfocused single element transducer (1 MHz, 2 cm diameter; Olympus, Center Valley, PA) was used to deliver the US energy needed for MB oscillation. It was connected to an amplifier (AG Series Amplifier, T&C Power Conversion, Inc., Rochester, NY) and driven by the signal generator of a therapy and imaging probe system (TIPS, Philips, Briarcliff Manor, NY) [35]. A pressure of 1.25 MPa was chosen based on a pilot study where with the exposure settings used, no detrimental bioeffects were noted in the muscle tissue. A clinical imaging US probe (6-12 MHz, Sonos 5500, Philips) was used for image guidance and target alignment of the transducer at 1.5 cm from skin level. The US exposure started 1 min after MBs + pDNA infusion. The target tissue was the skeletal muscle of both hindlimbs and the right side was always insonated before the left. Injection types and US parameters were varied for the different groups. In the control group the same experimental parameters from the group with the highest gene expression were chosen but without adding MBs. Therefore this group accounts for the effect of MBs in US-mediated transfection, while taking into account any effect from US alone and pDNA i.v. injection. Table 4.1 gives a detailed description of the conditions used in different experimental groups.

Table 4.1 Experimental parameters for all groups. Each column describes the experimental conditions applied per hindlimb (i.e. sonication) listing all parameters that differ between groups. The following parameters were kept unchanged for all sonications: US frequency = 1 MHz, negative peak acoustic pressure = 1.25 MPa, pulse repetition interval (PRI) = 30 s, SonoVue® MBs, 200 µg pDNA. Group 9 is a negative control. Due to experimental errors in e.g. syringe pump and setting of US parameters, some hindlimbs were not counted.

	1	2	3	4	5	6	7	8	9
nr. of animals	6	4	4	4	6	5	4	3	3
nr. of sonicated hindlimbs	12	7	8	6	11	10	8	4	6
number of cycles/exposure	5000	5000	5000	5000	5000	50000	5000	5000	5000
number of exposures	18	18	18	18	18	18	34	34	18
time US ON (min)	8.5	8.5	8.5	8.5	8.5	8.5	16.5	16.5	8.5
pDNA before US ON	pDNA-luc								
type	1 min infusion @ 10 µL/min								
sequence	Bolus	bolus	bolus	infusion	infusion	infusion	bolus + infusion	infusion	only pDNA
[MBs] / sonication	2x 50 µL @ 1.5, 5.5 min	4x 25 µL @ 1.5, 3.5, 5.5, 7.5 min	2x 50 µL @ 1.5, 5.5 min	10 µL/min	10 µL/min	10 µL/min	1x 50 µL @ 10 min; 5 µL/min from 10 min	5 µL/min	2x 50 µL @ 1.5, 5.5 min
Total volume / hindlimb (µL)	2 • 10 ⁸	2 • 10 ⁸	1 • 10 ⁸	2 • 10 ⁸	1 • 10 ⁸	1 • 10 ⁸	2 • 10 ⁸	2 • 10 ⁸	Saline
total protocol time / hindlimb (min)	10 µL during pre-infusion followed by 100 µL during sonication								
	9.5	9.5	9.5	9.5	9.5	9.5	17.5	17.5	9.5

(4) In vivo bioluminescence imaging

The efficiency of pDNA-luc delivery was assessed *in vivo* by bioluminescence imaging of luciferase activity using an IVIS Spectrum system (Perkin-Elmer, Waltham, MA). Mice were anesthetized with isoflurane, injected with 150 mg/kg D-luciferin (Synchem, Felsberg Germany) *i.p.*, and placed in the IVIS system, followed by eight consecutive scans (2 min acquisition time/scan). In a pilot experiment comprising four transfected areas, the time course of luciferase expression was measured at days 2, 3, 4, 5, 8, and found to be highest between days 5-8. Hence, for all experiments described in this study, the animals were scanned seven days after sonication. Images were processed using the vendor's software (Living Image 4.2) and are depicted in radiance units (photons/second/cm²/steradian or p/s/cm²/sr). Analysis was performed by drawing an ellipsoidal region of interest (ROI) over the sonicated areas (hindlimbs) and the highest total flux value (photons/second or p/s) detected from all eight scans was used in all calculations.

(5) Histology

The animals were euthanized and the formaldehyde fixed skeletal muscle samples were embedded in paraffin, sliced into 5 µm-thick sections (Microtome Shandon Finesse ME+, Thermo Scientific) and stained with heamatoxylin-eosin (H&E).

Statistical analysis

Commercial software (SPSS, IBM, Armonk, NY) was used for statistical analysis (normality, Kruskal-Wallis, Dunn's tests, Mann-Whitney U test).

Results

In vivo bioluminescence imaging

The signal intensity in bioluminescence is proportional to the amount of functional luciferase and is therefore considered as an imaging-biomarker for successful gene transfection with pDNA-luc [36]. A total of 73 sonicated hindlimbs were imaged across all groups with representative examples of *in vivo* bioluminescence measurements (total flux, photons per second: p/s) and are shown in Figure 4.3. Increases in bioluminescence signal above background were detected only in US exposed areas.

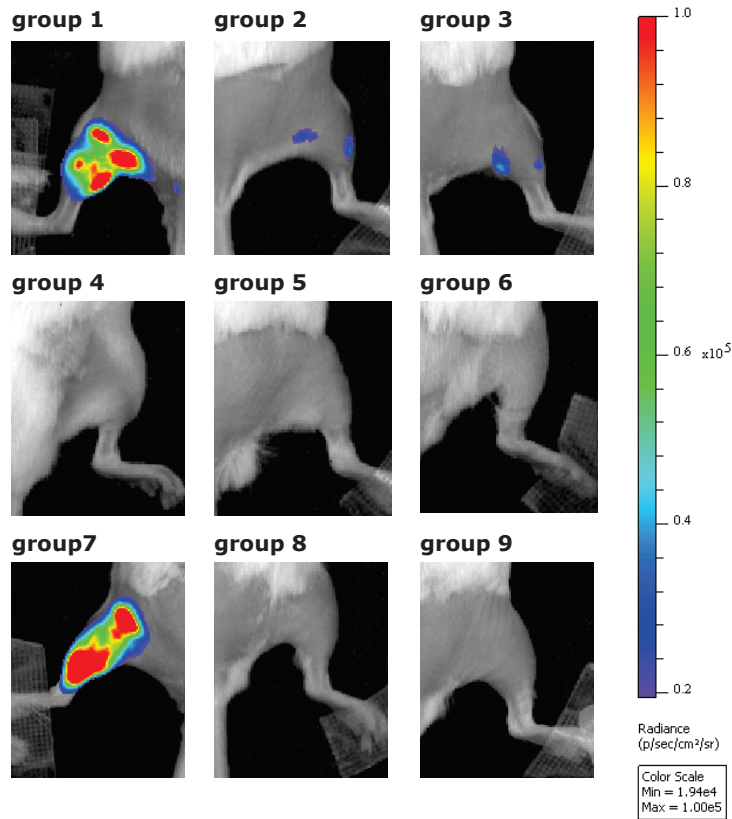


Figure 4.3 *In vivo* bioluminescence. Representative bioluminescence images ($p/s/cm^2/sr$) overlaid on B&W photographs of the respective animal. The highest intensity image per group is shown. All images are at the same intensity scale. The minimum scale value corresponds to intensities observed in controls.

Data analysis

Different experimental parameters were changed in order to evaluate their effect on UMGD. All results show a strong intra-group variability where data obtained in groups 5, 6 and 8-9 pass the normality test, while data of the remaining groups (1, 2, 3, 4, and 7) do not. Thus, all data were analyzed using robust non-parametric methods to detect inter-group median significant differences (Kruskal-Wallis, Dunn's tests). Statistical significance was considered at $p < 0.05$. Direct inter-group comparisons are ideal between groups in which only one parameter is different. These comparisons are indicated in Table 4.2. For example, the top left cell shows that the effect of changing from a 2x bolus injections (group 1) against 4x bolus injections (group 2) can be directly compared.

Table 4.2 Inter-group comparisons. Possible comparisons between groups that differ in only

Ultrasound-mediated gene delivery of naked plasmid DNA
in skeletal muscles: a case for bolus injections

one experimental parameter. The data should be read as row by column, i.e., the top line in each cell is the parameter from the row group (e.g. top left cell: group 1 with 2x bolus can be directly compared to group 2 with 4x bolus).

Groups	2	3	4	5	6	8	9
1	2x bolus vs 4 x bolus	2x [MBs] vs 1x [MBs]	2x bolus vs infusion 4x bolus vs infusion	-	-		MBs vs No MBs
2	-	-		-	-	-	-
3	-	-	-	2x bolus vs infusion	-	-	MBs vs No MBs
4	-	-	-	2x [MBs] vs 1x [MBs]	-	-	-
5	-	-	-	-	5k cycles vs 50k cycles	-	-
7	-	-	-	-	-	1x bolus vs infusion	-

The respective total flux values obtained in each experiment are plotted in Figure 4.4. The absolute values for the medians are depicted in Table 4.3 (see also Table S4.1 in supplementary information). The ratios to control group per transfection can be seen in Table S4.2 (supplementary information). Below, the results are presented according to the type of injection given: infusion, bolus, and bolus vs. infusion. The data are compared according to their medians.

First, the baseline bioluminescence total flux levels were determined from animals that received pDNA-luc but no MBs (group 9; $1.59 \pm 0.105 \cdot 10^4$ p/s). All other parameters were the same as in group 1 (see Table 4.1).

Infusion: injecting $1 \cdot 10^8$ MBs + pDNA-luc (group 5) did not induce a significant bioluminescence signal increase compared to control ($p > 0.8$). Also, increasing the number of US cycles from 5000 to 50000 (group 6 vs. 5; $p > 0.8$) did not yield any measurable bioluminescence (group 6 vs. control: $p > 0.8$). When doubling the MB concentration from $1 \cdot 10^8$ (group 4) to $2 \cdot 10^8$ (group 5) no significant increase in the measured bioluminescence ($p = 0.065$). However, group 4 yielded higher bioluminescence than the control group 9 ($p = 0.005$). When the infusion speed was halved to $5 \mu\text{L}/\text{min}$ and $2 \cdot 10^8$ MBs used (group 8) the bioluminescence levels were not significantly different compared to the control group 9 ($p = 0.298$). Combining one bolus injection followed by infusion at $5 \mu\text{L}/\text{min}$ (group 7) also did not result in an increase in bioluminescence signal compared to control group 9 ($p = 0.078$).

Bolus vs. infusion: changing from constant infusion to two $50 \mu\text{L}$ bolus injections (group 5 vs. 3), both with $1 \cdot 10^8$ MBs, did not significantly increase the bioluminescence signal ($p > 0.9$). When the MBs concentration was increased to $2 \cdot 10^8$, the two bolus injections group did not significantly differ from the constant infusion counterpart ($p > 0.9$; group 1 vs. 4) nor from the two bolus

injections with $1 \cdot 10^8$ MBs (group 1 vs. 3; $p > 0.9$). However, group 1 showed a clear increase in bioluminescence compared to the constant infusion group using $1 \cdot 10^8$ MBs (group 1 vs. 5; $p = 0.009$) and control group 9 ($p = 0.001$). Separating the two boli into four bolus injections (25 μ L each; group 2 vs. 1) showed no significant effect ($p = 0.298$). The four boli were also not different from the constant infusion group 4 ($p = 0.662$) nor from the control group 9 ($p > 0.9$). For every experimental group there was no significant difference between bioluminescence values on right hindlimbs compared to the left ($p > 0.126$).

Interestingly, the highest increase (101x over highest control) was measured in one experiment belonging to group 7 (Table S4.2, supplementary information). Still, there is a clear prevalence of bioluminescence values above 10^5 p/s for group 1 compared to groups 2, 3, 4, and 7 (respectively, 58%, 14%, 13%, 25%) which is reflected by the medians (Fig. 4.4 and supplementary information Fig. S4.1). Overall, the results indicate that total flux values corresponding to at least 5 fold increases over the highest control, were obtained only when one of three conditions was met: (1) one or two bolus injections; (2) a higher concentration of MBs ($2 \cdot 10^8$ vs. $1 \cdot 10^8$); (3) both '(1)' and '(2)'.

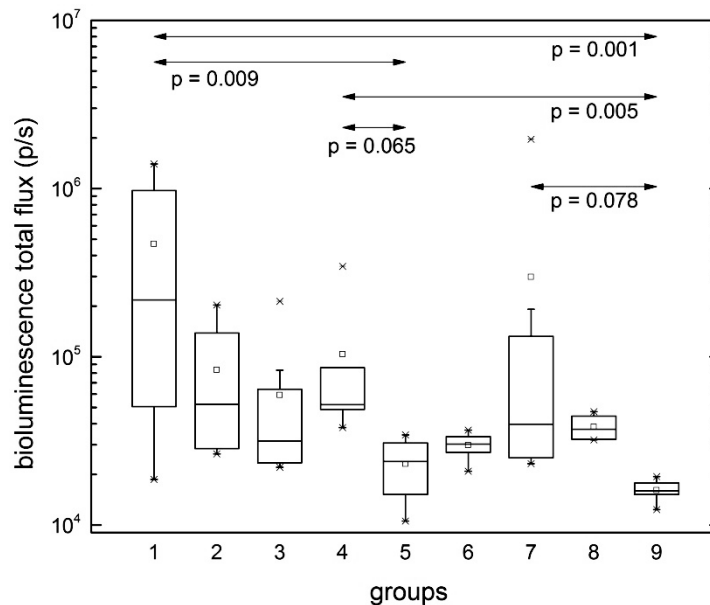


Figure 4.4 Bioluminescence quantification in vivo. Box plot representation of the total flux (p/s) for all experimental groups. '-' - 5th and 95th percentiles; 'x' - 1st and 99th percentiles; '□' - mean.

Table 4.3 Group medians and medians ratios to control.

Ultrasound-mediated gene delivery of naked plasmid DNA
in skeletal muscles: a case for bolus injections

group	median (p/s)	ratio (median / median group 9)
1	2.18•10 ⁵	13.7
2	2.64•10 ⁴	1.7
3	3.16•10 ⁴	2.0
4	5.18•10 ⁴	3.3
5	2.38•10 ⁴	1.5
6	2.93•10 ⁴	1.8
7	3.97•10 ⁴	2.5
8	3.70•10 ⁴	2.3
9	1.59•10 ⁴	1.0

Histology

After US sonications, animals were very active in their cages with all normal behaviors present. After recovery from anesthesia, no gait abnormalities, stress or pain related signs nor weight loss were observed. The skin in the US-exposed areas did not show any signs of irritation and/or damage, e.g. inflammation, edema, bleeding, blood vessel rupture to the naked eye.

Sonicated hindlimb muscle tissues from all groups were examined for US induced detrimental bioeffects. The H&E stained histology slides for all groups did not show any signs of fiber damage, erythrocyte leakage, enlarged muscle fibers gaps, or white blood cell infiltration (Fig. 4.5).

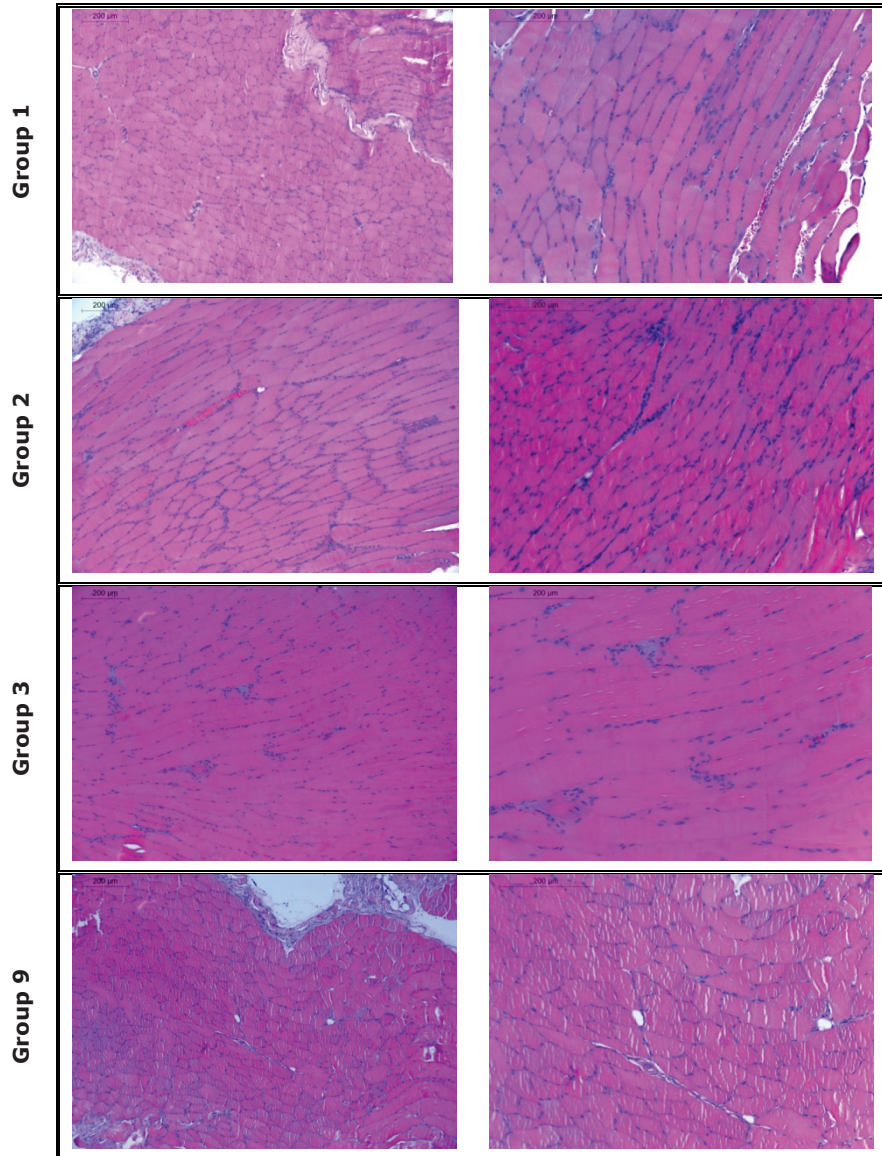


Figure 4.5 Histology of tissue specimens after US exposure. Representative formaldehyde fixed, H&E stained histology slides of skeletal muscles from seven days after sonications. Tissue is compact and erythrocytes are only seen inside blood vessels. Scale bar is 200 μm .

Discussion

The aim of this study was to explore the experimental parameters that are important to US mediated transfection of muscle tissue with pDNA. As a target organ we chose skeletal muscle, which presents an ideal target organ for gene

transfection, especially for proteins to be secreted. It is easily accessible, constitutes ca. 30% of the normal human adult body mass, has ample blood vascular supply, the nuclei within muscle fibers are post-mitotic, and each fiber can persist throughout the lifetime of an individual providing the foundations for continuous production of a transgene [37]. As a gene vector, we decided for naked pDNA carrying a gene encoding a luciferase reporter for bioluminescence imaging. The pDNA was used in its native form with no further chemical modifications and/or coupling to cationic structures. Unprotected pDNA in circulation is quickly degraded by nucleases (half-life < 1 min) and is further metabolized in the liver within 5 min [34]. While the use of cationic gene delivery vehicles may prevent degradation in circulation on the one side, they affect the pharmacokinetics on the other, and are also more prone to be passively taken up by different tissues, especially by the lungs [34]. Thus, a reliable and rapid method for delivery of naked pDNA may be advantageous. Our US protocol comprised the use of MBs, where we chose for SonoVue®. These MBs are clinically used as US contrast agents and commercially available facilitating clinical translation and reproducibility. Also, both pDNA and SonoVue® are negatively charged and will therefore not attract each other [33]. Both MBs and pDNA were injected systemically via the tail vein. This route of administration would allow the sonication of any vascularized tissue in the body accessible by the US beam within the circulation time of MBs and pDNA (ca. 1 min). The exact mechanisms behind this technique are still not completely understood. Thus, it is still an active topic of research discussed in depth in dedicated studies [2, 38, 39]. The parameters used seem to be safe, as no histological detrimental bioeffects were noted. However, unwanted effects such as microvascular leakage accompanied by capillary damage, and erythrocyte extravasation with resulting edema and inflammation have been reported when exposing biological tissues to US and MBs [40]. A thorough biochemical analysis on exposed tissues should be performed when considering clinical translation studies. For the number of MBs injected in one mouse, the maximum amount of gas (SF₆ from the SonoVue® MBs) was calculated to be approx. 16 µL. Since only a small volume of the total vasculature was exposed to US, a correspondingly small volume of gas was released from cavitated MBs which are not expected to be sufficient to cause damages such as air thrombus.

Localized noninvasive gene transfection was achieved as only US exposed tissue showed increases in bioluminescence signal. The main parameters that were varied are the concentration of MBs (range: 1•10⁸ to 2•10⁸), way of administration (bolus vs. infusion), and to a lesser extent the used US protocol (number of cycles). Ultrasound frequency and peak acoustic pressure were kept constant at values that do not lead to tissue damage observable in histology. The results suggest that the presence and concentration of MBs is crucial for efficient UMGD, which is consistent with most studies in UMGD [2, 38]. This is

supported by the finding that higher gene expression is observed for bolus injections of MBs compared to infusions as the former gives during the time span of US exposure a higher MB concentration in the vasculature than the latter though the overall number of MBs is the same. However, the groups where animals received bolus injections showed considerably higher inter-animal variability than groups with constant infusion. These findings are in agreement with the work of O'Reilly et al. [41] in the brain where long infusions produced more consistent results than manual bolus but at a decreased mean outcome (differences found before and after sonication in the brain measured by contrast enhanced T_1 -weighted MRI). It cannot be ruled out that the manual bolus and thus the effective number of MBs in the US sonicated volume was a source of this unintended variability, though we tried to minimize MBs flotation and aggregation by periodically turning the syringe with MBs and catheter tubing to the tail vein. Other parameters, such as the presence of air bubbles in the US-gel, US reflections/scattering from the bone structures in the hind limbs, pDNA and MBs inter-batch differences, might have contributed to an increased intra-group variability observed. In fact, this type of variability has been registered in other studies involving gene transfection in vivo [11, 42-44].

Unfortunately, it is impossible to inject via constant infusion an amount of MBs + pDNA that achieves concentrations comparable to a bolus injection as the total amount of injected material would present an extremely high dose. For reference, the maximum clinical human dose of SonoVue® is ca. $1.2 \cdot 10^7$ MBs/kg [45] while in our experiments in mice already $3 \cdot 10^9$ - $8 \cdot 10^9$ MBs/kg were injected.

In other studies, different routes of administration for both MBs and pDNA have been used, including: intramuscular injection [8, 9, 14, 30, 46-48], intratumoral injection [27, 48], injection directly in vessels in internal organs (e.g. portal vein) [17, 49], hydrodynamic injection [50], and clamping of organ's vessels for direct injection [22]. In comparison to intravenous injections, these routes allow one to obtain high local concentrations of MBs and pDNA and thus show high but usually local gene transfection. A strong limitation of these procedures is their invasiveness, restrictions with respect to reachable locations, and impracticality of multiple injections. Another important aspect between intramuscular and intravenous injection protocols is the ratio between transfected myocytes and endothelial cells. In the current study, the overall expression rate was investigated, and immunohistochemistry was not performed to investigate the spatial distribution of transfection. The latter has been investigated by others that showed that after intramuscular injections the primary transfected cells are myocytes followed by endothelial cells and the opposite for intravenous injections [8, 10].

A considerable amount of literature has been published on UMGD. Table 4.4 lists selected publications from which it was possible to extract the ratios on their

bioluminescence signal between sonicated groups with respect to controls. For a fair comparison, it is important to note that bioluminescence readings can be obtained in two ways, *in vitro* and/or *in vivo*. In the former, bioluminescence is measured after dissection on homogenized tissue, which yields luciferase in solution. This approach has higher sensitivity compared to *in vivo* imaging, and should be taken into account when comparing outcomes of different experiments. In our experiments we have used naked pDNA intravenously injected together with MBs and achieved a maximum ratio (highest sonicated/highest control) of 101x, determined by *in vivo* bioluminescence imaging. The works of Vu et al. [12] and Chen et al. [20] have the highest ratios, 1250x, however measured *in vitro*. Both report therapeutic potential with those settings by improving whole body glucose homeostasis in mice and increasing serum insulin levels in rats, respectively. Chen et al. used MBs bound to pDNA complexed with lipofectamine but did not publish data on control pancreas where no US was applied. In the study of Vu et al. the skeletal muscle of mice was exposed to a five times higher amount of both pDNA and MBs compared to our experiments. The impact of the amount of MBs used on the outcome varies considerably between studies. For example, Song et al. [17] report no improvement above $1 \cdot 10^8$ MBs (Definity®), Panje et al. [11] optimized it to $1 \cdot 10^7$ MBs (cationic MBs) and $1 \cdot 10^8$ MBs (neutral MBs) while it was only $1.25 \cdot 10^6$ MBs (SonoVue®) for Lin et al [51] (for particle delivery, not pDNA). When examining bioluminescence ratios measured *in vivo* (Table 4.4) the work of Panje et al. obtained the highest ratios in skeletal muscle at 840x for cationic MBs that bind pDNA and 580x for neutral MBs. Unfortunately, they do not have results on the therapeutic potential at those experimental conditions. As noted above, the *in vitro* and *in vivo* measurements of the same samples leads to considerably different results as demonstrated in the work of Delalande et al. [24], where a ratio of 10x was obtained *in vivo* compared to a ratio of 130x obtained on the homogenates of the same samples.

The main insight from the present study is that transfection rates are strongly improved with increased number of MBs present in the vasculature during US sonication. As the overall number of bubbles that can be safely injected is limited, the best approach is the injection of a highly concentrated MB suspension as a bolus. Overall transfection could be further improved combining a bolus injection of MB with other experimental conditions that have been shown to improve transfection before. For example, Burke et al. [15] have reported a 20-fold increase in luciferase expression when they filtered their MBs population to favor a smaller size closer to 1 μm in diameter and a 60-fold increase when they complexed the pDNA with PEI. Also, Panje et al. [11] improved their results with naked pDNA by 27-fold after binding pDNA to the MBs, effectively protecting it from circulating nucleases.

Finally, an interesting aspect deals with the circulation half-life of the SonoVue®

Chapter 4

MBs (6 min in humans) and distribution half-life in blood (1 min in humans) [32]. After the intravenous bolus injection, the solution circulates through the sonicated area as a "bolus" only during the first passages. Since the interval between exposures was 30 s only the first exposure (perhaps the second) would interact with a MBs + pDNA bolus. The remaining exposures would see considerably fewer or even no MBs + pDNA. Future studies where the pDNA is labeled with either fluorescent or radioactive agents would provide more insights into the experimental variability observed and exact location of extravasated pDNA.

Table 4.4. Selected publications on UMGD with published bioluminescence values.

ref.	injection		MBs type	target tissue	US	luciferase measurement	ratio (highest positive/highest control)
	pDNA	MBs					
[29]	iv (100 µg)	iv (1•10 ⁹)	lipid ¹ (complexed to pDNA)	tumor (mouse)	Sonos 7500; 1.3 MHz; MI 1.6; 30 min	in vitro (RLU/ mg/min)	2
[15]	iv / im (40 µg)	iv (1•10 ⁶)	albumin ¹	skeletal muscle (mouse)	unfocused; 1 MHz; 0.6 MPa; 5x300 cycles every 10 s; 12 min	in vivo (p/s)	180 (PEI-pDNA / noUS) 3 (naked pDNA / noUS)
[24]	itd (10 µg)	itd (5•10 ⁵)	BR14®	tendon (mouse)	unfocused; 1 MHz; 0.2 MPa; 40% DC; PRF 10 kHz; 10 min	in vitro (RLU/ mg) in vivo (p/s)	130 (in vitro) 10 (in vivo)
[11]	iv (50 µg)	iv (1•10 ⁸)	cationic ¹ and neutral lipid	skeletal muscle (mouse)	unfocused; 1 MHz; 2 W/cm ² ; 50 % DC; 5 min	in vivo (p/s/ cm ² /sr)	840 (cationic / noUS) 580 (neutral / noUS)
[12]	iv (1 mg)	iv (1•10 ⁹)	Definity® (incubated with pDNA)	skeletal muscle (mouse)	Vevo® sonigene; 1 MHz; 50% DC	in vitro (RLU/ µg)	1250 (sonicated / noUS)
[52]	ia (10 µg)	ia (-)	bubble liposomes ¹	tumor (mouse)	Sonopore 4000; 0.7 MHz; 50% DC; 1.2 W/cm ² ; 2 min	in vitro (RLU/ mg)	500 (sonicated / noMBs)
[17]	iv ³ (150 µg)	iv ³ (1•10 ⁹)	Definity®	liver (mouse)	unfocused; 1.1 MHz; 20 cycles; PRF 13.9 Hz, 2.7 MPa; 1.5 min	in vitro (RLU/ mg)	20 (sonicated / noMBs) 200 (sonicated / pDNA alone)
[22]	iv ⁴ (50 µg)	iv ⁴ (1•10 ⁸)	Optison®	kidney (rat)	Sonitron 2000; 1 W/cm ² ; 3 min	in vivo (p/s)	6 (US alone/noUS) 9 (sonicated / noUS)/
[48]	im (20 µg)	im (8•10 ⁶)	Sonidel® MB101	skeletal muscle (mouse)	Sonidel SP 100; 1 MHz, 1.9 W/cm ² ; 0.167 MPa; 3 min	in vivo (p/s)	8 (sonicated / noMBs)
[14]	im (20 µg)	im (-)	lipid ¹	skeletal muscle (mouse)	1 MHz; 3 W/cm ² ; 20% DC; 200 cycles; PRF 1000 Hz; 60 s	in vivo (p/s)	52 (sonicated / noUS)
[21]	iv ⁵ (50 µg)	iv ⁵ (1•10 ⁸)	Optison®	kidney (rat)	Rich-Mar; 1 MHz; 5% power output; PRF 30s; 60 s	in vitro (RLU/ mg)	40 (sonicated / noMBs)

Chapter 4

[20]	iv ² (250 µg)	iv ² (5.2•10 ⁹)	inf	pancreas (rat)	Sonos 5500; 1.3 MHz; MI 1.3; ECG trigger: 4 exposures/4 cardiac cycles; 20 min	1250 (sonicated / muscle)
------	-----------------------------	---	-----	-------------------	---	------------------------------

Legend: ¹-¹- information not given; ¹ - not commercially available; ² - intra-jugular; ³ - surgically exposed liver and injection directly in portal vein branch; ⁴ - surgical exposure and renal vein clamped for injection; ⁵ - left renal artery and vein with temporary clipping; bol - bolus; inf - infusion; ia - intra-arterial; im - intramuscular; itd - intra-tendon; iv - intravenous; MI - mechanical index; p/s - photons/second; noMBs - MBs removal only parameter changed; noUS - US removal only parameter changed

Conclusion

In this study pDNA was delivered into the skeletal muscles of mice using UMGD. The data support that the number of MBs present in the vasculature during the US sonication time is the most decisive parameter to achieve high transfection levels. Taking the outcome of other studies into account, the plasma level of the pDNA needs to be sufficiently high for successful transfection using a non-invasive approach with intravenous injection of MBs and pDNA. As the experimental parameter space in UMGD (from US settings to types of MBs) allows considerable variations, the challenge for a potential clinical translation is in making these procedures reliable, robust and repeatable.

Acknowledgements

The authors are grateful to Balasundar Raju and Eugene Leyvi for their contributions on the definition of experimental protocols and comments on the manuscript. This project was funded in part by the EU FP7 project Sonodrugs (NMP4-LA-2008-213706).

References

- [1] S.L. Ginn, I.E. Alexander, M.L. Edelstein, M.R. Abedi, J. Wixon, Gene therapy clinical trials worldwide to 2012 - an update, *J Gene Med*, 15 (2013) 65-77.
- [2] C.M. Panje, D.S. Wang, J.K. Willmann, Ultrasound and Microbubble-Mediated Gene Delivery in Cancer: Progress and Perspectives, *Invest Radiol*, (2013).
- [3] P.G. Sanches, H. Grull, O.C. Steinbach, See, reach, treat: ultrasound-triggered image-guided drug delivery, *Ther Deliv*, 2 (2011) 919-934.
- [4] F.Y. Yang, P.Y. Lee, Efficiency of drug delivery enhanced by acoustic pressure during blood-brain barrier disruption induced by focused ultrasound, *Int J Nanomedicine*, 7 (2012) 2573-2582.
- [5] M.A. O'Reilly, K. Hynynen, Ultrasound enhanced drug delivery to the brain and central nervous system, *Int J Hyperthermia*, 28 (2012) 386-396.
- [6] L.H. Treat, N. McDannold, N. Vykhodtseva, Y. Zhang, K. Tam, K. Hynynen, Targeted delivery of doxorubicin to the rat brain at therapeutic levels using MRI-guided focused ultrasound, *Int J Cancer*, 121 (2007) 901-907.
- [7] P.G. Sanches, R. Rossin, M. Bohmer, K. Tiemann, H. Grull, Real-time imaging and kinetics measurements of focused ultrasound-induced extravasation in skeletal muscle using SPECT/CT, *J Control Release*, 168 (2013) 262-270.
- [8] J. Kobulnik, M.A. Kuliszewski, D.J. Stewart, J.R. Lindner, H. Leong-Poi, Comparison of gene delivery techniques for therapeutic angiogenesis ultrasound-mediated destruction of carrier microbubbles versus direct intramuscular injection, *J Am Coll Cardiol*, 54 (2009) 1735-1742.
- [9] T. Kodama, A. Aoi, Y. Watanabe, S. Horie, M. Kodama, L. Li, R. Chen, N. Teramoto, H. Morikawa, S. Mori, M. Fukumoto, Evaluation of transfection efficiency in skeletal muscle using nano/microbubbles and ultrasound, *Ultrasound Med Biol*, 36 (2010) 1196-1205.
- [10] H. Leong-Poi, M.A. Kuliszewski, M. Lekas, M. Sibbald, K. Teichert-Kuliszewska, A.L. Klibanov, D.J. Stewart, J.R. Lindner, Therapeutic arteriogenesis by ultrasound-mediated VEGF165 plasmid gene delivery to chronically ischemic skeletal muscle, *Circ Res*, 101 (2007) 295-303.
- [11] C.M. Panje, D.S. Wang, M.A. Pysz, R. Paulmurugan, Y. Ren, F. Tranquart, L. Tian, J.K. Willmann, Ultrasound-mediated gene delivery with cationic versus neutral microbubbles: effect of DNA and microbubble dose on in vivo transfection efficiency, *Theranostics*, 2 (2012) 1078-1091.
- [12] V. Vu, Y. Liu, S. Sen, A. Xu, G. Sweeney, Delivery of adiponectin gene to skeletal muscle using ultrasound targeted microbubbles improves insulin sensitivity and whole body glucose homeostasis, *Am J Physiol Endocrinol Metab*, 304 (2013) E168-175.
- [13] X. Wang, H.D. Liang, B. Dong, Q.L. Lu, M.J. Blomley, Gene transfer with microbubble ultrasound and plasmid DNA into skeletal muscle of mice: comparison between commercially available microbubble contrast agents, *Radiology*, 237 (2005) 224-229.
- [14] Y. Watanabe, S. Horie, Y. Funaki, Y. Kikuchi, H. Yamazaki, K. Ishii, S. Mori, G. Vassaux, T. Kodama,

Delivery of Na/I symporter gene into skeletal muscle using nanobubbles and ultrasound: visualization of gene expression by PET, *J Nucl Med*, 51 (2010) 951-958.

- [15] C.W. Burke, J.S. Suk, A.J. Kim, Y.H. Hsiang, A.L. Klivanov, J. Hanes, R.J. Price, Markedly enhanced skeletal muscle transfection achieved by the ultrasound-targeted delivery of non-viral gene nanocarriers with microbubbles, *J Control Release*, 162 (2012) 414-421.
- [16] B.I. Raju, E. Leyvi, R. Seip, S. Sethuraman, X. Luo, A. Bird, S. Li, D. Koeberl, Enhanced gene expression of systemically administered plasmid DNA in the liver with therapeutic ultrasound and microbubbles, *IEEE Trans Ultrason Ferroelectr Freq Control*, 60 (2013) 88-96.
- [17] S. Song, M. Noble, S. Sun, L. Chen, A.A. Brayman, C.H. Miao, Efficient Microbubble- and Ultrasound-Mediated Plasmid DNA Delivery into a Specific Rat Liver Lobe via a Targeted Injection and Acoustic Exposure Using a Novel Ultrasound System, *Mol Pharm*, (2012).
- [18] R. Bekeredjian, S. Chen, P.A. Frenkel, P.A. Grayburn, R.V. Shohet, Ultrasound-targeted microbubble destruction can repeatedly direct highly specific plasmid expression to the heart, *Circulation*, 108 (2003) 1022-1026.
- [19] H. Fujii, Z. Sun, S.H. Li, J. Wu, S. Fazel, R.D. Weisel, H. Rakowski, J. Lindner, R.K. Li, Ultrasound-targeted gene delivery induces angiogenesis after a myocardial infarction in mice, *JACC Cardiovasc Imaging*, 2 (2009) 869-879.
- [20] S. Chen, J.H. Ding, R. Bekeredjian, B.Z. Yang, R.V. Shohet, S.A. Johnston, H.E. Hohmeier, C.B. Newgard, P.A. Grayburn, Efficient gene delivery to pancreatic islets with ultrasonic microbubble destruction technology, *Proc Natl Acad Sci U S A*, 103 (2006) 8469-8474.
- [21] H. Koike, N. Tomita, H. Azuma, Y. Taniyama, K. Yamasaki, Y. Kunugiza, K. Tachibana, T. Ogihara, R. Morishita, An efficient gene transfer method mediated by ultrasound and microbubbles into the kidney, *J Gene Med*, 7 (2005) 108-116.
- [22] Y. Xing, E.C. Pua, X. Lu, P. Zhong, Low-amplitude ultrasound enhances hydrodynamic-based gene delivery to rat kidney, *Biochem Biophys Res Commun*, 386 (2009) 217-222.
- [23] M. Shimamura, N. Sato, Y. Taniyama, S. Yamamoto, M. Endoh, H. Kurinami, M. Aoki, T. Ogihara, Y. Kaneda, R. Morishita, Development of efficient plasmid DNA transfer into adult rat central nervous system using microbubble-enhanced ultrasound, *Gene Ther*, 11 (2004) 1532-1539.
- [24] A. Delalande, A. Bouakaz, G. Renault, F. Tabareau, S. Kotopoulos, P. Midoux, B. Arbeille, R. Uzbekov, S. Chakravarti, M. Postema, C. Pichon, Ultrasound and microbubble-assisted gene delivery in Achilles tendons: long lasting gene expression and restoration of fibromodulin KO phenotype, *J Control Release*, 156 (2011) 223-230.
- [25] A. Delalande, M.F. Bureau, P. Midoux, A. Bouakaz, C. Pichon, Ultrasound-assisted microbubbles gene transfer in tendons for gene therapy, *Ultrasonics*, 50 (2010) 269-272.
- [26] Z.Y. Chen, K. Liang, M.X. Xie, X.F. Wang, Q. Lu, J. Zhang, Induced apoptosis with ultrasound-mediated microbubble destruction and shRNA targeting survivin in transplanted tumors, *Adv Ther*, 26 (2009) 99-106.
- [27] M. Duvshani-Eshet, O. Benny, A. Morgenstern, M. Machluf, Therapeutic ultrasound facilitates antiangiogenic gene delivery and inhibits prostate tumor growth, *Mol Cancer Ther*, 6 (2007) 2371-2382.
- [28] K.M. Dittmar, J. Xie, F. Hunter, C. Trimble, M. Bur, V. Frenkel, K.C. Li, Pulsed high-intensity focused ultrasound enhances systemic administration of naked DNA in squamous cell carcinoma model: initial experience, *Radiology*, 235 (2005) 541-546.
- [29] A.R. Carson, C.F. McTiernan, L. Lavery, A. Hodnick, M. Grata, X. Leng, J. Wang, X. Chen, R.A. Modzelewski, F.S. Villanueva, Gene therapy of carcinoma using ultrasound-targeted microbubble destruction, *Ultrasound Med Biol*, 37 (2011) 393-402.
- [30] D. Sheyn, N. Kimelman-Bleich, G. Pelled, Y. Zilberman, D. Gazit, Z. Gazit, Ultrasound-based nonviral gene delivery induces bone formation in vivo, *Gene Ther*, 15 (2008) 257-266.
- [31] D. Luo, W.M. Saltzman, Enhancement of transfection by physical concentration of DNA at the cell surface, *Nat Biotechnol*, 18 (2000) 893-895.
- [32] M. Schneider, SonoVue, a new ultrasound contrast agent, *Eur Radiol*, 9 Suppl 3 (1999) S347-348.
- [33] A.P. Miller, N.C. Nanda, Contrast echocardiography: new agents, *Ultrasound Med Biol*, 30 (2004) 425-434.
- [34] M. Nishikawa, Y. Takakura, M. Hashida, Theoretical considerations involving the pharmacokinetics of plasmid DNA, *Adv Drug Deliv Rev*, 57 (2005) 675-688.
- [35] R. Seip, C.T. Chin, C.S. Hall, B.I. Raju, A. Ghanem, K. Tiemann, Targeted ultrasound-mediated delivery of nanoparticles: on the development of a new HIFU-based therapy and imaging device, *IEEE transactions on bio-medical engineering*, 57 (2010) 61-70.
- [36] G.R. Rettig, M. McAnuff, D. Liu, J.S. Kim, K.G. Rice, Quantitative bioluminescence imaging of transgene expression in vivo, *Anal Biochem*, 355 (2006) 90-94.
- [37] Q.L. Lu, G. Bou-Gharios, T.A. Partridge, Non-viral gene delivery in skeletal muscle: a protein factory, *Gene Ther*, 10 (2003) 131-142.
- [38] A. Delalande, S. Kotopoulos, M. Postema, P. Midoux, C. Pichon, Sonoporation: Mechanistic insights and ongoing challenges for gene transfer, *Gene*, (2013).
- [39] J. Castle, M. Butts, A. Healey, K. Kent, M. Marino, S.B. Feinstein, Ultrasound-mediated targeted drug delivery: recent success and remaining challenges, *Am J Physiol Heart Circ Physiol*, 304 (2013) H350-357.
- [40] D.L. Miller, M.A. Averkiou, A.A. Brayman, E.C. Everbach, C.K. Holland, J.H. Wible, Jr., J. Wu, Bioeffects considerations for diagnostic ultrasound contrast agents, *Journal of ultrasound in medicine : official journal of the American Institute of Ultrasound in Medicine*, 27 (2008) 611-632; quiz 633-616.
- [41] M.A. O'Reilly, A.C. Waspe, M. Ganguly, K. Hynynen, Focused-ultrasound disruption of the blood-brain barrier using closely-timed short pulses: influence of sonication parameters and injection rate, *Ultrasound Med Biol*, 37 (2011) 587-594.
- [42] M. Manthorpe, F. Cornefert-Jensen, J. Hartikka, J. Felgner, A. Rundell, M. Margalith, V. Dwarki, Gene therapy by intramuscular injection of plasmid DNA: studies on firefly luciferase gene expression in mice, *Hum Gene Ther*, 4 (1993) 419-431.

Ultrasound-mediated gene delivery of naked plasmid DNA
in skeletal muscles: a case for bolus injections

- [43] P.A. Frenkel, S. Chen, T. Thai, R.V. Shohet, P.A. Grayburn, DNA-loaded albumin microbubbles enhance ultrasound-mediated transfection in vitro, *Ultrasound Med Biol*, 28 (2002) 817-822.
- [44] P.E. Huber, M.J. Mann, L.G. Melo, A. Ehsan, D. Kong, L. Zhang, M. Rezvani, P. Peschke, F. Jolesz, V.J. Dzau, K. Hynynen, Focused ultrasound (HIFU) induces localized enhancement of reporter gene expression in rabbit carotid artery, *Gene Ther*, 10 (2003) 1600-1607.
- [45] EMA, http://www.ema.europa.eu/docs/en_GB/document_library/EPAR_-_Product_Information/human/000303/WC500055380.pdf, in, 2006.
- [46] Y. Taniyama, K. Tachibana, K. Hiraoka, T. Namba, K. Yamasaki, N. Hashiya, M. Aoki, T. Ogihara, K. Yasufumi, R. Morishita, Local delivery of plasmid DNA into rat carotid artery using ultrasound, *Circulation*, 105 (2002) 1233-1239.
- [47] L. Kowalczyk, M. Boudinet, M. El Sanharawi, E. Touchard, M.C. Naud, A. Saied, J.C. Jeanny, F. Behar-Cohen, P. Laugier, In vivo gene transfer into the ocular ciliary muscle mediated by ultrasound and microbubbles, *Ultrasound Med Biol*, 37 (2011) 1814-1827.
- [48] Y.S. Li, E. Davidson, C.N. Reid, A.P. McHale, Optimising ultrasound-mediated gene transfer (sonoporation) in vitro and prolonged expression of a transgene in vivo: potential applications for gene therapy of cancer, *Cancer Lett*, 273 (2009) 62-69.
- [49] J.M. Erikson, G.L. Freeman, B. Chandrasekar, Ultrasound-targeted antisense oligonucleotide attenuates ischemia/reperfusion-induced myocardial tumor necrosis factor-alpha, *J Mol Cell Cardiol*, 35 (2003) 119-130.
- [50] C.I. Wooddell, J.O. Hegge, G. Zhang, M.G. Sebestyen, M. Noble, J.B. Griffin, L.V. Pfannes, H. Herweijer, J.E. Hagstrom, S. Braun, T. Huss, J.A. Wolff, Dose response in rodents and nonhuman primates after hydrodynamic limb vein delivery of naked plasmid DNA, *Hum Gene Ther*, 22 (2011) 889-903.
- [51] C.Y. Lin, Y.L. Huang, J.R. Li, F.H. Chang, W.L. Lin, Effects of focused ultrasound and microbubbles on the vascular permeability of nanoparticles delivered into mouse tumors, *Ultrasound Med Biol*, 36 (2010) 1460-1469.
- [52] R. Suzuki, T. Takizawa, Y. Negishi, N. Utoguchi, K. Sawamura, K. Tanaka, E. Namai, Y. Oda, Y. Matsumura, K. Maruyama, Tumor specific ultrasound enhanced gene transfer in vivo with novel liposomal bubbles, *J Control Release*, 125 (2008) 137-144.

Supplementary information

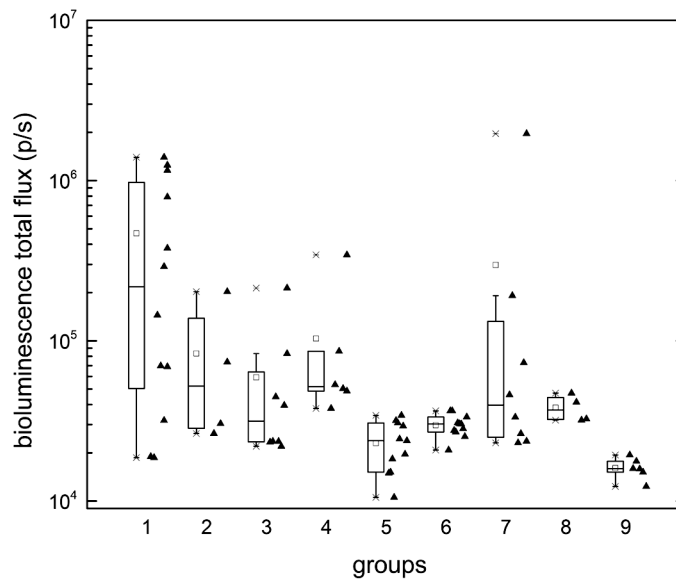


Figure S4.1 Bioluminescence quantification in vivo. Box plot representation of the total flux (p/s) for all experimental groups. '▲' - Individual data points per group are represent on the right side of each box; '–' - 5th and 95th percentile; 'x' - 1st and 99th percentile; '□' - mean.

Table S4.1 Calculated statistical values per group. Bootstrap median calculations (statistical

inference based on building a sampling distribution for a statistic by resampling from the data at hand) were computed to obtain the median standard errors and confidence intervals (using R, The R Foundation for Statistical Computing, Vienna, Austria).

group	median (p/s)	standard error	95% confidence interval	
			low	high
1	$2.18 \cdot 10^5$	$2.41 \cdot 10^5$	$4.40 \cdot 10^4$	$7.90 \cdot 10^5$
2	$2.64 \cdot 10^4$	$2.46 \cdot 10^4$	$1.06 \cdot 10^4$	$7.37 \cdot 10^4$
3	$3.16 \cdot 10^4$	$1.76 \cdot 10^4$	$2.33 \cdot 10^4$	$6.40 \cdot 10^4$
4	$5.18 \cdot 10^4$	$4.41 \cdot 10^4$	$4.32 \cdot 10^4$	$2.15 \cdot 10^5$
5	$2.38 \cdot 10^4$	$4.13 \cdot 10^3$	$1.50 \cdot 10^4$	$2.94 \cdot 10^4$
6	$2.93 \cdot 10^4$	$1.39 \cdot 10^3$	$2.61 \cdot 10^4$	$3.08 \cdot 10^4$
7	$3.97 \cdot 10^4$	$1.23 \cdot 10^5$	$2.37 \cdot 10^4$	$1.91 \cdot 10^5$
8	$3.70 \cdot 10^4$	$4.54 \cdot 10^3$	$3.20 \cdot 10^4$	$4.43 \cdot 10^4$
9	$1.59 \cdot 10^4$	$1.05 \cdot 10^3$	$1.37 \cdot 10^4$	$1.77 \cdot 10^4$

Table S4.2 Numbers indicate the factor of bioluminescence increase compared to the control experiment (highest value). Each cell represents one sonication (hindlimb) within each group. For clarity, the table is ordered in descending values of ratios per sonication for each group and does not represent the order of consecutive sonications performed.

sonications	groups								
	1	2	3	4	5	6	7	8	9
1	72	10	11	18	2	2	101	2	1
2	64	4	4	4	2	2	10	2	1
3	60	2	2	3	2	2	4	2	1
4	41	1	2	3	1	2	2	0	1
5	20	1	1	3	1	2	2		1
6	15	1	1	2	1	1	1		1
7	7	1	1		1	1	1		
8	4		1		1	1	1		
9	4				1	1			
10	2				1	1			
11	1				1				
12	1								

A note on the the osmolarity of the injected MBs+pDNA solution and the presence of EDTA

The solution of MBs+pDNA injected per exposure site had a volume of 100 μL . This volume is composed of a mixture of TE buffer (10 mM Tris.Cl and 1 mM EDTA) and 0.9% NaCl (150 mM NaCl). Maximum amounts per 100 μL were 2×10^8 (0.3×10^{-15} mol) for MBs and 200 μg (ca. 31×10^{-12} mol) for pDNA. A solution of 0.9% NaCl can be considered isotonic (approx. 300 osmol/L). Since the total injected volume was a combination of the 0.9% NaCl with a Tris solution clearly hypotonic and a negligent contribution from the MBS and pDNA to the final osmolarity we can conclude that the injected solution osmolarity was above 150 but below 300 osmol/L and thus was hypotonic. Since we are injecting approx. 2x 2.5 % of the total blood volume of a mouse in the two bolus injections we do not expect detrimental biological effects.

The maximum total EDTA concentration injected in one animal is more than 1000x lower than the LD50 values (56 mg/kg). Though EDTA will most likely chelate some calcium in blood, we do not expect any effect as the LD50 is directly related to this depletion of ions where we stay a factor 1000 below.

Manthorpe et al. (M. Manthorpe et al., Gene therapy by intramuscular injection of plasmid DNA: studies on firefly luciferase gene expression in mice, Hum Gene Ther, 4 (1993) 419-431) verified that the presence of EDTA during intramuscular injection of pDNA did have a detrimental effect on gene expression.



**Bone metastasis
imaging with
SPECT/CT/MRI: a
preclinical toolbox for
therapy studies**

Based on:

P.G. Sanches, S. Peters, R. Rossin, E.L. Kaijzel, I. Que, C. Löwik, H. Grüll, *Bone metastasis imaging with SPECT/CT/MRI: a preclinical toolbox for therapy studies*, Bone, submitted, under review

Abstract

Bone is one of the most common metastatic target sites in breast cancer, with more than 200 thousand new cases of invasive cancer diagnosed in the US alone in 2011. We set out to establish a multimodality imaging platform for bone metastases in small animals as a tool to non-invasively quantify metastasis growth, imaging the ensuing bone lesions and possibly the response to treatment. To this end, a mouse model of osteolytic metastatic bone tumors was characterized with SPECT/CT and MRI over time. A bone-metastasis forming cell line, MDA-MB-231, was genetically modified to stably express the reporter gene herpes simplex virus-1 thymidine kinase (*hsv-1 tk*). The intracellular accumulation of the radiolabeled tracer [¹²³I]FIAU promoted by HSV-1 TK specifically pinpoints the location of tumor cells which can be imaged *in vivo* by SPECT.

First, a study using tumors implanted subcutaneously was performed. The SPECT/MRI overlays and the *ex vivo* γ -counting showed a linear correlation in terms of %ID/cm³ ($R^2 = 0.93$) and %ID/g ($R^2 = 0.77$), respectively. Then, metastasis growth was imaged weekly by SPECT/CT and T₂-weighted MRI over a maximum of 40 days post-intracardiac injection of tumor cells. The animals developed multiple bone metastases in diverse sites, namely: femur, tibia, iliac crest, skull and shoulder blade. The first activity spots detectable with SPECT, around day 20 post-cell injection, were smaller than 2 mm³ and not yet visible by MRI and increased in volume and in %ID over the weeks. Osteolytic bone lesions were visible by CT (*in vivo*) and μ CT (*ex vivo*). The SPECT/MRI overlays also showed a linear correlation in terms of %ID/cm³ ($R^2 = 0.86$).

In conclusion, a new multimodality imaging platform has been established that non-invasively combines images of active tumor areas (SPECT), tumor volume (MRI) and the corresponding bone lesions (CT and μ CT). To our knowledge this is the first report where the combination of soft tissue information from MRI, of bone lesions by CT, and reporter gene imaging by SPECT is used to non-invasively follow metastatic bone lesions.

Keywords: bone metastasis; HSV-1 TK; FIAU; SPECT; CT; MRI

Introduction

Bone is one of the most common metastatic target sites in patients suffering from advanced solid tumors such as breast and prostate cancer, with an incidence of approx. 80% [1-3]. When a primary tumor progresses to form bone metastases the disease is nearly incurable, leading to severe morbidity and reduced quality of life. The understanding of processes leading to skeletal metastasis formation is of utmost importance to develop new treatment options [4]. To this end several preclinical animal models of osteotropic cancers have been developed [1, 5, 6]. Most commonly, *in vitro* cultured cancer cells are disseminated in circulation through a tail vein or intracardiac injection. As an alternative, tumor cells can also be injected directly in the bone. The intracardiac injection of selected bone-seeking breast cancer cells leads to the appearance of bone metastases spread throughout the entire skeleton [5, 7, 8]. In order to follow and quantify metastasis growth the use of non-invasive *in vivo* imaging is essential. In this context, reporter gene imaging approaches using genetically modified cancer cells are particularly useful as they allow to follow endogenous biological processes such as cell growth and metastatic spread *in vivo* [9].

Many reporter gene options exist, such as luciferase enzymes and fluorescent proteins (e.g. green fluorescent protein, GFP) which are detectable with optical systems. A linear correlation was found between the bioluminescence signal from intracranial [10, 11], lung [12], and liver tumors [13] and their respective volume measured by magnetic resonance imaging (MRI). However, despite recent technical improvements [14, 15], optical imaging has shortcomings especially when studying deep seated tumors or bone metastasis formation due to possible light absorption at the bone cortex and other tissues. Song et al. found that small metastases in the brain imaged by MRI were not seen with bioluminescence imaging, probably due to scattering of photons at the skull [16]. Also, van der Pluijm et al. [8] found that bone metastasis-related osteolysis as quantified by X-ray images did not necessarily correlate with the tumor burden defined by the optical signal from the luciferase-expressing metastases. A nuclear imaging approach may be more suited to locate bone lesions and quantify tumor growth because gamma-rays do not scatter significantly *in vivo*. Also, nuclear imaging has direct clinical translation in part due to the low amounts of tracer needed to achieve contrast.

Several reporter gene approaches for nuclear imaging have been investigated, in particular based on the reporter gene expressing the herpes simplex virus 1 thymidine kinase (HSV-1 TK) enzyme [9, 17]. Upon enzyme expression, *hsv-1 tk* transfected cells trap specific kinase substrates intracellularly, typically thymidine analogs such as 2'-fluoro-2'-deoxy-1- β -D-arabinofuranosyl-5-iodouracil (FIAU) [18]. The cellular uptake of radioactive FIAU (Fig. 5.1) can be imaged and quantified using sensitive nuclear techniques with high spatial

resolution such as single photon emission computed tomography (SPECT) [19] and positron emission tomography (PET) [20] depending on the radioactive isotope used. Also, it was demonstrated that the accumulation of FIAU in HSV-1 TK expressing tumors correlates with the level of *tk* mRNA and thus, indirectly, with cell viability [18]. Multimodal imaging approaches are arising which combine optical imaging, SPECT or PET with MRI and computed tomography (CT) to provide anatomical reference in soft tissue and bone, respectively [7, 9, 21-26]. However, a comprehensive study correlating nuclear imaging of a reporter gene to tumor volume determined with MRI specifically in the context of bone metastasis formation is lacking.

In this study, a mouse model of osteolytic bone metastasis obtained with cells expressing HSV-1 TK (MDA-MB-231-LITG or LITG) was characterized with SPECT, CT, and MRI over time. First, the uptake of the nuclear reporter [^{125}I]FIAU in cells was studied *in vitro*. Next, a subcutaneous tumor model was set up to evaluate the kinetics of [^{123}I]FIAU accumulation *in vivo* with SPECT/CT imaging. Finally, a metastasis model obtained with intracardiac injection of LITG cells was used to sequentially monitor the metastasis formation and growth in bones using a multimodal SPECT/MRI/CT imaging approach. In both the subcutaneous and metastatic tumor models a correlation between the %ID from SPECT and the tumor volume from MRI was found. Finally, we assessed the feasibility of using this multimodality platform to simultaneously image the reporter gene expression, and the uptake of a radiolabeled drug (i.e. a radiolabeled pendant of the clinically used liposomal doxorubicin, Doxil[®] [27]) with dual isotope SPECT imaging.

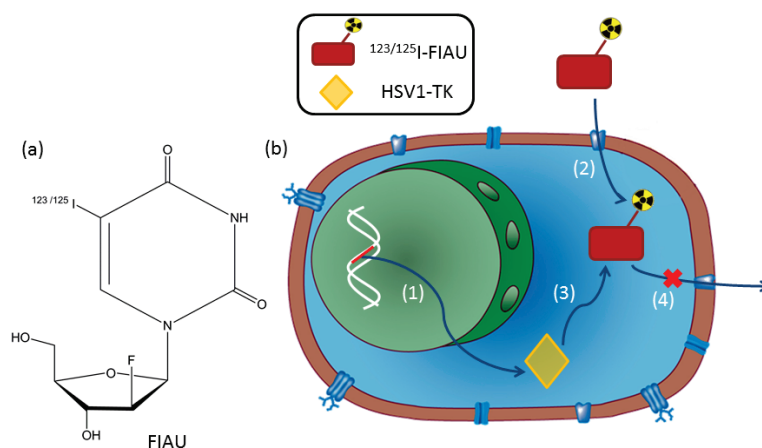


Figure 5.1 Reporter gene imaging mechanism. (a) chemical structure of [$^{123/125}\text{I}$]FIAU (2'-fluoro-2'-deoxy-1- β -D-arabinofuranosyl-5-iodouracil); (b) schematic of a genetically modified MDA-MB-231-LITG cell which (1) constitutively expresses the reporter enzyme HSV-1 TK; (2) upon entering the cell, the tracer [$^{123/125}\text{I}$]FIAU is phosphorylated by the (3) HSV-1-TK enzyme thereby becoming unable to leave the cell (4).

Materials and Methods

Materials

1,2-Dipalmitoyl-*sn*-glycero-3-phosphoethanolamine-N-[methoxy(polyethyleneglycol)-2000] (DPPE-PEG2000), hydrogenated-L- α -phosphatidylcholine (HSPC) and cholesterol were purchased from Avanti Polar Lipids (Alabaster, AL). 1,4,7,10-Tetraazacyclododecane-1,4,7,10-tetraacetic acid -1,2-distearoyl-*sn*-glycero-3-phosphoethanolamine-N-[amino(polyethylene glycol)-2000] (DOTA-DSPE) was synthesized according to Hak et al. [28]. Sodium [^{123}I]iodide and [^{177}Lu]lutetium chloride solutions were obtained from GE Healthcare (Fairfield, CT) and Perkin-Elmer (Waltham, MA), respectively. All other reagents and solvents were obtained from Sigma-Aldrich (St. Louis, MO) and used without further purification, unless otherwise stated. Water was distilled and deionized (18 M Ω cm) with a MilliQ system (Millipore, Billerica, MA) before use.

Tumor cells

The wild type human breast adenocarcinoma cell line MDA-MB-231 (WT) was transduced with lentivirus carrying a triscistronic vector containing a cytomegalovirus promoter (CMV), firefly luciferase (*luc*), internal ribosome entry site (IRES), and *hsv-1 tk* fused to *egfp* (LITG) [29]. The LITG cells were grown in monolayer in Dulbecco's Modified Enhanced Medium supplemented with 4.5 g/L glucose (Life Technologies, Waltham, MA), 10% fetal bovine serum, 2 mM glutaMAX™ (Life Technologies), 100 IU penicillin and 100 $\mu\text{g}/\text{mL}$ streptomycin (Life Technologies). The cells were incubated at 37 °C with 5% CO₂. The expression of HSV-1 TK was assessed by measuring the fluorescence signal of the fused GFP by flow cytometry analysis (FACS Canto II, BD Bioscience, San Jose, CA; supp. information, Fig S5.1). The activity of HSV-1 TK was confirmed by assessing the sensitivity of the cells to ganciclovir (Calbiochem, Billerica, MA), an agent that becomes cytotoxic after interaction with HSV-1 TK, by determining its effect on cell proliferation (supplementary information Fig. S5.2).

[^{125}I]FIAU labeling for *in vitro* studies

[^{125}I]Iodide in 0.05 M NaOH (approx. 10 MBq) was added to 25 μg of the FIAU precursor 5-trimethylstannyl-1-(2-deoxy-2-fluoro-b-D-arabinofuranosyl)uracil (FTAU, ABX, Radeberg, Germany) in 45 μL acetonitrile (MeCN) followed by 5 μL of 1:3 H₂O₂ / acetic acid (v/v). The solution was incubated for two minutes at RT, then the reaction was quenched with 5 μL of saturated Na₂S₂O₅ in water, and diluted in 2.5 mL of water. The crude labeling mixture was purified with a Sep-Pak® C18 Light cartridge (Waters, Milford, MA) according to the manufacturer's instructions and recovered in 1 mL EtOH. A sample of the purified solution was diluted with 0.9% NaCl to 5% EtOH and the radiochemical purity was assessed

by high pressure liquid chromatography (HPLC, supplementary information Fig. S5.3). The remaining ethanolic solution was dried at 70 °C under a gentle stream of N₂ and the residue was dissolved in 0.9% NaCl at the desired activity concentration for *in vitro* studies.

[¹²³I]FIAU labeling for in vivo studies

FIAU was labeled with ¹²³I (65 MBq, approx. 5 µL) as described above. The crude labeling mixture was loaded on a Sep-Pak® C18 Light cartridge. The reaction vial was rinsed with 2.5 mL water, this solution was also passed through the Sep-Pak® cartridge and it was then dried with 5 mL of air. [¹²³I] FIAU was eluted from the cartridge with 1 mL EtOH into a vial containing gentisic acid (20 mM final concentration). The EtOH was removed and the residue was dissolved in 0.9% NaCl at the desired activity concentration for *in vivo* studies. Radiochemical purity of the obtained [¹²³I]FIAU was assessed by HPLC (supp. information Fig. S5.4).

¹⁷⁷Lu-labeled liposomal formulation of doxorubicin

A ¹⁷⁷Lu-radiolabeled liposomal formulation of doxorubicin (similar to the clinically used Doxil® formulation [27]), was prepared based on previously published methods [30, 31], with minor modifications (supplementary information, Fig. S5.4).

FIAU stability in mouse serum

The stability of [¹²⁵I]FIAU was assessed in 50% mouse serum (Innovative Research, Novi, MI) at 37 °C. Samples (100 µL) were taken at 0, 30, 60, 90, 120, 180, 240 min and 24 h and two-fold diluted with ice cold MeCN to precipitate serum proteins. The mixture was centrifuged for 5 min at 13,400 rcf. The supernatant was separated from the pellet, and the radioactivity in both supernatant and pellet was measured in a γ-counter (γ-energy window: 10-80 keV, Wizard 1480, Perkin-Elmer). The solution was then filtered through 0.22 µm, five-fold diluted with 0.9% NaCl and analyzed by HPLC (supplementary information Fig. S5.5).

FIAU uptake in vitro

An *in vitro* uptake experiment was performed to investigate the accumulation of [¹²⁵I]FIAU in LITG with respect to WT cells. Cells were plated in 6-well plates at a 3, 6, and 9×10⁵ cells/well density, in triplicate, 24 h prior to the experiment. Each well was washed twice with phosphate buffered saline (PBS), then 1 mL of medium containing 0.2 MBq of [¹²⁵I]FIAU was added in triplicate. After 20 or 60 min incubation at 37 °C, the wells were washed twice with 1 mL PBS. Subsequently, the cells were lysed by addition of 400 µL lysing buffer (2% (v/v) Igepal® CA-630 in 1% (v/v) sodium dodecyl sulfate in PBS) followed by 30 min

incubation at RT. The lysate was transferred to 2 mL vials and the radioactivity was measured in a γ -counter. Due to the different numbers of cells per well, the counts were normalized to the wet weight of the transferred lysate.

Animal studies

All animal procedures were approved by the ethical review committee of the Maastricht University Hospital (The Netherlands) and were performed according to the principles of laboratory animal care [32] and the Dutch national law "Wet op Dierproeven" (Stb 1985, 336). Nude female mice (Balb/c^{nu/nu}; Charles River Laboratories, France) were housed in an enriched environment in filter top cages under standard conditions (23-25 °C, 50-60 % humidity, and 12 h light-dark cycles) before the experiment, with sterilized standard food and water given *ad libitum*. To diminish thyroid iodide uptake, 0.1% NaI (w/v) was added to the animal's drinking water 48 h prior to tracer injection.

Tumor induction

Subcutaneous tumors: 3×10^6 LITG tumor cells in 100 μ L PBS were injected in the left flank of 6-8 weeks old mice. The control group received 3×10^6 WT tumor cells. Tumor sizes were measured with a caliper and ranged from 100 to 414 mm³ at the time of imaging.

Bone metastases: Tumor cells were suspended in sterile PBS at a concentration of 1.5×10^6 cells/mL and kept on iced water before use, to prevent cell clumping. Then, the cells were loaded and unloaded 3 times through a 24G needle in a 1 mL syringe. Finally, 150 μ L of the cell suspension were loaded into a 29G 1 mL syringe followed by intracardiac injection of 1.5×10^5 cells (100 μ L) in 4-5 week old mice under anesthesia.

Multimodal imaging of tumors

Noninvasive imaging was performed using a small-animal SPECT/CT system equipped with four detector heads and converging multi-pinhole collimators (nine pinholes per collimator, 1.4 mm aperture, nanoSPECT/CT®, Bioscan, Washington, DC) and a Philips Achieva 3.0 T human MRI scanner with a dedicated mouse solenoid coil. The SPECT scanner was calibrated with a cylindrical phantom filled with ¹²³I solutions of known activity.

Subcutaneous tumors: To determine the kinetics of [¹²³I]FIAU tumor uptake and the changes in tumor-to-muscle ratio over time, three mice (under anesthesia) were i.v. injected with approx. 40 MBq [¹²³I]FIAU in 100 μ L saline followed by dynamic SPECT scans (12 projections/scan, 30 s/projection, 7 min 30 s/scan, 140 min scan time, $0.3 \times 0.3 \times 0.3$ mm³ voxels, energy window: 143.1-174.9 keV) and by a CT scan (45 keV, 2 s/projection, and 240 projections/scan; Fig. 5.2a). In order to quantify tumor growth, i.e. tracer accumulation vs. tumor size, 14 mice (LITG tumors) and four control mice (WT tumors) were injected (awake)

with approx. 40 MBq [^{123}I]FIAU and scanned around the tumor region at 1 h p.i. by MRI (T_2 -weighted turbo spin echo with 7602 ms repetition time (TR), 30 ms echo time (TE), turbo spin echo factor (TSE) 8, field of view $40 \times 30 \text{ mm}^2$, $0.25 \times 0.25 \times 1 \text{ mm}^3$ voxels, 20 slices, 160 reconstruction matrix) followed by static SPECT (12 projections/scan, 400 s/projection, $0.3 \times 0.3 \times 0.3 \text{ mm}^3$ voxels) and CT (45 keV, 2 s/projection, 240 projections/scan) at 2 h p.i. The animals were euthanized at 3 h post-tracer injection (Fig. 5.2b).

Bone metastases: Six mice were injected with approx. 50 MBq [^{123}I]FIAU and full body images were acquired with SPECT (24 projections/scan, 150 s/projection, $0.3 \times 0.3 \times 0.3 \text{ mm}^3$ voxels), CT (55 kV, 2 s/projection, 360 projections), and MRI (T_2 -weighted 3D TSE, with DRIVE pulse, respiration triggered, with minimum TR 500 ms, 'shortest' TE, TSE factor 9, $0.3 \times 0.3 \times 0.3 \text{ mm}^3$ voxels, 320 reconstruction matrix) approx. 13-16 h post-tracer injection. For bone metastases imaging, the animals were kept supine on the same dedicated mouse bed with three position markers, i.e. 200 μL vials filled with 10 μL of an aqueous solution containing ^{123}I (for SPECT/MRI overlays). The animals were imaged at most three times each over a maximum period of 40 days (12 scans total) (Fig. 5.2c). After the last scan the animals were euthanized.

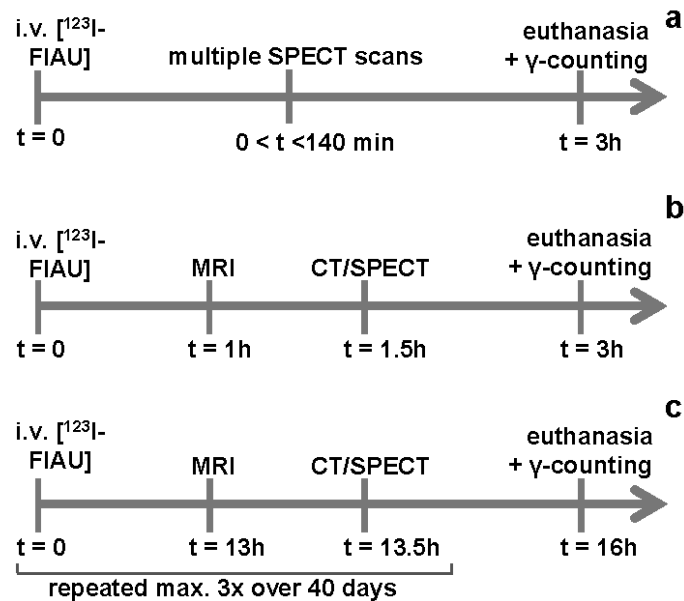


Figure 5.2 Experimental time lines. Mice bearing subcutaneous tumors were imaged by (a) dynamic SPECT + CT ($n = 3$) or by (b) static SPECT/CT + MRI ($n = 14$ LITG and $n = 4$ WT). (c) Mice with bone metastases were imaged by SPECT/CT + MRI ($n = 6$).

Dual isotope SPECT imaging using [^{123}I]FIAU and doxorubicin-encapsulated

¹⁷⁷Lu-liposomes

As a proof of concept, one mouse with induced bone metastases was injected with ¹⁷⁷Lu-labeled liposomes (26 MBq) at 5 mg/kg body weight of doxorubicin. Twenty four hours post-liposome injection the mouse was injected with [¹²³I]FIAU (45 MBq) and euthanized 16 h later. After euthanasia the mouse was immediately imaged by SPECT/CT (different parameter in SPECT scan: 360 s/projection; energy windows ¹⁷⁷Lu: 101.7-124.3 keV and 187.2-228.8 keV) and MRI.

Image analysis

Subcutaneous tumors. SPECT/CT data were analyzed using the software InVivoScope 1.41 (Bioscan) and the activity was quantified in terms of percentage of the injected dose (%ID) in tumor. MRI data were analyzed using the Imalytics 2.1 software (Philips Innovative Technologies, Aachen, Germany) and the tumor volumes were quantified in cm³.

Bone metastases. SPECT/CT data were analyzed as for subcutaneous tumors. SPECT/MR overlays were obtained and analyzed using Imalytics. For each metastasis, volumes of interest (ROIs) were manually drawn around the activity signal from SPECT (%ID) and around the tumor mass signal from MRI (cm³), independently.

Ex-vivo analysis

After euthanasia by cervical dislocation or isoflurane overdose, the mice were dissected, and organs and tissues of interest were harvested, weighed, and placed in 4% paraformaldehyde buffered to pH 7. Sample radioactivity was measured in a γ -counter along with standards to determine the injected dose per gram (%ID/g). The energy window of the counter was set to 138-180 keV for ¹²³I. The bone metastases were not measured by γ -counting as they could not be separated from the surrounding muscle and bone. These samples were imaged with μ CT (55 kVp, Scanco Medical, Brüttisellen, Switzerland) and used for histology.

Histology

Tissue areas containing bone and bone metastases were placed in 4% paraformaldehyde overnight. Bones were decalcified in 10% EDTA in PBS in 50 mL vials on a rolling bench top. The EDTA solution was replaced every 48 h until the bone structures were not visible anymore by CT (approx. 10 days). Then the samples were placed in an optimum cutting temperature matrix (Sakura Finetek, Alphen aan den Rijn, The Netherlands) and frozen in 2-methylbutane at -50 °C. Tissue sections (5-10 μ m) were obtained using a cryotome (FSE Cryostat Shandon, Thermo Scientific).

GFP staining: immunohistochemistry was carried out to detect GFP due to the

detrimental effects of sample processing preventing direct fluorescence microscopy. Frozen sections were stained with a rabbit monoclonal anti-GFP primary antibody (#G10362, Invitrogen, Life Technologies), diluted 1:80, followed by a fluorescently labeled secondary antibody (Alexa Fluor® 594 goat anti-rabbit IgG (H+L), #A11037, Invitrogen, Life Technologies) at 1:100 dilution. Cell nuclei were counterstained with DAPI diluted 1:100000.

Statistical analysis

Commercial software (SPSS, IBM, Armonk, NY) was used for statistical analysis (Levene's test for equality of variances, t-test). Statistical significance was considered at $p < 0.05$.

Results

[^{123/125}I]FIAU synthesis and in vitro stability

The radiochemical purity was always > 95% for both [^{123/125}I]FIAU before use, as confirmed by HPLC. During solid phase extraction purification, part of the labeled FIAU was lost in the loading/washing steps and the recovery was 80.3±10.2% (n = 14) and 57.0±12.4% (n = 26) for [¹²⁵I]FIAU and [¹²³I]FIAU, respectively. Gentisic acid was added to the purified [¹²³I]FIAU to avoid the formation of impurities caused by water radiolysis. [¹²⁵I]FIAU was stable in 50% mouse serum for up to 24h, as derived from HPLC analysis (Fig. S5.5).

FIAU accumulation in cells in vitro

The accumulation of [¹²⁵I]FIAU was up to 100-fold higher in LITG cells than in WT cells *in vitro* (Fig. 5.3b). Higher absolute uptake of [¹²⁵I]FIAU was observed when the incubation time and/or the cell number were increased. Following 20 min incubation, the LITG/WT ratio was similar for all three cell concentrations. However, after 60 min incubation the ratios decreased from 81:1 to 61:1 with increasing cell numbers, reasonably due to an increase in nonspecific [¹²⁵I]FIAU accumulation in WT cells.

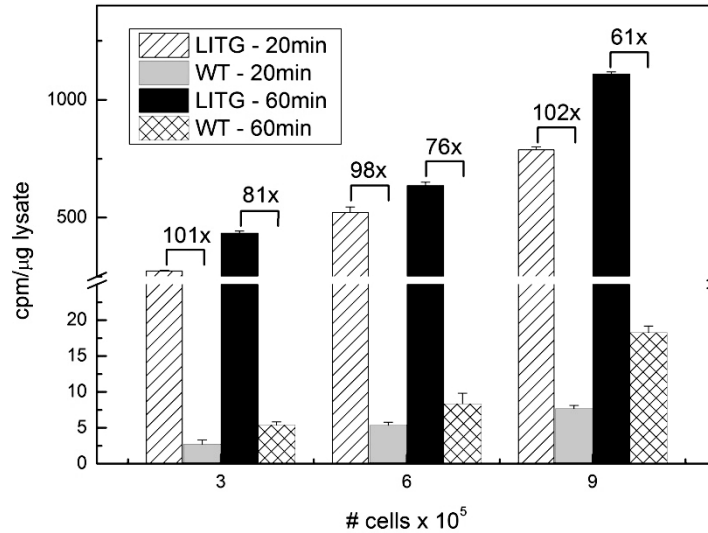


Figure 5.3 [¹²⁵I]FIAU accumulation in cells in vitro. Three different concentrations of LITG and WT cells were incubated with the same amount of [¹²⁵I]FIAU for 20 or 60 min. The bars are the mean of three experiments and the error bar is one standard deviation. The radioactivity uptake ratios for each LITG/WT pair are depicted above the bars. At each cell density, all four groups are significantly different ($p < 0.05$).

Uptake kinetics in vivo

The uptake of [¹²³I]FIAU in subcutaneous tumors and muscle (control) was quantified over a time period of 140 min p.i. from dynamic SPECT scans (Fig. 5.4a-e). The tumor uptake kinetics, in %ID, of the three animals scanned is shown in Figure 5.5. For all animals, an initial fast accumulation of activity was observed in tumors, followed by equilibrium after the first 120 min p.i. The mice had different tumor volumes (mouse 1-3: 535, 507, 226 mm³, respectively) and the larger the volume the higher the %ID value. An animated sequence of the kinetics from consecutive SPECT scans can be found in Figure S5.6 (supplementary information).

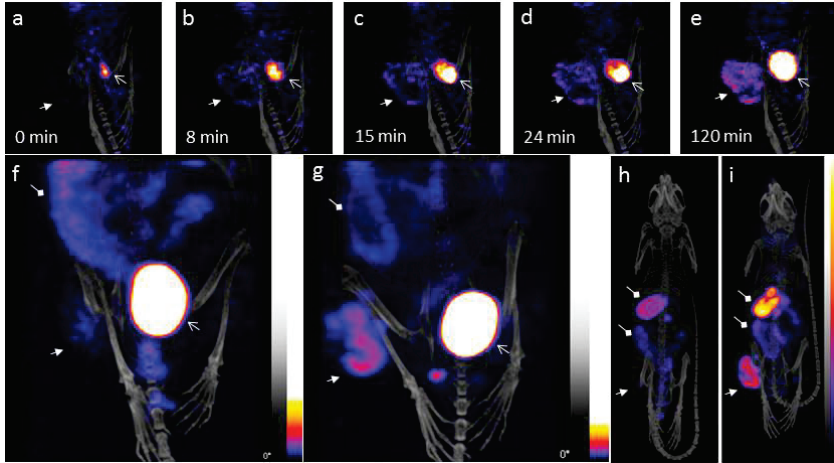


Figure 5.4 SPECT/CT imaging. (a-e) Uptake kinetics at 0, 8, 15, 24, and 120 min post [^{123}I]FIAU injection, respectively; Maximum intensity projections of mice bearing (h) WT and (i) LITG tumors imaged at 2 h p.i.; post mortem full body maximum intensity projections for the same (f) WT and (g) LITG mice. Both animals were injected with 40 MBq [^{123}I]FIAU. Open arrows: bladder; closed arrows: tumor; diamond arrows: stomach and intestines. Grouped images (a-e) and (f-g) and (h-i) are at the same max-min scale.

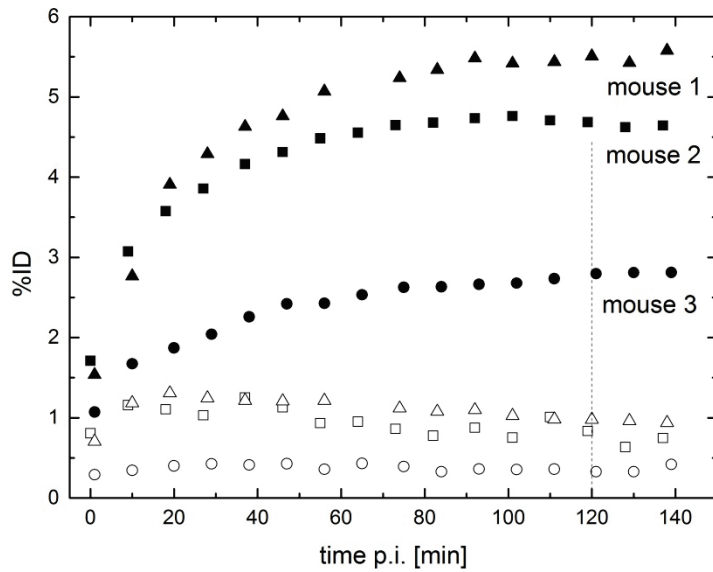


Figure 5.5 Tumor uptake kinetics. Activity from SPECT data in subcutaneous tumors (solid symbols) and respective control muscle (empty symbols; same size VOI as for tumor) plotted as a function of time post [^{123}I]FIAU injection. The tumors sizes for mice 1-3 were 535, 507, 226 mm³, respectively. The vertical dotted line shows the plateau (2 h p.i.). Subcutaneous tumor imaging and quantification

Mice bearing differently sized subcutaneous tumors were imaged to investigate the relationship between tumor size by MRI and [¹²³I]FIAU accumulation by SPECT (n = 14) in comparison with tumor weight (at dissection) and γ-counting (n = 11), as shown in Figure 5.6. In mice bearing LITG tumors a linear relationship was found for both SPECT/MRI

$$y [\%ID] = 5.093 \pm 0.380 \left[\% \frac{ID}{cm^3} \right] x [cm^3] - 0.065 \pm 0.114 [\%ID], R^2 = 0.93$$

and γ-counting/weight

$$[\%ID] = 5.963 \pm 0.998 \left[\% \frac{ID}{g} \right] x [g] + 0.191 \pm 0.205 [\%ID], R^2 = 0.77.$$

In WT tumors, both SPECT/MRI ($R^2 = 0.43$) and γ-counting/weight ($R^2 = 0.60$) followed very different relationships compared to LITG tumors, with significantly lower tracer uptake in terms of %ID/[cm³,g] ($p < 0.05$). The tracer uptake was higher in LITG, 5.10 ± 1.94 %ID/cm³ and 7.3 ± 3.85 %ID/g, compared to WT tumors, 2.48 ± 1.28 %ID/cm³ and 1.67 ± 0.40 %ID/g. In both LITG and WT tumors the %ID/cm³ values were not statistically different from the respective %ID/g values ($p > 0.05$). Examples of the SPECT/CT images from animals bearing LITG or WT tumors can be seen in Figure 5.5f-i. The measured *ex vivo* distribution of the radioactive tracer in the different tissues can be seen in Figure S5.7 (supplementary information).

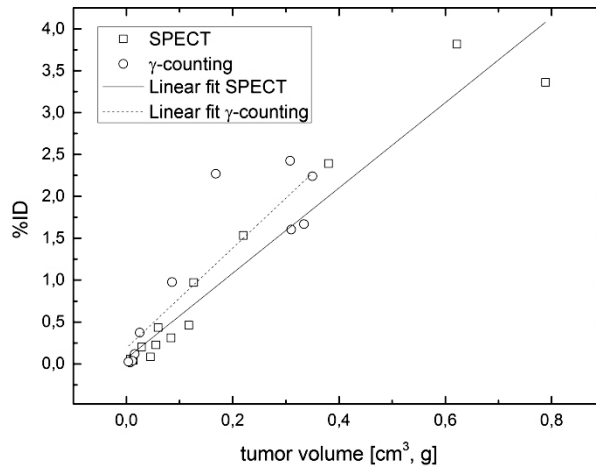


Figure 5.6 The correlations between %ID and tumor size by both SPECT/MRI and γ-counting/weight for the subcutaneous tumors are depicted. The data were fitted with a linear regression (Eq. 1 for %ID/cm³ and Eq. 2 for %ID/g. Each '□' and '○' symbol represents the quantification of one tumor (n = 14 for SPECT and n = 11 for γ-counting).

Bone metastases imaging and quantification

Upon cardiac injection of tumor cells, the animals developed multiple bone metastases in diverse sites (femur, tibia, iliac crest, scapula, and skull; Fig. 5.7a). In SPECT/MR overlaid images the activity spots corresponded nicely to tumor masses (Fig. 5.7b-c). In a different mouse, injection of radiolabeled doxorubicin-containing liposomes led to accumulation in the soft tumor tissue forming the bone metastasis on the tibia. This accumulation was visualized using dual isotope SPECT imaging overlaying the ^{177}Lu (liposomes) and ^{123}I (FIAU) signal (Fig 5.7f-h). *Ex vivo*, a hind limb with metastases on both the femur and tibia showed the osteolytic lesions by μCT (Fig. 5.8). The measured *ex vivo* distribution of the radioactive tracer in the different tissues can be seen in Figure S5.7 (supplementary information).

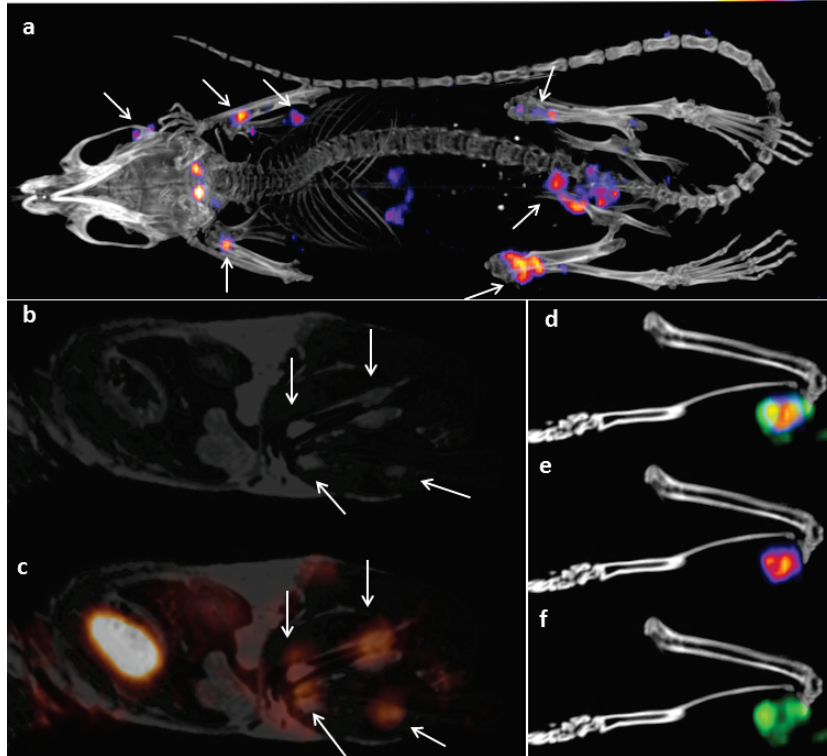


Figure 5.7 Imaging bone metastases. (a) Full body SPECT/CT of a mouse with multiple metastases (femur, tibia, scapula, skull, and scapula-humerus joint). (b) MRI coronal section of a mouse with four metastases in femur and tibia, 30 days post cardiac injection of tumor cells. (c) The SPECT/MR overlay shows a good correspondence between tumor masses and spots of radioactivity accumulation. (d-f) Accumulation of radiolabeled liposomal doxorubicin in the soft tissue of the bone metastasis in the tibia is visualized by (d) dual isotope SPECT imaging of (e) ^{123}I FIAU (red-blue) and (f) ^{177}Lu -liposomes (green). (a-c) were acquired at 13 h post ^{123}I FIAU injection; (d-f) were acquired post-mortem.

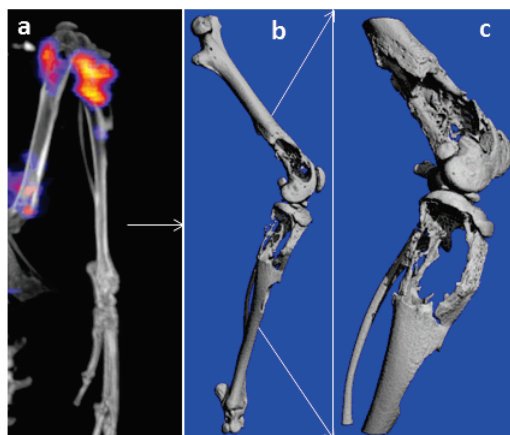


Figure 5.8 μCT . An example of the osteolytic nature of the bone lesions caused by the tumor metastases (a) the hind limb bone structure can be seen in greater detail on the μCT images (b-c) of a femur and tibia. (a) SPECT/CT acquired in vivo and (b-c) post-mortem.

Around day 20 post-cardiac injection, the smallest detectable metastases ($< 2 \text{ mm}^3$) were visible by FIAU-SPECT but were not yet clearly visible by MRI. Over the following weeks these metastases increased in volume with a resulting increased uptake (%ID) of FIAU (Fig. 5.9). Osteolytic bone destruction was visible by CT only after both SPECT and MRI signals were observed (> 28 days post tumor cell injections).

As for the subcutaneous tumors, also for the bone metastases a linear relationship was found between FIAU uptake and tumor size from the SPECT/MRI data (Fig. 5.10):

$$y[\%ID] = 1.713 \pm 0.098 \left[\% \frac{ID}{\text{cm}^3} \right] x[\text{cm}^3] - (6.045 \pm 12.5) \cdot 10^{-4} [\%ID], R^2 = 0.86 \quad (3)$$

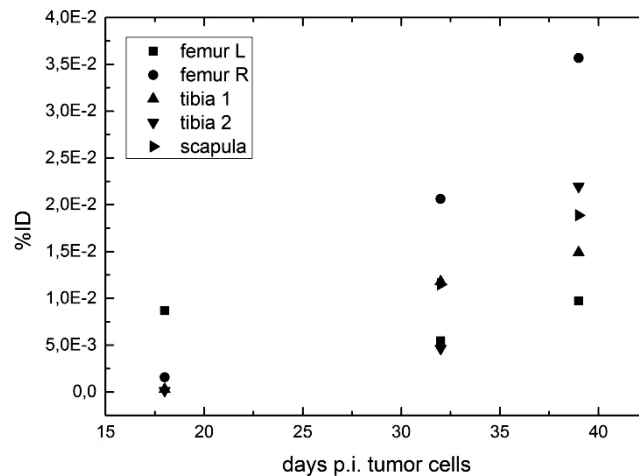


Figure 5.9 Uptake over time. %ID measured by SPECT for different metastases in the same animal imaged at day 18, 32, and 39 post cardiac injection of tumor cells. Tumor masses at 18 days p.i. were not visible by MRI.

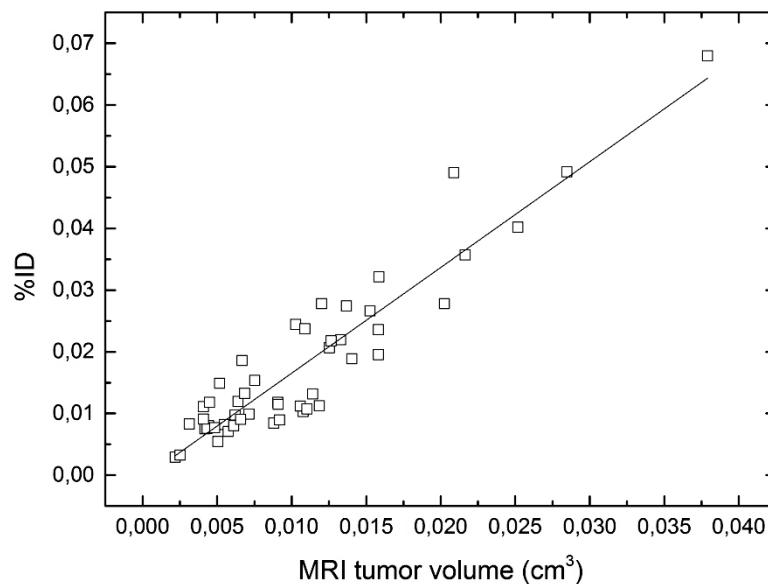


Figure 5.10 Correlation between %ID measured by SPECT and metastasis volume calculated from MRI. The data were fitted with a linear regression ($R^2 = 0.86$; Eq. 3). Each '□' symbol represents the quantification of one bone metastasis from a specific scan.

Histology

Histology of bone sections showed tumor cells located in the marrow and invading surrounding tissues such as muscle (Fig. 5.11). In the analyzed samples ($n = 25$), tumor cells were found only in areas of the bone where metastases were detected by SPECT/MRI.

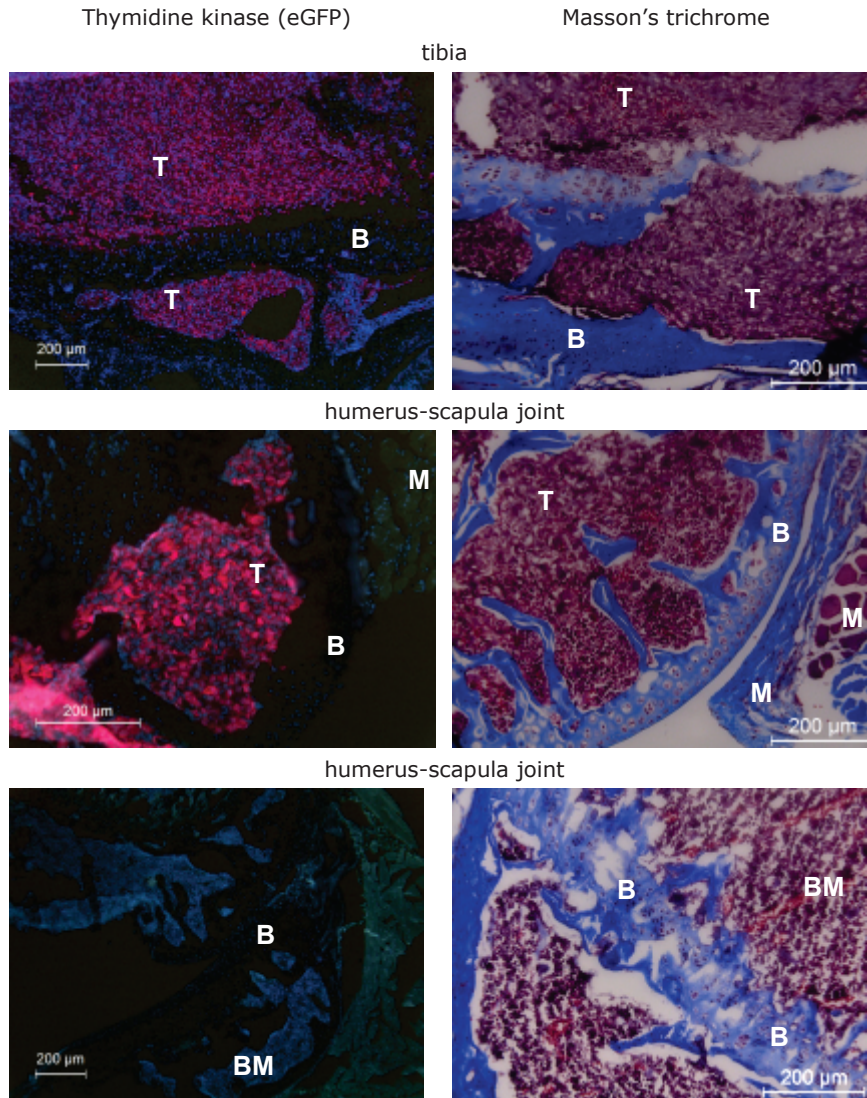


Figure 5.11 Histology of bone metastases. Left panels - Cryo-sections stained for GFP (red) and nuclei (blue). The muscle is also seen from its auto-fluorescence signal (light green). Right panels - corresponding cryo-sections stained with Masson's trichrome. Cytoplasm (light red/pink), connective tissue and bone (blue) and nuclei (dark brown/black) are visible. T: tumor; B: bone/cartilage; M: muscle; BM: normal bone marrow. Scale bars are 200 μm .

Discussion

Bone metastases have a mortality rate of nearly 100% and thus more insights into the disease process are urgently needed to derive new therapeutic strategies. Appropriate animal models and real time imaging of osteotropic

cancers provide major and critical information about tumor progression and skeletal metastasis. Our approach allows to noninvasively locate tumors and quantify growth, imaging the ensuing bone lesions, and to image a possible response to treatment. Other studies, using subcutaneous tumors, have also combined nuclear reporter gene imaging (SPECT, PET) with MRI but only to provide an anatomical reference for localization [19, 20, 33].

In this study, we first compared the uptake of the HSV-1 TK substrate [¹²³I]FIAU in subcutaneous tumors and bone metastases obtained from a breast cancer cell line stably transfected with the reporter gene. A linear correlation was found between the uptake of FIAU (%ID) detected by SPECT and the corresponding tumor volume calculated by MRI (cm³). As the uptake of FIAU in MDA-MB-231-LITG cells is a surrogate readout for the expression of the reporter gene and the uptake increases with the number of viable cells, as we showed *in vitro*, this correlation can be used to quantify the amount of viable tumor cells in a lesion [18, 19, 33]. SPECT image analysis for subcutaneous tumors and bone metastases yielded different slopes of approx. 5.1 %ID/cm³ compared to approx. 1.7 %ID/cm³, respectively. In our opinion several factors might contribute to this discrepancy. Most importantly, tumors that originate from a subcutaneous graft of tumor cells and tumors originating from tumor cells homing in the bone marrow after intracardiac injection strongly differ in terms of micro environment, morphology, and blood supply [1]. For these reasons, orthotopic and spontaneous tumor models are often considered more suitable than subcutaneous xenografts to evaluate new diagnostic and therapeutic tools in the preclinical setting. Also, the mice with metastatic tumors were imaged with SPECT 13 h post [¹²³I]FIAU injection, vs. the 2 h post injection imaging that was carried out in mice with subcutaneous xenografts. This delayed imaging protocol was chosen based on the slow tracer wash-out from muscle observed during the kinetic studies (Fig. 5.5). Also, 2 h post FIAU injection, the uptake in subcutaneous LITG tumors was only 2- and 4-fold higher, respectively in %ID/cm³ and %ID/g, than the corresponding WT tumors, which is much less than observed *in vitro*. This finding suggests non-specific FIAU accumulation in tumors at early time points [34]. During the 14 extra hours, [¹²³I]FIAU cleared from blood (from approx. 2.8 to 0.05 %ID/g) and muscle (from approx. 1.0 to 0.02 %ID/g) but, partially, also from the LITG metastases. However, the increased tumor-to-blood and tumor-to-muscle ratios allowed the detection of extremely small (< 2mm³ size) metastases with high contrast.

The exact co-registration of the sequentially acquired SPECT and MRI images of bone metastases turned out to be challenging. Great care was taken to avoid any movement of the animals between the scans and the same animal bed was used in both devices. Three fiducial markers attached to the animal bed were used as landmarks for SPECT and MRI image co-registration. Still, small movements (deep respiration of the animal under anesthesia and small spasms)

resulted in co-registration issues due to the millimeter size of the metastases spread over the whole skeleton. Therefore, separate VOIs for SPECT and MRI were drawn instead of the same VOI covering both signals, leading to slight mismatches in the tumor volumes considered for the analysis. Despite these challenges, SPECT was able to detect metastasis-related activity spots when no tumor mass was yet visible by MRI. This suggests that in our studies the minimal amount of tumor cells/mass needed for early detection was lower for SPECT than for MRI.

Since FIAU accumulation scales up with the amount of viable tumor cells, the presence of necrotic tumor regions or apoptotic cells caused by therapeutic treatments would lead to a lower overall tumor [^{123}I]FIAU uptake. This approach was shown in various preclinical mouse models of HSV-1 TK expressing subcutaneous tumors [25] and lung metastases [23], where treatment with ganciclovir led to a reduction in both specific FIAU uptake (%ID/g) and tumor volume compared to untreated controls. Other reporter gene approaches were evaluated for therapy monitoring. In a therapy study in mice bearing bone metastases of a *luc* expressing tumor, a significant reduction in tumor growth (detected by X-rays) was associated with a decrease in the *in vivo* bioluminescence signal from the tumor [7]. However, this approach bears the limitations of *in vivo* optical imaging, for noninvasive detection of deeply seated structures due to scattering and light absorbance by tissues.

We believe that our multimodality imaging approach combined with the bone metastasis mouse model could serve in drug development to quantify early therapy responses, which may not immediately translate into detectable morphological readouts, e.g. tumor volume shrinkage. Additionally, the morphological information from MRI as well as the skeletal bone information from the CT images would allow studying the downstream effects of a treatment. Dual-isotope SPECT studies allow to combine tumor/metastasis imaging with drug distribution/uptake quantification, which we showed here with a model radiolabeled drug carrier. Therefore, with this approach additional quantification of drug delivery in combination with tumor response assessment could be performed.

With respect to clinical translation, to date five clinical studies used reporter genes approaches (using HSV-1 TK and sodium iodide symporter) in combination with imaging to assess gene expression and possible effects of therapy [9, 35-38]. However, reporter gene approaches require upfront gene transfection of all tumor cells and, in particular, HSV-1 TK has the potential to elicit an immune reaction due to its viral origin. Human reporter gene systems currently being developed are expected to minimize immune responses. Therefore, future clinical applications of reporter systems could benefit the therapy strategies for, e.g., cancer and heart diseases [9, 39].

Conclusion

A multimodality imaging toolbox for preclinical studies on bone metastases was developed. To our knowledge this is the first report where the combination of soft tissue information from MRI, bone structure from CT, and reporter gene imaging by SPECT is used to follow metastatic bone lesions. The combination of reporter gene SPECT imaging, MRI and CT allows following the spread and growth of bone metastases in the whole skeleton noninvasively. Multi-isotope SPECT imaging adds extra functionality to this approach as it can give insights in drug accumulation at the target site, with a simultaneous quantification of therapeutic tumor load and tumor cell viability. This methodology holds promise in drug development to quantify early response of metastases to treatment, making this an important tool in the discovery of new and more effective anti-cancer therapies. The step from bench to bed can also be envisioned due to the ongoing development of non-immunogenic reporter gene systems for cell transfection in patients.

Acknowledgements

The authors would like to thank: Dr. Andreas Jacobs (European Institute of Molecular Imaging, University of Münster) for kindly supplying the LITG cassette; Caren van Kamen, Monique Berben, Carlijn van Helvert, and Marleen Hendriks for excellent technical assistance with the animals; Esther Kneepkens for helping with the liposomes; and Edwin Heijman for assistance with the MRI. This project was funded in part by the EU FP7 project Sonodrugs (NMP4-LA-2008-213706) and NanoNextNL (3D02, 3C02).

References

- [1] G. van der Horst, G. van der Pluijm, Preclinical models that illuminate the bone metastasis cascade, Recent results in cancer research. Fortschritte der Krebsforschung. Progres dans les recherches sur le cancer, 192 (2012) 1-31.
- [2] J.T. Buijs, G. van der Pluijm, Osteotropic cancers: from primary tumor to bone, Cancer letters, 273 (2009) 177-193.
- [3] K.N. Weilbaecher, T.A. Guise, L.K. McCauley, Cancer to bone: a fatal attraction, Nature reviews. Cancer, 11 (2011) 411-425.
- [4] G.R. Mundy, Metastasis to bone: causes, consequences and therapeutic opportunities, Nature reviews. Cancer, 2 (2002) 584-593.
- [5] F. Arguello, R.B. Baggs, C.N. Frantz, A murine model of experimental metastasis to bone and bone marrow, Cancer research, 48 (1988) 6876-6881.
- [6] Y. Kang, P.M. Siegel, W. Shu, M. Drobnjak, S.M. Kakonen, C. Cordon-Cardo, T.A. Guise, J. Massague, A multigenic program mediating breast cancer metastasis to bone, Cancer cell, 3 (2003) 537-549.
- [7] J.T. Buijs, N.V. Henriquez, P.G. van Overveld, G. van der Horst, I. Que, R. Schwaninger, C. Rentsch, P. Ten Dijke, A.M. Cleton-Jansen, K. Driouch, R. Lidereau, R. Bachelier, S. Vukicevic, P. Clezardin, S.E. Papapoulos, M.G. Cecchini, C.W. Lowik, G. van der Pluijm, Bone morphogenetic protein 7 in the development and treatment of bone metastases from breast cancer, Cancer research, 67 (2007) 8742-8751.
- [8] G. van der Pluijm, I. Que, B. Sijmons, J.T. Buijs, C.W. Lowik, A. Wetterwald, G.N. Thalmann, S.E. Papapoulos, M.G. Cecchini, Interference with the microenvironmental support impairs the de novo formation of bone metastases in vivo, Cancer research, 65 (2005) 7682-7690.
- [9] P. Brader, I. Serganova, R.G. Blasberg, Noninvasive molecular imaging using reporter genes, Journal of nuclear medicine : official publication, Society of Nuclear Medicine, 54 (2013) 167-172.

Chapter 5

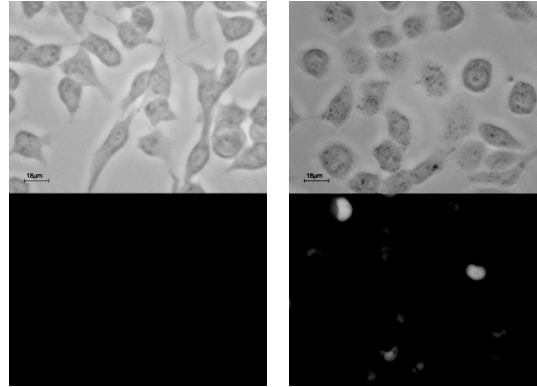
- [10] A. Rehemtulla, L.D. Stegman, S.J. Cardozo, S. Gupta, D.E. Hall, C.H. Contag, B.D. Ross, Rapid and quantitative assessment of cancer treatment response using in vivo bioluminescence imaging, *Neoplasia*, 2 (2000) 491-495.
- [11] S.C. Jost, L. Collins, S. Travers, D. Piwnica-Worms, J.R. Garbow, Measuring brain tumor growth: combined bioluminescence imaging-magnetic resonance imaging strategy, *Molecular imaging*, 8 (2009) 245-253.
- [12] A. Bianchi, S. Dufort, P.Y. Fortin, F. Lux, G. Raffard, N. Tassali, O. Tillement, J.L. Coll, Y. Cremillieux, In vivo MRI for effective non-invasive detection and follow-up of an orthotopic mouse model of lung cancer, *NMR in biomedicine*, (2014).
- [13] S.M. Thompson, M.R. Callstrom, B.E. Knudsen, J.L. Anderson, S.L. Sutor, K.A. Butters, C. Kuo, J.P. Grande, L.R. Roberts, D.A. Woodrum, Molecular bioluminescence imaging as a noninvasive tool for monitoring tumor growth and therapeutic response to MRI-guided laser ablation in a rat model of hepatocellular carcinoma, *Investigative radiology*, 48 (2013) 413-421.
- [14] T.J. Snoeks, A. Khmelinskii, B.P. Lelieveldt, E.L. Kaijzel, C.W. Lowik, Optical advances in skeletal imaging applied to bone metastases, *Bone*, 48 (2011) 106-114.
- [15] O. Peyruchaud, B. Winding, I. Pecheur, C.M. Serre, P. Delmas, P. Clezardin, Early detection of bone metastases in a murine model using fluorescent human breast cancer cells: application to the use of the bisphosphonate zoledronic acid in the treatment of osteolytic lesions, *Journal of bone and mineral research : the official journal of the American Society for Bone and Mineral Research*, 16 (2001) 2027-2034.
- [16] H.T. Song, E.K. Jordan, B.K. Lewis, W. Liu, J. Ganjei, B. Klaunberg, D. Despres, D. Palmieri, J.A. Frank, Rat model of metastatic breast cancer monitored by MRI at 3 tesla and bioluminescence imaging with histological correlation, *Journal of translational medicine*, 7 (2009) 88.
- [17] J.H. Kang, J.K. Chung, Molecular-genetic imaging based on reporter gene expression, *Journal of nuclear medicine : official publication, Society of Nuclear Medicine*, 49 Suppl 2 (2008) 164S-179S.
- [18] J.G. Tjuvajev, G. Stockhammer, R. Desai, H. Uehara, K. Watanabe, B. Gansbacher, R.G. Blasberg, Imaging the expression of transfected genes in vivo, *Cancer research*, 55 (1995) 6126-6132.
- [19] J.G. Tjuvajev, R. Finn, K. Watanabe, R. Joshi, T. Oku, J. Kennedy, B. Beattie, J. Koutcher, S. Larson, R.G. Blasberg, Noninvasive imaging of herpes virus thymidine kinase gene transfer and expression: a potential method for monitoring clinical gene therapy, *Cancer research*, 56 (1996) 4087-4095.
- [20] J.G. Tjuvajev, N. Avril, T. Oku, T. Sasajima, T. Miyagawa, R. Joshi, M. Safer, B. Beattie, G. DiResta, F. Daghighian, F. Augensen, J. Koutcher, J. Zweit, J. Humm, S.M. Larson, R. Finn, R. Blasberg, Imaging herpes virus thymidine kinase gene transfer and expression by positron emission tomography, *Cancer research*, 58 (1998) 4333-4341.
- [21] S. Cowey, A.A. Szafran, J. Kappes, K.R. Zinn, G.P. Siegal, R.A. Desmond, H. Kim, L. Evans, R.W. Hardy, Breast cancer metastasis to bone: evaluation of bioluminescent imaging and microSPECT/CT for detecting bone metastasis in immunodeficient mice, *Clinical & experimental metastasis*, 24 (2007) 389-401.
- [22] Y.-F. Chang, Y.-Y. Lin, H.-E. Wang, R.-S. Liu, F. Pang, J.-J. Hwang, Monitoring of tumor growth and metastasis potential in MDA-MB-435s/tk-luc human breast cancer xenografts, *Nuclear Instruments and Methods in Physics Research Section A: Accelerators, Spectrometers, Detectors and Associated Equipment*, 571 (2007) 155-159.
- [23] W.P. Deng, C.C. Wu, C.C. Lee, W.K. Yang, H.E. Wang, R.S. Liu, H.J. Wei, J.G. Gelovani, J.J. Hwang, D.M. Yang, Y.K. Fu, C.W. Wu, Serial in vivo imaging of the lung metastases model and gene therapy using HSV1-tk and ganciclovir, *Journal of nuclear medicine : official publication, Society of Nuclear Medicine*, 47 (2006) 877-884.
- [24] S.R. Choi, Z.P. Zhuang, A.M. Chacko, P.D. Acton, J. Tjuvajev-Gelovani, M. Doubrovin, D.C. Chu, H.F. Kung, SPECT imaging of herpes simplex virus type1 thymidine kinase gene expression by [(123)I]FIAU(1), *Academic radiology*, 12 (2005) 798-805.
- [25] K.M. Lin, C.H. Hsu, W.S. Chang, C.T. Chen, T.W. Lee, Human breast tumor cells express multimodal imaging reporter genes, *Molecular imaging and biology : MIB : the official publication of the Academy of Molecular Imaging*, 10 (2008) 253-263.
- [26] N.V. Henriquez, P.G. van Overveld, I. Que, J.T. Buijs, R. Bachelier, E.L. Kaijzel, C.W. Lowik, P. Clezardin, G. van der Pluijm, Advances in optical imaging and novel model systems for cancer metastasis research, *Clinical & experimental metastasis*, 24 (2007) 699-705.
- [27] S.A. Abraham, D.N. Waterhouse, L.D. Mayer, P.R. Cullis, T.D. Madden, M.B. Bally, The liposomal formulation of doxorubicin, *Methods in enzymology*, 391 (2005) 71-97.
- [28] S. Hak, H.M. Sanders, P. Agrawal, S. Langereis, H. Grull, H.M. Keizer, F. Arena, E. Terreno, G.J. Strijkers, K. Nicolay, A high relaxivity Gd(III)DOTA-DSPE-based liposomal contrast agent for magnetic resonance imaging, *European journal of pharmaceuticals and biopharmaceutics : official journal of Arbeitsgemeinschaft fur Pharmazeutische Verfahrenstechnik e.V.*, 72 (2009) 397-404.
- [29] A. Klose, Y. Waerzeggers, P. Monfared, S. Vukicevic, E.L. Kaijzel, A. Winkeler, C. Wickenhauser, C.W. Lowik, A.H. Jacobs, Imaging bone morphogenetic protein 7 induced cell cycle arrest in experimental gliomas, *Neoplasia*, 13 (2011) 276-285.
- [30] M. de Smet, S. Langereis, S. van den Bosch, K. Bitter, N.M. Hijnen, E. Heijman, H. Grull, SPECT/CT imaging of temperature-sensitive liposomes for MR-image guided drug delivery with high intensity focused ultrasound, *Journal of controlled release : official journal of the Controlled Release Society*, 169 (2013) 82-90.
- [31] M. de Smet, S. Langereis, S. van den Bosch, H. Grull, Temperature-sensitive liposomes for doxorubicin delivery under MRI guidance, *Journal of controlled release : official journal of the Controlled Release Society*, 143 (2010) 120-127.
- [32] Institute of Laboratory Animal Resources (U.S.). Committee on Care and Use of Laboratory Animals., Guide for the care and use of laboratory animals, in: NIH publication, U.S. Dept. of Health and Human Services, Public Health Service, Bethesda, Md., pp. v.
- [33] Y. Waerzeggers, M. Klein, H. Miletic, U. Himmelreich, H. Li, P. Monfared, U. Herrlinger, M. Hoehn, H.H.

Bone metastasis imaging with SPECT/CT/MRI: a preclinical toolbox for therapy studies

- Coenen, M. Weller, A. Winkeler, A.H. Jacobs, Multimodal imaging of neural progenitor cell fate in rodents, *Molecular imaging*, 7 (2008) 77-91.
- [34] R. Haubner, N. Avril, P.A. Hantzopoulos, B. Gansbacher, M. Schwaiger, In vivo imaging of herpes simplex virus type 1 thymidine kinase gene expression: early kinetics of radiolabelled FIAU, *European journal of nuclear medicine*, 27 (2000) 283-291.
- [35] I. Penuelas, G. Mazzolini, J.F. Boan, B. Sangro, J. Marti-Clement, M. Ruiz, J. Ruiz, N. Satyamurthy, C. Qian, J.R. Barrio, M.E. Phelps, J.A. Richter, S.S. Gambhir, J. Prieto, Positron emission tomography imaging of adenoviral-mediated transgene expression in liver cancer patients, *Gastroenterology*, 128 (2005) 1787-1795.
- [36] M.F. Dempsey, D. Wyper, J. Owens, S. Pimlott, V. Papanastassiou, J. Patterson, D.M. Hadley, A. Nicol, R. Rampling, S.M. Brown, Assessment of 123I-FIAU imaging of herpes simplex viral gene expression in the treatment of glioma, *Nuclear medicine communications*, 27 (2006) 611-617.
- [37] A. Jacobs, J. Voges, R. Reszka, M. Lercher, A. Gossmann, L. Kracht, C. Kaestle, R. Wagner, K. Wienhard, W.D. Heiss, Positron-emission tomography of vector-mediated gene expression in gene therapy for gliomas, *Lancet*, 358 (2001) 727-729.
- [38] K.N. Barton, H. Stricker, S.L. Brown, M. Elshaikh, I. Aref, M. Lu, J. Pegg, Y. Zhang, K.C. Karvelis, F. Siddiqui, J.H. Kim, S.O. Freytag, B. Movsas, Phase I study of noninvasive imaging of adenovirus-mediated gene expression in the human prostate, *Molecular therapy : the journal of the American Society of Gene Therapy*, 16 (2008) 1761-1769.
- [39] M.L. James, S.S. Gambhir, A molecular imaging primer: modalities, imaging agents, and applications, *Physiological reviews*, 92 (2012) 897-965.
- [40] J.G. Tjuvajev, M. Doubrovin, T. Akhurst, S. Cai, J. Balatoni, M.M. Alauddin, R. Finn, W. Bornmann, H. Thaler, P.S. Conti, R.G. Blasberg, Comparison of radiolabeled nucleoside probes (FIAU, FHBG, and FHPG) for PET imaging of HSV1-tk gene expression, *Journal of nuclear medicine : official publication, Society of Nuclear Medicine*, 43 (2002) 1072-1083.
- [41] W.P. Deng, W.K. Yang, W.F. Lai, R.S. Liu, J.J. Hwang, D.M. Yang, Y.K. Fu, H.E. Wang, Non-invasive in vivo imaging with radiolabelled FIAU for monitoring cancer gene therapy using herpes simplex virus type 1 thymidine kinase and ganciclovir, *European journal of nuclear medicine and molecular imaging*, 31 (2004) 99-109.
- [42] X. Lan, Y. Liu, Y. He, T. Wu, B. Zhang, Z. Gao, R. An, Y. Zhang, Autoradiography study and SPECT imaging of reporter gene HSV1-tk expression in heart, *Nuclear medicine and biology*, 37 (2010) 371-380.
- [43] M. Josefsson, T. Grunditz, T. Ohlsson, E. Ekblad, Sodium/iodide-symporter: distribution in different mammals and role in entero-thyroid circulation of iodide, *Acta physiologica Scandinavica*, 175 (2002) 129-137.
- [44] T.C. Chou, A. Feinberg, A.J. Grant, P. Vidal, U. Reichman, K.A. Watanabe, J.J. Fox, F.S. Philips, Pharmacological disposition and metabolic fate of 2'-fluoro-5-iodo-1-beta-D-arabinofuranosylcytosine in mice and rats, *Cancer research*, 41 (1981) 3336-3342.

Supplementary Information

A



B

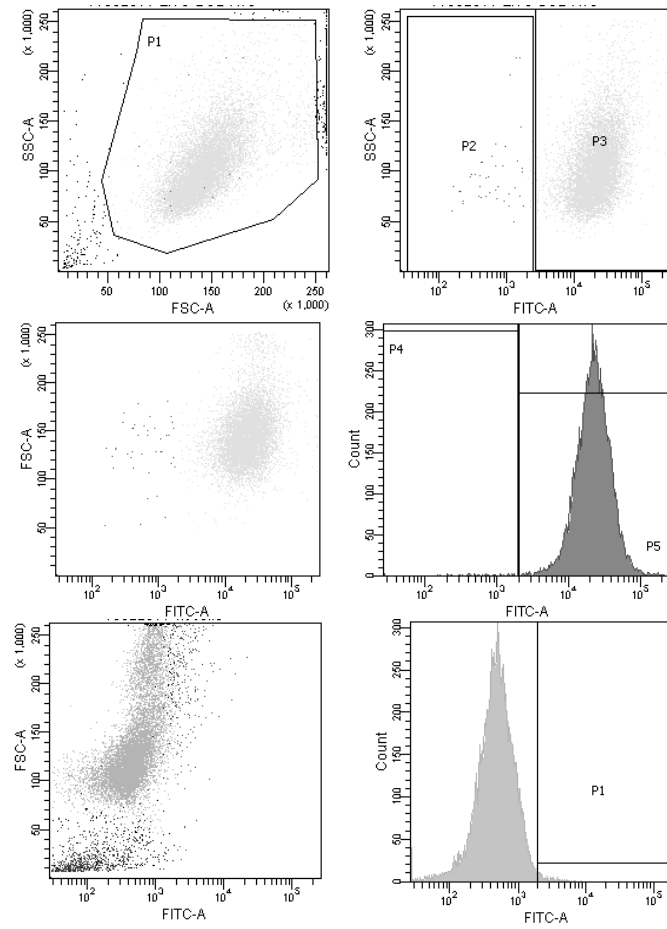


Figure S5.1 (A) Microscope images of MDA-MB-231 wild-type (WT) cells (left) and MDA-MB-231-LITG (LITG) cells (right). Upper panels: bright field images; Lower panels:

fluorescence images (excitation 480/40 nm). Magnification 40x; (B) FACS analysis of LITG (top) and WT cells (bottom). A total of 10,000 events per sample were collected. Cells were excited using an air-cooled solid state diode laser (488 nm) and the emission was collected through a 515-545 nm detector (FITC-A channel). In addition, forward-light scatter (FSC-H) and side-light scatter (SSC-H) data were collected for each sample.

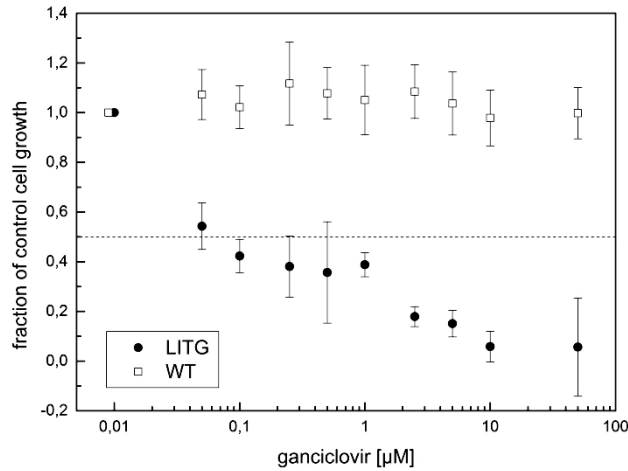
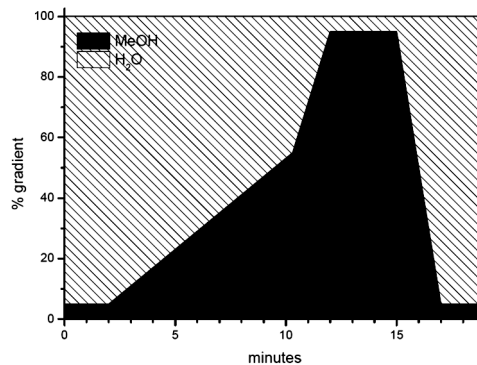


Figure S5.2 Sensitivity of MDA-MB-231 wild-type (WT) and MDA-MB-231-LITG (LITG) tumor cells to ganciclovir (GCV) determined with a MTT (3-(4,5-dimethylthiazol-2-yl)-2,5-diphenyltetrazolium bromide) viability assay. MTT is a yellow tetrazole derivative which is reduced to purple formazan in living cells. It is expected that WT cell proliferation and viability will not be affected by GCV at the concentrations used. Cells were plated in a 96-well plate in triplicate at densities that ensured 80% confluence at time of MTT assay (3000 cells/well for LITG cells and 5000 cells/well for WT cells) 24 h prior to the experiment. Then medium was replaced by medium containing GCV at concentrations ranging from 0-50 mM and the cells were incubated for 72 h. The medium was replaced daily to keep GCV concentration constant. After incubation, MTT was dissolved in pre-warmed medium at 5 mg/mL and passed through a 0.22 μm filter. Fifty μL of the MTT solution were added to each well and the plates were incubated for 120 min. The medium was gently aspirated and the formed formazan crystals were dissolved in 100 μL dimethylsulfoxide (DMSO). Absorbance at 560 nm was measured on a plate reader. The effective dose that produced a therapeutic response in 50% of the LITG cells (ED50) was determined from results derived from three independent experiments and calculated to be 0.15 μM. WT cell proliferation was not affected by incubation with the GCV concentrations used.

A



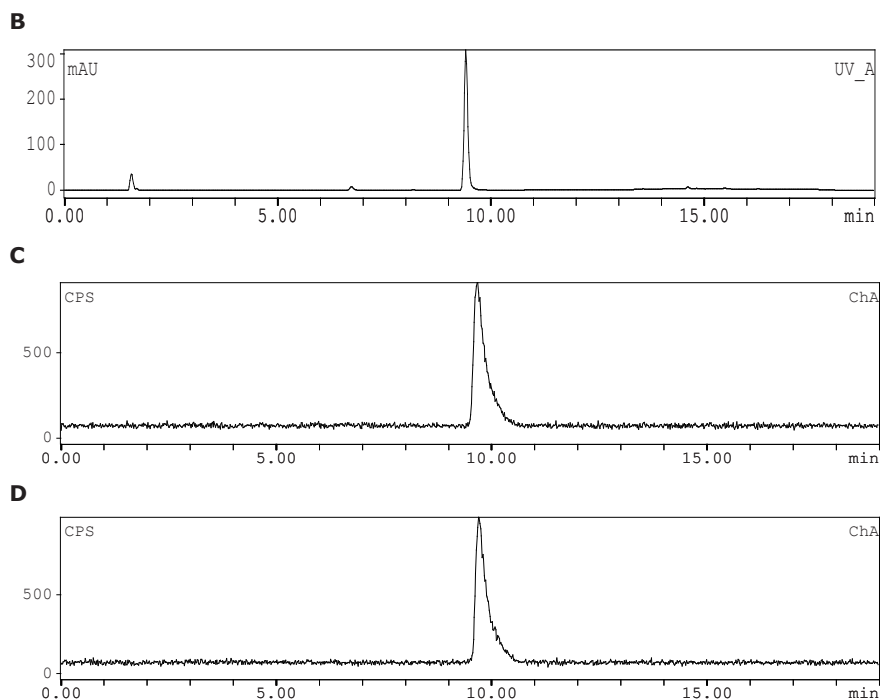


Figure S5.3 Radiochemical purity analysis and chemical identity determination of [^{123}I]FIAU. Analytical radio-HPLC was performed on an Agilent 1100 system equipped with UV and radioactivity (Gabi, Raytest) detectors in series. The analyte was injected on a C18 Eclipse XBD column (150×4.6 mm; $5 \mu\text{m}$ particle size) and eluted with a linear gradient (A) of H_2O /methanol at 1 mL min^{-1} . (B) Elution profile of the FIAU standard (UV profile; $R_t = 9.4$ min); elution profile of (C) the crude and (D) sep-pak purified [^{123}I]FIAU re-dissolved in 0.9% NaCl (radioactive profile; $R_t = 9.8$ min).

^{177}Lu -labeled liposomal formulation of doxorubicin

A ^{177}Lu -radiolabeled liposomal formulation of doxorubicin similar to the clinically used Doxil® formulation [27], was prepared based on previously published methods [30, 31], with minor modifications: the liposomes were composed of HSPC:Cholesterol:DPPE-PEG₂₀₀₀:DOTA-DSPE = 75:50:3:1 (molar ratio). A total amount of 115 μmol of phospholipids and cholesterol were dissolved in a solution of chloroform/methanol (4:1, v/v). The organic solvents were removed under vacuum until a thin lipid film was formed, which was further dried overnight under a nitrogen flow. The lipid film was hydrated at 60 °C with a 240 mM $(\text{NH}_4)_2\text{SO}_4$ buffer (pH 5.4). The suspension was extruded at 60 °C successively through a 200 nm filter (two times) and a 100 nm filter (six times). After extrusion, the extra-liposomal buffer was replaced by HEPES buffered saline (HBS), pH 7.4 (20 mM HEPES, 137 mM NaCl) by gel filtration through a PD-10 desalting column (GE Healthcare). Subsequently, a doxorubicin solution (AvaChem Scientific, San Antonio, TX) in HBS (5 mg/mL) was added to the liposomes at a 20:1 phospholipid-to-doxorubicin weight ratio and incubated at 37 °C for 90 min. Finally, the liposome solution was passed through a PD-10 column to remove traces of free doxorubicin. The intraliposomal doxorubicin concentration (2.63 ± 0.07 ng/mL) was determined using fluorescence measurements (Perkin Elmer LS55, $\lambda_{\text{ex}} = 485$ nm and $\lambda_{\text{em}} = 590$ nm) after destruction of the liposomes with Triton X-100. The hydrodynamic radius of the liposomes (simple fit: 72.25 nm) in HBS was determined using dynamic light scattering (ALV/CGS-3 Compact Goniometer System, ALV-GmbH, Landen, Germany).

Bone metastasis imaging with SPECT/CT/MRI:
a preclinical toolbox for therapy studies

Radiolabeling. 100 μL of liposomes solution was transferred to a vial containing 5 μL of 2 M ammonium acetate buffer pH 5.5 and approx. 96 MBq of ^{177}Lu (1.5 μL). The solution was incubated for 1.5 h at 50 $^{\circ}\text{C}$, then 1 μL of 10 mM DTPA in 0.9% NaCl was added and the solution was incubated for 10 min at RT. The crude mixture was purified using a 7 kDa Zeba $^{\circledR}$ desalting Spin column (Thermo Scientific, Waltham, MA) pre-equilibrated with HBS to remove unbound ^{177}Lu and exchange the buffer. The radiochemical yield was assessed by thin layer chromatography (iTLC-SG plates, Varian Inc., Palo Alto, CA) using 200 mM EDTA in 0.9% NaCl as the running buffer (Fig. S5.4).

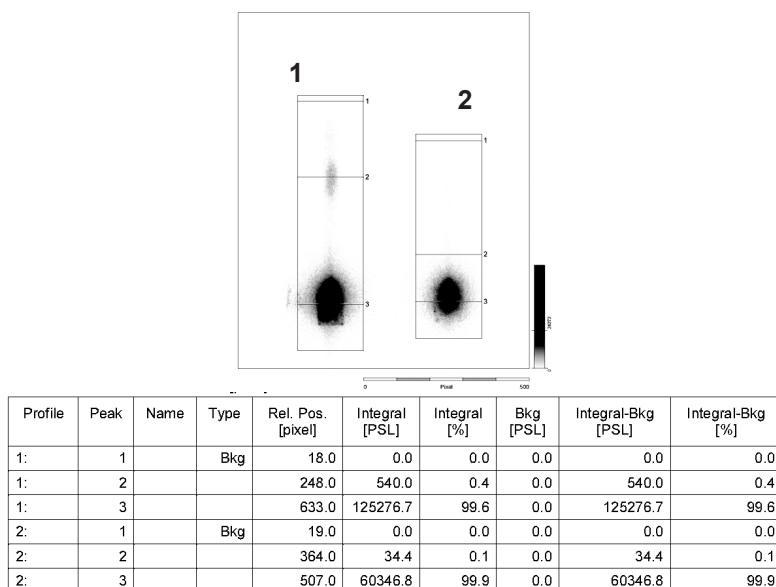
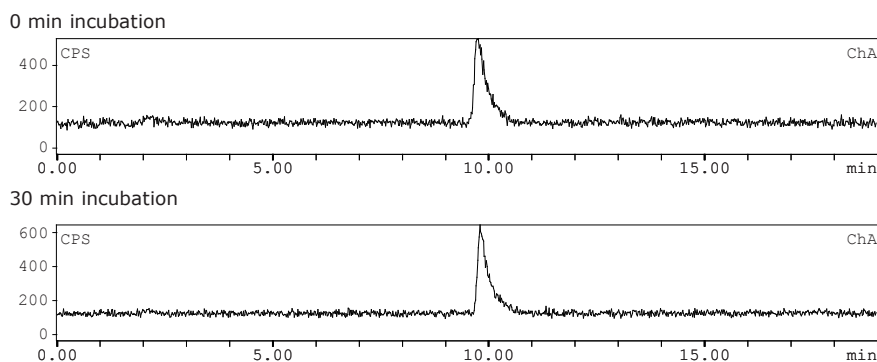


Figure S5.4 Radiolabeling yields and radiochemical purity of doxorubicin-encapsulated ^{177}Lu -liposomes after DTPA challenge (1) and after size exclusion purification and buffer exchange (2). The radiochemical purity was assessed by TLC which was performed on instant TLC silica gel strips (Varian Inc.) eluted with 0.9% NaCl containing 200 mM EDTA. Under these conditions the free ^{177}Lu migrates with $R_f = 0.9$, while the doxorubicin-encapsulated ^{177}Lu -liposomes remain at the origin. The strips were imaged on a phosphor imager (FLA-7000; Fujifilm), and the labeling yields/purity were quantified using AIDA Image Analyzer software.



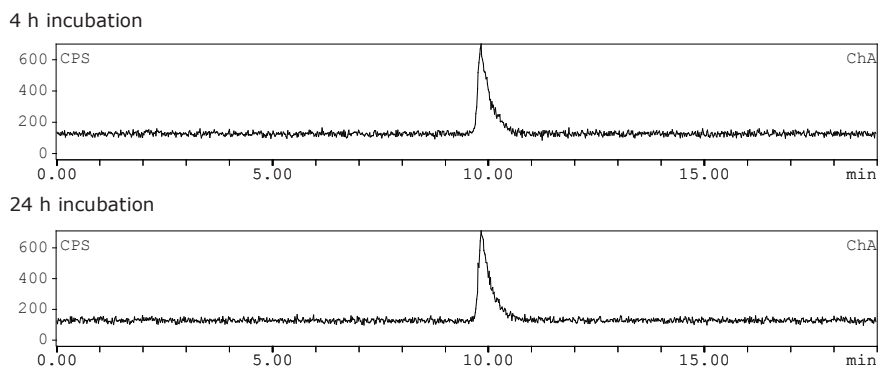


Figure S5.5 [^{125}I]FIAU stability in 50% mouse serum. (a-c) examples of [^{123}I]FIAU HPLC elution profiles at 0, 0.5, 4, and 24 h of incubation. The sample was incubated at 37 °C and 300 rpm. Samples (100 μL) were taken at 0 and 30 min, 1, 1.5, 2, 3, 4 and 24 h and diluted 2-fold with ice cold MeCN to precipitate the serum proteins. The mixture was centrifuged for five minutes at 12,000 rpm. Supernatant was separated from pellet by pipetting, passed through a 0.22 μm filter and diluted in 0.9% NaCl. Radiochemical purity was always > 95%, as verified by HPLC. The activity recovered in the supernatants was > 90% from the total activity (supernatant + pellet), as analyzed by γ -counting.

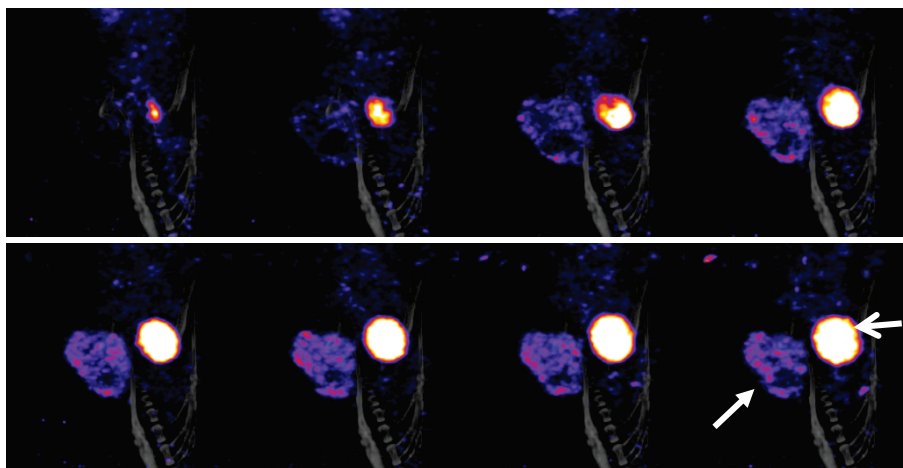


Figure S5.6 SPECT/CT imaging of a mouse with subcutaneous MDA-MB-231-LITG tumor (hind-limb). Stills from animated sequence of scan 1, 3, 7, 15, 21, 30, 40, and 48 of 48 consecutive SPECT scans. The mouse was injected intravenously with approx. 40 MBq [^{123}I]FIAU in 100 μL saline followed by dynamic SPECT scans (12 projections/scan, 30 s/projection, approx. 4 min/scan, 140 min scan time) and by a CT scan (45 keV, 2 s/projection, and 240 projections/scan). Open arrow: bladder; closed arrow: tumor.

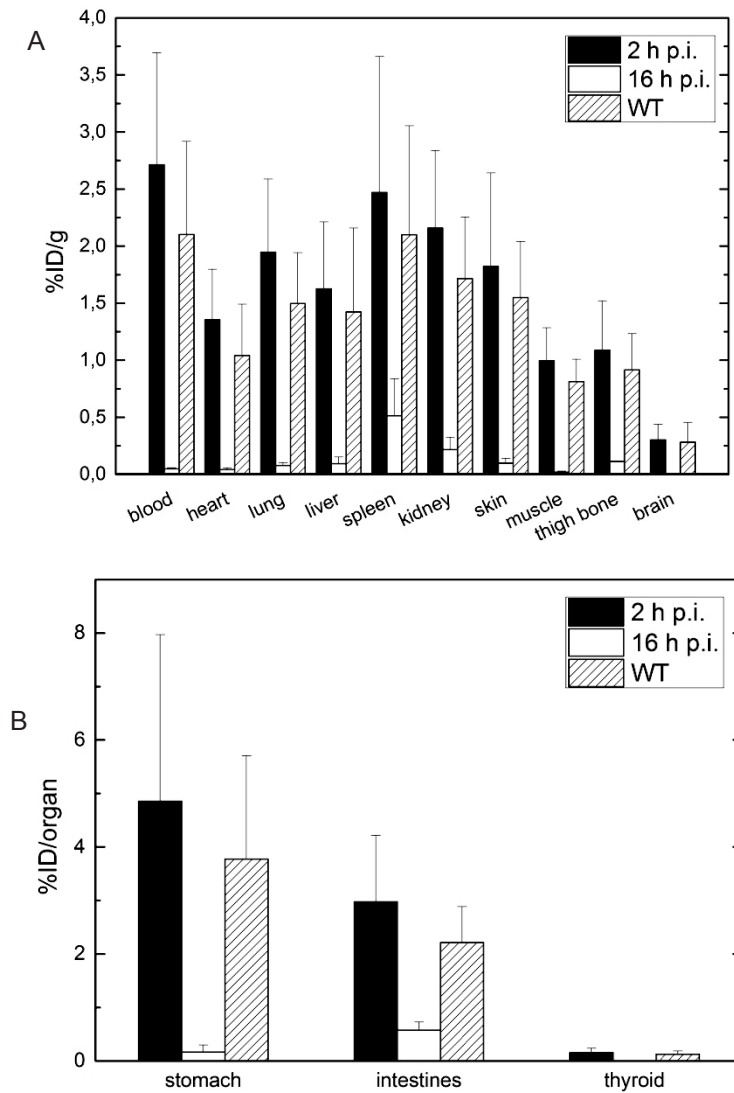


Figure S5.7 Normal tissue biodistribution of $[^{123}\text{I}]\text{FIAU}$ in mice bearing subcutaneous MDA-MB-231-LITG (solid bars; $n = 11$) and bone metastases (empty bars; $n = 4$), 2 and 16 h post tracer injection, respectively. The control mice (WT, striped bars; $n = 4$) had subcutaneous tumors obtained from MDA-MB-231 wild-type cells. The bars in (A) and (B) represent the mean percentage injected dose per gram (%ID/g and %ID/organ, respectively) and the error bars one standard deviation. The data show non-specific FIAU uptake in all selected organs and a pronounced washout of radioactivity from blood and tissues between 2 h and 16 h post-tracer injection. High uptake in stomachs, which were not emptied before γ -counting, was seen in other *in vivo* studies with radioactive FIAU [20, 23, 40-42] and would suggest *in vivo* degradation and iodide accumulation in the gastric mucosa via the sodium/iodide symporter [43]. However, the low uptake in thyroid suggests that no tracer de-iodination occurred *in vivo*. Therefore intact $[^{123}\text{I}]\text{FIAU}$ might also accumulate in the gastrointestinal tract [44]. Also, $[^{123}\text{I}]\text{FIAU}$ was mainly excreted intact

through the kidneys, in the urine, as confirmed by radio-HPLC.

Table S5.1 Quantification data from subcutaneous tumors. Animals 4, 7, 8 were not used for γ -counting.

	mouse	%ID SPECT	volume MRI (mL)	%ID/cm ³		%ID γ -counting	weight (g)	%ID/g			
				mean	SD			mean	SD		
LIT G	1	0.06	0.01	8.11	5.10	1.94	0.04	0.01	3.17	7.30	3.85
	2	0.04	0.01	4.42			0.02	0.01	2.28		
	3	0.04	0.01	3.27			0.03	0.004	7.00		
	4	0.20	0.03	7.01							
	5	0.08	0.05	1.84			0.12	0.02	7.55		
	6	0.23	0.06	4.05			0.37	0.03	14.81		
	7	0.43	0.06	7.27							
	8	0.31	0.08	3.68							
	9	0.46	0.12	3.92			0.66	0.09	7.65		
	10	0.97	0.13	7.67			2.26	0.17	13.46		
	11	2.39	0.38	6.29			2.24	0.35	6.40		
	12	1.53	0.45	3.44			1.67	0.33	4.99		
	13	3.82	0.62	6.14			2.42	0.31	7.87		
	14	3.36	0.79	4.26			1.60	0.31	5.17		
WT	1	0.62	0.15	4.19	2.48	1.28	0.34	0.19	1.77	1.67	0.40
	2	0.38	0.16	2.34			0.27	0.15	1.72		
	3	0.45	0.20	2.27			0.30	0.15	2.06		
	4	0.24	0.22	1.09			0.14	0.12	1.11		

References

- [1] S.A. Abraham, D.N. Waterhouse, L.D. Mayer, P.R. Cullis, T.D. Madden, M.B. Bally, The liposomal formulation of doxorubicin, *Methods in enzymology*, 391 (2005) 71-97.
- [2] M. de Smet, S. Langereis, S. van den Bosch, K. Bitter, N.M. Hijnen, E. Heijman, H. Grull, SPECT/CT imaging of temperature-sensitive liposomes for MR-image guided drug delivery with high intensity focused ultrasound, *Journal of controlled release : official journal of the Controlled Release Society*, 169 (2013) 82-90.
- [3] M. de Smet, S. Langereis, S. van den Bosch, H. Grull, Temperature-sensitive liposomes for doxorubicin delivery under MRI guidance, *Journal of controlled release : official journal of the Controlled Release Society*, 143 (2010) 120-127.
- [4] J.G. Tjuvajev, M. Doubrovin, T. Akhurst, S. Cai, J. Balatoni, M.M. Alauddin, R. Finn, W. Bornmann, H. Thaler, P.S. Conti, R.G. Blasberg, Comparison of radiolabeled nucleoside probes (FIAU, FHBG, and FHPG)

Bone metastasis imaging with SPECT/CT/MRI:
a preclinical toolbox for therapy studies

- for PET imaging of HSV1-tk gene expression, *Journal of nuclear medicine : official publication, Society of Nuclear Medicine*, 43 (2002) 1072-1083.
- [5] W.P. Deng, C.C. Wu, C.C. Lee, W.K. Yang, H.E. Wang, R.S. Liu, H.J. Wei, J.G. Gelovani, J.J. Hwang, D.M. Yang, Y.K. Fu, C.W. Wu, Serial in vivo imaging of the lung metastases model and gene therapy using HSV1-tk and ganciclovir, *Journal of nuclear medicine : official publication, Society of Nuclear Medicine*, 47 (2006) 877-884.
- [6] W.P. Deng, W.K. Yang, W.F. Lai, R.S. Liu, J.J. Hwang, D.M. Yang, Y.K. Fu, H.E. Wang, Non-invasive in vivo imaging with radiolabelled FIAU for monitoring cancer gene therapy using herpes simplex virus type 1 thymidine kinase and ganciclovir, *European journal of nuclear medicine and molecular imaging*, 31 (2004) 99-109.
- [7] X. Lan, Y. Liu, Y. He, T. Wu, B. Zhang, Z. Gao, R. An, Y. Zhang, Autoradiography study and SPECT imaging of reporter gene HSV1-tk expression in heart, *Nuclear medicine and biology*, 37 (2010) 371-380.
- [8] J.G. Tjuvajev, N. Avril, T. Oku, T. Sasajima, T. Miyagawa, R. Joshi, M. Safer, B. Beattie, G. DiResta, F. Daghighian, F. Augensen, J. Koutcher, J. Zweit, J. Humm, S.M. Larson, R. Finn, R. Blasberg, Imaging herpes virus thymidine kinase gene transfer and expression by positron emission tomography, *Cancer research*, 58 (1998) 4333-4341.
- [9] M. Josefsson, T. Grunditz, T. Ohlsson, E. Ekblad, Sodium/iodide-symporter: distribution in different mammals and role in entero-thyroid circulation of iodide, *Acta physiologica Scandinavica*, 175 (2002) 129-137.
- [10] T.C. Chou, A. Feinberg, A.J. Grant, P. Vidal, U. Reichman, K.A. Watanabe, J.J. Fox, F.S. Philips, Pharmacological disposition and metabolic fate of 2'-fluoro-5-iodo-1-beta-D-arabinofuranosylcytosine in mice and rats, *Cancer research*, 41 (1981) 3336-3342.





**Imaging regeneration:
the axolotl way**

Abstract

Many diseases but also accidents lead to a damage of tissues, organs or limbs or other crucial structures that do not restore as the regenerative potential of humans and also most mammals is very limited. The salamander axolotl (*Ambystoma mexicanum*) however, is capable of complete complex structure (e.g. limbs, tail and heart) regeneration in a scar-free process. A pool of progenitor cells (known as the 'blastema') forms on the site of injury, proliferates and differentiates to regenerate the damaged tissue. Even though this process has been extensively researched in developmental biology, it has not been imaged *in vivo* using the non-invasive techniques of Magnetic Resonance Imaging (MRI) and Computed Tomography (CT). Thus, we have developed axolotl imaging protocols for CT and MRI and assessed the feasibility of these techniques in studying axolotl tail regeneration and heart anatomy & function. The distal 3-4 cm tail tips of axolotls were amputated and the ensuing regeneration was periodically imaged. The blastema was visible from approx. 20 days post amputation (p.a.) on MRI. A rod of cartilage projected out from the spinal cord into the tail tip at day 29 p.a. New muscle tissue was observed after 60 days p.a. The appearance of ossified vertebrae was seen by both CT and MRI from day 80 p.a. The formation of new blood vessels (aorta and vena cava) was observed at 19 days p.a. in the angiograms. New smaller vessels we observed at roughly the same time but were only visible on T2 weighted anatomy images. The high definition (< 200 μm) image sets depicting the heart anatomy closely matched previously published anatomical features. A ventricle ejection fraction of 55-62% was calculated from a preliminary functional analysis of the cardiac cycle. This analysis is still ongoing as several challenges associated with the difficulty in delineating the ventricle cavity from the cardiac walls still need to be addressed.

For the first time both MRI and CT were used to non-invasively image the regeneration process in an axolotl. Further imaging protocols optimization should allow the observation of smaller tissue changes. The prospective heart data show a potential application of functional MRI imaging in a regenerative heart study.

Keywords: regeneration, axolotl, MRI, CT, heart, amphibian

Introduction

Regeneration is the replacement of tissues, organs or body parts and restoration of their function after (partial) loss or injury. In humans but also most mammals, the regenerative potential is rather limited and often restricted to certain tissues. Examples for cyclical regeneration are maintenance of skin, renewal of the intestinal lining, new blood and blood vessel formation, hair, bone, as well as the generation of new neurons in the brain are all part of cyclical regeneration [1]. However, many diseases but also accidents lead to a damage of tissues, organs, limbs or other crucial structures that do not restore. For example, current predictions suggest that the prevalence of limb amputations will steadily increase in the next 40 years due to the increasing incidence of obesity and associated diseases such as diabetes and atherosclerosis [2, 3]. In some cases, a prosthesis (e.g. leg prosthetics) is able to replace the loss of function, but these types of solutions pale in comparison to the regeneration of a fully functional limb. Also for tissue regeneration, only a few limited examples exist in humans. For example, the liver may regrow a large portion up to its original size when enough hepatocytes remain to proliferate [4]. In most other cases, the wound healing mechanisms lead to scar formation [5]. Scar tissue is the result of extracellular matrix deposition by fibroblasts at the wound site effectively replacing the affected tissue leaving the original functional capacities of that tissue diminished. A typical example is the remodelling of the cardiac muscle in the left ventricle after a cardiac infarction. Here, the replacement fibrotic tissue has limited contractile function and difficulties adopting the electrical gradient, leading to further heart problems [6-8].

Currently the clinical applications of regenerative medicine approaches are limited, however promising progresses have been made in stimulating stem activity and bioengineering new scaffolds [9-11]. In 2013 Song *et al.* managed to recover kidney function in rats by transplanting a matrix scaffold of a rat kidney, decellularized and reseeded *in vitro* [12]. Stem cell isolation and artificial manipulation to induce morphogenesis of complex structures is one of the main approaches in mammalian regeneration [11]. In a recent clinical trial it was suggested that left ventricular function in ischaemic heart disease patients can possibly be salvaged by injection of bone marrow stem cells, but was unsuccessful [13]. The enormous complexity of the current stem cell based approaches is a reason to consider new alternatives and complementary approaches.

The axolotl as an animal model for regeneration

Interestingly, not all vertebrate tetrapods face the same type of challenges in regeneration.

Namely, the axolotl (*Ambystoma mexicanum*) is an aquatic salamander with the ability to regenerate lost extremities (limbs and tail) in addition to parts of most organs as long as the functions critical to its survival remain intact [9, 14]. It belongs to the order of caudata/urodela (salamanders) in the class of Amphibia. It is an inducible obligatory neotene, meaning that it keeps its larval form through its life span under normal conditions (Fig. 6.1) [15].

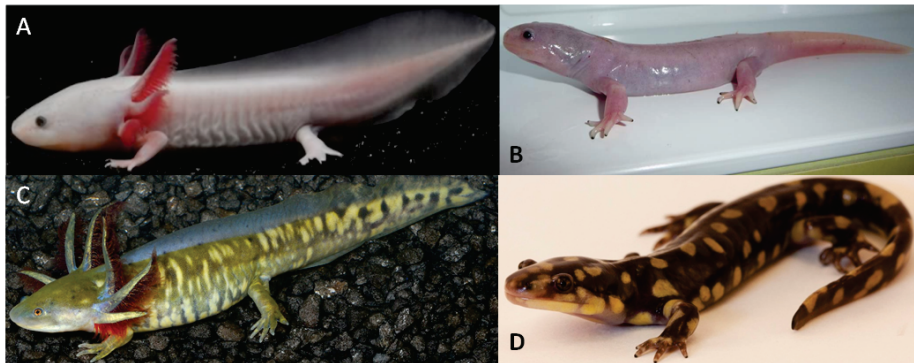


Figure 6.1 An axolotl in its normal larval appearance that is typically maintained for life (A); its metamorphosed counterpart (B); a larval tiger salamander bears great similarities to the axolotl (C); and an adult metamorphosed tiger salamander (D) [16-18].

Adulthood and sexual maturity are reached in 12 to 18 months [19, 20]. Regeneration in salamanders is common in the larval stages, but some urodele amphibians such as the axolotl and newt retain this ability throughout their entire life making them two of the most apt regenerators among vertebrates [9, 21]. In contrast, anuran amphibians such as the frog revert to scar-based healing once they have metamorphosed into their adult form [21]. The regenerative capacity through the different life stages of mammals, urodele- and anuran amphibians is displayed in Figure 6.2 [9].

The axolotl, rarely if ever, undergoes metamorphosis under normal conditions, thus retaining its juvenile characteristics, such as the external gills and aquatic housing environment [20, 22]. If metamorphosis is induced by thyroid hormones (artificially), the axolotl will undergo heavy physiological changes to become a terrestrial salamander, similar to the tiger salamander (*Ambystoma tigrinum*, Fig 6.1D) [15]. It will maintain its regenerative potential, but at a reduced rate and fidelity [20]. Still, the facultative metamorphosis of axolotls offers us a way to study its effects on anatomy, physiology, and regeneration [23].

The axolotl, rarely if ever, undergoes metamorphosis under normal conditions, thus retaining its juvenile characteristics, such as the external gills and aquatic housing environment [20, 22]. If metamorphosis is induced by thyroid hormones (artificially), the axolotl will undergo heavy physiological changes to become a terrestrial salamander, similar to the tiger salamander (*Ambystoma tigrinum*, Fig

6.1D) [15]. It will maintain its regenerative potential, but at a reduced rate and fidelity [20]. Still, the facultative metamorphosis of axolotls offers us a way to study its effects on anatomy, physiology, and regeneration [23].

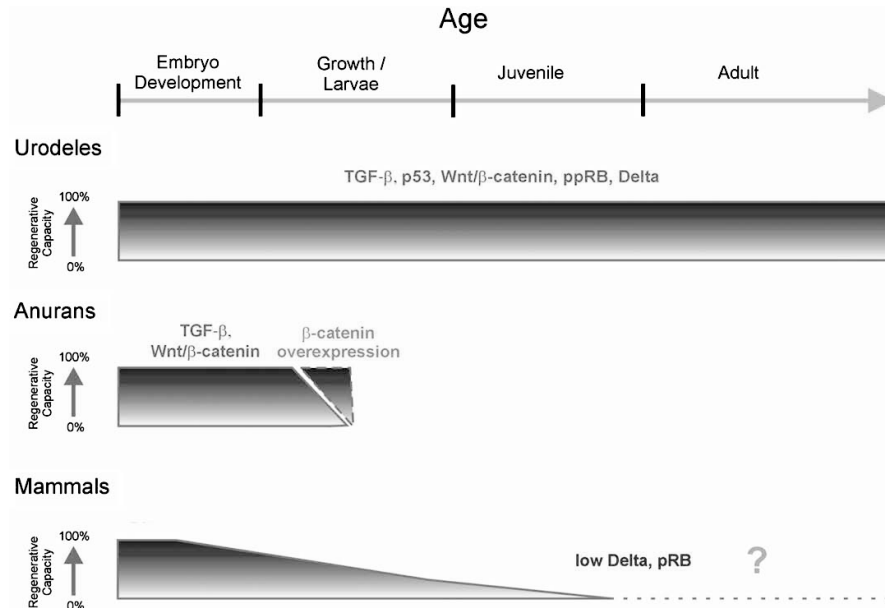


Figure 6.2 Lifetime regenerative capacity for mammals, urodele- and anuran amphibians. The anurans have a steep drop in regenerative ability during early stages of metamorphosis. Mammals lose most of their regenerative abilities before birth. Urodeles appear to maintain regeneration through life by maintaining certain gene expression patterns. Image reproduced from [9].

The molecular and genetic pathways of axolotl limb and tail regeneration have been extensively analysed by molecular and cell biology techniques such as immunoblotting and quantitative polymerase chain reaction, and the morphological changes by histology, microscopy and genetically modified axolotls expressing e.g. fluorescent proteins [24-31]. The axolotl is capable of regenerating nearly every structure of its body, including parts of the heart, forebrain, spinal cord and entire limbs when enough tissue remains intact [32-35]. This is achieved by the formation of a diverse pluripotent progenitor cell pool by dedifferentiation of existing cells and migration of resident stem cells [36-38]. This pool is referred to as the 'blastema' and is highly similar to the growth bud in embryonic development (Fig. 6.3).

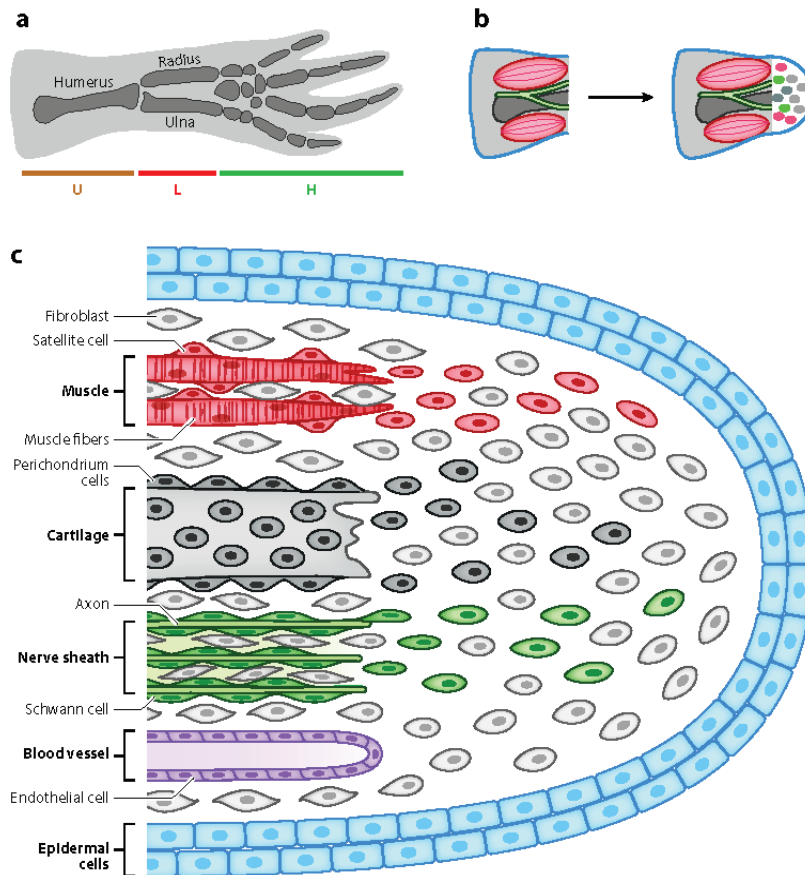


Figure 6.3 Segments of an axolotl front limb; hand (H), lower arm (L) and upper arm (U) (a). Formation of a blastema underneath the wound epidermis, after limb amputation (b). The contribution of different cell types to the blastema cell pool (c). Image copied from [38].

In 2004, Endo *et al.* described the stepwise model for limb regeneration (Fig.6.4) describing the different signals required for progression to the next stage of development and the possible (detrimental) outcomes when one of these signals is not present [39]. One possible detrimental event of an interrupted or absent signal (e.g. a deviated nerve) is the abrupt end of limb regeneration, resulting in the formation of a stump. The regenerative process can roughly be divided in three major phases: wound healing, dedifferentiation and redevelopment [36, 37]. The last phase is further subdivided into the early bud, medium bud, late bud, palette and outgrowth stages [37]. Interestingly, the blastema cells already receive information on their final identity and position as early as three days post-amputation/wound [25]. New structures are placed in a proximal to distal direction, using the remaining tissue as a scaffold [28, 40, 41]. Nerves are one of the first structures to regrow, as the regenerative process is highly dependent

on nerve signals [36]. Blood vessels are the second structure to regenerate, being restored through an angiogenesis-like process [36]. The next step is restoration of bone and muscle [36]. A skeleton will be formed from cartilage-like cells. Ossification into actual bone may occur later [42]. Grim & Carlson showed that forelimb muscle regenerates in a proximo-distal gradient, and later in a radio-ulnar gradient (in the case of a limb) [43]. In other words, the upper arm will form first, then the hand, and the thumb is the first digit to appear. As for tail regeneration, a similar proximo-distal pattern is seen in which muscle sections (myotomes) will finalize proximally while the outgrowth of the blastema continues distally [24].

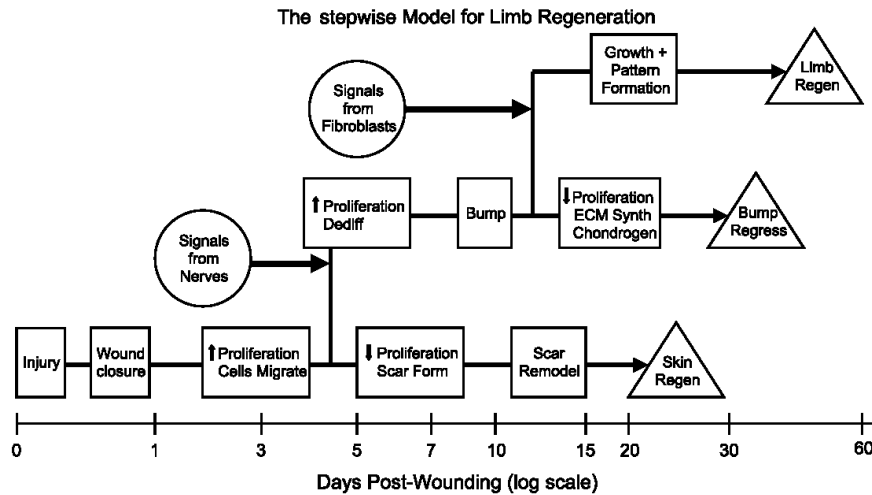


Figure 6.4. Stepwise model of axolotl regeneration, as presented by Endo *et al.* [39]. Lack of required signals can lead to a variety of detrimental outcomes.

The time it takes for lost structures to return depends largely on age. In 2014, Monaghan *et al.* [20] investigated the effects of age and development stage on regeneration and found that three month old axolotls completed regeneration in approx. 66 days, whereas nine month olds only regenerated approx. 56% of the lost structures at this point. However, it remains unclear if this difference is caused by the sheer mass that needs to be regenerated or if cell cycle pathways (rate of growth) are affected by aging.

A disadvantage of most of the aforementioned techniques used in developmental biology, e.g. histology, is that animals need to be sacrificed to acquire data. In particular, for longitudinal studies of regeneration, multiple animals have to be euthanized and thus it is not possible to obtain detailed information from all stages of regeneration from only one individual. Modern non-invasive *in vivo* imaging techniques, such as Magnetic Resonance Imaging (MRI) and Computed

Tomography (CT) allow repeated, high resolution and full body imaging of tissues *in vivo*. This gives the possibility to track the complete regenerative process in each animal. Lauridsen *et al.* published the first abstract depicting a study on axolotls where the fate of iron oxide labelled blastema cells were imaged with MRI in 2010, but surprisingly little has been published since then [44, 45]. Both CT and ultrasound (US) have shown their use in imaging cartilage and bone formation, but are seldom used in regeneration studies [46].

The heart is another topic of great interest in axolotls because they are able to regenerate it after injury [32]. The normal heart cycle of the axolotl is different from mammals [47] (Fig. 6.5). The salamander heart has only three chambers (two atria and 1 ventricle) but has a large sinus venosus (that disappears in post-embryonic mammals) that is part of the wave of contraction. The sinus venosus receives de-oxygenated blood and leads it into the right atrium. The common pulmonary vein shares its ventral wall with the sinus and lead oxygenated blood directly into the left atrium. The sinus then contracts causing blood to pass into the atria through the sinu-atrial junction. The septum of the atria consists of thin muscle extending from the cardiac walls of both atria. Blood is then pumped from both atria through the atrio-ventricular junction in the single chambered ventricle simultaneously. The endocardium lining the ventricular cavity extends into a muscular spongework inside the chamber that extends all the way to the epicardium. The axolotl does not possess coronary arteries and relies on the blood in the chamber to nourish the ventricular muscle. The inner muscle mass is responsible for most of the contractile function, and squeezes the blood into the bulbus cordis like a sponge. The bulbus and truncus arteriosus are considerably large and also contract to spread blood through the body. Oxygen-poor blood enters the ventricle slightly earlier than oxygen-rich blood and prefers the pulmonary arteries due to a lower resistance. The oxygen-rich blood then takes the remaining routes.

In 2010, Cano-Martínez *et al.* studied the heart function of axolotls *ex-vivo* after 10% of the ventricle wall was removed and allowed to regenerate for up to 90 days [32]. They found that the functional capacity of the heart would restore accordingly with the structural recovery of the myocardium. The axolotl heart was then proposed as potential *in vivo* model for underlying heart regeneration mechanisms in adult vertebrates. Imaging and measuring the cardiac function with MRI is an ideal technique, as is already done in mice [48]. These protocols will be essential in future studies involving the *in vivo* recovery of heart function after induced injury. At the time of writing this manuscript, an abstract from a congress was published where heart infarction was induced in axolotls and the cardiac function recovery followed with MRI and ultrasound [45].

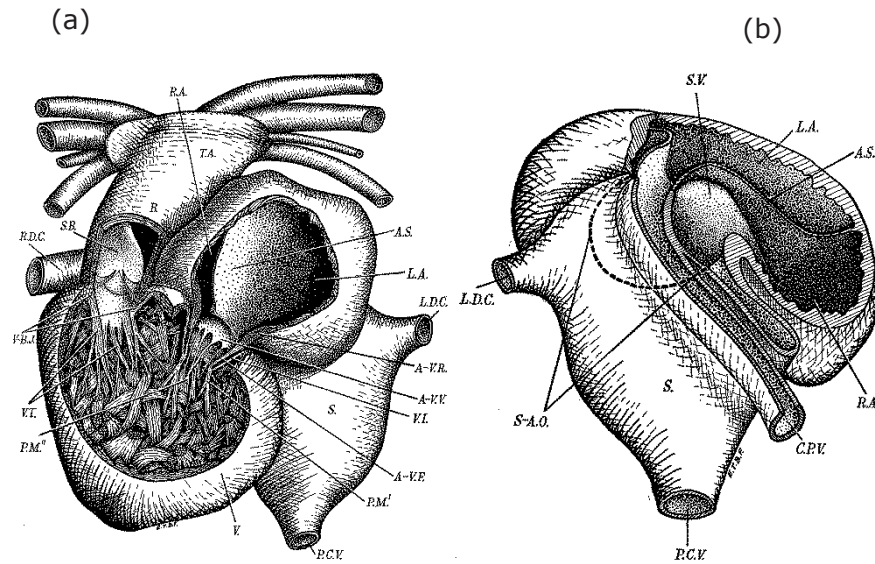


Figure 6.5 Salamander heart depictions. (a) Ventral view and (b) dorsal view. A.S. atrial septum; A-V.F. atrio-ventricular funnel; A-V.R. atrio-ventricular ring; A-V.V. atrio-ventricular valve; B. bulbus; C.P.V. common pulmonary artery; L.A. left atrium; L.D.C. left duct of Cuvier; P.C.V. post-caval vein; P.M'. pappilary muscles attached to A-V funnel; P.M". pappilary muscles attached to chordae tendinae of A-V valve; R.A. right atrium; R.D.C. right duct of Cuvier; S. sinus; S-A.O. sinu-atrial opening; S.B. septum bulbi; S.V. sinus valve; T.A. truncus arteriosus; V. ventricle; V-B.J. ventriculo-bulbar junction; V.I. ventricular invagination; V.T. ventricular trabeculae. Images copied from [47].

Aim of this study

In this study we have used both MRI and CT to non-invasively study two different processes of the axolotl *in vivo*: (1) regeneration of an amputated tail; and (2) heart anatomy and function. To study regeneration, the distal 3.5-4 cm of the tail were amputated and followed by (bi)weekly MRI and CT scans until full regeneration and function were achieved. The evolution of blood vessels, muscle, nerves, bone and cartilage was assessed. The heart was imaged with dynamic *in vivo* MRI scans to allow functional analysis, e.g. ejection fraction and cardiac output. In the end, the feasibility and future perspectives of non-invasive *in vivo* modern imaging techniques in regenerative medicine are discussed.

Materials and Methods

All reagents and solvents were obtained from Sigma-Aldrich and used without further purification, unless otherwise stated.

Axolotls and experimental plan

Fifteen Axolotls (14 golden- and 1 white-albino) were purchased from the Ambystoma Genetic Stock Centre[®] (Kentucky, USA). Three axolotls (golden) were selected for protocol definition and scanning parameters optimization for MRI and CT. In addition, these animals were used for anatomical and functional cardiac imaging with US and MRI. In our regeneration study; two axolotls (one golden, one white) had the distal 3.5-4 cm of their tails amputated. The anatomy during regeneration of these tails was then followed over respectively 2 and 3 months using MRI, CT and photography. Three axolotls were used for the heart function study. All experiments were performed on animals between 7 and 15 months old, weighing between 16 and 80 grams and a length (snout-to-tail tip) of 13 to 18 cm.

Animals were housed in individual tanks of 43.5 x 23 x 19.5 cm³ filled with 40% Holtfreter's Solution (HFS; 100% HFS: 3.46 g NaCl, 0.05 g KCl, 0.1 g CaCl₂ and 0.2 g MgSO₄·7H₂O in 1 L Toxivec[®] (Sera, Heinsberg, Germany) -treated tap water) in a dedicated aquarium setup (Fleuren-Nooijen[®], Nederweert, the Netherlands; supplementary information Fig. S1). Tanks were cleaned daily to remove faeces, dust, skin sheddings, bacteria and algae with an aquarium grade vacuum pump (Profi-Cleany, Europet-Bernina International[®], Iserlohn, Germany). Once a week, approx. 50-60 litres of HFS from the system were refreshed (10-12.5% of total volume). Axolotls were fed a diet of Axolotl/Newt Pro-Range laboratory grade pellets (Pollywog[®], Malvern, UK). Five small pellets (0.06 g) were given to small axolotls later replaced by two large pellets (0.24 g) once they were deemed large enough to swallow them. All animal experiments and procedures were approved by the ethical review committee of the Maastricht University Hospital (the Netherlands) and were performed according to the principles of laboratory animal care (US Committee on care and Use of Laboratory Animals [49]) and the Dutch national law "Wet op Dierproeven" (Stb 1985, 336).

Anaesthesia, recovery, and euthanasia

Anaesthesia was induced using an aqueous solution of benzocaine. A concentrated stock of benzocaine was first dissolved in absolute ethanol. All used benzocaine solutions were then dissolved in 40% HFS (buffered to pH 7.4 with NaHCO₃) to the appropriate concentrations (Table 6.1) before use, with a final EtOH concentration < 5%. The animal was placed in a container with a small layer of 0.02% benzocaine to induce anaesthesia followed by partial submersion with the anaesthetic solution. An animal was considered to be fully anesthetized when it did not attempt to turn-around for 30 seconds when placed on its back (turn-around reflex). Anaesthesia was maintained during the experiments with a lower concentrated benzocaine solution (Table 6.1). During the experiments the animals were completely wrapped in a Kimwipe (Kimberly-Clark, Irving, TX) soaked with the anaesthetic solution. Additional maintenance benzocaine was

periodically added to the Kimwipe during the experiments to maintain anaesthesia and hydration. A Minerve mouse bed (Equipment veterinaire Minerve®, Esternay, France) was modified to hold an axolotl and a layer of liquid for up to 5 hours (Fig. 6.6) was used for both the MRI and CT scans. When imaging the regeneration of the tail, the tail of the animal was laid on a plastic wedge in order to keep it flat and to align the spine (Fig. 6.7C). Visual markers, i.e. two glass capillaries filled with water, were placed under the wedge indicating where the tip of the tail should be positioned.

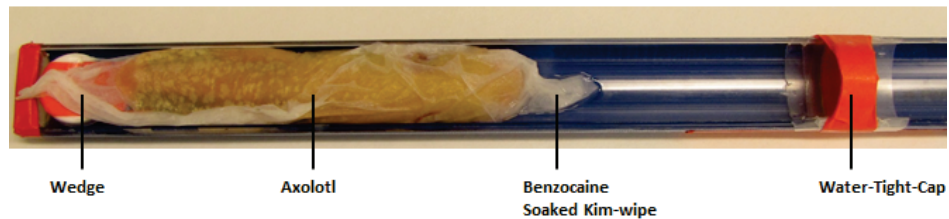


Figure 6.6 The modified Minerve® is a bed able to support one axolotl in both CT and MRI scanners. Parafilm®, tape and a plastic bottle cap were used to make the bed water tight.

The axolotl's heart beat was determined roughly every 35-45 min thereafter using either ultrasound (15 MHz linear array transducer, Philips ATL® HDI5000, Philips Healthcare, Best, the Netherlands) or the MRI. To recover the animal from anaesthesia the Kimwipe was removed and the animal gently washed with 40% HFS and then partially submerged in a layer of 40% HFS. An animal was considered sufficiently recovered (and thus able to return to its tank) once it was able to turn upright after being placed on his back (recovery of turn-around reflex). Animals were sacrificed using a 200 mg/kg body weight pentobarbital overdose injected intraperitoneally.

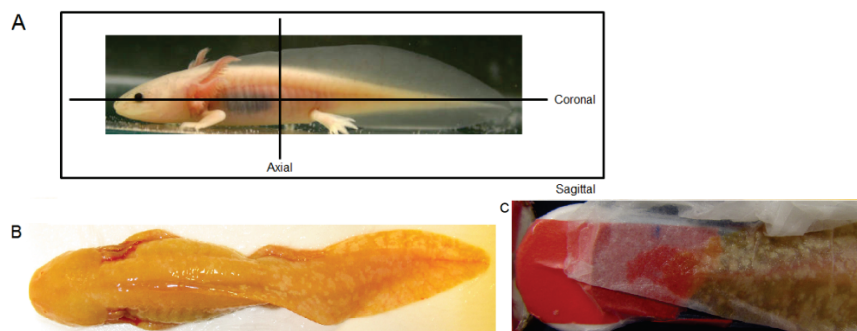


Figure 6.7 (A) Anatomical planes in normal axolotl anatomy. The black lines and box represent the slices made through the body in MRI. Out of the water, the axolotl's tail rotates 90° due to lack of support (B). It is important to note that when a sagittal scan is performed with MRI, the image represents a coronal section in normal anatomy. (C) On the

wedge the tail is laid flat and the elevation of the wedge ensures that the tail remained straight. The blue line marks where the tip of the tail was positioned. Two glass capillaries filled with water were placed underneath the wedge, to serve as a positional marker for MRI and CT scans.

Table 6.1. Summary of benzocaine concentrations used.

Axotl weight	Previous anaesthesia moments	Induction concentration (%)	Induction time (min)	Maintenance concentration (%)	Re-application time (h)	Recovery time (min)
≤ 30 g	≤ 4	0.02	10-15	0.01	2.5	10-25
	> 4	0.02	15-20	0.015	2.5	20-30
> 30g	≤ 4	0.02	10-15	0.015	2.5	20-30
	> 4	0.02-0.03	10-20	0.015	2.5	15-25

MRI imaging

MRI scans were obtained using a 1H 35mm Quadtransceiver radiofrequency coil (model 1P T9311, Bruker Biospin®, Ettlingen, Germany), inserted in a preclinical 9.4 T small animal MRI (Bruker BioSpec®). The anatomical planes of the axotl are presented in Fig. 6.7. For the tail images only, because the tail was rotated 90° the coronal anatomical axis corresponds to the sagittal axis from MRI images. General anatomy images (including the beating heart) were first acquired in non-amputated animals. In amputated animals only the tail area was imaged. An overview of used scans and their parameters can be found in Table 6.2. A RARE-T1 sequence was used to obtain a fast anatomical overview that served as a baseline for slice orientation, i.e. a coronal scan of the tail displayed the spine in such a way that the sagittal (coronal in anatomical axes, Fig. 6.7A) slices could be orientated to slice directly through the length of it. Higher resolution anatomical images were obtained with a TurboRARE-T2 sequence. During tail regeneration, we used a sagittal scan covering the distal 4.5 cm of the tail and an axial scan covering the regenerating and the healthy part of the tail (approx. 2 cm). Angiograms from the full body were obtained with a FLASH-TOF 2D flow compensated sequence. Diffusion Tensor imaging (DTI) was used on both control and regenerating tails to visualise the skeletal muscle fibre orientation. To analyse the cardiac function one heart was scanned with an Intragate-FLASH sequence in three perpendicular orientations. These orientations were defined according to the structural characteristics seen in the heart. One animal was scanned 4 consecutive times. In between each scan the animal bed was removed from the scanner and placed back slightly rotated. This way it was possible to verify if the standard orientations defined were reproducible. An INTRAGATE-FLASH sequence was also used as a method for measuring the axotl heartbeat [50].

Table 6.2. List of MRI scans and their parameters. (AVG = average(s); FOV = field of view; HQ = high quality; ID = inter-slice distance; LQ = low quality; MQ = medium quality; ST = slice thickness; TE = echo time; TR = repetition time).

	TR (ms)	TE (ms)	AVG	FOV (cm)	Matrix	Voxel size (µm)	ST (mm)	ID (mm)	# of slices	# of repetitions
RARE-T1	700-2000	8.5	1	4.5*2	256*256	176*78	0.5	0.55	20-50	1
TurboRARE-T2	450-6000	36	4	4.5*2 or 3*2.5	384*384	117*53 or 78*56	0.55	0.55	40-50	1
FLASH-TOF 2D-flow comp	18	4	4	3*3	256*256	117*117	0.4	0.25	120-150	1
TurboRARE-3D	1500	45		3*3*4	256*256*128	117*117*312	40	0.31	1	1
disc SE DTI 10 directions	2500	20.4	1	4.5*3	256*128	176*234	0.5	0.55	11	1
INTRAGATE-FLASH LQ	6	2.9	1	3*3	192*192	156*156	1	N/A	1	100
INTRAGATE-FLASH MQ	6	2.9	1	3*3	256*256	117*117	1	N/A	1	250
INTRAGATE-FLASH HQ	6.7	3.2	1	3*3	384*384	78*78	1	N/A	1	250

CT imaging

The axolotl skeleton was imaged using a small animal NanoSPECT/CT™ scanner (Mediso Medical Imaging Systems Ltd., Budapest, Hungary). The following parameters were used: 45 kVp, 2000 ms per projection, 360 projections, pitch of 1 and ultrafine setting.

Amputation

Anaesthesia was induced and maintained with 0.02% benzocaine during the whole procedure. The axolotl was subcutaneously injected with buprenorphine (14 mg/kg body weight) and gentamycin (2.5 mg/kg body weight, repeated every 72 h for 15 days, intramuscular). The animal was placed under a dissection microscope (Leica MZ6, Leica Microsystems®, Wetzlar, Germany) and a cut was made 3.5-4 cm from the tip of the tail using a #22 Swann-Morton scalpel in a single smooth motion. The wound remained untouched for the next ten minutes, allowing the bleeding to stop naturally. The animal was then recovered from anaesthesia.

Image/data processing

The MRI RARE-T1, TurboRARE-T2, and INTRAGATE-FLASH scans were analysed using the software ParaVision® 5.1. Angiograms (FLASH-TOF scans) were processed with Mathematica® (Wolfram, Oxfordshire, UK), which produced a maximum intensity projection (MIP) image from the raw data. The DTI images were processed with Mathematica® and then loaded into vIST/e® (Imaging Science and Technology Eindhoven group, TU/e, Eindhoven, the Netherlands) for fibre tracking analysis. Functional heart data was analysed with QMassMR 7.6® (Mediso medical imaging Systems): first, the inner ventricle walls at systole and end diastole stages were delineated. The software automatically calculated the respective volumes. Ejection fraction was defined as the difference between end diastolic volume and systole volume divided by end diastolic volume. The cardiac output was defined as the product of the ejection fraction and the heart rate. CT scans were reconstructed and processed using the vendor's own software (InVivoScope® 2.00, BIOSCAN Inc., Poway, US). Statistical analysis using One-way ANOVA was performed with a significance of 0.05 (using SPSS, IBM).

Results

General anatomy imaging

Figures 6.8-6.10 show anatomical images acquired with MRI. The T2-weighted scans had a higher resolution than the T1-weighted which allowed a better distinction between different anatomical structures (Fig. 6.8A-B). The heart and the major blood vessels were easily seen in the angiograms (Fig. 6.8C). In contrast, the majority of the smaller vessels and capillaries were not seen by angiography even though they were visible to the naked eye.

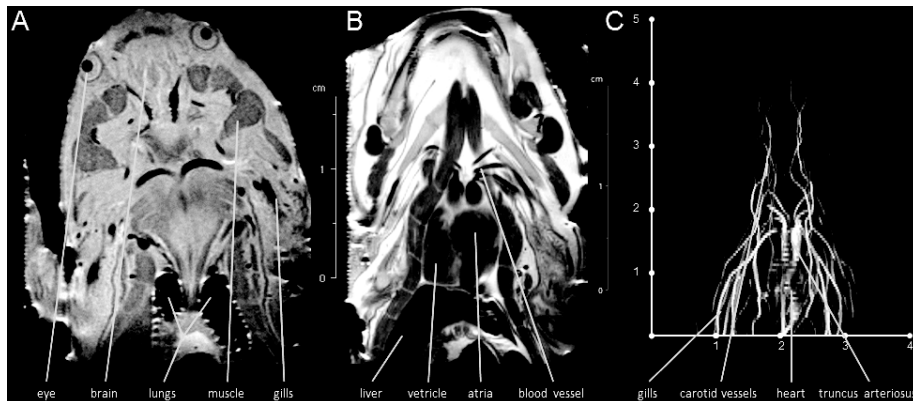


Figure 6.8 Anatomical scans. In all panels the snout is at the top and the rest of the body is at the bottom. (A) a coronal T1 weighted image of the head where the eyes and the two nostrils in between are visible. The black regions below the (fore)brain seem to be part of the skull. The packs of muscle seen to the lateral sides of the head are most likely involved

in moving the jaw [51]. The (semi)circular black structures with clearly defined borders are blood vessels. The two larger ones in the centre (1 cm above the lungs) are leading out of or in to the heart, whereas the ones on the side are in the gills; (B) a coronal T2 weighted image of the head, showing the heart, part of the liver and muscle lining the body cavity (long semi-vertical grey structures to the left and right of heart). Different compartments of the heart can be defined, as well as the truncus arteriosus (immediately above the ventricle and atria) and blood vessels leading into the body. The black streak at the top of the image is part of the jaw; (C) an angiogram of the head, showing the heart, carotid vessels and the gills. Movement artefacts slightly distort the heart. The gills can be identified as groups of large vessels to the side of the body. These large vessels sprout into many small capillaries (the frilly part of the gills) and exchange oxygen directly with the water [51]. The carotid arteries and veins can be seen projecting upward from the heart into the head (C). Scale bars are in cm.

Organs such as the liver, stomach (with food pellets inside), heart, gills, brain, aorta and the spine are all shown in Figure 6.9. The characteristic myotomes (muscle ridges perpendicular to the spine, Fig. 6.7A-B) along the trunk of the axolotl are visible in Fig. 6.10A. Images of the limbs were also obtained (Fig. 6.10 A-C). Obtaining an image orientation where a whole limb is seen (humerus to finger tips) was not achieved. The use of a 3D scan allowed to get such an imaging plane however a compromise in image resolution had to be made to compensate the otherwise not practical scan time (hours). Interestingly, in the axial slices (Fig. 9C-D) it is possible to distinguish what appear to be individual skin glands. The tail was easy to align while lying on the inclined plastic wedge (Fig. 6.10). In both T1-weighted coronal and T2-weighted sagittal images blood vessels, spine, and muscles could be seen (Fig. 6.10D-E, respectively). Fiber tracking was performed on the tail and it showed a prevalence of muscle fibers oriented in a cranial to caudal direction. The spinal nerve bundle was also visible.

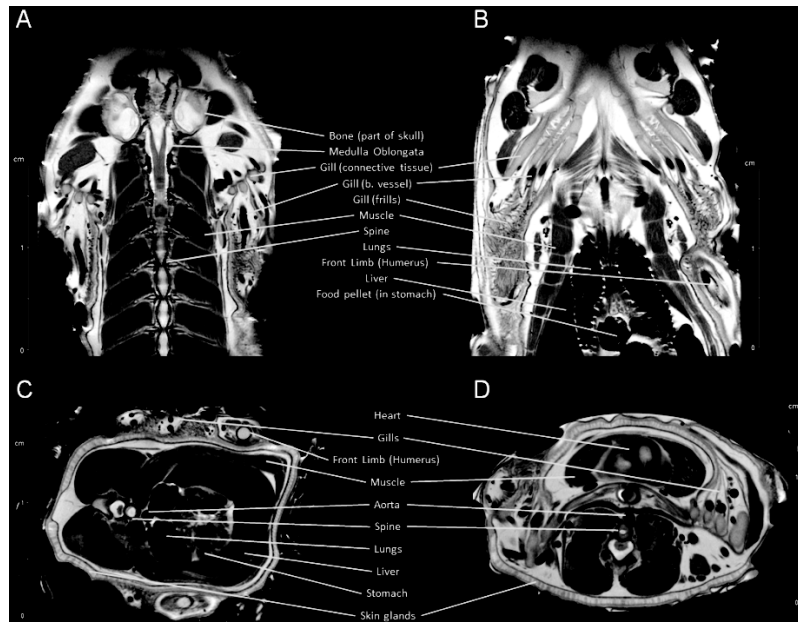


Figure 6.9 T2-weighted scans of the axolotl head and upper body. (A) the back muscle is clearly defined in myotomes aligned with the spine (with ribs in between). The nerve bundle branches into left and right shortly after the spinal cord begins; (B) the gills have connective tissue and muscle at the base (responsible for their movement) and thick blood vessels running through them, the frilly part (consisting of many small hair like vessels) is also visible. Part of the stomach is seen, with intact food; (C) the spine, upper arms, gills and muscle are easily distinguishable in the axial sections, and the skin is lined with round skin glands that secrete mucus to keep the skin slimy and hydrated (C+D). The gills are seen as a piece of connective tissue containing several blood vessels (C) and are still separated by a layer of connective tissue after they enter the body (D). The humerus of both front limbs is visible (C) as a lining of dense bone (black) with bone marrow in the centre (light grey). Panels A-B: snout on top and rest of body on bottom; Panel C – ventral side right and dorsal side down. Panels A – ventral side left; Panel D – ventral side up and dorsal side down.

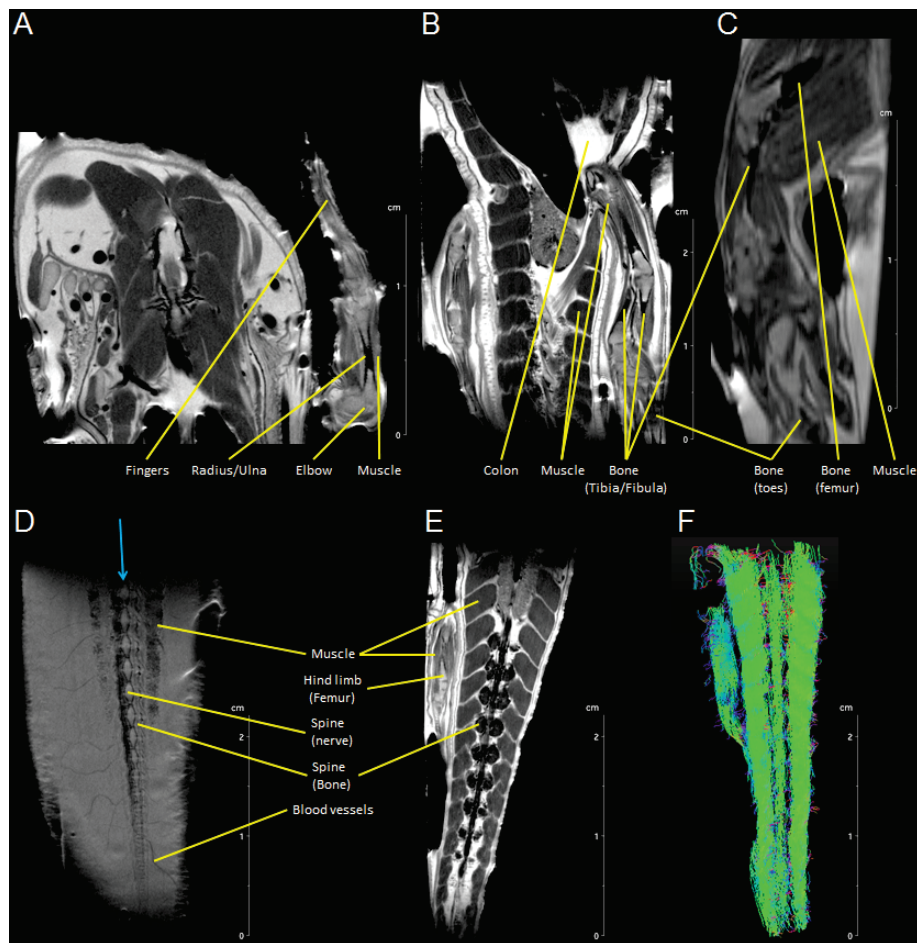


Figure 6.10 Anatomical scans of the front-, hind limb and tail. T2-weighted images of the front limb (A) and the hind limb are seen (B); (C) A 3D T2-weighted scan of the hind limb; (D) T1-weighted coronal scan of the tail. This scan was used to orientate sagittal slices parallel to the spine (blue arrow); (E) T2-weighted sagittal scan orientated from the blue arrow in (D). It displays the organized muscle sections, spine, and main blood vessels (not seen in this plane); (F) DTI fibre tracking of the axolotl tail. Fibres parallel (green) and perpendicular (blue) to the imaging plane are seen. The vertical nerve bundle in the middle

corresponds to the vertical black canal seen in (E). On the left side of the tail part of the hind limb is seen. Scale bar in the images is in cm.

An angiogram of the complete tail is presented in Figure 6.11. It was clearly seen that the thicker proximal half of the tail has an overall higher quality than the thinner distal part (Fig. 6.11A-B). Also, in the angiograms it was not possible to image the full vasculature of the tail since the smaller blood vessels were not visible (Fig. 6.11C vs. D).

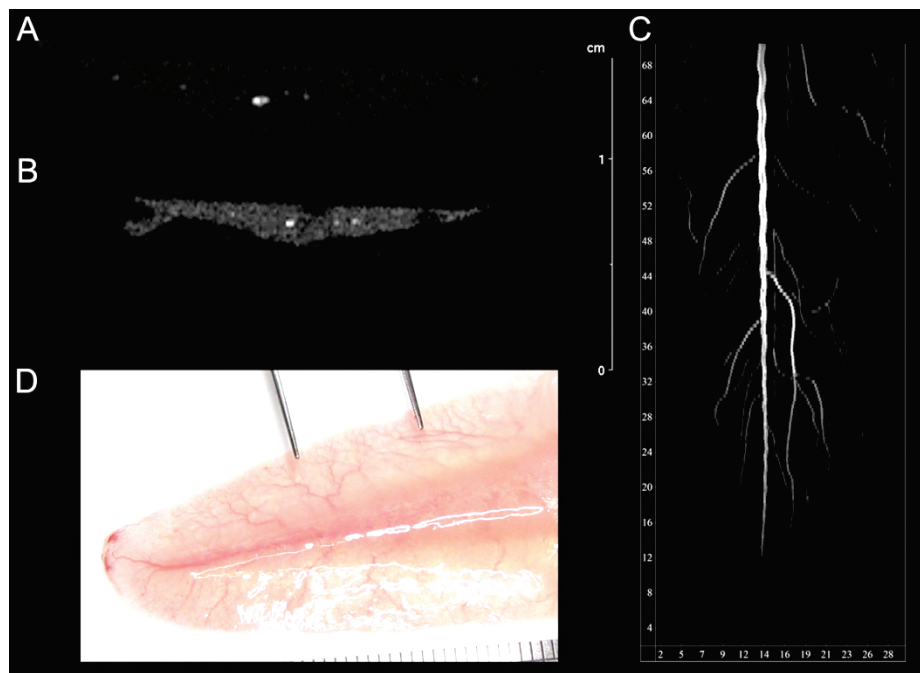


Figure 6.11 Example of processed angiogram data. Slices of a more proximal and thicker part of the tail (A) and a more distal and thinner part (B) are shown. (C) full maximum intensity projection angiogram after processing with Mathematica® (snout is up and caudal is down); (D) photograph of the distal 4 cm of another tail. Notice the amount of blood vessels visible by eye and compare with the panel (C). Scale bars in cm for panels A-C. In panel D two black lines represent 1 mm.

Figure 6.12A shows a full body angiogram. Most notably are the heart, gills, the carotid vessels, the aorta and vena cava. Additionally, the lower body shows larger vessels sprouting off the aorta and vena cava. These are likely providing blood to the urogenital tract [51]. The chest area also shows several larger vessels (next to the aorta and vena cava) that might be related to the lungs. In the CT scan (Fig. 6.12B) the most intense signals originate from four structures in the skull. The two positioned most posteriorly are probably part of the operculum, a bony flap at the base of the gills. The remaining two structures might be related to the jaw or part of the parietal bone. It is also possible that

these 4 dense structures form the otoliths (balance organs). The jaw appears denser than other structures as it contains three hundred teeth (not visible on the CT image). In contrast, the joints of the shoulder/hip, elbow/knee and wrist/ankle appear black on the CT, suggesting these are actually cartilaginous. In the front limbs, the phalanges and metacarpals are visible, but the carpal bones are not. The same is observed in the hind limbs. Lastly, the vertebrae become considerably smaller and less dense towards the tip, with the very end not showing on the CT.

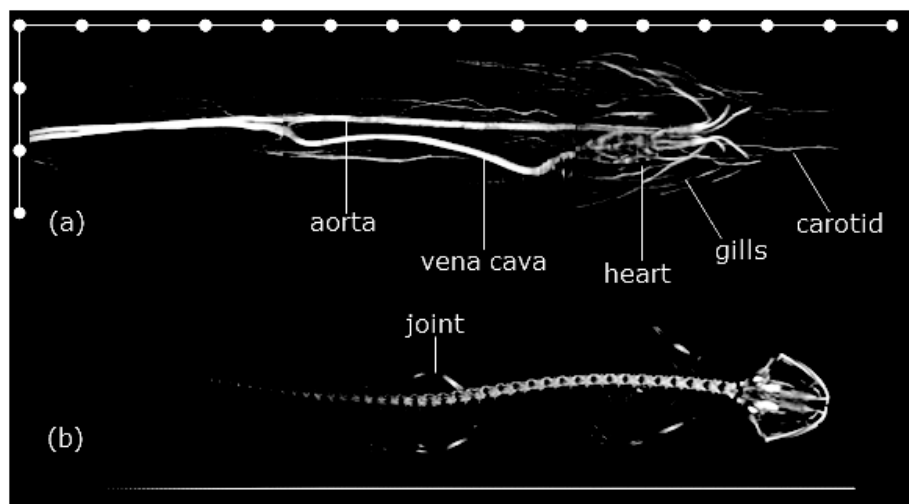


Figure 6.12 Full body scans. (A) montage of three angiograms showing the axolotl body from snout to cloaca (right-to-left). The heart, carotid vessels, gills, aorta and vena cava are identifiable. Some smaller (not as bright) vasculature is seen, presumably belonging to the lungs and urogenital tract; (B) CT scan of an 8 months old axolotl. The bone structures are generally not very dense, although exceptions include the teeth/jaw, sternum and four structures in the skull. Note how the joints appear black, indicating these structures are cartilaginous.

Imaging regenerating tails

Two axolotls had their tails amputated at 3.5 and 4 cm from the tip, respectively. The regeneration was followed with photography, MRI and CT over the course of 117 (axolotl 1, 11 months old) and 61 (axolotl 2, 12 months old) days (Fig. 6.13). Axolotl 1 regenerated a total length of 2 cm after just less than 4 months and axolotl 2 regenerated just over 1 cm in 3 months, which is approx. the same as axolotl 1 at this time point. During this period, axolotl 1 had a natural growth in length of approx. 69% and axolotl 2 of 33% (difference between the same two vertebrae inter-distance), which should be kept in mind when determining what the final length of the regenerate should be. In photography and MRI, a blastema started to protrude from the spinal cord around day 22 (axolotl 1) and 26 (axolotl 2) post-amputation. It grew distally and laterally and appeared to be vascularized [31, 37]. Larger vessel started

forming around day 40 p.a. A cartilage rod, i.e. the frame of cartilage on which the ependymal tube (dorsal) and aorta/vena cava (ventral) rest [31], originating from the spine grew distally into the tip of the tail. Later during regeneration (80 days p.a. on CT images), this cartilage rod would calcify to form the bone of the vertebrae in the spinal cord. The regenerating nerves of the spine use this rod as a scaffold but were not distinguished from it on the MRI images at that time. In contrast, the regenerating blood vessels are visible in T2-weighted images, although no distinction could be made between the aorta and vena cava on sagittal scans (Fig. 6.14). The vertebral discs became apparent on day 93 p.a., when dark formations appeared around the cartilage rod. Noteworthy, the final size of these vertebral discs is larger than the original, due to natural animal growth. Muscle appeared to regenerate laterally from the spinal cord from day 57 p.a. in axolotl 1, but it was smaller and could only be seen at day 61 p.a. in the axial scans for axolotl 2. The muscle grew out from the existing muscle tissue in a proximal to distal direction [14].

Angiograms of a regenerating tail are presented in Figure 6.13 and in greater detail in Figure 6.15. Regeneration of the vena cava and aorta becomes apparent at 35 days p.a., although distinguishing them from each other was not possible close to and distally to the amputation plane in the sagittal slices. Formation of blood vessels was only seen *after* the blastema was established. Some of the larger vessels also were not visible in all scans. For example, Figure 6.15 shows the aorta and vena cava down until the plane of amputation on day 4 p.a. On day 22 p.a., the most distal part has much less signal. Furthermore, some of the larger vessels sprouting out into the tail are not visible on every scan (i.e. Figure 6.15 day 4 compared to day 29). Many scans suffered from a high amount of noise. This was caused by an abnormally high intensity of surrounding tissues due to an absence or insufficient amount of signal from the blood vessels. This problem started occurring from day 107 (axolotl 1) and day 14 (axolotl 2) onward and appeared consistent in nature. Axolotl 1 still showed a considerable amount of regenerated blood vessels distal to the plane of amputation (approx. 1.5 cm), but didn't display the smaller vessels present in the blastema.

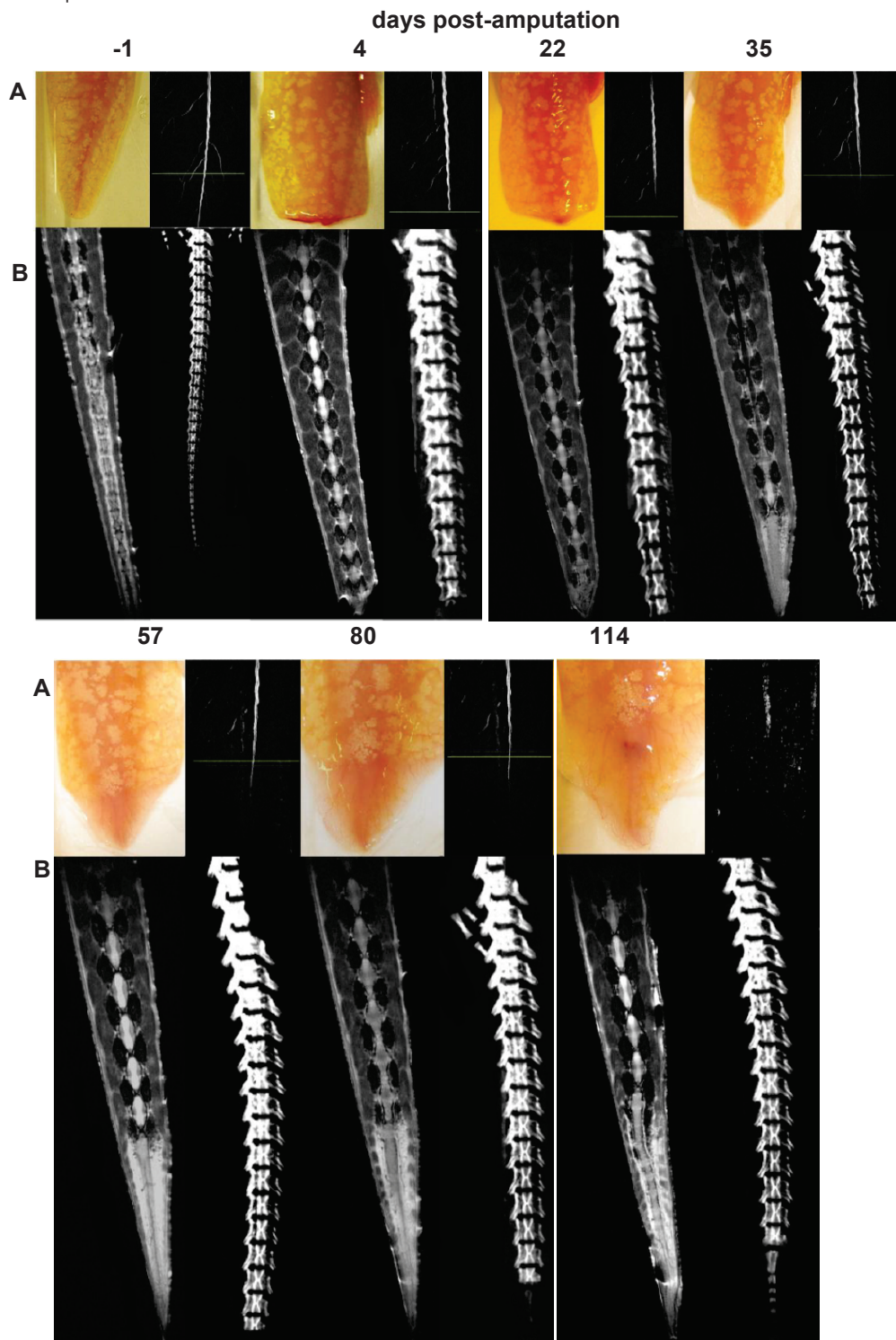


Figure 6.13 Tail regeneration of axolotl 1. (a) photographs (left) matched to MRI angiograms (right), the plane of amputation is represented by the green bar; (b) T2 weighted MRI (left) and corresponding CT (right) scans. New nerves and vasculature are seen from day 22 onwards. Muscle and calcified bone structures are visible from day 80. CT on day -1 is from a different axolotl of similar size.

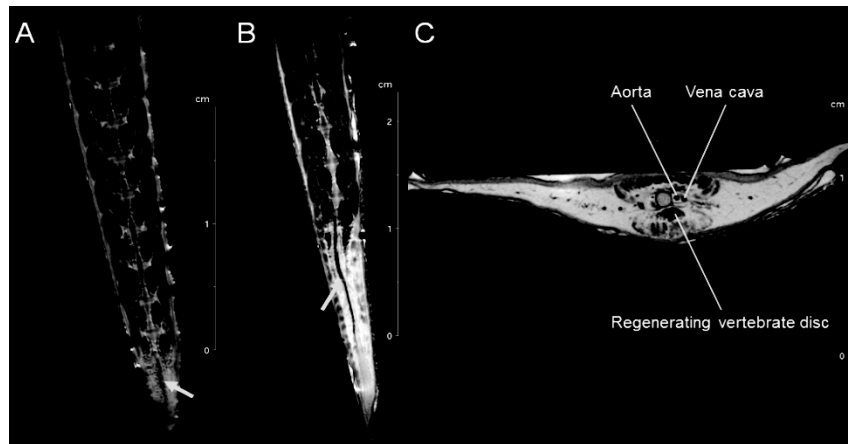


Figure 6.14 T2-weighted scans of axolotl 1's regenerating tail at day 29 p.a. (A) and day 114 p.a. (B). These are the same scans from Fig. 6.13, but on a different slice level. Here, the formation of the major blood vessel(s) (aorta and vena cava) in the tail becomes apparent (indicated by arrows). Small black dots (particularly noticeable in panel (A)) might indicate the small regenerating blood vessels of the blastema. In axial slices of the regenerating tail (here 114 days p.a.) the aorta and vena cava can clearly be distinguished (C). In addition, other blood vessels are noted as small black dots or streaks in the rest of the tail, not to be confused with the black lining around the cartilage rod or regenerating vertebrate discs (bone).

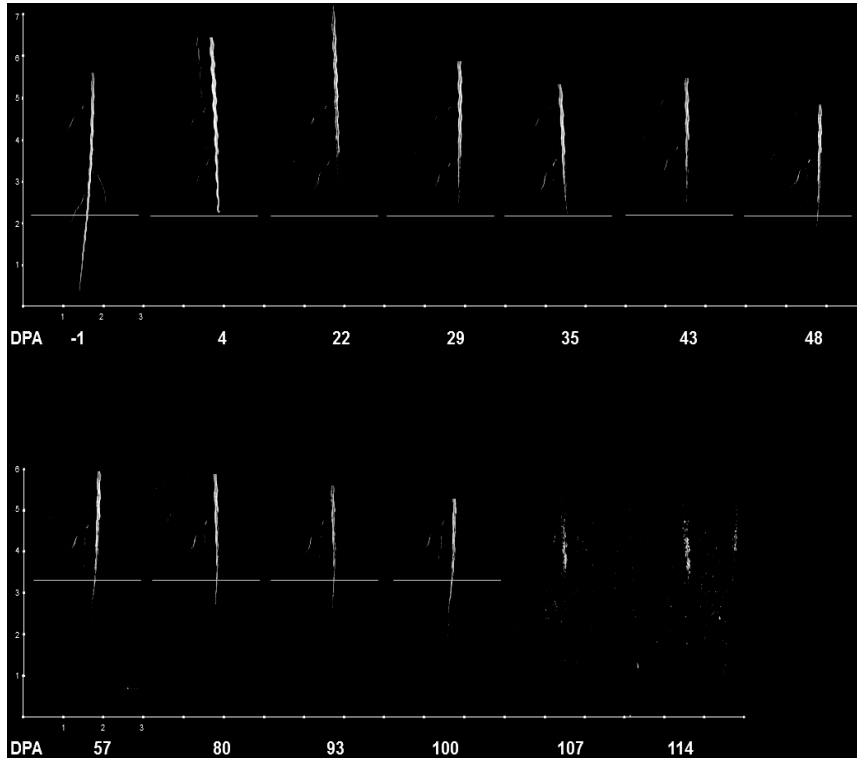


Figure 6.15 Angiogram of the regenerating tail of axolotl 1. The plane of amputation was estimated and indicated by a horizontal bar. Outgrowth beyond this plane was seen around day 35 p.a. and becomes more apparent on day 48 p.a. On day 107 and 114 p.a., the signal obtained belongs to surrounding tissue and no actual blood vessels were imaged. (DPA = days post amputation). Scale bars are in cm.

The appearance of ossified vertebrae was specifically imaged with CT. Axolotl 2 did not regenerate any bone within the observation period (not shown). As for axolotl 1, Figure 6.13 shows that the first calcified vertebrae arose around day 80 p.a. They appeared and grew in a proximal-distal direction. On day 107 p.a. calcification of spinous processes were seen for the most proximal regenerated vertebra.

In the axial T2-weighted images of the regenerating tail of axolotl 2 the cartilage rod can be seen over the whole regenerated structure (Fig. 6.16). A muscle lining formed laterally from the spinal cord (indicated by yellow arrows), and matured (and forms myotomes) in a medial to lateral direction. The proximity of the muscle to the nerve canal depends on the presence of a vertebral disc, e.g. in the healthy 61 DPA slice the muscle is separated from the nerves by a vertebral disc (indicated by a pink arrow). Many black spots or small streaks are noted in the light grey tissue surrounding the centre of the tail. These are the many small blood vessels of the membranous part of the tail, which show up on

the T2-weighted scans around the same time as they can be noted by eye (day 20-26 p.a.). In contrast to the sagittal scans, the vena cava and aorta can be distinguished from each other. A more prominent example of this observation is presented in Figure 6.14. This rod appears to originate from the annulus fibrosus disci intervertebralis (intervertebral fibrocartilage) having a similar color in the MRI image. This is a similar finding as Echeverri *et al.*, who claimed that this rod forms in place of the larval notochord (which later becomes the nucleus pulposus, the gel-like substance surrounded by the fibrocartilage) and that the boundary between these two marks the plane of amputation [24].

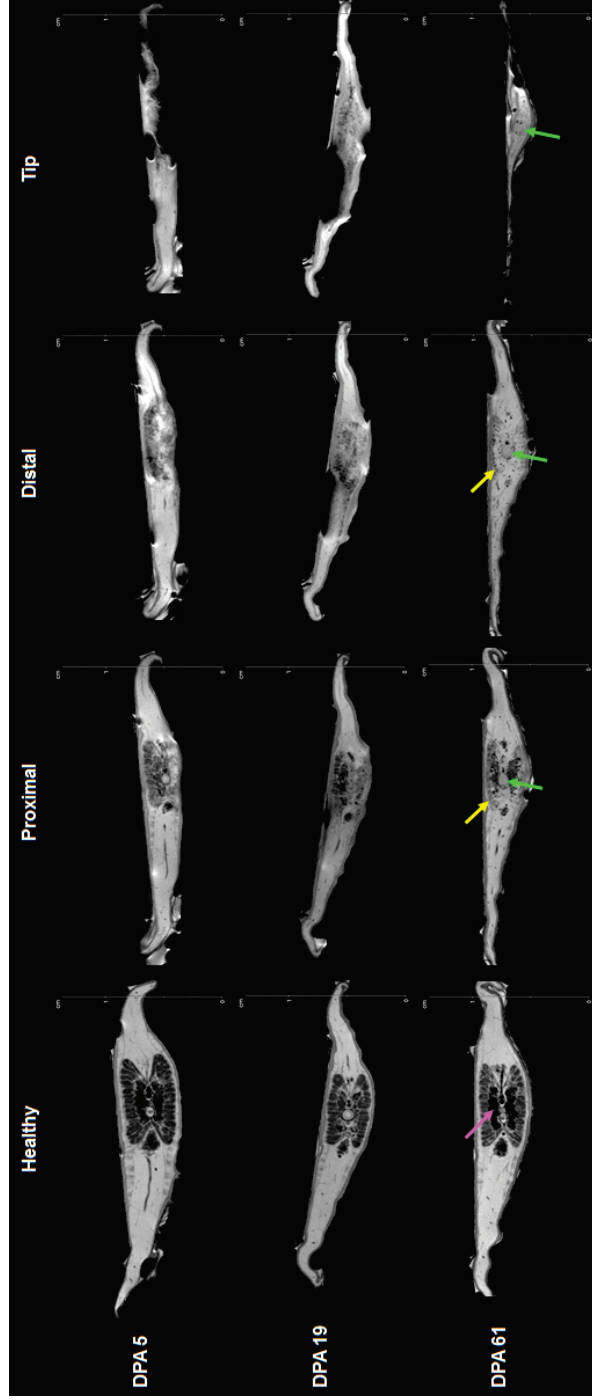


Figure 6.16 T2-weighted axial slices of axolotl 2's regenerating tail. At 5 days after amputation the tip is not defined yet; by 19 days after amputation, many black spots ('fragments') in the distal and tip slice are visible. These may represent small blood vessels present in the bud or maybe even groups of migrating cells (the actual blastema). The former is most likely true, due to the similar black coloration of existing blood vessels. At 61 days post amputation, the proximal slice shows the cartilage rod surrounded by early vertebral disc structures (black, either cartilage or bone) and fragmented muscle (dark grey). The vena cava and aorta are found ventral to the cartilage rod (to the right on the images). The distal slice shows only the cartilage rod, blood vessels and laterally regenerated muscle. The tip slice depicts a small cartilage rod and a few blood vessels. An interesting dark grey structure can be seen dorsally of the spine on healthy slices (to the left of the spine on these images). Dissection of a control animal showed this was a firm cartilaginous structure running from base to tip of the tail. (yellow arrow: muscle lining, green arrow: cartilage rod, pink arrow: vertebrate disc) (DPA = days post amputation, Healthy = normal tissue, Proximal = structures close to plane of amputation, Distal = structures located more distally from the plane of amputation, Tip = the last slice covering the very tip of the tail). Note that the Kimwipe can sometimes be seen at the edges of the skin, and typically causes artifacts especially in the tip slices.

Imaging the heart

The sinus is large and appears to function as a fourth chamber contracting in sequence with the other cavities (Fig. 6.17). A large mass of contracting muscle was seen inside the ventricle. This mass resembled a sponge- or basketweave-like network of muscle [47]. The blood was seen seeping through the mesh to reach the edge of the cavity, most likely to supply the cardiac wall with nutrients [47, 52]. Lastly, we saw that the outer walls of the heart barely move during the cardiac cycle. This further supports the notion that most of the contractile function of the ventricle comes from the inner muscle network rather than the cardiac walls. The INTRAGATE-FLASH sequence was used to produce 25-frame movies with different orientations of the cardiac cycle (Fig. 6.17).

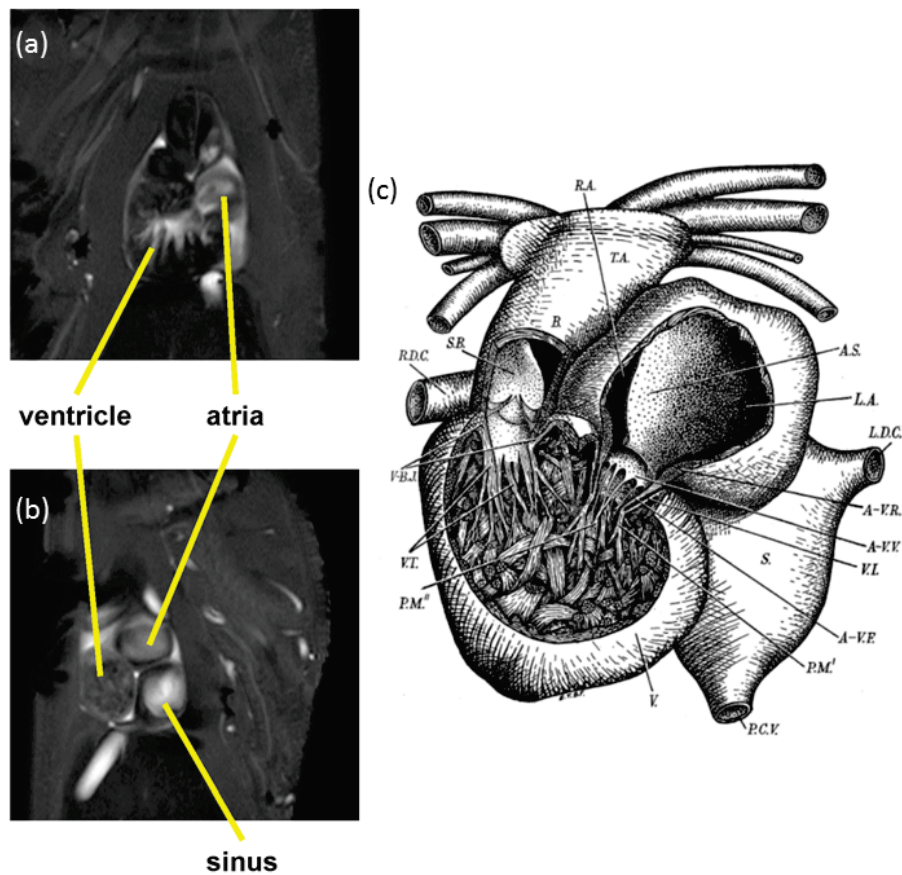


Figure 6.17 Intragate-FLASH scans of the heart. (a) coronal-oriented slice and (b) sagittal-oriented slice; (c) the salamander heart, as described by Davies and Francis [47]. Described in detail in Figure 6.5. Unlike mammals there are only three chambers (two atria (R.A.+L.A.) and one large ventricle(V.)), but the sizable sinus (S) appears to contract with the rest of the heart to pump blood into the atria. Separation of oxygen-rich and -poor blood happens purely on spatial position as the atria pump into the ventricle quasi-simultaneously. The

inner ventricle consists of a basket-weave-like network of muscle bundles. Most of the contractile power comes from this network, rather than the outer lining of the heart.

These initial scans allowed us to standardize the geometric axes used to obtain the image datasets from which the cardiac function analysis was made (Fig. 6.18).

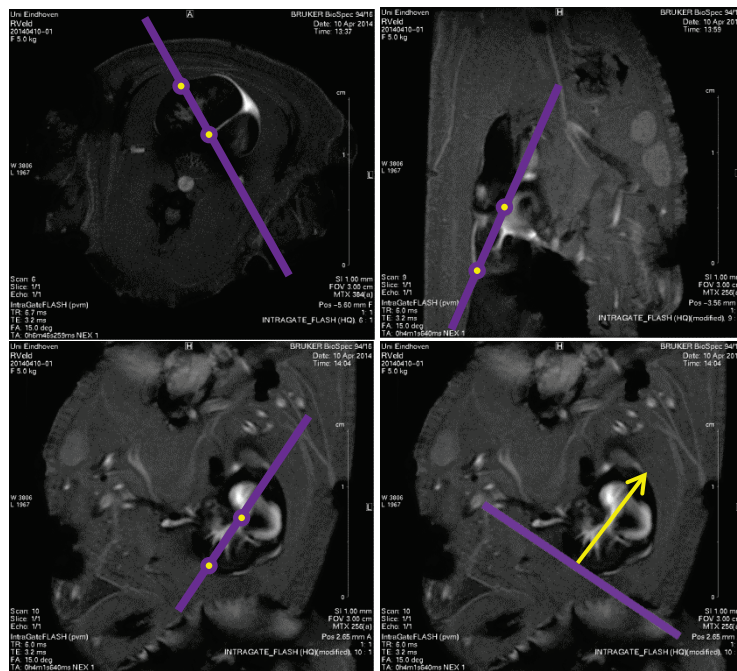


Figure 6.18 (A) apparent long axis: cuts the half-way mark of the ventricle on the top left side and the bottom of the V-S wall; (B) long axis 1 (perpendicular A): cut through apex and middle of heart; (C) long axis 2 (perpendicular to B): line through apex and atro-ventricular valve rotating the image to do so; (D) short axis: rotate previous line 90° and obtain the axial slice orientation.

The size difference of the inner muscle spongework of the ventricle during systole and diastole was used to calculate the ejection fraction, as this appeared to provide most of the contractile function. Indeed, this mass grew in size and became filled with blood during diastole and then contracted and shrunk to a much smaller size during systole (Fig. 6.19). The ejection fraction and cardiac output were defined for the first and second long axes, but not for the short axis series as the transition between ventricle and atria was not clearly definable. The results of this experiment are summarized in Table. No statistical difference was found between the ejection fraction calculated by the first and second axes ($p < 0.05$). This was valid for both within and between animals.

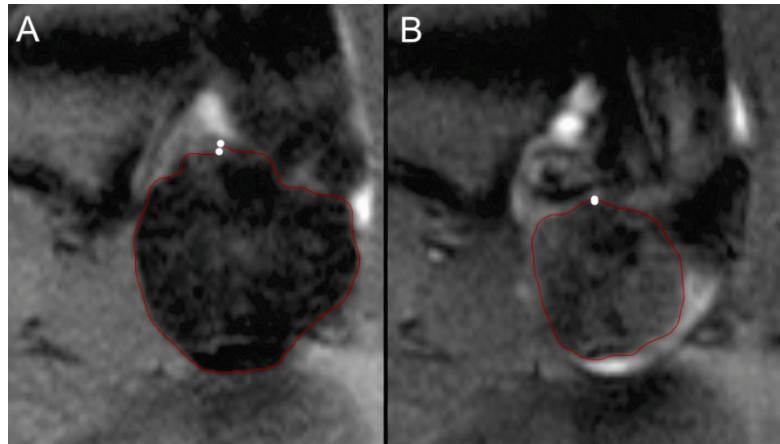


Figure 6.19 Definition of the inner heart muscle of the ventricle, in a long axis 1 INTRAGATE-FLASH scan. During diastole (A) the inner muscle mass of the heart is considerably larger than during systole (B). The red lining indicates the contours of the inner muscle mass (spongework).

Table 3. Ejection fraction and cardiac output of three axolotls, measured three separate times within one anaesthesia moment for both axes.

Animal	Iteration #	Heart Rate (bpm)	Ejection Fraction (%)				Cardiac output (mL/min)	
			Long axis 1	Mean \pm SD	Long axis 2	Mean \pm SD	Long axis 1	Long axis 2
1	1	42	65	64 \pm 5	51	52 \pm 11	76	31
	2	30	68		64		86	40
	3	27	59		42		51	22
2	1	41	54	57 \pm 8	36	49 \pm 12	46	36
	2	32	67		56		67	56
	3	26	51		56		51	56
3	1	38	61	66 \pm 5	70	64 \pm 8	63	50
	2	27	71		67		91	52
	3	28	65		55		84	33
Total means \pm SD			62 \pm 7		55 \pm 11			

Discussion

In this study we have shown that MRI and CT offer a feasible approach to monitor the regeneration of axolotls non-invasively, *in vivo* and longitudinally in single animals. Most anatomical structures of the tail and body (with exception of early regenerating nerves) were distinguishable with MRI. On axial slices it was possible to image individual skin glands. In fact, in a study by Holder *et al.* it was shown that the glands increase proportionally to the axolotl's length [53]. In our images the glands diameter was approx. 200 μ m from a 14 cm long animal and

in Holder's work a 13.5 to 16.5 cm animal would have glands ranging from 80 to 190 μm .

In contrast to the limbs, the tail was much larger and more practical to orientate. It proved difficult to image the early stages of regeneration (wound closure, formation of wound epithelium and AEC) due to the considerable small size of the wound. At 2 months post amputation the muscle seemed to regenerate in a medial to lateral fashion, and regained its natural orientation and organization proximally while the regenerative process continued distally. The axial slices of the regenerating tail emphasized the proximal to distal direction in the regenerative process, as the proximal slices always show a more advanced stage of regeneration compared to the distal and tip slices. The organization of muscle into myotomes was already observed as early as 57 days p.a. in axolotl 1 and became well defined by day 80 p.a. In addition, a ventro-dorsal gradient suggested in forelimb muscle regeneration was not seen in the tail [54]. The gradients of muscle regeneration in the fore and hindlimbs were studied in depth by Diogo et. al. [54] that only saw the ventro-dorsal gradient in the forelimbs. Our data seems to suggest that only the forelimbs have this gradient. In contrast, regenerated muscle was not seen in axolotl 2 at day 61 p.a. This could be explained by an age/size difference, as axolotl 2 was 1 month older at the day of amputation [20, 37, 55].

The regenerating spinal cord first projected a cartilage rod into the tip of the tail, which may be used as a support structure by blood vessels (aorta, vena cava) and nerves [31]. Calcification of new vertebrae was seen after three months p.a., but it was unclear if vertebrae formation started earlier than this (as cartilaginous discs). Innervation of the early blastema (< 30 days p.a.) was not seen with MRI. However, as nerve bundles (surrounded by CSF) of the spinal canal are easily distinguishable in healthy tissue, we expect to see regeneration of these structures at a later date. The fact that new blood vessels were only seen after the blastema was formed supports Mescher's notion that angiogenesis is suppressed until the blastema has formed [56]. In fact, the T2-weighted scans showed rich vascularization of the (early) blastema.

The angiogram scans were only able to display major vessels in the tail and were sometimes faced with reduced quality. The FLASH-TOF sequence saturates stationary tissue and relies on the inflowing blood to produce a fully relaxed T1 signal. Therefore, if blood flow is not fast enough in these vessels, it is possible that they remained saturated. The considerable loss of image quality in the regeneration study compared to the control animals can probably be attributed to a lack of detectable ^1H protons in the thin end of the tail. As the tail regenerated, the total volume in the field of view diminished due to the thinner regenerating part now occupying a larger percentage of the space. Possible solutions include further parameter optimization (with probable increase in scan time) and/or the use of contrast agents. The notion that blood vessels

regenerate by extension of existing ones in an angiogenesis-like process is supported by the fact that the main vessels of the regenerate sprouted from the aorta/vena cava and grew in length over time [36]. Coronal orientated scans were not made because the tail was too thin to obtain enough anatomical slices. Axial T2-weighted scans were added to the scanning protocol as they offered more insights into the regeneration stage for each tail section. In particular it was useful for describing the differences in proximal and distal regenerating structures. DTI did not become part of the standard imaging protocol due to its lengthiness (30 minutes). Still, it was performed sporadically to assess its feasibility in later studies.

The prospective heart study showed the different compartments and some of the unique characteristics of the axolotl heart. We were also interested in the possibilities of *in vivo* axolotl cardiac function imaging, and attempted to use MRI for the calculation of ejection fraction and cardiac output. The mouse cardiac protocols already defined within our group were not easily translatable to the three-chambered axolotl heart [47]. In the mouse method, the long and short axes of the heart are obtained. Cardiac function can then be retrieved by calculating the surface difference of the ventricle wall between systole and diastole. Therefore, standard axolotl heart axes had to be defined, as this had not been done previously. Only in a conference abstract published while writing this report did a group in Denmark state that MRI was used to follow cardiac function [45]. However, the methods used were not published. The outer cardiac wall appears stationary during contraction and most of the contractile power comes from an inner network of muscle in the ventricle. Calculation of cardiac functions, such as ejection fraction and cardiac output, is ongoing. The preliminary analysis showed that the measurements of ejection fraction for the two long axes that we defined were not statistically different. Also, during one anaesthesia moment the heart rate of the axolotl decreases substantially from approx. 50 bpm at rest to < 30 after approx. 4 h. This variability also compromised the analysis of the cardiac output and future studies to gather more data points at the same heart rates would be ideal.

This study sheds some light on the contributions that non-invasive molecular imaging can give to the fields of developmental biology and regenerative medicine. The use of molecular “bullets”, targeted to e.g. fibrin, angiogenesis markers, or ^{99m}Tc -MDP for bone activity, are examples of possible future studies.

Conclusion

In summary, we defined standard operating procedures for both the handling and scanning of axolotls in MRI, CT and US. We showed that the structures of regenerating axolotl tails are identifiable by MRI and that the calcification of newly regenerating vertebrae can be seen with both MRI and CT. In addition, we

have laid out the ground work for future metamorphosis studies in which we will image the changes of the axolotl body after metamorphosis and see how this transformation influences regenerative rate, capacity and efficiency. We believe that the clinical translation of amphibian regeneration is only a question of time and molecular imaging will be a fundamental tool to use at that moment.

Acknowledgements

We would like to thank the following people without which this research would not have been possible: David Veraard, Wolter de Graaf, Gustav Strijkers, Valentina Mazzoli, Rolf Lamerichs.

References

- [1] K.D. Poss, Advances in understanding tissue regenerative capacity and mechanisms in animals, *Nature reviews. Genetics*, 11 (2010) 710-722.
- [2] K. Ziegler-Graham, E.J. MacKenzie, P.L. Ephraim, T.G. Trivison, R. Brookmeyer, Estimating the Prevalence of Limb Loss in the United States: 2005 to 2050, *Archives of Physical Medicine and Rehabilitation*, 89 (2008) 422-429.
- [3] Annual Number (in Thousands) of New Cases of Diagnosed Diabetes Among Adults Aged 18–79 Years, United States, 1980–2011, Centers for Disease Control and Prevention (CDC), National Center for Health Statistics, Division of Health Interview Statistics, 2012.
- [4] N. Fausto, J.S. Campbell, The role of hepatocytes and oval cells in liver regeneration and repopulation, *Mech Dev*, 120 (2003) 117-130.
- [5] V. Kumar, A. Abbas, N. Fausto, R. Mitchell, *Robbin's Basic Pathology*, 8 ed., Elsevier, Chapter 3, 2007.
- [6] P. Seale, M.A. Rudnicki, A New Look at the Origin, Function, and "Stem-Cell" Status of Muscle Satellite Cells, *Developmental Biology*, 218 (2000) 115-124.
- [7] R.D. Brown, S.K. Ambler, M.D. Mitchell, C.S. Long, THE CARDIAC FIBROBLAST: Therapeutic Target in Myocardial Remodeling and Failure, *Annual Review of Pharmacology and Toxicology*, 45 (2005) 657-687.
- [8] G. Ertl, S. Frantz, Healing after myocardial infarction, *Cardiovascular Research*, 66 (2005) page 22-32.
- [9] S. Roy, S. Gatién, Regeneration in axolotls: a model to aim for!, *Experimental Gerontology*, 43 (2008) 968-973.
- [10] E.M. Tanaka, Regeneration: If They Can Do It, Why Can't We?, *Cell*, 113 (2003) 559-562.
- [11] A. Terzic, T.J. Nelson, Regenerative medicine primer, *Mayo Clinic proceedings*, 88 (2013) 766-775.
- [12] J.J. Song, J.P. Guyette, S.E. Gilpin, G. Gonzalez, J.P. Vacanti, H.C. Ott, Regeneration and experimental orthotopic transplantation of a bioengineered kidney, *Nat Med*, 19 (2013) 646-651.
- [13] B.A. Nasser, W. Ebell, M. Dandel, M. Kukucka, R. Gebker, A. Doltra, C. Knosalla, Y.-H. Choi, R. Hetzer, C. Stamm, Autologous CD133+ bone marrow cells and bypass grafting for regeneration of ischaemic myocardium: the Cardio133 trial, *European Heart Journal*, 35 (2014) 1263-1274.
- [14] C. McCusker, D.M. Gardiner, The Axolotl Model for Regeneration and Aging Research: A Mini-Review, *Gerontology*, 57 (2011) 565-571.
- [15] L. Adkins, *Keeping axolotls*, Interpet Publishing, 2009.
- [16] Founder John Clare, User 'Roz26', Axolotl hobbyist photographs of paedomorph tiger salamander and metamorph axolotl, in, 2010.
- [17] R. Denton, Tiger salamander photoshoot, posted on author's science blog, in, 2012.
- [18] User 'fishyguy', stock photo leucistic Axolotl for '2012 Amphibian Catalogue', in, 2012.
- [19] Valerie A. Tornini, Kenneth D. Poss, Keeping at Arm's Length during Regeneration, *Developmental Cell*, 29 (2014) 139-145.
- [20] J.R. Monaghan, A.C. Stier, F. Michonneau, M.D. Smith, B. Pasch, M. Maden, A.W. Seifert, Experimentally induced metamorphosis in axolotls reduces regenerative rate and fidelity, *Regeneration*, 1 (2014) 2-14.
- [21] J.W. Godwin, N. Rosenthal, Scar-free wound healing and regeneration in amphibians: Immunological influences on regenerative success, *Differentiation*, (2014).
- [22] R.B. Page, S.R. Voss, Induction of Metamorphosis in Axolotls (*Ambystoma mexicanum*), *Cold Spring Harbor Protocols*, 2009 (2009) pdb.prot5268.
- [23] J.R. Tata, Amphibian metamorphosis as a model for studying the developmental actions of thyroid hormone, *Biochimie*, 81 (1999) 359-366.
- [24] K. Echeverri, J.D.W. Clarke, E.M. Tanaka, In Vivo Imaging Indicates Muscle Fiber Dedifferentiation Is a Major Contributor to the Regenerating Tail Blastema, *Developmental Biology*, 236 (2001) 151-164.
- [25] K. Echeverri, E.M. Tanaka, Proximodistal patterning during limb regeneration, *Developmental Biology*, 279 (2005) 391-401.
- [26] M. Kragl, D. Knapp, E. Nacu, S. Khattak, M. Maden, H.H. Epperlein, E.M. Tanaka, Cells keep a memory of their tissue origin during axolotl limb regeneration, *Nature*, 460 (2009) 60-65.

- [27] L. Mchedlishvili, H.H. Epperlein, A. Telzerow, E.M. Tanaka, A clonal analysis of neural progenitors during axolotl spinal cord regeneration reveals evidence for both spatially restricted and multipotent progenitors, *Development*, 134 (2007) 2083-2093.
- [28] D.L. Stocum, J.A. Cameron, Looking proximally and distally: 100 years of limb regeneration and beyond, *Developmental Dynamics*, 240 (2011) 943-968.
- [29] M.A. Torok, D.M. Gardiner, J.-C. Izpisua-Belmonte, S.V. Bryant, Sonic Hedgehog (shh) expression in developing and regenerating axolotl limbs, *Journal of Experimental Zoology*, 284 (1999) 197-206.
- [30] E.V. Yang, D.M. Gardiner, M.R.J. Carlson, C.A. Nugas, S.V. Bryant, Expression of Mmp-9 and related matrix metalloproteinase genes during axolotl limb regeneration, *Developmental Dynamics*, 216 (1999) 2-9.
- [31] E. Schnapp, M. Kragl, L. Rubin, E.M. Tanaka, Hedgehog signaling controls dorsoventral patterning, blastema cell proliferation and cartilage induction during axolotl tail regeneration, *Development*, 132 (2005) 3243-3253.
- [32] A. Cano-Martinez, A. Vargas-Gonzalez, V. Guarner-Lans, E. Prado-Zayago, M. Leon-Oleda, B. Nieto-Lima, Functional and structural regeneration in the axolotl heart (*Ambystoma mexicanum*) after partial ventricular amputation, *Arch Cardiol Mex*, 80 (2010) 79-86.
- [33] M. Maden, L.A. Manwell, B.K. Ormerod, Proliferation zones in the axolotl brain and regeneration of the telencephalon, *Neural Dev*, 8 (2013) 1749-8104.
- [34] E.A.G. Chernoff, D.L. Stocum, H.L.D. Nye, J.A. Cameron, Urodele spinal cord regeneration and related processes, *Developmental Dynamics*, 226 (2003) 295-307.
- [35] C. Hutchison, M. Pilote, S. Roy, The axolotl limb: A model for bone development, regeneration and fracture healing, *Bone*, 40 (2007) 45-56.
- [36] S.V. Bryant, T. Endo, D.M. Gardiner, Vertebrate limb regeneration and the origin of limb stem cells, *Int J Dev Biol*, 46 (2002) 887-896.
- [37] P.W. Tank, B.M. Carlson, T.G. Connelly, A staging system for forelimb regeneration in the axolotl, *Ambystoma mexicanum*, *Journal of Morphology*, 150 (1976) 117-128.
- [38] E. Nacu, E.M. Tanaka, Limb Regeneration: A New Development?, *Annual Review of Cell and Developmental Biology*, 27 (2011) 409-440.
- [39] T. Endo, S.V. Bryant, D.M. Gardiner, A stepwise model system for limb regeneration, *Dev Biol*, 270 (2004) 135-145.
- [40] H.L. Nye, J.A. Cameron, E.A. Chernoff, D.L. Stocum, Regeneration of the urodele limb: a review, *Developmental dynamics : an official publication of the American Association of Anatomists*, 226 (2003) 280-294.
- [41] C.D. McCusker, D.M. Gardiner, Understanding positional cues in salamander limb regeneration: implications for optimizing cell-based regenerative therapies, *Disease models & mechanisms*, 7 (2014) 593-599.
- [42] F. Song, B. Li, D.L. Stocum, Amphibians as research models for regenerative medicine, *Organogenesis*, 6 (2010) 141-150.
- [43] M. Grim, B. Carlson, A comparison of morphogenesis of muscles of the forearm and hand during ontogenesis and regeneration in the axolotl (*Ambystoma mexicanum*), *Zeitschrift für Anatomie und Entwicklungsgeschichte*, 145 (1974) 149-167.
- [44] H. Lauridsen, N.B. Kjær, M. Bek, C. Laustsen, H. Stødkilde-Jørgensen, M. Pedersen, Visualisation of axolotl blastema cells and pig endothelial progenitor cells using very small super paramagnetic iron oxide particles in MRI: A technique with applications for non invasive visualisation of regenerative processes, in: 3rd international congress on stem cells and tissue formation, Dresden, Germany., 2010.
- [45] H. Lauridsen, M. Pedersen, Rebuilding a heart: complete regeneration after myocardial infarction in the axolotl (1151.1), *The FASEB Journal*, 28 (2014).
- [46] G.P. Kulbisky, D.W. Rickey, M.H. Reed, N. Björklund, R. Gordon, The axolotl as an animal model for the comparison of 3-D ultrasound with plain film radiography, *Ultrasound in Medicine & Biology*, 25 (1999) 969-975.
- [47] F. Davies, E.T.B. Francis, The Heart of the Salamander (*Salamandra salamandra*, L.), with Special Reference to the Conducting (Connecting) System and Its Bearing on the Phylogeny of the Conducting Systems of Mammalian and Avian Hearts, *Philosophical Transactions of the Royal Society of London. Series B, Biological Sciences*, 231 (1941) 99-130.
- [48] B.J. van Nierop, H.C. van Assen, E.D. van Deel, L.B.P. Niesen, D.J. Duncker, G.J. Strijkers, K. Nicolay, Phenotyping of Left and Right Ventricular Function in Mouse Models of Compensated Hypertrophy and Heart Failure with Cardiac MRI, *PLoS One*, 8 (2013) e55424.
- [49] U.S. Institute of Laboratory Animal Resources; Committee on Care and use of laboratory Animals, Guide for the Care and Use of Laboratory Animals: Eighth Edition, The National Academies Press, US Dept. of Health and Human Services, Public Health Service, Bethesda, Md., 2011.
- [50] E. Heijman, W. de Graaf, C. Diekmann, A. Nauerth, G. Strijkers, K. Nicolay, Retrospective CINE MRI of the mouse heart, in: *Proc. Intl. Soc. Mag. Reson. Med*, 2006, pp. 1209.
- [51] E.T. Francis, F.J. Cole, J. Hanken, The anatomy of the salamander, Oxford university press, 1934.
- [52] D.J. McKenzie, E.W. Taylor, Cardioventilatory responses to hypoxia and NaCN in the neotenic axolotl, *Respiration Physiology*, 106 (1996) 255-262.
- [53] N. Holder, R. Glade, Skin glands in the axolotl: the creation and maintenance of a spacing pattern, *Journal of embryology and experimental morphology*, 79 (1984) 97-112.
- [54] R. Diogo, E. Nacu, E.M. Tanaka, Is salamander limb regeneration really perfect? Anatomical and morphogenetic analysis of forelimb muscle regeneration in GFP-transgenic axolotls as a basis for regenerative, developmental, and evolutionary studies, *Anatomical record (Hoboken, N.J. : 2007)*, 297 (2014) 1076-1089.
- [55] H.E. Young, C.F. Bailey, B.K. Dalley, Gross morphological analysis of limb regeneration in postmetamorphic adult *Ambystoma*, *The Anatomical Record*, 206 (1983) 295-306.
- [56] A.L. Mescher, The cellular basis of limb regeneration in urodeles, *International Journal of*

Developmental Biology, 40 (1996) 785-795.

Supplementary Information

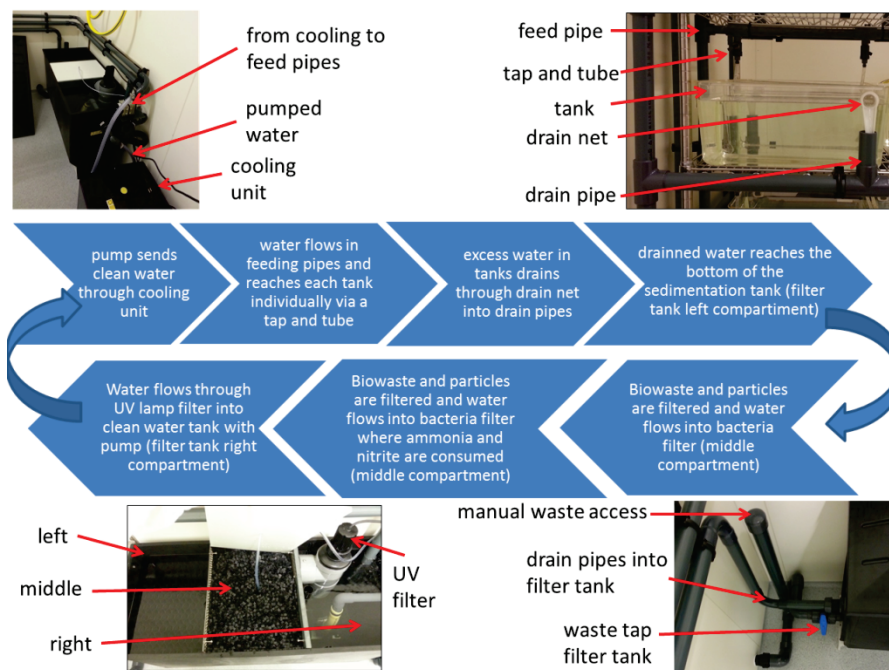


Figure S6.1 Dedicated axolotl aquarium setup. The pump sends filtered 40% HFS to each of the 16 tanks through a series of pipes (top right). Water flow is regulated per cage, and excess water is flows through a metal net and drains into the filter tank. Here, the water is cleaned by sedimentation (left compartment), biofiltration (middle compartment) and UV treatment (right compartment).

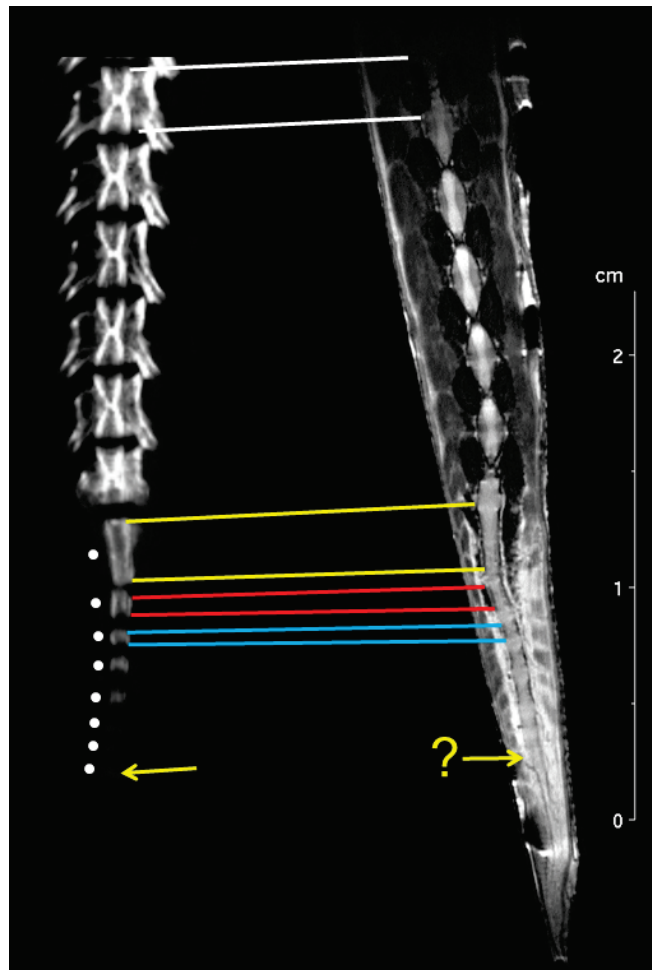


Figure S6.2 A side-by-side comparison of regenerating tail vertebrae on T2 and CT in axolotl 1 at 114 DPA. The white lines indicate the 6th healthy vertebral disc cranial to the plane of amputation. Yellow lines indicate the first regenerating disc caudal to the plane of amputation. The 2nd and 3rd regenerating discs are also indicated, with red and blue lines respectively. The 8 regenerating discs are marked with a white dot on the CT image. Note that the final three discs are barely visible, but were easily identifiable when the grey-scale is adjusted (over-exposing the image). The position of the 8th regenerating disc is pointed out by yellow arrows, but could not be identified on the T2 weighted image.



General discussion

Molecular imaging in drug delivery, oncology and regenerative medicine

Over the last decade, Molecular Imaging has been established as a powerful tool in preclinical and translational research to visualize and characterize biological processes at cellular and tissue level *in vivo*. In this thesis, Molecular Imaging is used to investigate research questions related to drug delivery, oncology and regenerative medicine.

Molecular imaging for application in ultrasound-mediated drug delivery

Chapter 3 and **4** of this thesis describe experiments, where Molecular Imaging is used to investigate US-mediated drug delivery. This research question is motivated by the fact that many potentially potent therapeutic drugs (e.g. nucleic acids or biologicals) are, upon injection, either too large or biochemically incapable of reaching their extravascular and intracellular targets but stay inside the blood pool. Ultrasound in combination with microbubbles has been proposed as a possible solution to this challenge as US-induced cavitation leads to a transient permeabilization of blood vessels (extravasation) and cellular membranes (sonoporation) allowing above drugs to extravasate and to pass cellular membranes. The transitory US-induced extravasation and sonoporation effects have been subject of intense research over the past decades. Since surprisingly little was known about the parameters important to US-mediated extravasation, we performed a set of US drug delivery experiments using skeletal muscle as a target organ for the site-directed delivery of an 8 nm model drug. **Chapter 3** describes a molecular imaging study using SPECT to follow and quantify the extravasation kinetics of the radiolabeled model drug after US exposure. The US-induced permeability allowed extravasation of the model drug, but was transient in nature and reduced with a half-life of approx. 21 min. At the same time of our study, Marty *et al.* presented a mathematical model to compute the closure time of the blood-brain-barrier after US-induced permeabilization [1]. The model considers the permeability of blood vessels as pores that are induced by cavitation and subsequently close with a certain rate. The model allows to predict the extravasation half-life for molecules as function of their hydrodynamic diameter. Interestingly, above model predicts for our model drug with a diameter of 8 nm an extravasation half-life of 27 min, which is well in agreement with the value measured in our study. There are important implications if we consider the inter-study variability of the US parameters, organs, and animal models used. First, we have used skeletal muscle and Marty *et al.* the brain as a target organ. Second, it has been shown that the US parameters greatly influence the permeabilization effect. For example, Hynynen *et al.* showed how an increase in US pressure from 1 to 3.3 MPa almost doubled the half closure time [2]. Third, higher amount of MBs leads to increased

endothelial gaps formation and thus more extravasation [3]. Fourth, a particle's extravasation level increases when the time between US delivery and the particle's presence in the bloodstream is shorter, independently of particle size (co-injection approach). We therefore proposed that the model of Marty *et al.* describes a tissue independent US-mediated extravasation mechanism, i.e. pores created by US, have the same closure half-life for different tissues given the same treatment conditions (US and MB).

Based on these findings we then explored the use of US in gene delivery. **Chapter 4** describes the use of optical imaging to quantify US-mediated gene transfection employing a plasmid that encodes for an optical reporter gene. Ultrasound-mediated gene transfection has been proposed as an alternative to virus-based gene delivery approaches. Viral vectors have the ability to cross cellular membranes and thus seem like an ideal carrier. However, viral vectors raise safety concerns about induced immune responses and the danger of insertional mutagenesis. This has led to the research of alternative carriers such as pDNA vectors, even though they cannot passively enter cells, are quickly degraded while in circulation, and typically suffer from low transfection levels. Several chemical modification approaches have been developed to protect these vectors and to facilitate their intracellular uptake such as complexation with cationic structures. However, this uptake is mainly nonspecific and toxicity concerns exist. Therefore, the use of US with MBs to noninvasively and locally deliver naked pDNA is an interesting solution. However, the parameter space in a US gene delivery scheme is large. Correspondingly, existing literature shows varying experimental conditions that hamper a comparison of the results. We therefore explored in **Chapter 4** the effect of different parameters on the efficacy of gene transfection *in vivo*. We have shown that the injected amount of MB is a determining factor in gene delivery. Moreover, the use of bolus injections instead of a continuous infusion allows to locally achieve much higher dose levels of MB that lead to higher gene expression levels. The results are also consistent with the finding presented in **Chapter 3**, as the number of cavitation induced pores in endothelial layers and most likely also in adjacent cells scales with the number of MBs. However, as cavitation can also induce tissue damage, gene transfection efficacy has to be optimized in view of adverse bioeffects.

Molecular imaging for application in oncology research

In **Chapter 5** we have applied the concept of reporter gene imaging using SPECT to study the formation of bone metastases. Bone metastases occur in about 70-80% of all patients suffering from solid tumors. These metastases are considered incurable leaving only palliative treatment to ensure a reasonable quality of life [4-6]. Thus, a better understanding of the process leading to bone

metastasis formation and their possible treatment is needed. We have used SPECT imaging to follow and quantify the formation of bone metastasis in a mouse. To that aim, we modified a breast cancer cell line to stably express the reporter gene HSV-1 TK. Subsequently, these cancer cells can be quantified *in vivo* with SPECT using the radiolabeled substrate [¹²³I]FIAU. After cardiac injection of these reporter gene expressing cells, SPECT could be used to follow bone metastasis formation. In a dual modality approach using SPECT/MRI the tumor volume measured by SPECT could be compared to volumes measured with MRI, showing a linear correlation between the SPECT and MRI data. However, SPECT imaging was able to find and quantify smaller lesions compared to MRI. Furthermore, the tumor caused a downstream osteolytic reaction in the surrounding bone leading to a degradation of the bone tissue as imaged with CT and μ CT. Additionally, we performed a pilot experiment where a radiolabeled liposomal doxorubicin formulation was injected in a mouse with bone metastases. Using dual-isotope SPECT/MRI it was possible to image the reporter gene expression from the metastases overlaid with the signal from the liposomes. The dual isotope data showed an accumulation of the liposomes in the tumor tissue of the lesion. The liposomal doxorubicin formulation is similar to the clinically used liposomal drug Doxil[®], which is prescribed to treat metastasized breast cancer.

Though not yet performed in our study, our data suggest that this multimodality imaging platform and mouse model could be used to quantify the bone metastases response to above drug treatment. More general, this molecular imaging approach could serve as a platform in the preclinical testing of new drugs, where FIAU uptake could be used as readout for cell viability, while MRI reports on the overall tumor volume.

Although the imaging modalities used are clinically translatable, the methodology of using reporter genes for imaging therapeutic responses is clinically challenging. The latter means that tumors would have to be transfected/transduced with the reporter gene before imaging, which is challenging with current technologies. Most likely, a viral approach is most suited at this point in time, however, this approach may raise immune response concerns. Nonetheless, clinical trials have been performed where a virus carrying the reporter gene was directly injected in gliomas [7, 8] and it was possible to image the gene expression noninvasively using PET and [¹²⁴I]FIAU. The prodrug ganciclovir (cytotoxic after interaction with HSV-1 TK) was also tested as a treatment option but the clinical response was poor [7]. The development of new reporter gene systems, ideally of human origin, is underway which together with the future progress in gene delivery methods is expected to create new treatment opportunities.

Imaging for application in regenerative medicine

In **Chapter 6** of this thesis, imaging is used to study tissue regeneration after injury *in vivo*. The physical healing process in humans following damage to an organ or even after an amputation leads to the formation of scar tissue, in most cases. This tissue does not possess the functional capacity of the healthy tissue, i.e. it represents an incomplete regenerative process. Consequently, there is a considerable body of research dedicated to solving this challenge including, but not limited to, bioengineering of new tissues, direct transplantations, stem cell implantation, and prosthesis. In the past centuries impressive progress has been achieved. For example, it took three centuries to go from the first (deadly) blood transfusions in the 17th century to the first successful heart transplant in 1967; and, nowadays, laboratory fabricated long lasting heart valves are regularly used [9, 10]. Currently stem cell applications are particularly important, as their potential to grow and/or stimulate functional regeneration of new organs has been recognized. Still, the current complexity associated with this approach asks for further research, or even for alternative solutions. On a fundamental level, research is needed to better understand how the full functional regeneration of a complex organ works. Fortunately, with salamanders, nature provides an inspiring example. The axolotl is an aquatic salamander capable of regenerating most organs (e.g. heart, brain, limb, tail, and kidney) throughout its lifetime. Their natural regeneration process depends on the accumulation of stem cells at the site of injury from which the new tissues originate. This process has been extensively studied, mainly with *in vitro* techniques. However, modern *in vivo* molecular imaging techniques have scarcely been used with this animal. In **Chapter 6** we performed an exploratory study on the capabilities of MRI and CT in imaging the regeneration of tails after amputation. The formation of the blastema and its evolution was visible by MRI over time. Also, the different regenerating structures (blood vessels, nerves, muscles, and vertebrae) could be distinguished. Blood vessels and the spinal nerve were the first regenerating structures visible followed by muscle and later the calcified vertebrae. In a parallel experiment MRI-based protocols for evaluating the cardiac function in axolotls were also defined. The imaging protocols establish the axolotl as an animal model to later study regeneration after a cardiac infarct. Understanding how a new tissue regenerates from the stand point of images obtained from preclinical noninvasive systems, although not yet applicable, will be a necessary step towards the clinical translation and follow up of a future hypothetical regenerating organ in humans [11-13].

Quo vadis?

Overall, molecular imaging has transformed our understanding of diseases and

therapeutic processes [14]. It represents a paradigm shift from imaging morphological and physiological (e.g. blood flow) properties of tissues to imaging specific cellular and molecular events [15, 16]. In preclinical research, it can be expected that even more molecular imaging approaches will be developed and tested in the context of biomedical and translational research as well as drug development. In a clinical setting, molecular imaging will provide *in vivo* information that will complement parameters obtained with *in vitro* methods (e.g. biopsy-based genomics or proteomics). Altogether, imaging based information will complement *in vitro* data for a more personalized patient treatment with high impact on overall patient management [17].

Personal note

Molecular imaging has only just begun to scratch the surface of its implications in the clinic and I am hopeful that within my lifetime it will be possible to store a digital snapshot of my full mind/memory for cloning purposes!

References

- [1] B. Marty, B. Larrat, M. Van Landeghem, C. Robic, P. Robert, M. Port, D. Le Bihan, M. Pernot, M. Tanter, F. Lethimonnier, S. Meriaux, Dynamic study of blood-brain barrier closure after its disruption using ultrasound: a quantitative analysis, *Journal of cerebral blood flow and metabolism : official journal of the International Society of Cerebral Blood Flow and Metabolism*, 32 (2012) 1948-1958.
- [2] K. Hynynen, N. McDannold, N. Vykhodtseva, F.A. Jolesz, Noninvasive MR imaging-guided focal opening of the blood-brain barrier in rabbits, *Radiology*, 220 (2001) 640-646.
- [3] M.A. O'Reilly, K. Hynynen, Ultrasound enhanced drug delivery to the brain and central nervous system, *Int J Hyperthermia*, 28 (2012) 386-396.
- [4] J.T. Buijs, G. van der Pluijm, Osteotropic cancers: from primary tumor to bone, *Cancer letters*, 273 (2009) 177-193.
- [5] G. van der Horst, G. van der Pluijm, Preclinical models that illuminate the bone metastasis cascade, Recent results in cancer research. *Fortschritte der Krebsforschung. Progres dans les recherches sur le cancer*, 192 (2012) 1-31.
- [6] K.N. Weilbaecher, T.A. Guise, L.K. McCauley, Cancer to bone: a fatal attraction, *Nature reviews. Cancer*, 11 (2011) 411-425.
- [7] A. Jacobs, J. Voges, R. Reszka, M. Lercher, A. Gossmann, L. Kracht, C. Kaestle, R. Wagner, K. Wienhard, W.D. Heiss, Positron-emission tomography of vector-mediated gene expression in gene therapy for gliomas, *Lancet*, 358 (2001) 727-729.
- [8] M.F. Dempsey, D. Wyper, J. Owens, S. Pimlott, V. Papanastassiou, J. Patterson, D.M. Hadley, A. Nicol, R. Rampling, S.M. Brown, Assessment of 123I-FIAU imaging of herpes simplex viral gene expression in the treatment of glioma, *Nuclear medicine communications*, 27 (2006) 611-617.
- [9] G. Orlando, K.J. Wood, R.J. Stratta, J.J. Yoo, A. Atala, S. Soker, Regenerative medicine and organ transplantation: past, present, and future, *Transplantation*, 91 (2011) 1310-1317.
- [10] T.E. Starzl, History of clinical transplantation, *World journal of surgery*, 24 (2000) 759-782.
- [11] I.Y. Chen, J.C. Wu, Molecular imaging: the key to advancing cardiac stem cell therapy, *Trends in cardiovascular medicine*, 23 (2013) 201-210.
- [12] H. Lauridsen, M. Pedersen, Rebuilding a heart: complete regeneration after myocardial infarction in the axolotl (1151.1), *The FASEB Journal*, 28 (2014).
- [13] A. Cano-Martinez, A. Vargas-Gonzalez, V. Guarner-Lans, E. Prado-Zayago, M. Leon-Oleda, B. Nieto-Lima, Functional and structural regeneration in the axolotl heart (*Ambystoma mexicanum*) after partial ventricular amputation, *Arch Cardiol Mex*, 80 (2010) 79-86.
- [14] R. Weissleder, A. Rehemtulla, S.S. Gambir, *Molecular Imaging: principles and practice*, PMPH - USA, Connecticut, 2010.
- [15] R. Weissleder, *Molecular imaging: exploring the next frontier*, *Radiology*, 212 (1999) 609-614.
- [16] E. Sala, H. Vargas, O. Donati, W. Weber, H. Hricak, Role of Molecular Imaging in the Era of Personalized Medicine: A Review, in: A. Luna, J.C. Vilanova, L.C. Hygino da Cruz Jr, S.E. Rossi (Eds.) *Functional Imaging in Oncology*, Springer Berlin Heidelberg, 2014, pp. 43-58.
- [17] A.D. Nunn, Molecular imaging and personalized medicine: an uncertain future, *Cancer biotherapy & radiopharmaceuticals*, 22 (2007) 722-739.

Ethical Paragraph

Chapters 3 and 4. The technique of ultrasound mediated drug delivery as such is especially related to new non-invasive therapeutic options in oncology, cardiology and regenerative medicine. Local gene delivery holds great promise to treat diseases at a genetic level rather than at phenomenological level. In this thesis methods for both drug delivery and gene delivery were developed.

Chapter 5. Cancer is one of the leading causes of death worldwide. According to the World Health Organization the number of deaths from cancer worldwide are projected to continue rising, with an estimated 13.1 million deaths in 2030 (www.who.int). Therefore, research to explore new cancer treatments is of utmost importance in order to improve the treatment efficacy and reduce the treatment burden on patients. In this thesis, a multimodality imaging platform for imaging bone metastases in small animals was developed.

Chapter 6. Many current therapies do not offer a complete cure but leave the patient partially disabled or with organs functioning at a reduced level. Exploiting and stimulating the body's own capabilities to regenerate tissue would decrease disease associated morbidity. Any fundamental insights on how these processes can be stimulated and applied in higher animals and finally humans present a medical breakthrough towards better medical care. The outlook of having developed curative approaches based on regenerative medicine and its impact on society outweighs in our opinion the discomfort of the animals in this study. As much as possible, all assays were developed and used *in vitro* avoiding unnecessary animal studies. However, for preclinical validation and clinical translation of the developed methods in this thesis, it is essential to gain knowledge about their behavior *in vivo*. For medical and ethical reasons, these new methods cannot be tested directly into humans; therefore the use of animal models was the only option for the final tests.

All preclinical studies performed for this thesis were approved by the animal welfare committee of Maastricht University (the Netherlands). For each experiment, the amount of animals used, as well as the discomfort they experienced, was weighed against the importance of the obtained data. The maintenance and care of the experimental animals was in compliance with the guidelines set by the institutional animal care committee, accredited by the National Department of Health.

Molecular imaging as a tool in drug delivery, oncology, and regenerative medicine

Summary

The aim of this thesis is to explore the use of Molecular Imaging to study processes related to drug delivery, oncology, and regenerative medicine.

In **chapter 1** the importance of Molecular Imaging in (pre)clinical research is reviewed and the imaging techniques used are introduced.

Site directed delivery of drugs remains one of the biggest challenges in pharmaceutical research to improve efficacy while reducing side effects. Many potentially potent therapeutic drugs (e.g. nucleic acids or biologicals) are, upon injection, either too large or biochemically incapable of reaching their extravascular and intracellular targets but stay inside the blood pool. Ultrasound (US) may offer a solution for this delivery dilemma. This approach is introduced in more detail in **chapter 2**. The pressure waves of US can drive circulating microbubbles (MBs), clinically used as US contrast agents, into a forced oscillation state inducing local transient permeability of the blood vessel endothelium (mediating extravasation) as well as cell membranes (sonoporation). The transitory US-induced extravasation and sonoporation effects have been subject of intense research over the past decades. **Chapters 3 and 4** describe experiments, where Molecular Imaging is used to study US-induced drug delivery and gene transfection, respectively.

Since surprisingly little was known about the parameters important to US-mediated extravasation, we performed a set of US drug delivery experiments using skeletal muscle as a target organ for the site-directed delivery of an 8 nm model drug. In **chapter 3**, Molecular Imaging with SPECT was used to follow the extravasation of the radiolabeled model drug from the vascular system subsequent to a sonication with focused US in the presence of MBs. The US-induced permeability allowed extravasation of the model drug, but was transient in nature and reduced with a half-life of approx. 21 min.

Based on these findings we then explored the use of US in gene delivery. Viral vectors have the ability to cross cellular membranes and thus seem like an ideal carrier. However, viral vectors raise safety concerns about induced immune responses and the danger of insertional mutagenesis. This has led to the research of alternative carriers such as pDNA vectors, even though they cannot passively enter cells, are quickly degraded while in circulation, and typically suffer from low transfection levels. Therefore, US-mediated gene transfection

Summary

has been proposed as an alternative to virus-based gene delivery approaches. However, the parameter space in a US gene delivery scheme is large and literature shows varying experimental conditions that hamper a comparison of the results. In **chapter 4**, US-mediated delivery of a genetic vector in the muscle tissue of mice is described, where optical imaging was used to localize and quantify gene expression. We have shown that the injected amount of MB is a determining factor in gene delivery. Moreover, the use of bolus injections instead of a continuous infusion allows to locally achieve much higher dose levels of MB that lead to higher gene expression levels.

Chapter 5 explores the use of Molecular Imaging in oncology to investigate the formation of bone metastases of breast cancer. These metastases are considered incurable leaving only palliative treatment to ensure a reasonable quality of life. Thus, a better understanding of the process leading to bone metastasis formation and their possible treatment is needed. To this aim, the concept of reporter gene imaging was extended to follow and quantify the development of bone metastases in mice using a multimodal SPECT/MRI approach. We have used a modified breast cancer cell line stably expressing the reporter gene HSV-1 TK. Subsequently, these cancer cells can be quantified *in vivo* with SPECT using the radiolabeled substrate [¹²³I]FIAU. After cardiac injection of these reporter gene expressing cells, the tumor activity measured by SPECT could be compared to volumes measured with MRI, over 40 days, showing a linear correlation between the SPECT and MRI data. However, SPECT imaging was able to find and quantify smaller lesions compared to MRI. Furthermore, the tumor caused a downstream osteolytic reaction in the surrounding bone leading to a degradation of the bone tissue as imaged with CT and μ CT. Additionally, we performed a pilot experiment where a radiolabeled liposomal doxorubicin formulation was injected in a mouse with bone metastases. Using dual-isotope SPECT/MRI it was possible to image the reporter gene expression from the metastases overlaid with the signal from the liposomes. The dual isotope data showed an accumulation of the liposomes in the tumor tissue of the lesion. The liposomal doxorubicin formulation is similar to the clinically used liposomal drug Doxil[®], which is prescribed to treat metastasized breast cancer.

In **chapter 6** of this thesis, imaging is used to study tissue regeneration after injury *in vivo*. The physical healing process in humans following damage to an organ or even after an amputation leads to the formation of scar tissue, in most cases. This tissue does not possess the functional capacity of the healthy tissue, i.e. it represents an incomplete regenerative process. Consequently, there is a considerable body of research dedicated to solving this challenge including, but not limited to, bioengineering of new tissues, direct transplantations, stem cell implantation, and prosthesis. Still, the current complexity associated with this

approach asks for further research. The axolotl is an aquatic salamander capable of regenerating most organs (e.g. heart, brain, limb, tail, and kidney) throughout its lifetime. Their natural regeneration process depends on the accumulation of stem cells at the site of injury from which the new tissues originate. This process has been extensively studied, mainly with *in vitro* techniques. However, modern *in vivo* Molecular Imaging techniques have scarcely been used with this animal.

We performed an exploratory study on the capabilities of MRI and CT in imaging the regeneration of tails after amputation. The formation of the blastema and its evolution was visible by MRI over time. Also, the different regenerating structures (blood vessels, nerves, muscles, and vertebrae) could be distinguished. Blood vessels and the spinal nerve were the first regenerating structures visible followed by muscle and later the calcified vertebrae. In a parallel experiment MRI-based protocols for evaluating the cardiac function in axolotls were also defined. The imaging protocols establish the axolotl as an animal model to later study regeneration after a cardiac infarct. The results demonstrate the power of noninvasive imaging as for the first time such regrowth processes could be followed on a tissue level.

The thesis ends with **chapter 7**, giving a summarizing discussion, sketching the future perspectives of Molecular Imaging in biomedical research.

Summary

Acknowledgements

Well, here we are. You have just opened this thesis, looking for the discussion of results, eager to get intellectually drunk by the fantastic scientific contributions this collection of studies embodies and... BAM... you hit the Acknowledgements pages. You did not want to at first but now that you are here you are wondering: "hmm... let's see now... where is my name???". This is your lucky day because I can guarantee your name is written here (if it is not please email me at: where.is.my.name.you.ungrateful.portuquese@gmail.com for a full refund of the price you paid for this thesis).

(I did not follow a specific order for the acknowledgements... I only chose the first and last paragraphs)

First and foremost, Herr Professor Holger Gröll. The chocolate provider during those moments of stress that all researchers love to hate! He was also my supervisor. I think the greatest compliment I can give is stating that I hope that every PhD student out there has or will have a supervisor like you. You truly love research and you will stop at nothing to help and support your students. I mean, which other supervisor has a meeting at his place with a table of appetizers ready waiting for the bottle of a full bodied red wine I was bringing plus the draft version of a paper to review (chapter 3 by the way)? And he actually kept a straight face when I showed up with dreadlocks 4 months after signing the contract! There is not enough space to write about all the trips, conferences, and stories, so I will simply write some keywords to jog your memory Holger: *Helsinki expensive*; *"Schnella"*; *Eyjafjallajökull*; *Vinius*; *fire spiting*; *Excel sheets*; *axolotl*; *hotel-on-fire*. I hope we can continue to open bottles for many years to come and replace the title of "supreme supervisor" with "friend". Thank you for everything!

However, my Dutch adventure back in 2008 started with another "boss": Marcel Böhmer. He guided me through an internship at Philips and spiced up my interest in ultrasound and microbubbles which led to the Ph.D. During this time I got my ass kicked in squash (he made me run some 10 km in one game) and then in jogging in Bordeaux (I had to ask him to stop so I could take a breath). I am still confident I will get him on a capoeira class so I can have my revenge! Always supportive, and a great source for tools whenever I had to "klussen in huis", you were fundamental both inside and outside the lab. Dank je wel!

Although a PhD student from the TU/e, 99% of my time was spent in the laboratories of Philips Research. As such, I worked with several group leaders. Klaas Nicolay, from the Biomedical NMR TU/e group, thank you for your support throughout these years (and my apologies for only working with MRI towards the

Acknowledgements

very end) and for being my co-promoter! Oliver, Wendy, René, and Matthias thank you for facilitating the integration of the PhD students into the Philips Research teams and always making us feel part of the team. I learned a lot from your different leadership styles!

All the Philips Research staff I have worked with! There are too many to thank to for making my life easier and helping me develop as a researcher. To name but a few (simply because they were more directly involved in my projects): Charles, Ceciel, Edwin, Katia, Sander, Iris, Monique, Gerry, Katrin, Sandra, Tilman, Marc, Johan, Erica, Roland, Dirk, Suzanne. Sander, thank you for your artistic help with the images! Raffa, this would not have been possible without you. From the 6h00 experiments to the teachings on radiochemistry you were relentless (there was this one time you threw a calculator against me from 4 m away because I did something stupid but other than that great job!). Plus, of course, all the social life outside the lab to help keeping the head going inside the lab! Grazie mille!

CPV! The ladies (and David and Jo!!) that made the in vivo work possible: Caren, Carlijn, Melanie, Marleen, Marije.

The Biomedical NMR group! Thank you for always keeping a great atmosphere for both work and social life. A special thanks to Roel Cyril Op't Veld, Wolter de Graaf, and Gustav Strijkers without whom the Axolotl project would probably have failed!

The Grülltjes (aka AIO's)! Best start with the elderly. Anke! The "mother" to us all in the beginning and keeper of an exquisite collection of CT images of random insects found on the floor! Mariska, always with a PD-10 column in the chemistry lab! Good times we had during Sonodrugs! Sander, the in-your-face-mister-Nobel-prize-winner! The daily room temperature 7UP will stay with me for a long time! Nicole, I managed to finish without keeping my promise of understanding your super-fast Dutch with the ever present laughter in the middle! Good to have your enthusiasm around! Lucas, it-is-not-going-to-work, Starmans! Thank you for all the discussions and fresh carrots! Sin Yuin, your need to organize multicultural dinners was lekker (but you have to try wine one of these days!)? Good luck with your final writing... you are almost there! Steffie, I was lucky to support you during your MSc research and I think this new adventure you will go into will fit your professional ambitions like a glove! Esther, I still cannot understand how you manage to use that book worthy handwritten font in your lab books! Enjoy your PhD, have fun doing it! Tiemen, the whiskey man! Your fire starting skills are awesome! Good luck!

Klaus Tiemann, thank you for having me in your lab in Münster for 5 months for

the TIPS deep dive! Mareike, it was some crazy years with a lot of experiments but in the end something worked! A lab out of an empty room and an empty room out of a lab in the end (full circle).

Many thanks to my PhD defense committee members Kostas Kostarelos, Silvio Aime, Fabian Kiessling, Chrit Moonen, Carlijn Bouten, and Peter Hilbers for their comments and for being there for the defense.

Sonodrugs: The European project my PhD was a part of! Fifteen partners, 6 countries, 8 meetings, great people, parties, and yes, also science! We had a great start in Helsinki with national finish songs karaoke and dancing ending on the sunny and warm beaches of Cyprus!

The friends! You were not in the lab but you filled up my social life and that is priceless. There were way too many parties, dinners, and borrels so I will mention some references only: Eindhoven Italian Mafia (e.g. Valerio, Emanuella, Ginny and Albe, and many more), Capoeira crew, Tommi (India man!), Ana and Roman, Sol and Juan, Meritxell and Marco, Eszti and Rapha, Esther and Marc, Toy, Elsa, Cabeças, Pima, Rapoula, Tiago, Mellitus, Matos, Almeida, Fraga ... (cannot put you all!!!!!!)!

To all who were not mentioned in the text above: Thank you! (I blame my aging brain for that omission).

Família! Sempre presentes, sempre a apoiar... não se pode pedir mais! Por vezes, posso não ter dado a entender mas o facto de estarem aí foi fundamental! Beijos e abraços a todos. Francisco, sempre um porto seguro! Um beijo especial à Avó Melita!

Mãe, Pai, não é fácil estar longe tanto tempo seguido. No entanto, estão sempre prontos a ajudar no que for preciso. Foram muitos anos a "apostar" num filho e espero que identifiquem neste doutoramento os frutos da vossa persistência e carinho. Obrigado!

Life never walks alone. Its deadly sidekick is ubiquitous. And I hate that. Creating life is, at the moment, the only way to subdue the sidekick... to add a deeper meaning to life itself. Mariana, starting a family with you was the best thing of my life. Sure, we had fun in the beginning like most couples in love but then came the decision to have children and that took things to a whole new level. Clara and Xavier are most probably the best children in the world and the best thing we ever did. You were already my other half, adding emotions to reasoning and organization to chaos, but since 2012 we have added meaning to life. Obrigado aos três por fazerem parte da minha vida!

Acknowledgements

The names... most of them!

René Aarnink, Desiree Abdurrachim, Silvio Aime, João Almeida, Erica Aussems-Custers, Mike Averkiou, Corinna Bashiroto, Ad de Beer, Monique Berben, Monique Berben, Ayache Bouakaz, Carlijn Bouten, Marcel Böhmer, António Brisson, Sol Cabrera, Luís Carvalho, António Marques Costa, Rosa Marques Costa, Aissatu Mendes Dias, Roman Dittmar, Tiago Domingos, Katia Donato, Sander van Duijnhoven, Aaldert Elevelt, Fabrizio Evangelista, Federico Feliziani, Alessio Filippi, Emanuella Fioretta, Davide Fontanarosa, Filipe Fraga, Wilma Goldstein-Hermans, Wolter de Graaf, Armando Granate, Floortje de Groot, MIH group, Holger Grüll, Nicole Haex, Steffanie Hectors, Edwin Heijman, Carlijn van Helvert, Marleen Hendriks, Nicole Hijnen, Peter Hilbers, Igor Jacobs, Cassie Jones, Marion de Jong, Nico de Jong, Eric Kaijzel, Caren van Kamen, Fabian Kiessling, Suzanne Kivits, Esther Kneepkens, Rolf Lamerichs, Sander Langereis, Tilman Lappchen, Amélia Leitão, José Luís Leitão, Eugene Leyvi, Elsa Lobos, Clemens Löwik, Johan Lub, Christophoros Mannaris, Carlos Marques, Helena Marques, Marco Masserani, Luís Matos, Valentina Mazzoli, Denis Merkel, Roland van de Molengraaf, Chrit Moonen, Rick Moonen, Abdallah Motaal, Tiemen van Mourik, Mareike Mühlmeister, Miranda Nabben, Jules Nelissen, Klaas Nicolaij, Leonie Niessen, Roel Op't Veld, Steffie Peters, Pedro Pimentel, Jeanine Poppers, Meritxell Puig, Juan Quiroga, Balsundar Raju, Miguel Ramos, João Rapoula, Marc Robillard, Dirk Roos, Raffaella Rossin, Guido Salmasso, Francisco Sanches, Isabel Sanches, João Manuel Sanches, José Manuel Sanches, Tom Schreurs, Ralf Seip, Charles Sio, Mariska de Smet, Ana Soares, Gerry van Someren, Luc Starmans, Jürg Stippman, Gustav Strijkers, Zach Taylor, Esther Thole, Klaus Tiemann, Katrien Vandoorne, Sara Venturini, David Veraard, Iris Verel, Anke de Vries, Roland Vulders, Bart Wessels, Nico Willard, Siem Wouters, Sin Yui Yeo, Anna Yudina, Valerio Zerbi

List of publications

Full papers

1. P.G. Sanches, S. Peters, R. Rossin, E.L. Kaijzel, I. Que, C.W.G.M. Löwik, H. Grüll, *Bone metastasis imaging with SPECT/CT/MRI: a preclinical toolbox for therapy studies*, Bone, submitted, under review
2. P.G. Sanches, M. Mühlmeister, R. Seip, E. Kaijzel, C. Löwik, M. Böhmer, K. Tiemann, H. Grüll, Ultrasound-mediated gene delivery of naked plasmid DNA in skeletal muscles: A case for bolus injections, *J Control Release*, (2014).
3. P.G. Sanches, R. Rossin, M. Böhmer, K. Tiemann, H. Grüll, *Real-time imaging and kinetics measurements of focused ultrasound-induced extravasation in skeletal muscle using SPECT/CT*, *J Control Release*, 168 (2013) 262-270
4. P.G. Sanches, H. Grüll, O.C. Steinbach, "See, reach, treat: ultrasound-triggered image-guided drug delivery", *Therapeutic Delivery* 2(7), 2011

Abstracts (first author only)

1. P. Sanches, R. Rossin, E. Kaijzel, I. Que, R. Hoeben, C.W.G.M. Löwik, H. Grüll, "Multimodality imaging of bone metastases", 18th NKRv workshop, Netherlands, 2013
2. P. Sanches, R. Rossin, E. Kaijzel, I. Que, R. Hoeben, C.W.G.M. Löwik, H. Grüll, "Multimodality imaging of breast cancer bone metastases", World Molecular Imaging Conference, Ireland, 2012
3. P. Sanches, M. Mühlmeister, K. Tiemann, H. Grüll, "Ultrasound-mediated gene delivery to skeletal muscles *in vivo*", International Society of Therapeutic Ultrasound Symposium, Germany, 2012
4. P. Sanches, M. Böhmer, K. Tiemann, H. Grüll, "*In vivo* gene transfection mediated by focused ultrasound". World Molecular Imaging Conference, USA, 2011
5. P. Sanches, R. Rossin, M. Böhmer, K. Tiemann, H. Grüll, "Ultrasound drug delivery: *in vivo* SPECT/CT imaging and quantification", Biomedica Life Science Summit, Netherlands, 2011
6. P. Sanches, R. Rossin, M. Böhmer, K. Tiemann, H. Grüll, "Focused ultrasound induced extravasation: *in vivo* SPECT/CT imaging and quantification", Topics in Molecular Imaging Conference, France, 2011
7. P. Sanches, R. Rossin, M. Böhmer, K. Tiemann, K. Nicolaij, H. Grüll, "In vivo SPECT/CT imaging of focused ultrasound induced extravasation." *Nuclear Medicine and Biology* 37(6): 722-722, 2010

List of publications

8. P. Sanches, R. Rossin, M. Böhmer, K. Tiemann, K. Nicolaj, H. Grüll, "In vivo SPECT/CT imaging of focused ultrasound-induced extravasation", Technetium and Other Radiometals in Chemistry and Medicine Symposium, Italy, 2010
9. P. Sanches, R. Rossin, M. Böhmer, K. Tiemann, K. Nicolaj, H. Grüll, "Quantification of ultrasound-mediated local drug delivery with nuclear techniques", Biomedica Life Science Summit, Germany, 2010
10. P. Sanches, R. Rossin, M. Böhmer, K. Tiemann, H. Grüll, "SPECT-CT imaging and quantification of focused ultrasound induced extravasation", 15th European Symposium on Ultrasound Contrast Imaging, Netherlands, 2010

Conference proceedings (published)

1. P. Sanches, R. Rossin, M. Böhmer, K. Tiemann, K. Nicolaj, H. Grüll, "In vivo SPECT/CT imaging of focused ultrasound induced extravasation", in: U. Mazzi, W.C. Eckelman, W.A. Volkert (Eds.) Technetium and Other Radiometals in Chemistry and Medicine, SGEEditorali, Padova, Italy, pp. 547-550. ISBN 9788889884140, 2010 (Proceedings Terachem 2010 conference)

Invited presentations

1. Sanches *et al.* "Multimodal molecular imaging - an overview of studies in our laboratories", Bioscan User Meeting, Ireland, 2012

Invited Lecturer

1. Topic: "The axolotl: an animal model for regenerative medicine", Working with laboratory animals, Dutch Article 9, University of Maastricht, Netherlands, since 2013